Consejo Superior de Investigaciones Científicas - CSIC
Instituto de Ciencias de la Tierra "Jaume Almera"- ICTJA-CSIC

3D seismic imaging and geological modeling of the Hontomín CO_2 storage site, Spain

Tesis realizada por Juan Alcalde Martín para optar al título de Doctor dentro del programa de doctorado de Ciencias de la Tierra de la Universidad de Barcelona bajo la dirección de los doctores David Martí y Ramon Carbonell.

Juan Alcalde Martín

Barcelona, mayo de 2014

Directores: Tutor:

Dr. David Martí Dr. Ramon Carbonell Dr. Juan José Ledo

Esta tesis se ha realizado gracias al apoyo de la Fundación Ciudad de la Energía, a través de la ayuda para la realización de tesis doctorales en almacenamiento geológico de CO2, al acuerdo CSIC-CIUDEN ALM-09-027, para los estudios geofísicos encaminados a definir la estructura geológica seleccionada para la Planta de Desarrollo Tecnológico de Hontomín: Sísmica de reflexión 3D, tomografía sísmica, VSP y Red sísmica, con cargo al presupuesto de gastos del Ministerio de Industria, Energía y Turismo. Asimismo, este trabajo ha sido cofinanciado por el Programa Energético Europeo para la Recuperación (PEER), en el marco del proyecto OXYCFB300 Compostilla.

A mi abuela y a Placi

I don't want to live in a hole anymore. I'm going to do something about it.

-Fantastic Mr. Fox-

AGRADECIMIENTOS

Agradezco a la Fundación Ciudad de la Energía–CIUDEN que me haya proporcionado los medios necesarios para llevar a cabo esta tesis.

Aún no puedo creer que esté escribiendo los agradecimientos de mi propia tesis. He pensado en este momento desde que entré por la puerta del Almera en 2009, recién llegado a Barcelona y con la cabeza llena de dudas (y pelo). He pensado mucho en ello porque eso solo significa una cosa: que la tesis ya está escrita, que por fin voy a ponerle punto y final a este proceso durante el que he sentido alegrías, penas, frustración, ilusión e incluso ganas de matar. Ha sido un proceso arduo, lleno de trabas científicas y personales, y, por eso, tengo mucho que agradecer quienes me han acompañado durante estos años y me ha ayudado a llegar hasta aquí.

En primer lugar quiero dar las gracias a mis directores de tesis, los doctores D. Ramon Carbonell, D. David Martí y a D. Christopher Juhlin por su confianza y ayuda. Ramon, muchas gracias por confiar en mí desde el principio y por haber estado disponible siempre que te he necesitado. Siempre has sido optimista y me has dado el empujón que necesitaba mientras he ido dando mis primeros pasos en el mundo de la investigación. David, gracias por haber estado siempre ahí para lo bueno y para lo malo. Más que un director de tesis, te has portado siempre como un verdadero amigo. Me alegro mucho de que te decidieses a dirigirme. Chris, jag skulle vilja tacka dig för din expertis och hjälp (som har varit ovärdelig för databehandlingen) och för att du har visat hur ett riktigt proffs arbetar.

También tengo que darle las gracias a la gente de mi grupo de trabajo sin las que nunca habría sacado esto para adelante. En primer lugar gracias a la infatigable Puy Ayarza, que me metió el gusanillo de la geofísica en la universidad y me puso en bandeja mi primer trabajo y mi beca de doctorado. Puy, sin ti no estaría donde estoy ahora mismo, así que gracias de corazón. Y hablando de corazón, tampoco puedo olvidarme del hombre con el corazón más grande de este mundillo y *alma mater* del proyecto, Andrés Pérez Estaún. Andrés, no me importa lo que digan los médicos: ¡tienes un corazón de oro! ¡Vuelve pronto, que no hay nadie como tú! Por supuesto no me puedo olvidar de los *Tres Mosqueteros*, David, Ignacio y Eduard. Menos mal que habéis trabajado codo a codo conmigo, porque sin vuestra ayuda probablemente hubiera dejado el doctorado hace un par de años. Gracias por vuestro ánimo, ayuda y, no menos importante, por vuestro buen humor. Nacho, no cambies nunca, ya no quedan personas buenas y amables (y calvas) como tú. Y no hagas caso a los otros dos, ¡eres un tío "guay"! Eduard, m'agradaria arribar a ser la quarta part del geòleg i professional que tu ets. Gràcies de tot cor per ajudar-me amb la geologia, traient temps d'on no el tenies. Sense tu, no hauríem fet res de res.

During these years, I am honoured to have worked with many professionals and I am grateful to all of them. I would like to thank especially two persons that kindly aided me when I was completely lost. Alireza, thank you for your help with the data processing and for showing me the meaning of "hard work"; it was a pleasure working with you. Merci charles pour votre aide sur l'expérience VSP. J'espère que nous aurons bientôt l'occasion de partager une bonne bouteille de vin! I would also like to thank the people from the University of Edinburgh and especially Mark Wilkinson, who believed in me before finishing this thesis.

Tampoco puedo olvidarme de los compañeros de fatigas, precarios y camaradas de estos años. Para toda la *people* del Almera, Mar, Alba, Lavi, Gio, los alocados Jan y Siddique, el productivo Xevi (¡visca Olot!) y demás precarios: mucho ánimo con vuestras tesis, suerte, que sí que se puede, hay luz al final del túnel, y todos los demás clichés que se os ocurran. ¡Y un fuerte abrazo para todos! Al resto de compañeros con los que he coincidido trabajando también quiero darles las gracias por estos años: Mario, Bea, Sofía, Imma y en general a todo el Almera; a toda la gente maja de CIUDEN, la Universidad de Barcelona y de Uppsala; a mis compañeros de Máster y, en general, a todo aquel con quien he compartido horas de quejas, llantos, risas y *tontunas*. Special thanks to my two friends in Uppsala, Monika and Daniel, who helped to survive the severe Swedish winter; friendship is found even in the most remote locations. Daniel, the Pirate Project was a success and it was all because of you; ahoy! También, cómo no, al ideólogo del proyecto Checomor: Emili, allá donde estés, ya sabes que el Flanders sueco te está vigilando. Y mucho ánimo a los becarios de CIUDEN con los que he compartido la ¿suerte? de estar en este proyecto: a los que se marcharon antes de tiempo (Laura, Manuel, Eloi y María) y, sobre todo, a los que vivieron el día a día conmigo en Ponferrada: Amanda, Javi y Jacobo; ánimo, mucha suerte; ¡volveremos a vernos y a compartir un buen solomillo!

Quiero darle las gracias a la gente ajena al trabajo que he conocido y me ha soportado desde pequeño, los mejores amigos que nadie pueda tener. Sin duda gracias a la *Olympics&Negrita Crew* (“Tender” Davis y Luizao) por las innumerables horas de *taponcines* y buenos momentos. Davis, sin ti nada hubiera sido igual; eres el mejor compañero de piso que el Conde Crápula podría desear. Luis, muchas gracias por ser un buen amigo, por tener siempre un buen consejo a mano y por arreglarme la impresora. También muchas gracias a Martuncias, mi queridísima compañera de aventuras, y a Javi, con quién tan bien lo pasé en Alcañiz y con quien acabaré montando una empresa de cualquier chorrada y forrándonos. Asimismo a mis amigos de la carrera, sobre todo a los malvados Paula, Álex y Carmenchu; todos sabíamos que no volveríamos a vivir juntos en la misma ciudad, pero siempre me tendréis ahí para insultaros desde el cariño. Y por supuesto, a mis amigos de toda la vida, a mi querida Santísima Inquisición, a Julio, Astu, Ole, Manu, Guille, Zato, Nice y Carballo, que siempre han estado ahí para lo bueno y lo para malo (y de paso para bajarme los *humines* cuando lo he necesitado, por qué no decirlo); chavales: ¡sois los mejores!. Y un extra para Carballo con el que he compartido tantos buenos momentos en Barcelona; ¡ánimo colega, que ya falta poco!

El mundo de la investigación puede ser duro, desagradecido, competitivo, incluso salvaje. Sin embargo, a veces algo distinto aparece en el horizonte, como una manta en un día frío de Uppsala, como un paraguas en un día lluvioso de Ponferrada, como una luz en un día oscuro de Edimburgo y, también, por supuesto, como una buena paella en un día de resaca en Barcelona. A veces, algo te toca, te guía, te ayuda, te consuela, te anima. A ti, Xènia, te agradezco especialmente que hayas aparecido para iluminar mi vida.

Pero sobre todo quiero agradecerle a mi familia que me haya dado su apoyo incondicional desde que salí del cascarón. Gracias a mis primos y tíos, y en especial a Maru, Luis y Guzmán, sin cuyo cariño y comprensión no hubiera sobrevivido a la dureza salvaje del Raval (guiño, guiño).

Y gracias, de corazón, a mi familia más cercana: Luis, Amelia, César, Placi y la Gatita, a los que cada vez quiero más a pesar de la distancia. Siempre estáis ahí para todo. Os echo de menos.

Y por último a mi abuela, la más maja de todas las abuelas del mundo mundial. Siempre te recordaré.

Sois los mejores.

You are the best.

Sou els millors.

Juan Alcalde Martín

Edimburgo, 2014.

CONTENTS

PROLOGUE

This thesis is organized as a compendium of three scientific articles, published in peer-reviewed, scientific journals indexed in the "Journal Citation Report" of the Institute for Scientific Information (ISI-JCR). The three articles describe the geological characterization of the Hontomín site by means of 3D seismic data, acquired for this purpose, as well as the available well-log and regional data. The 3D seismic experiment described in this thesis represents the first high-resolution 3D seismic dataset acquired on land by the Spanish academic research community.

The three articles form the core of this thesis and constitute the main scientific effort developed therein. These are:

- Alcalde, J., Martí, D., Calahorrano, A., Marzán, I., Ayarza, P., Carbonell, R., Juhlin, C. and Pérez-Estaún, A. 2013a. Active seismic characterization experiments of the Hontomín research facility for geological storage of CO2, Spain. International Journal of Greenhouse Gas Control, 19, 785-795.

- Alcalde, J., Martí, D., Juhlin, C., Malehmir, A., Sopher, D., Saura, E., Marzán, I., Ayarza, P., Calahorrano, A., Pérez-Estaún, A., and Carbonell, R. 2013b. 3D Reflection Seismic Imaging of the Hontomín structure in the Basque-Cantabrian Basin (Spain). Solid Earth4, pp. 481-496.

- Alcalde, J., Marzán, I., Saura, E., Martí, D., Ayarza, P., Juhlin, C., Pérez-Estaún, A., and Carbonell, R. 2014. 3D geological characterization of the Hontomín CO2 storage site, Spain: multidisciplinary approach from seismics, well-logging and regional data. Tectonophysics (accepted).

The thesis begins with an Introduction (**Chapter I**), in which the motivations and aims of the thesis are presented. These include the problematic derived from anthropogenic emissions of CO_2, and present Carbon Capture and Storage technology as an effective method to reach energetic sustainability. This chapter also includes the state-of-the-art seismic reflection method applied to CO2 storage, as well as an outline of the regional and local geology of the study area.

The first article (Alcalde et al., 2013a) constitutes **Chapter II** of the thesis. It presents and describes the active seismic experiments conducted at the Hontomín site for the seismic characterization. The data acquisition is described in detail, with an emphasis on the most relevant factors that affected the quality of the acquired data or that biased the processing applied. These factors include the geomorphological/topographical aspects of the study area, logistical issues during the acquisition. The effects on the seismic records of a near-surface velocity inversion are also discussed. This contribution also shows a preliminary seismic image of the subsurface, which allows outlining the general dome shape of the target structure.

The second article (Alcalde et al., 2013b) comprises **Chapter III** of the thesis. It outlines the processing applied to the seismic data that led to the final migrated seismic image. It includes a detailed discussion about which processes were more effective in enhancing the quality of the obtained image (i.e., source matching, static corrections and 3D-DMO correction). The image was judged to be suitable for interpretation and constitutes the primary seismic model, to be used as reference baseline during the monitoring stage. Furthermore, the top of the Jurassic dome structure was mapped, allowing us to provide an overall estimation of the size of the target structure, which is a 107 m2 elongated dome with a maximum CO2 storage capacity of 1.2 Gt.

The third article (Alcalde et al., 2014), included in **Chapter IV** of the thesis, focuses on the interpretation of the seismic image and the building of a 3D geological model. The quality of the seismic data required a geologically driven approach to enable interpretation. This approach used a conceptual model as reference, which was inferred in the first place from the correlation of the available well-log data and later improved by the seismic facies analysis and the regional geological data. The conceptual model was used to interpret the seismic data and resulted in a 9-layered 3D geological model and a thorough description of the fault system present in the area.

EXTENDED SUMMARY

S.1.- INTRODUCTION

The amount of CO_2 emitted into the atmosphere due to human activities (mainly due to fossil fuel consumption) has produced an enhancement of the greenhouse effect evidenced by a rise in Earth's surface temperature ("global warming") (IPCC 2007). Theoretical considerations on energy consumption estimations for the following decades suggest that our dependency on fossil fuels will be total (IPCC, 2005). The European Union (EU) approved in 2008 a set of regulations in order to meet the climate and energy targets for 2020 (Streimikiene, 2012), including the Carbon Capture and Storage (CCS) technology (Directive 2009/31/EC; Annex 1). This CCS technology attempts to reach energetic sustainability (Lovell, 2011) by extracting the CO_2 from the combustion residues in large scale industrial emissions ("capture"), transport it and store it in feasible geological formations where it does not contribute to global warming ("storage").

The geological storage of CO_2 (GSC) in deep saline aquifers provides a great storage potential, especially in countries without extensive natural energy resources, such as Spain (Dooley et al., 2004, IPCC 2005; IEA GHG, 2009; Pérez-Estaún et al., 2009). A potential deep saline aquifer site should meet a number of requirements in order to be considered suitable for GSC (Bachu, 2003; Orr, 2004; Baines and Worden, 2004; Chadwick et al., 2008; CO2CRC, 2009; IEA GHG, 2009; Pérez-Estaún et al., 2009). These include (1) a formation or a number of formations with the appropriate physical properties (porosity, permeability, thickness) for the CO_2 storage (reservoir); (2) a confined saline aquifer within the target formations which demonstrates the efficacy of seal formations; (3) a formation or a number of formations immediately above the reservoir with a proven impermeability to the migration of the injected CO_2 (seal); and (4) to be placed at sufficient depth (below 800 m), in which the carbon dioxide can be injected in supercritical state, which is favorable for the injection, amongst others.

The European Union with its European Energy Programme for Recovery (http://ec.europa.eu/energy/eepr/index_en.htm) funds a number of GSC projects. Amongst them, the "Compostilla OXYCFB300 Project" (www.compostillaproject.eu) is currently being undertaken in Spain under the leadership of the CIUDEN

Foundation (www.ciuden.es). The storage program inside the Compostilla project involves the development of a Technological Development Plant (TDP) dedicated to geological storage in Hontomín (Burgos, Spain), the study area presented here (Fig. S.1). The objective of this GSC site is the creation of a scientific laboratory that will develop the knowledge and state-of-the-art technologies needed for GSC. This research facility aims to provide a multidisciplinary understanding of the processes taking place within the reservoir and seal at the storage site. It should also demonstrate the feasibility and help to reduce the costs of its industrial application.

This thesis focuses on the geological characterization and suitability assessment for GSC of the Hontomín site, by means of the 3D seismic dataset acquired for this purpose. The 3D seismic reflection data provides useful information for unraveling the 3D geological architecture of the reservoir-seal and overlying structures, and places constraints on the fault geometry and distribution (e.g. Thomson and Hutton, 2004; Juhlin et al., 2007; Malehmir and Bellefleur, 2009). Furthermore, the seismic technique is sensitive to some of the changes in physical properties produced by the injection of CO_2 in the storage formations (e.g., Rutqvist and Tsang, 2002; Arts et al., 2004; Chadwick et al., 2005; Alsuahil, 2011). An assessment of the suitability of the baseline seismic model for monitoring purposes is also included in this work.

S.2. AIMS OF THE THESIS

The aims of this thesis include the seismic baseline modeling and geological characterization of the Hontomín CO_2 storage site, by means of the 3D seismic reflection and well-log data. The resulting geological model is used to assess the suitability of the site for GSC purposes.

The aims related to the seismic baseline modeling are:

a) Develop and implement a processing sequence aimed at obtaining a 3D seismic image of the subsurface that is suitable for geological interpretation.
b) Study, characterize and understand the main geological features affecting the quality of the final image.

c) Identify the key processing steps with a higher impact on the quality of the final image.
d) Analyze the suitability of the processed dataset for the monitoring of CO_2.

The aims related to the geological characterization at the Hontomín storage site are:

a) Obtain a 3D structural model of the Hontomín subsurface through seismic interpretation, including the geometry and detailed distribution of the main geological layers and faults.
b) Provide a geodynamical, tectonic and stratigraphic model of the Hontomín structure within its regional geological frame.

The aims related to the assessment of the suitability of Hontomín for GSC purposes are:

a) Analize the site characteristics to ensure the safety, security and suitability of the Hontomín site for GSC, based on the resulting geological model.
b) Identify the most suitable position for the projected injection and monitoring boreholes.
c) Provide the scale of the Hontomín structure in terms of maximum CO_2 storage capacity and calculate the maximum capacity of the selected storage structure.

S.3. STRUCTURE OF THE THESIS

This thesis is organized as a compendium of three scientific articles, published in peer-reviewed, high-impact scientific journals indexed in the "Journal Citation Report" of the Institute for Scientific Information (ISI-JCR). The three articles describe the geological characterization of the Hontomín site by means of the use of 3D seismic data, acquired for this purpose, as well as the available well-log and regional data.

The three articles form the core of this thesis and constitute the main scientific effort developed therein. These are:

- Alcalde, J., Martí, D., Calahorrano, A., Marzán, I., Ayarza, P., Carbonell, R., Juhlin, C. and Pérez-Estaún, A. 2013a.Active seismic characterization experiments of the Hontomín research facility for geological storage of CO2, Spain. International Journal of Greenhouse Gas Control, 19, 785-795.
- Alcalde, J., Martí, D., Juhlin, C., Malehmir, A., Sopher, D., Saura, E., Marzán, I., Ayarza, P., Calahorrano, A., Pérez-Estaún, A., and Carbonell, R. 2013b.3D Reflection Seismic Imaging of the Hontomín structure in the Basque-Cantabrian Basin (Spain).Solid Earth4, pp. 481-496.
- Alcalde, J., Marzán, I., Saura, E., Martí, D., Ayarza, P., Juhlin, C., Pérez-Estaún, A., and Carbonell, R. 2013c. 3D geological characterization of the Hontomín CO2 storage site, Spain: multidisciplinary approach from seismics, well-logging and regional data. Tectonophysics (submitted).

The thesis begins with an Introduction (Chapter I) in which the motivations and aims of the thesis are presented. These include the problematic derived from anthropogenic emissions of CO_2 is exposed, and the CCS technology is presented as an effective technology to reach an energetic sustainability. This Chapter also includes the state of the art of the seismic reflection method applied to CO_2 storage, as well as an outline of the regional and local geology of the study area are also included in the this Chapter.

The first article (Alcalde et al., 2013a) constitutes the Chapter II of the thesis. It presents and describes the active seismic experiments acquired in the Hontomín GSC site for the seismic characterization. The data acquisition is described in detail, with an emphasis on the most relevant factors that affected the quality of the acquired data or that biased the processing applied. The article also shows a preliminary seismic image of the subsurface, that allows outlining the general dome shape of the target structure.

The second article (Alcalde et al., 2013b) composes the Chapter III of the thesis. It outlines the processing applied to the seismic data that led to the final migrated seismic image. It includes a detailed discussion about which processes were more effective to enhance the quality of the obtained image. The image is suitable for interpretation and constitutes the primary seismic model, to be used as reference baseline during the monitoring stage. Furthermore, the top of the Jurassic dome structure was mapped, allowing us to provide an overall estimation of the size of the target structure.

The third article, included in the Chapter IV of the thesis, focuses on the interpretation of the seismic image and the building of a 3D geological model. The quality of the seismic data required a geologically driven approach to achieve the interpretation. This approach used a conceptual model as reference, which was inferred in first place from the correlation of the available well-log data and later improved by the seismic facies analysis and the regional geological data. The conceptual model was used to interpret the seismic data and resulted in a 9-layered 3D geological model and a thorough description of the fault system present in the area.

S.4. GEOLOGICAL SETTING OF HONTOMÍN

The CO_2 storage site of Hontomín is enclosed in the southern section of the Mesozoic Basque-Cantabrian Basin, named “Plataforma Burgalesa” (Serrano and Martínez del Olmo, 1990; Tavani, 2012) (Fig. S.1). This domain is located in the northern junction of the Cenozoic Duero and Ebro basins, forming an ESE-dipping monocline bounded by the Sierra de Cantabria Thrust to the North and the Ubierna Fault System to the South (Tavani, 2012).

Three main deformation stages, affected the study area during the Mesozoic and Cenozoic (Tavani, 2012; Tavani et al., 2013). First, a Permian-Triassic extensional stage led to the development of ESE-WNW and E-W trending faults (Ziegler, 1989; García-Mondéjar et al., 1996). The second rifting event, linked to the opening of the North Atlantic and Bay of Biscay (Le Pichon and Sibuet 1971; Montadert et al. 1979; Ziegler 1988; García-Mondéjar et al., 1996) generated the Plataforma Burgalesa along with the Basque-Cantabrian basin. This event inherited ESE-WNW striking faults and generated NNE-SSW striking extensional faults, oriented at an angle of 75-80^o with the previous faults (Tavani and Muñoz, 2012; Tavani et al., 2013). During this second rifting event, Upper Triassic Keuper evaporites acted as a major decoupling zone, imposing different deformation styles in the cover sequences and in the Paleozoic basement (Tavani et al., 2011; Alcalde et al., 2013b; Tavani et al., 2013). In particular, this decoupling enabled the development of extensional forced folds in the supra-salt cover, led by coeval evaporite migration and faulting in the sub-salt basement (Tavani et al., 2013). Finally, the latter Pyrenean orogeny originated a compressional environment which caused reverse, right-lateral and left-lateral reactivations of inherited faults (Tavani et al., 2011; Quintà and Tavani, 2012; Tavani et al., 2013).

From a stratigraphic perspective, the Mesozoic succession in the Hontomín structure starts with the evaporites and clays of the Triassic Keuper Facies, which forms the core of the target dome. The Lower Jurassic is composed of evaporites, dolomites and marls, and lies over the Keuper Facies (Pujalte et al., 2004; Quesada et al., 2005). The upper part of the Lower Jurassic and the Middle Jurassic series is constituted by shallow marine carbonates and hemipelagic ramp sediments which can be divided in four units: Lower Jurassic (1) Carbonate, (2) Marly and (3) Pelletic Lias units and a Middle Jurassic carbonate (4) Dogger unit. The Purbeck Facies (Late Jurassic-Early Cretaceous in age) is formed by clays, sandstone and carbonate rocks, placed uncomformably on top of the Jurassic marine rocks. The Lower Cretaceous succession is completed by siliclastic sediments of the Weald Facies, and the Escucha and Utrillas formations. They are made of fluvial deposits that alternate channel filling sandstones and flood plain shale sediments. The uppermost rocks exposed in the Hontomín area are Upper Cretaceous carbonates and Cenozoic rocks (lacustrine and detritic) lying uncomformably over the Mesozoic successions (Vera, 2004).

The reservoir and seal formations are Jurassic in age, and form in the Hontomín area a dome-like structure with an overall extent of 5x3 km2. The target CO_2 injection point is a saline aquifer included in the carbonate reservoir-seal system at about 1500 m deep. The target reservoir formation is formed by a dolostone unit known as “Carniolas” and an oolitic limestone. The reservoir levels contain saline water with more than 20 g/l of NaCl. The minimum thickness of the reservoir units is 100 m. The potential upper seal unit comprises marlstones and black shales from a hemipelagic ramp (Pliensbachian and Toarcian; Vera, 2004).

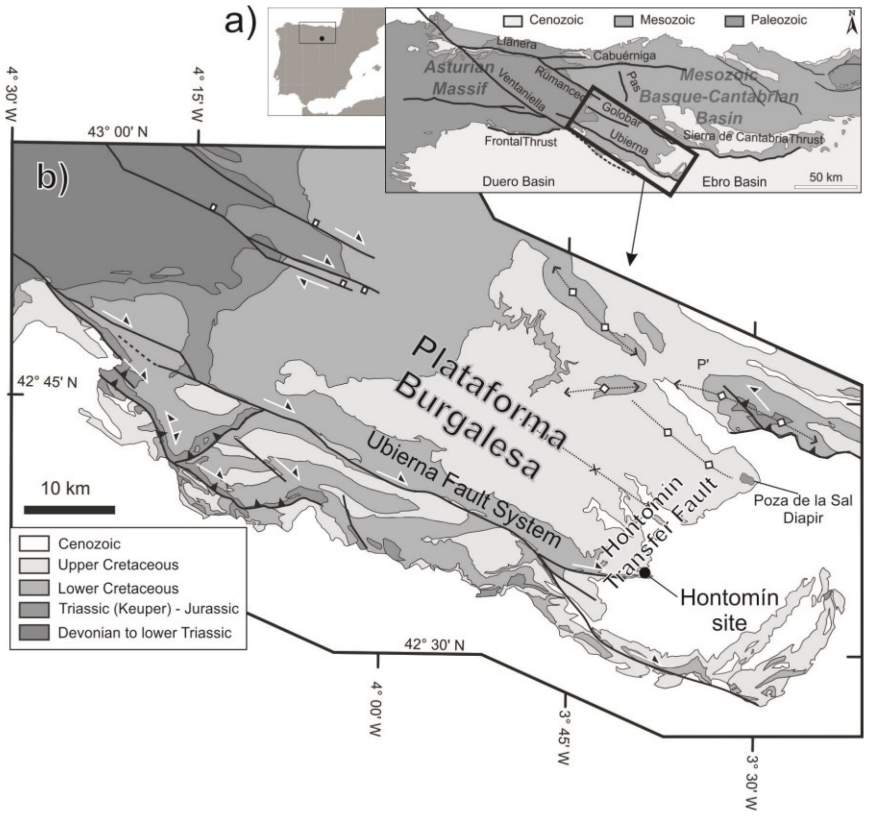

Fig. S.1: (a) Location of the study area within the Iberian Peninsula, and geological map of the Basque-Cantabrian Basin and Asturian Massif area with labels of the main features (modified from Tavani et al., 2013); (b) geological map of the southern portion of the Basque-Cantabrian Basin, with detail of the Plataforma Burgalesa and the Hontomín location (modified from Tavani et al. 2011).

S.5. 3D SEISMIC MODELING

S.5.1. Data acquisition

The acquisition parameters of the Hontomín 3D seismic survey were selected based on the knowledge derived from previous studies in the area, including surface geology, vintage 2D seismics and well-log correlation data (Gemodels/UB 2011, internal report).

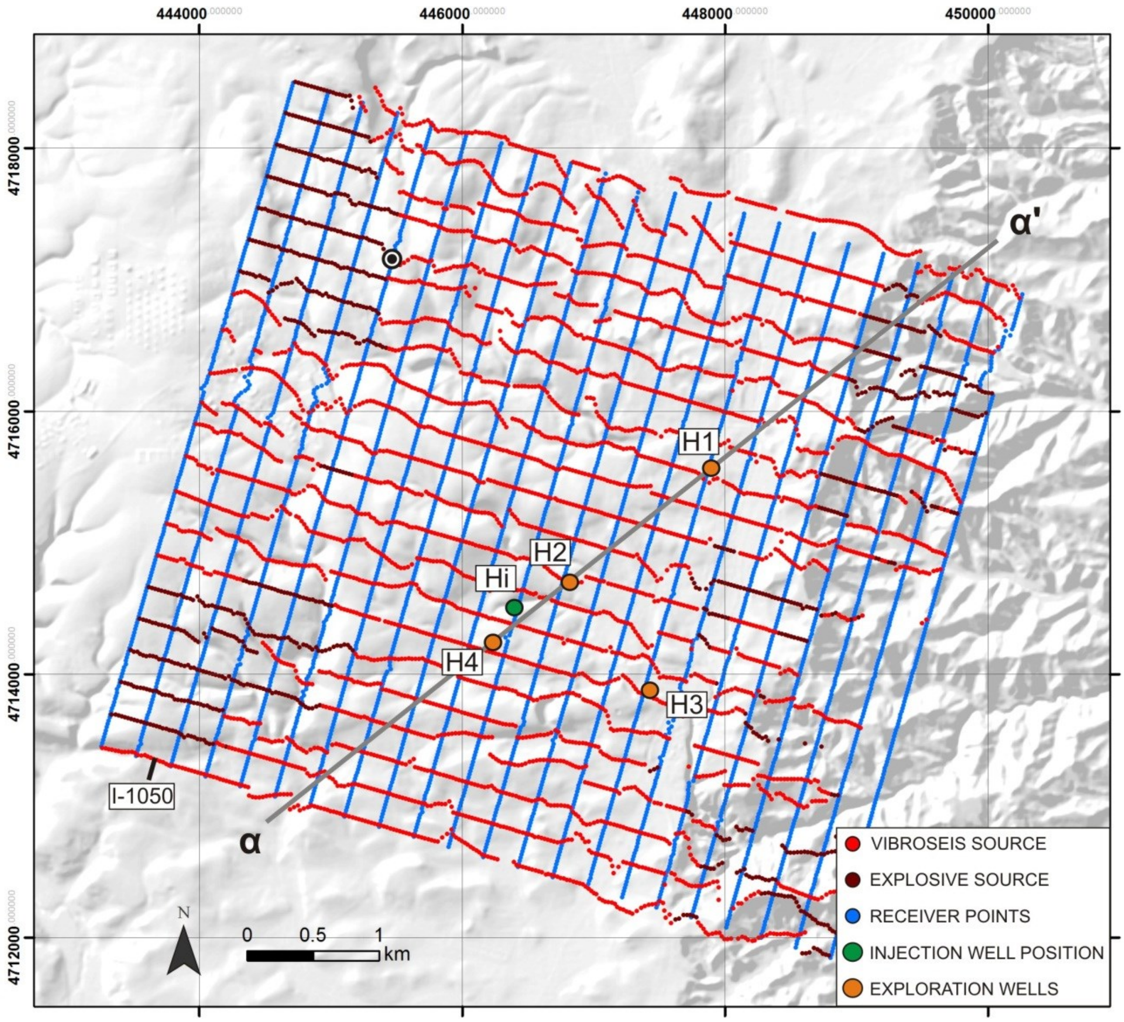

Fig. S.2: Map with the position of the elements of the 3D seismic reflection experiment acquired in Hontomín. Light red points mark the position of Vibroseis source shot points. Deep red points mark the position of the explosive source shot points. Blue points mark the receiver positions. The green circle marks the proposed position for the CO_2 injection borehole. The orange circles mark the position of previous boreholes (drilled for oil exploration).

The 3D seismic reflection survey covered 36 km^2. The acquisition area was selected to illuminate/image the target structure in all its extension. The survey geometry included 22 source lines perpendicular to 22 receiver lines, with intervals of 25 m between sources and receivers (Fig. S.2). The distance between receiver lines was 250 m, and source lines 275 m. The survey was acquired in 5 stages corresponding to different patches (swaths), with patches at the edge of the survey consisting of 6 active receiver lines, and the inner patches consisting of 10 receiver lines. A maximum of 120 channels were active per receiver line, resulting in a maximum of 1200 traces per shot gather.

The survey was originally designed to be fully acquired with a Vibroseis source (M22 vibrators). However, logistical issues (mainly due to the rough topography in the eastern part) forced the use of explosives in about 24% of the acquired data. The selected parameters for the Vibroseis source were two 16-s sweeps, with an 8-80 Hz bandwidth. The explosive source consisted of 450 g of explosives, deployed in three 1.5 m deep holes for each shot point.

S.5.2. Data processing

The relatively regular pattern of the acquisition geometry (Fig. S.2) gives a natural bin size of 12.5 X 12.5 m for the CDP bins, resulting in a maximum CDP fold of 36 traces/CDP. This fold value is relatively conventional in land surveys and for reservoir characterization (Ashton et al. 1994; Roche, 1997) and affordable from the academic point of view. The available well-log data indicate that the lithologies with higher impedance contrast are located above 1400 ms twt in most cases. Taking this into account the data were processed down to 1500 ms. The processing flow was designed and implemented in order to enhance the S/N ratio and image the target structures (Table 1).

Two energy sources, Vibroseis and dynamite, were utilized in the survey (Fig. S.2), and efforts were made to match the wavelets and bulk time shifts between both types, in order to improve the lateral continuity of the final stacked volume. In this sense, a phase and time shift was applied resulting in enhanced reflector continuity and strength in areas of the stacked section, which contained both dynamite, and Vibroseis traces in the pre-stack gathers.

Table S.1: processing steps applied to the seismic data.

Step	Parameters
1	Read 1.5 s SEG-Y data
	Trace edition: 140000 traces removed (3.2 %)
	First break picking (manual): 500 m offset range, 670,000 times picked
2	Spherical divergence correction
3	Source matching: -150° phase shift, 20 ms time shift applied to the explosive data
4	Surface consistent deconvolution: filter 100 ms, gap 14 ms, white noise 0.1 %
5	Elevation statics: datum 1070 m, replacement velocity 3500 m/s
5	Refraction static corrections
8	Air wave mute
9	Spectral equalization: 20 Hz window length, 20-30-90-120 Hz bandpass filter
10	Time-variant bandpass Filter: 35-50-100-140 Hz at 0-300 ms 27-40-85-120 Hz at 500-800 ms 20-30-70-100 Hz at 900-1500 ms
11	Residual statics (alternate with velocity analisys)
12	Velocity Analysis
13	AGC: 250 ms
14	NMO: 50% stretch mute
15	3D DMO correction
16	Stack
17	Trace balance: window 300-1300 ms
18	Butterworth bandpass filter: 20-30-100-135 Hz (0.5-0.95-0.95-0.5)
19	Post-stack deconvolution: gap=20 ms
20	Spectral equalization: 20 Hz window length, BP=20-30-80-100 Hz
21	F_{XY}-deconvolution: Inline and crossline directions
22	2.5 Finite-difference time migration, 45° algorithm
23	Top mute

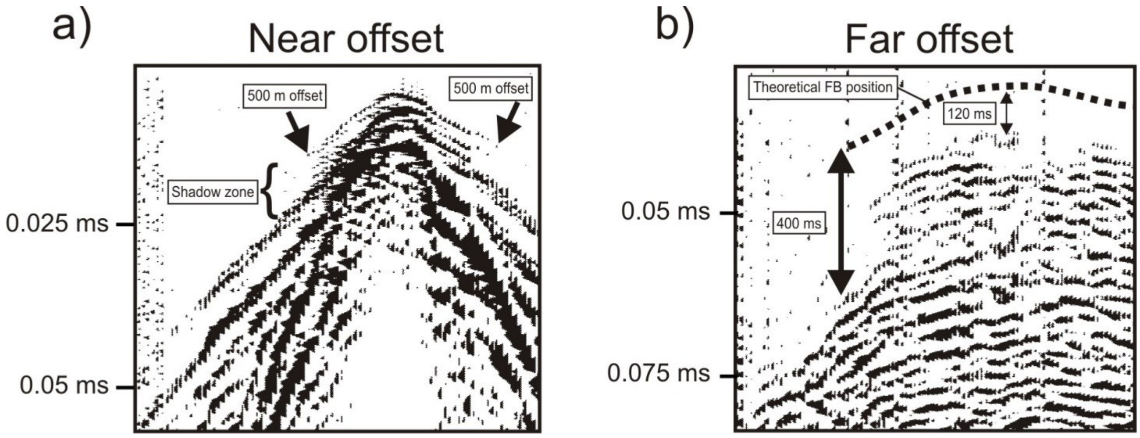

Fig. S.3: Example zoom of the upper part of two set of traces showing the effects of the "shadow zone" in the data at a) near offset and b) far offset.

Certain corrections were performed in order to diminish the disparity in the amplitudes and frequency content of the shot-gathers. The frequency contents were equalized by the use of combined bandpass filtering and spectral equalization in the pre- and post-stack stages. The high amplitude contrast forced the use of AGC and trace balancing (250 and 300-1300 ms time windows, respectively), since the spherical divergence correction did not completely equalize the amplitudes.

As observed in similarly difficult reservoir imaging experiments, the most relevant processing steps for reaching a good final image were the elevation and refraction static corrections (e.g. Juhlin 1995; Malehmir et al., 2012). In the Hontomín case, they were essential for improving the final image due to the large topographic changes (up to 200 m) and heterogeneous geology present in the study area. This complex shallow subsurface generated a "shadow zone", resulting in lack of clear first arrivals in the data at offsets greater than 300 m (Fig. S.3), observed as a sharp (Fig. S.3a) or as gradual loss of amplitude (black arrows in Fig. S.3b) with increasing offset. The existence of this shadow zone added difficulty to the picking of first arrivals in the near offset traces, and impossible at offsets larger than about 700 m. In spite of this difficulty, more than 670,000 first breaks, ranging from 0-500 m offsets, were manually picked. The resultant static model was very successful in improving the seismic image, which is in accordance with the heterogeneous surface geology.

Velocity analysis after static corrections provided further support for the existence of a velocity inversion between 200 to 500 ms. The NMO-velocity reduction in this interval ranged from 300 to 600 m/s. The CDP gathers show disrupted reflections before and after NMO corrections. After a satisfactory NMO model had been obtained, a 3D Kirchhoff DMO code (based on Hale and Artley, 1993) was applied to the pre-stack data, using the NMO velocities as initial input. Although the Hontomín structures are not steeply dipping, the 3D DMO processed volume shows increased coherency and improved definition of the flanks of the dome, as well as improvement in the continuity of reflections. Post-stack F-XY-deconvolution in the inline and crossline directions was implemented to remove random noise and further increase coherency. A 45° finite-difference post-stack time migration algorithm was chosen, due to the spatial variation of the velocities present in the study area.

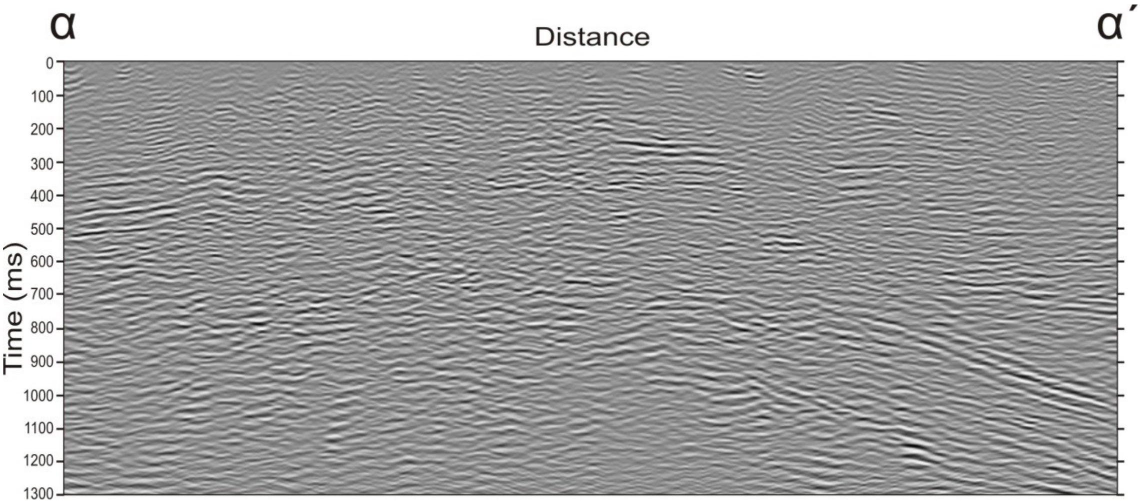

Fig. S.4: First 1300 ms of the migrated section α-α' (location marked in Fig. S.2) processed with the flow outlined in Table 1.

S.5.3. Analysis of the seismic model

The time-lapse monitoring of injected CO_2 requires that changes in the reservoir properties (i.e., saturation, pressure and temperature) caused by the injection of the CO_2 produce a detectable change in the seismic parameters (i.e., P and S-wave velocity and density) (Urosevic et al., 2010; Dixit et al., 2012). Among other properties, seismic monitoring commonly examines the variations in travel time (i.e., changes in velocity) and amplitude (i.e., changes in impedance) of the reflections in order to map the spatial extent of the injected CO_2. In the Hontomín seismic model, the velocity model used to convert the sedimentary layers to depth was extracted from the sonic logs, adapted to the 3D structures mapped and finally checked against the NMO-velocity model to ensure its consistency. The resulting velocity model is therefore coherent with the interpreted horizons and well constrained around the injection area and, thus, could be considered an appropriate baseline velocity model. The use of AGC within the workflow (Table S.1) helped to obtain a good quality final image, which is essential for the interpretation process. However, AGC can impair the suitability of the seismic baseline model because it overprints the amplitude character of the dataset. The AGC could be replaced by true amplitude recovery processes (e.g., spherical divergence and linear gains) in the processing sequence, before the dataset is used as a reference in a time-lapse monitoring study based on amplitude variations. A detailed test on the parameters of these processes could provide an effective tool for equalizing the amplitudes without losing the “amplitude character” of the traces, which AGC could erase (Maslen, 2014).

S.6. GEOLOGICAL MODELING

S.6.1. Seismic interpretation

To address the interpretation of the complex migrated final section, a geologically supervised interpretation was carried out based on a pre-defined conceptual model. This interpretation approach benefited from well-log, seismic and regional geology; however, the well-log correlation was the starting point of the conceptual modelling. The 39 interpreted well-tops were analyzed to identify possible tecto-sedimentary events, which were subsequently dated based on the thickness relationships of the formations with each other. These proposed events were then checked and correlated with the events determined in regional works carried out in the study area (e.g., Serrano and Martínez del Olmo, 1990; García-Mondéjar, 1996; Tavani et al., 2011 and 2013; Quintà and Tavani, 2012; Tavani and

Muñoz, 2012). This approach allowed detailed delineation of 8 surfaces, from Jurassic to Cenozoic (Fig. S.4 and S.5), and 4 sets of faults (Fig. S.6).

The analysis of the fault system was a critical step in the geological modelling process because the faults determine the main structural changes in the Hontomín subsurface and provide the major indications of the potential tecto-sedimentary events occurred in the area. Four sets of faults were identified in the seismic cube: set "N", "X", "S" and "E" (Fig. S.6). Sets "N" and "X" are normal faults affecting Jurassic units, whereas set "S" and "E" faults affect the entire sedimentary column. Two major faults corresponding to the latter sets ("Southern-Fault" and "Eastern-Fault", respectively) divide the study area in three structural blocks: the Eastern, the Central and the Southern block (Fig. S.6). This division is observed in all the interpreted layers.

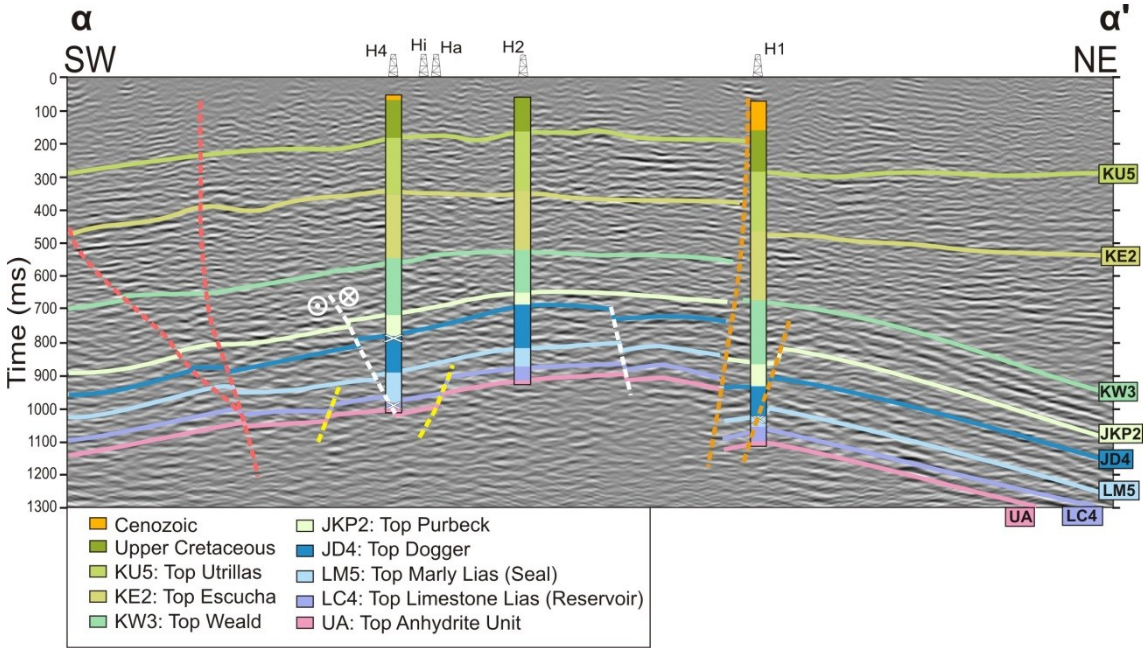

Fig. S.4: First 1300 ms of the migrated section α-α' (location marked in Fig. S.2) with the final interpretation of the main horizons (continuous lines) and faults (dashed lines). The well-tops from wells H4, H2 and H1 are included. The white crosses mark the well positions intersected by faults (from well-logs).

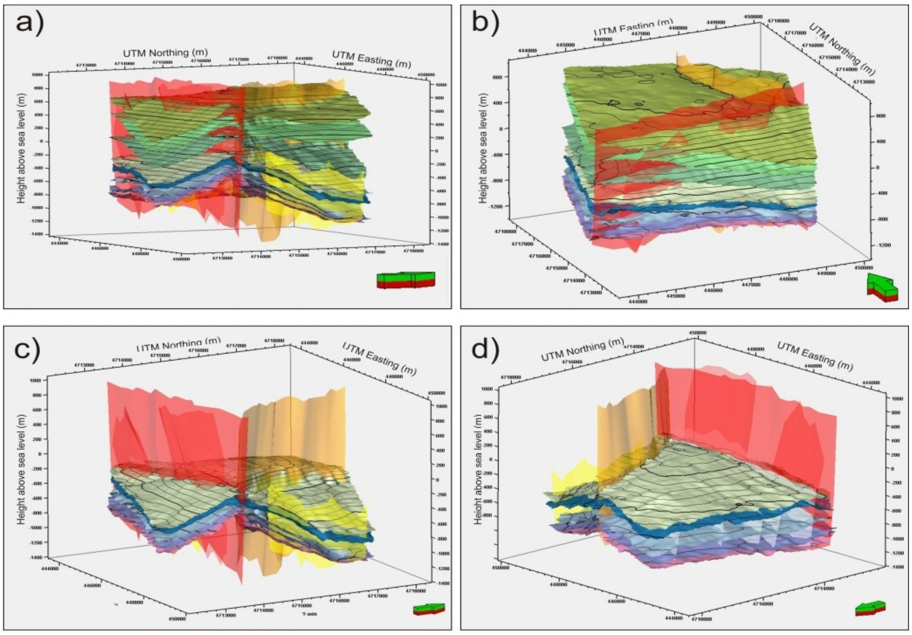

Fig. S.5: 3D visualization of the resulting 8-layered geological model (a and b) and detail of the target dome structure (Jurassic) (c and d).

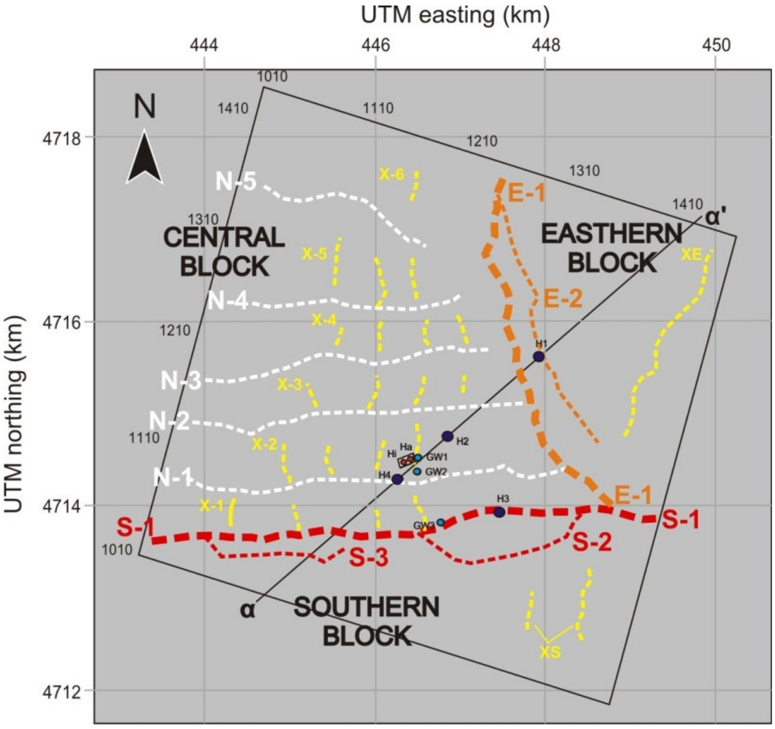

Fig. S.6: General distribution and labelling of the main faults interpreted in the study area. The position of profile α-α' and of the wells is shown.

Set “X” and “N” are both normal displacement faults affecting the Early Jurassic Limestone and Marly Lias units. Set N faults separate blocks with varying thicknesses in the Jurassic units and are fossilized by the top of the Purbeck formation. The N-1 shows a thicker Weald succession on the southern than on the northern wall, suggesting that it was active for a longer period than in the remaining faults of set N. Set “X” faults were first inferred based on observations made regarding the thicknesses of the Marly Lias unit. Other set X faults were observed in the entire volume as disconnected faults affecting sediments up to the Marly Lias.

S.6.2. Geological evolution of the Hontomín structure

The geological model obtained from the interpretation of the 3D seismic dataset (Fig. S.5) allowed us to infer the evolutionary history of the Hontomín structure, which is integrated into the regional framework. Three main stages are proposed in this model (Fig. S.7): (1) a local, small-scale fracturing stage during Late Lias; (2) a regional fracturing stage during the Late Jurassic-Early Cretaceous extension; and (3) a regional tectonic shortening stage associated with fault inversion, occurring during the Alpine compressional stage.

The first deformation stage described is related to the generation of the set X faults (Fig. S.7-1). Their origin is puzzling, since there is no evidence of a regional extensional event between the Triassic and the Late Jurassic-Early Cretaceous rifting periods (e.g., Ziegler, 1989; García-Mondéjar, 1996; Quintà and Tavani, 2012; Tavani, 2012; Tavani et al., 2013). We propose that the possible origin could be salt movements by differential loading related to Triassic basement faults originated in the Triassic rifting event. The salt migration could have produced a gentle dome growth and generate normal faults on the flanks (Fig. S.7-1). This stage could also have been the origin of the Eastern fault as a set of aligned N-S faults, which eventually merged during a later reactivation.

The second event corresponds to a regional extensional period occurring during the Late Jurassic-Early Cretaceous (Fig. S.7-2) and is related to the generation of Set N faults. During this stage, the Hontomín dome started its major development by a forced fold mechanism generated by the WNW-ESE Ubierna Fault and the oblique NNE-SSW Hontomín Fault (Tavani et. al., 2013).

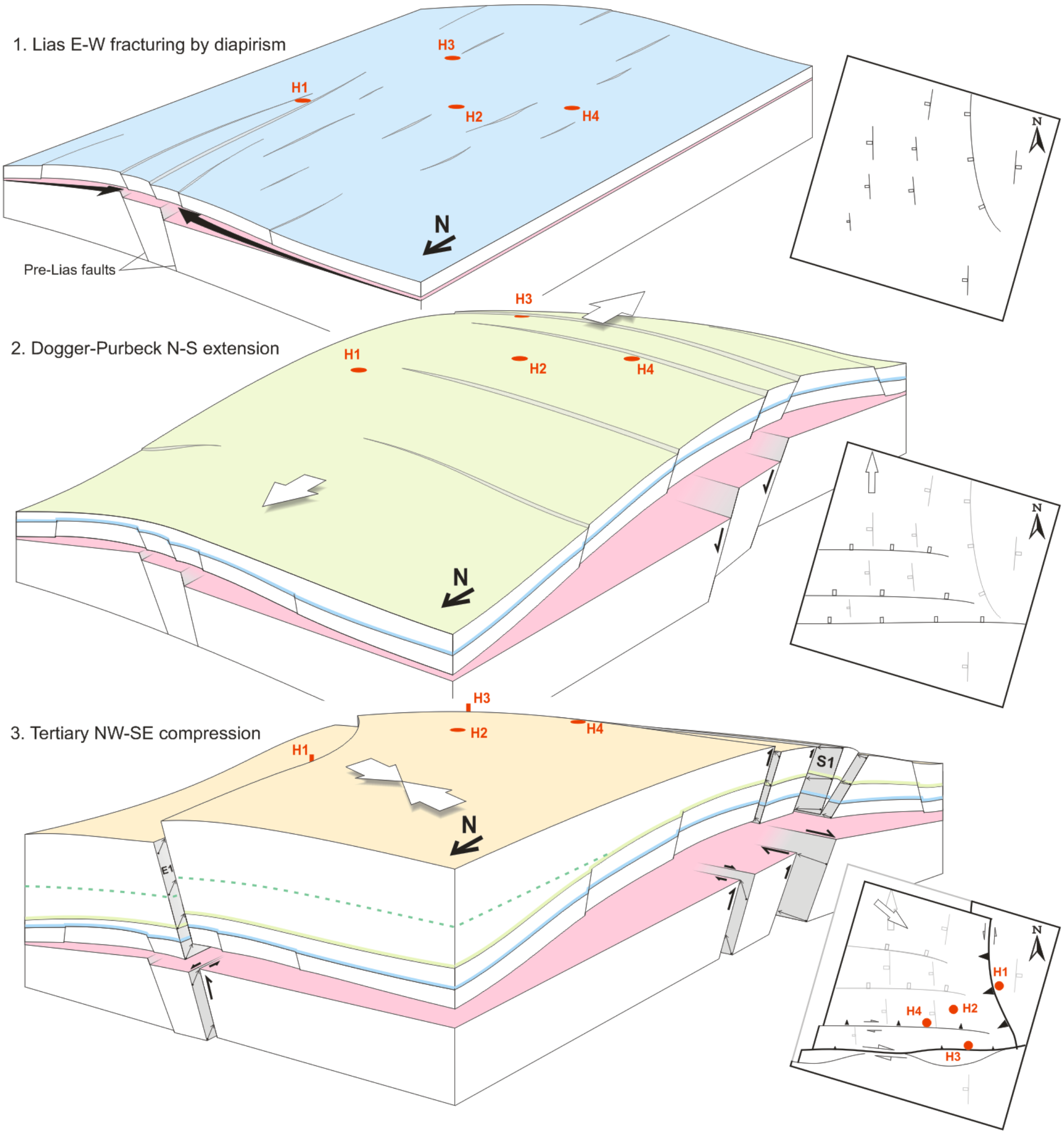

Fig. S.7: The sequence of the three main geological events for the zone. Pink color represents the Keuper detachment level. 1) E-W Triassic evaporites migration during deposition of Marly Lias produces a slight accommodation folding of the Trias-Lias cover and poor development of normal faults, forming a N-S oriented anticline. 2) N-S extension during deposition of Purbeck produces faulting on the basement and covers and triggers N-S salt migration and forms a dome-like structure. 3) NW-SE Cenozoic compression breaks the structure reactivating and inverting the mains east (E1) and south (S1) faults, producing a wedge-thrusting of the NW block. The green dashed line represents a Cretaceous layer onlapping the dome-like structure. In: Alcalde et al., 2014.

A W-E oriented basement normal fault forced the folding and the halokinetic growth of the Hontomín dome structure. The Southern fault would have originally formed as several minor set N-like segments located above a structurally weak zone, which were subsequently merged.

The third deformation stage took place during the Alpine compression (Fig. S.7-3). This stage is characterized by the inversion of previous structures, mostly focused on the Southern and Eastern faults. The location of the Hontomín structure on the SE tip of the Ubierna fault, formed at this stage (Tavani et al., 2011), resulted in a decisive influence of this fault on the final geometry of the Hontomín dome. The Southern fault was mostly inverted as a right lateral strike-slip fault with a small vertical component, whereas the Eastern fault was mostly inverted as a reverse fault with a gentle left-lateral component (Fig. S.7-3). During the inversion stage the Triassic materials stacked against the Southern and Eastern faults, increasing the structural relief of the Dome.

S.7. CONTRIBUTION TO THE CO_2 STORAGE SITE

S.7.1. Suitability of the Hontomín Site for GSC

The resulting geological model provides detailed characteristics of the structures involved in the GSC in Hontomín (including the target reservoir and seal formations, the fracture system and the overburden) and, hence, it is an essential tool for evaluating the safety, security and suitability of the Hontomín site for CO_2 storage. We have used the geological model to evaluate the suitability of certain characteristics of the Hontomín site for GSC purposes (Table S.2).

- Several formations have been identified in the sedimentary column as potential reservoirs and seals according to their properties, with the Lias Limestone and the Marly Lias, respectively, being selected as the target reservoir and seal formations.

Table S.2: Site selection criteria for ensuring the safety and security of CO_2 storage and suitability of the Hontomín site. Colored cells indicate criterions assessed completely (green) or partially (yellow) in this work. Modified from IEA GHG, 2009.

Criterion Level	No.	Criterion	Eliminatory or unfavorable	Preferred or favorable	Assessment at Hontomín
Critical	1	Reservoir–seal pairs; extensive and competent barrier to vertical flow	Poor, discontinuous, faulted and/or breached	Intermediate and excellent; many pairs (multi-layered system)	✓
	2	Pressure regime	Over-pressured: pressure gradients greater than 14 kPa/m	Pressure gradients less than 12 kPa/m	✓
	3	Monitoring potential	Absent	Present	✓
	4	Affecting protected ground water quality	Yes	No	✓
Essential	5	Seismicity	High	Moderate or less	✓
	6	Faulting and fracturing intensity	Extensive	Limited to moderate	✓
	7	Hydrogeology	Short flow systems, or compaction flow; Saline aquifers in communication with protected groundwater aquifers	Intermediate and regional-scale flow	✓
Desirable	8	Depth	<750-800 m	>800 m	✓
	9	Located within fold belts	Yes	No	✓
	10	Adverse diagenesis	Significant	Low to moderate	✓
	11	Geothermal regime	Gradients ≥ 35 ºC/km and/or high surface temperature	Gradients < 35 ºC/km and low surface temperature	—
	12	Temperature	< 35 ºC	≥ 35 ºC	✓
	13	Pressure	< 7.5 MPa	≥ 7.5 MPa	✓
	14	Thickness	< 20 m	≥ 20 m	✓
	15	Porosity	< 10%	≥ 10%	✓
	16	Permeability	< 20 mD	≥ 20 mD	—
	17	Caprock thickness	< 10 m	≥ 10 m	✓
	18	Well density	High	Low to moderate	✓

✓ Suitable × Unsuitable —Unknown/Non-applicable

- The monitoring potential with seismic methods, discussed above, is adequate. The seismic baseline modelling carried out in the study area is appropriate to the characteristics (i.e., size, depth, thickness of the target formations etc.) of the Hontomín site.
- The Hontomín area was more fractured than expected based on the previous geological and geophysical data available for the region (Fig. S.6). The fault system identified at Hontomín (Fig. S.6) could produce a certain degree of compartmentalization that, given the amount of CO_2 to be injected, will not constitute a risk factor. On the other hand, this fracturing can provide additional research opportunities, as Hontomín was conceived as a subsurface research infrastructure. The interaction of the CO_2 with the reservoir can be further investigated in this case.

The geological characterization carried out at the Hontomín site incorporated practical information about the desirable characteristics for a GSC site, including target formation thicknesses, target depth of injection and rock properties derived from the well-logs. The average thickness of the target reservoir and seal formations (over 80 m and 100 m in both cases) and porosity are adequate considering the capacity and injectivity requirements. Further hydrogeological tests should be carried out to obtain the permeability values.

S.7.2. Injection and monitoring wells location

The 3D seismic images of this work provided key information for determining the most suitable position for the injection and monitoring wells. The first approach to their current location was based on the identification of the apex and the major fault structures. Based on this geometry, the position of the injection (Hi) and monitoring (Ha) wells was chosen to lie over the steepest flank of the dome, at approximately 500 m of the structural apex, which is located near the H2 well. The position was selected with the goal of finding the maximum gradient direction, which is contained approximately in the H4-H2 direction (Fig. S.8.a). This geometry will produce a faster migration of the injected CO_2, benefiting the monitoring experiments.

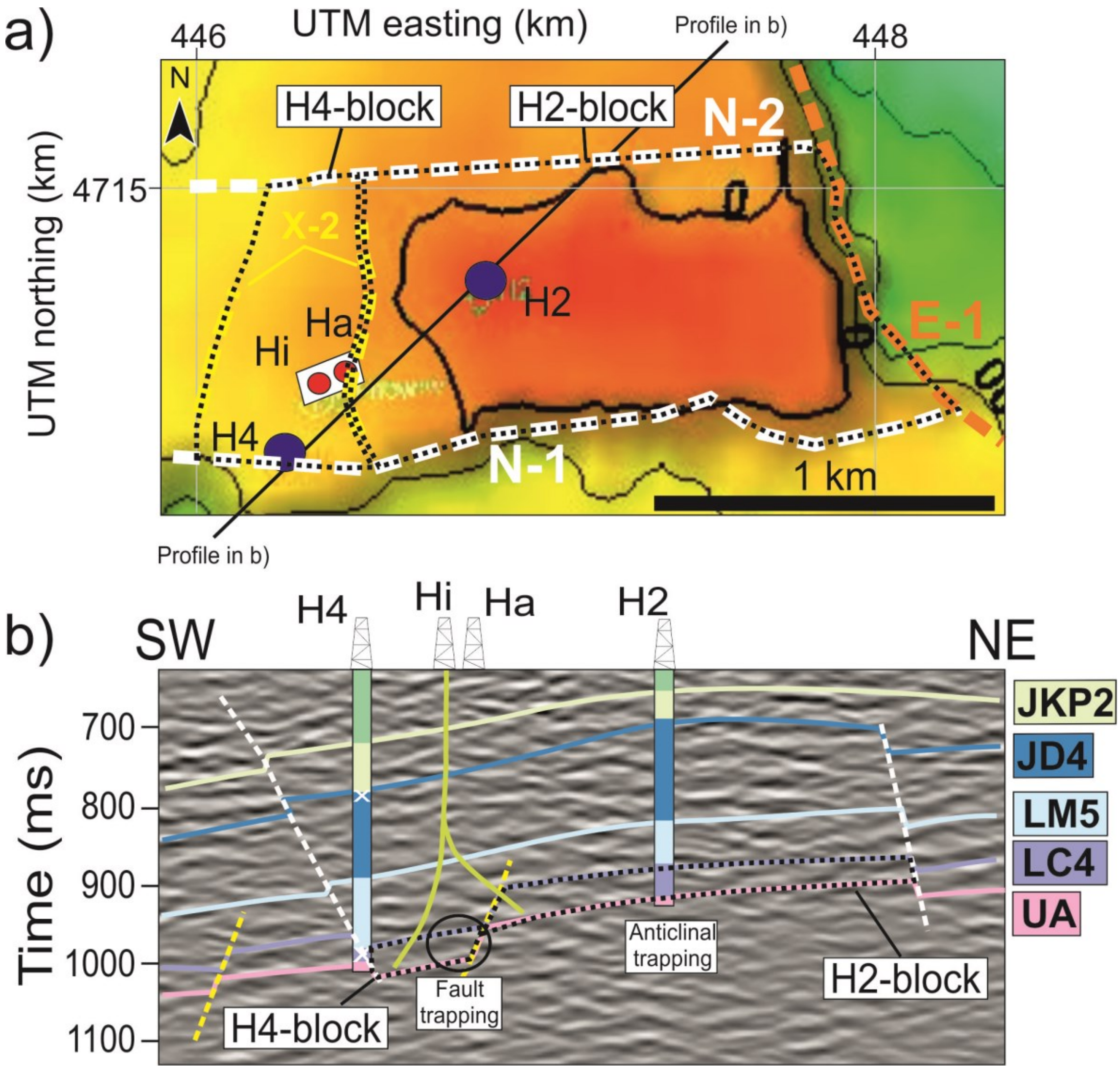

Fig. S.8: a) Position of the two potential CO_2 reservoirs, the H4-block and H2-block, limited by N-1, N-2, E-1, and two X-2 faults at S, N, E and W, respectively. b) Zoom of the potential reservoirs with the two trapping mechanisms available: fault trapping for the H4-block and anticlinal trapping for the H2-block.

S.7.3. Storage capacity calculation

The Jurassic structure was identified as a pseudo-triangle dome, with the two main faults – Eastern and Southern – representing two of the sides, and a third side being determined subjectively at the two-way-time that the dome changes from symmetric to elongated (i.e., approximately 850 ms) (Fig. S.5). The calculated area of the dome structure is $9.4 \cdot 10^6$ m^2. In order to provide an estimation of the scale and potential of the Jurassic dome structure, the maximum storage capacity was calculated as a function of the available storage volume and the density of the CO_2 at the storage conditions. Thus, a maximum CO_2 storage capacity of 1.2 Gt of CO_2 is expected in the Hontomín Jurassic dome structure.

The same assumptions were used to calculate the maximum storage capacities of the H2 and H4 blocks (Fig. S.8). The H4 block has a total area of $2.366 \cdot 10^6$ m^2. The H2 block's area is larger ($1.076\ 10^7$ m^2). The total volume of these two blocks ranges from $1.695 \cdot 10^7$ m^3 in the H4 block, to $9.275 \cdot 10^7$ m^3 in the H2 block. The calculated maximum theoretical storage capacity is 0.65 Mt of CO_2 for the H4 block reservoir and 5.2 Mt of CO_2 for the H2 block reservoir. Furthermore, the connectivity of both reservoirs would imply an increase of the overall M_{CO2}, which would equal 5.85 Mt of CO_2.

S.8. CONCLUSIONS

The aims of this thesis include the seismic baseline modeling and geological characterization of the Hontomín CO_2 storage site, by means of the 3D seismic reflection and well-log data have been achieved within the three published papers. The proposed results represent the first high resolution image of the storage site. The resulting geological model is crucial to assess the suitability of the Hontomín site for GSC purposes.

The 3D seismic survey design was suitable to the imaging aims, in terms of areal coverage, data redundancy and vertical and horizontal resolution at the target depths. The acquired data was deeply influenced by the intricate near surface geology and the mixed sedimentary media (carbonate and siliciclastic) present in the study area. The complex near-surface characterized by a velocity inversion generated a shadow zone in the data, producing unexpected complications in the static correction calculations and reducing the overall quality of the data. Static corrections proved to be the most important step within the data processing flow. The mixed source wavelets were matched utilizing a self-developed code that performed the appropriate time and phase shift to the traces, producing a similar matching result as that of the standard match filtering, with an easier implementation. Other processing steps that showed decisive to achieve a quality final image included the DMO correction, frequency filtering and amplitude equalization.

The interpretation of the seismic volume was based on a conceptual model was built based on the available dataset (i.e., well-log, seismic and regional geology), using the well-log data as primary factor. This approach allowed detailed delineation of 8 surfaces, from Jurassic to Cenozoic, and 4 sets of faults.

The geological model obtained with this approach allowed inferring the three main stages in the evolution of the Hontomín structure: (1) a local, small scale N-S fracturing stage during Late Lias, possibly related to salt mobilization during early growth stages of the dome; (2) a regional fracturing stage during the Late Jurassic-Early Cretaceous extension, generating W-E normal faults; and (3) a regional tectonic shortening stage associated to fault inversion, occurring during the Alpine compressional stage inverting some of the pre-existing extensional faults.

The model was used to assess the suitability of the Hontomín site for GSC by evaluating the properties of the underground structures. Several formations were identified as potential reservoirs and seals throughout the sedimentary column. Within them, Limestone and Marly Lias represent the most suitable reservoir and seal formations respectively, thanks to their properties (e.g., porosity, permeability, depth, thickness etc.). Our resulting model shows that the Hontomín area is more fractured than what was believed before the seismic characterization survey was acquired. In spite of this fracturing, the Hontomín structure has been positively evaluated to host the GSC pilot plant. The position of the injection and monitoring boreholes was selected based on the results of this work. They were located at the steepest flank of the dome, aiming to find the maximum gradient direction to produce a faster migration of the injected CO_2, benefiting the monitoring experiments. At this location, two potential reservoir blocks can be reached by the two boreholes. The H4 block is smaller and has a steeper dip than the H2 block. Their maximum storage capacity was calculated in order to provide an overall idea of the scale of the two blocks. This resulted in a maximum theoretical storage capacity of 0.65 Mt of CO_2 for the H4 block reservoir and 5.2 Mt of CO_2 for the H2 block reservoir, giving a combined capacity of 5.85 Mt of CO_2.

The 3D seismic model obtained could be potentially used as baseline reference model to detect and measure changes produced by the injected CO_2 plume during the monitoring stage. The resulting velocity model is coherent with the interpreted horizons and well constrained around the injection area which is suitable for monitoring changes in velocity properties. The use of AGC within the workflow helped to obtain a good quality final image, but it should be replaced by true amplitude recovery processes in the processing sequence before the dataset could be used as a reference in a time-lapse monitoring study based on amplitude variations.

CHAPTER I

INTRODUCTION

1.1. MOTIVATION AND OVERVIEW

1.1.1. The CO_2 problem

The planet Earth is constantly irradiated by the Sun, but only about a 50% of this radiation reaches its surface. In order to maintain a thermal equilibrium, the Earth must radiate the same amount back to outer space. This percentage is insufficient to maintain the Earth's temperature above 0°C, one of the primary conditions for supporting life. The atmosphere absorbs and reradiates part of this energy back to the Earth, trapping warmth and allowing the planet to hold living beings (International Energy Agency, IEA, http://iea.org). This process is called "natural greenhouse effect", and is a fundamental part of the Earth's temperature self-regulation method. The atmospheric elements that produce the greenhouse effect are known as greenhouse gasses. Among them, carbon dioxide (CO_2) is the second major constituent and larger contributor to the greenhouse effect, after the water vapor (Kiehl and Trenberth, 1997). In 1896, Svante Arrhenius was the first to calculate the effect of variations in atmospheric CO_2 concentration on the Earth's surface temperature.

From the 18th century onwards, with the arrival of the Industrial Revolution, the amount of CO_2 emitted into the atmosphere due to human activities increased dramatically, mainly due to fossil fuel consumption (IPCC 2007). This increment in atmospheric CO_2 has resulted in an enhancement of the greenhouse effect (called "anthropogenic greenhouse effect") and therefore in a rise in Earth's surface temperature ("global warming") (IPCC 2007) (Fig. 1.1).

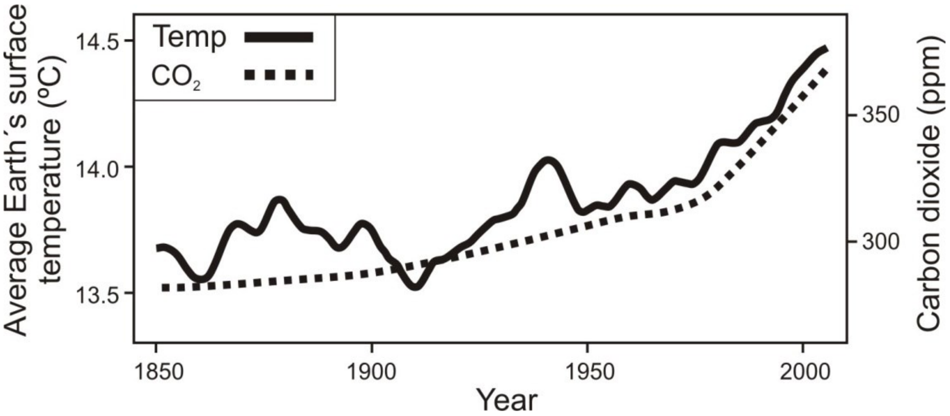

Fig.1.1: Average Earth surface temperature (°C) and CO_2 concentration (ppm) records in the last 160 years. Modified from IPCC 2007.

Theoretical considerations on energy consumption estimations for the following decades (Fig. 1.2) (IPCC, 2005) suggest that: a) there is a tendency of deceleration (but not reduction) of the energy consumption in the future; b) most of our energy needs are and will be met by fossil fuels, (oil, gas, coal); and c) presently, the dependency on fossil fuels is total. Since the actual energy consumption keeps rising (enhanced by the arrival on the scene of new developing countries), and it is impossible to avoid the use of fossil fuels, a technological solution that will deal with the resultant CO_2 emissions becomes mandatory.

The European Union (EU) approved in 2008 a set of regulations in order to meet the climate and energy targets for 2020 (Streimikiene, 2012): (1) a 20% reduction in EU greenhouse gas emissions from 1990 levels; (2) a raise in the share of EU energy consumption produced from renewable resources to 20%, as well as a share of biofuels up to 10% in transport fuels; (3) a 20% improvement in the EU's energy efficiency by reducing consumption. One of the vehicles used to reach these targets, which the EU is encouraging its member countries to implement is Carbon Capture and Storage (CCS) technology (Directive 2009/31/EC).

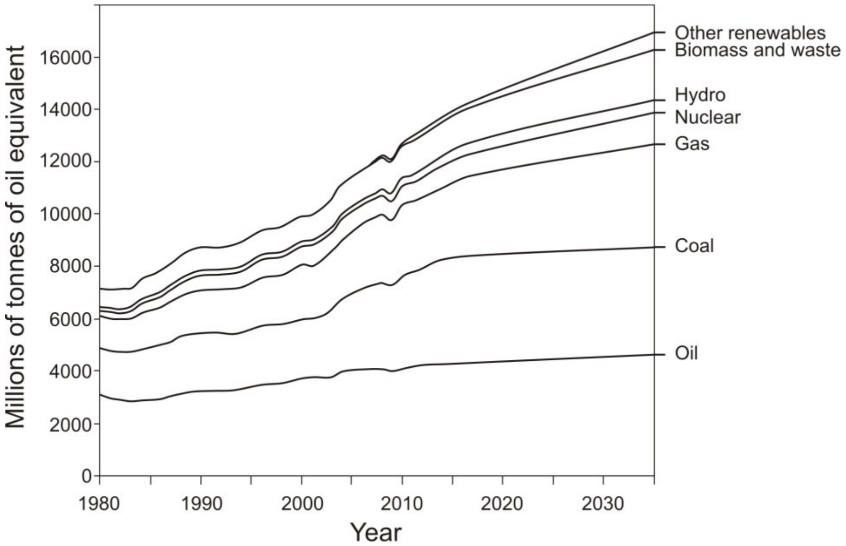

Fig. 1.2: Theoretical estimations of energy consumption. Modified from IEA WEO, 2011.

1.1.2. Carbon Capture and Storage

CCS constitutes one of the main courses of action for attempting to reach energetic sustainability (Lovell, 2011). CCS technology aims to extract the CO_2 from the combustion residues and store it in feasible geological formations where it does not contribute to global warming. The objective is to reduce the amount of CO_2 emitted into the atmosphere through fossil fuels use, so that they may still be used without aggravating the greenhouse effect. The CCS process comprises three main stages (Fig. 1.3): first, the CO_2 from large scale industrial emissions (e.g., cement factories, oil refineries, thermal power plants etc. in which CO_2 emissions are ample and concentrated) is separated from other elements present in the combustion ("capture"); then, the CO_2 is transported to a suitable location ("transport") and stored away from the atmosphere for a long period of time ("storage").

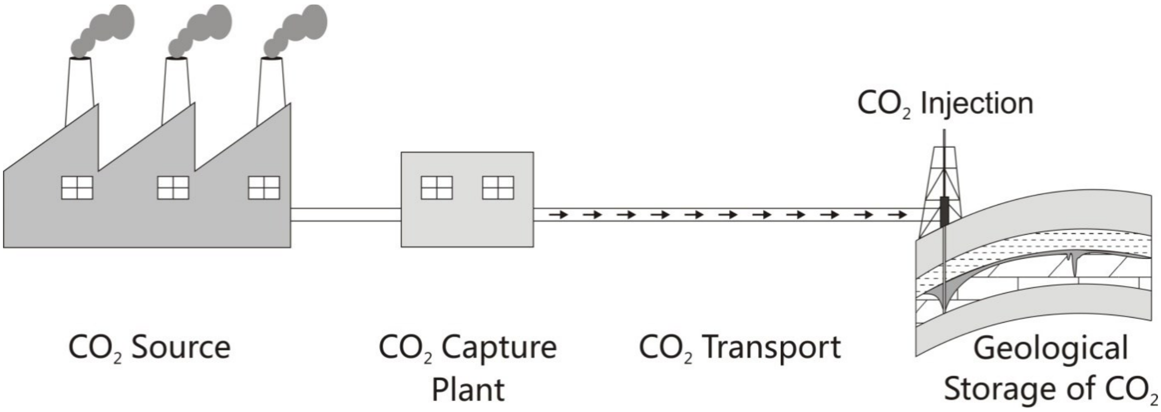

Fig. 1.3: Scheme of the Carbon Capture and Storage process.

1.1.3. Geological Storage of CO_2

The geological storage of CO_2 for industrial purposes can be performed in deep formations such as oil and gas fields, coal beds and saline aquifers (Bachu, 2000; IPCC 2005). Among these, saline aquifers provide the greatest storage potential (Dooley et al., 2004, IPCC 2005; IEA GHG, 2009), especially in countries without extensive natural energy resources, such as Spain (Pérez-Estaún et al., 2009). A potential deep saline aquifer site should meet a number of requirements in order to be considered suitable for GSC (Bachu, 2003; Orr, 2004; Baines and Worden, 2004; Chadwick et al., 2008; CO2CRC, 2009; IEA GHG, 2009; Pérez-Estaún et al., 2009) (Fig. 1.4):

- The existence of a formation or a number of formations with the appropriate physical properties for the CO_2 storage (reservoir). That includes high porosity (over 10%) and permeability (over 200 mD) formations, with a suitable thickness and capacity (large enough to store the planned amount of CO_2). The existence of a confined aquifer within the target formations demonstrates the efficacy of seal formations. The aquifer should have a high salinity (over 10 g/l) to ensure that the water is not suitable for consumption or irrigation.
- The existence of a formation or a number of formations immediately above the reservoir with a proven impermeability to the migration of the injected CO_2 (seal).
- To be placed at sufficient depth. The point beyond which the carbon dioxide is in supercritical state (critical point) is set at 31.1ºC and 7.38 MPa (Bachu, 2000). At this state, the CO_2 has a high density, allowing the injection of larger amounts of CO_2 than in gas state. Its viscosity is lower than that of the water or brine, which facilitates its injection into the reservoir. It is also immiscible with water and has a lower density, so the CO_2 will migrate towards the top of the reservoir formation after the injection, favoring the injection process. These parameters are reached at approximately 800 m depth in natural conditions (depending on the geothermal gradient, lithostatic pressure etc.).
- To be located in tectonically stable areas (i.e. low seismicity).
- Other desirable conditions include lack of/reduced lateral sealing (compartmentalization), non-complex and/or small size fault system, injection-induced pressures below geomechanical instability limits etc.

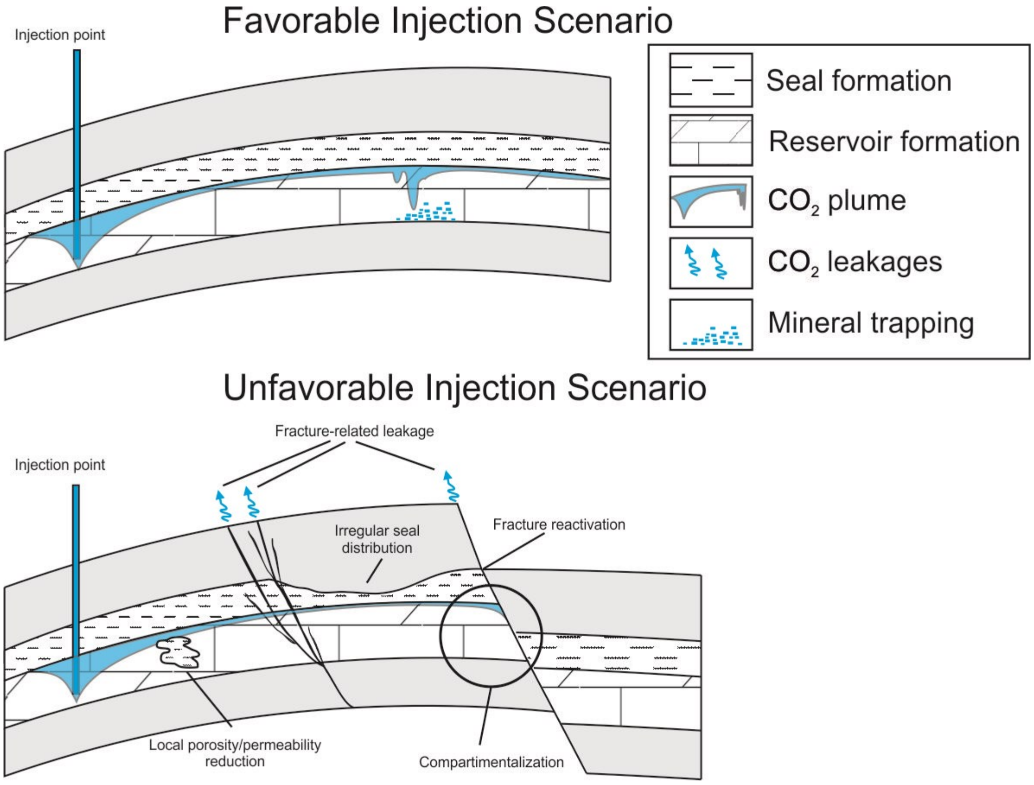

Fig. 1.4: Scheme of favorable and unfavorable scenarios for geological storage of CO_2.

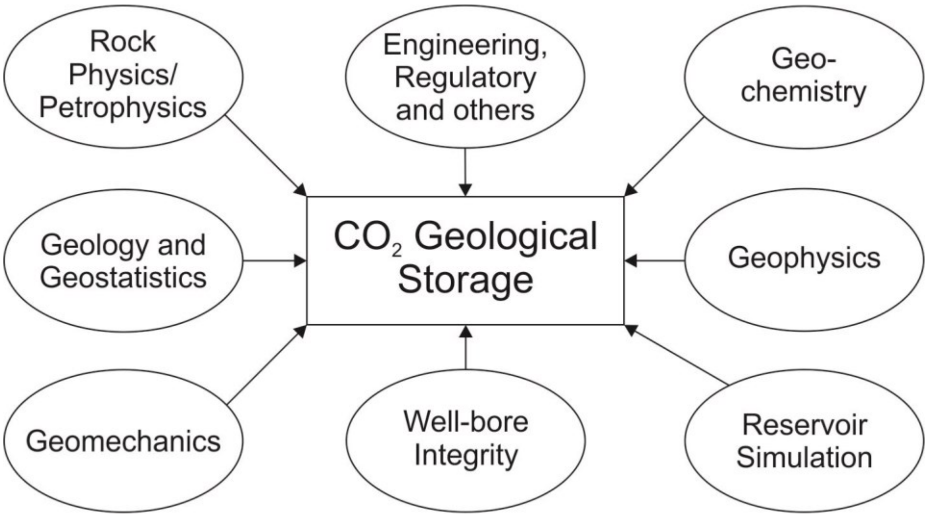

Fig. 1.5: Scheme of the disciplines involved in the CO_2 Geological Storage, with emphasis on geoscience. Modified from Alshuhail (2011).

Table 1.1: Site selection criteria for ensuring the safety and security of CO_2 storage and suitability of the Hontomín site. Blank cells mark criterions assessed completely or partially in this work. Modified from IEA GHG, 2009.

Criterion Level	No.	Criterion	Eliminatory or unfavorable	Preferred or favorable	Assessment at Hontomín
Critical	1	Reservoir-seal pairs; extensive and competent barrier to vertical flow	Poor, discontinuous, faulted and/or breached	Intermediate and excellent; many pairs (multi-layered system)	✓
	2	Pressure regime	Over-pressured: pressure gradients greater than 14 kPa/m	Pressure gradients less than 12 kPa/m	✓
	3	Monitoring potential	Absent	Present	✓
	4	Affecting protected ground water quality	Yes	No	✓
Essential	5	Seismicity	High	Moderate and less	✓
	6	Faulting and fracturing intensity	Extensive	Limited to moderate	×
	7	Hydrogeology	Short flow systems, or compaction flow; Saline aquifers in communication with protected groundwater aquifers	Intermediate and regional-scale flow	✓
Desirable	8	Depth	< 750-800 m	> 800 m	✓
	9	Located within fold belts	Yes	No	✓
	10	Adverse diagenesis	Significant	Low to moderate	✓
	11	Geothermal regime	Gradients ≥ 35 ºC/km and/or high surface temperature	Gradients < 35 ºC/km and low surface temperature	—
	12	Temperature	< 35 ºC	≥ 35 ºC	✓
	13	Pressure	< 7.5 MPa	≥ 7.5 MPa	✓
	14	Thickness	< 20 m	≥ 20 m	✓
	15	Porosity	< 10%	≥ 10%	×
	16	Permeability	< 20 mD	≥ 20 mD	—
	17	Caprock thickness	< 10 m	≥ 10 m	✓
	18	Well density	High	Low to moderate	✓

✓ Suitable **× Unsuitable** **—Unknown/Non-applicable**

In order to ensure the compliance of these requirements, a good knowledge of the subsurface structures is imperative (Table 1.1). This knowledge will serve to characterize the storage site for GSC in terms of feasibility, efficacy, capacity, security etc. from a multidisciplinary point of view, and therefore it is an essential step of the GSC process. Fig. 1.5 shows a simplified description of the main disciplines involved in this GSC and subsurface characterization. According to the European Union's directive (Directive 2009/31/EC), this characterization must include the storage site (defined as 'a volume area within a geological formation used for the geological storage of CO_2') and also the entire storage complex (defined as 'the storage site and surrounding geological domain, which can have an effect on overall storage integrity and security').

1.1.4. The Hontomín underground research facility

There are currently several CCS demonstration projects worldwide (GCCSI, 2012). The European Union with its European Energy Programme for Recovery (http://ec.europa.eu/energy/eepr/index_en.htm) funds a number of these projects, with the aim of: (1) understanding the different processes (physical, chemical, hydro-geological etc.) that are involved in CCS; (2) developing, testing and validating different techniques in order to refine the methods used and reduce the costs of its application; and (3) enhancing the visibility and social acceptance of CCS.

One of these projects is currently being undertaken in Spain under the leadership of the CIUDEN Foundation (www.ciuden.es). The "Compostilla OXYCFB300 Project" (www.compostillaproject.eu), is a major research effort aimed to demonstrate the viability of CCS and improve the social perception of the techniques involved. The "Compostilla" project contains a capture and a storage component, each of them linked to a Technological Development Plant (TDP). The capture TDP is located in Cubillos del Sil (León, Spain; Fig. 1.6) (Lupion et al., 2011a; 2011b). The storage program involves the development of a research facility dedicated to geological storage in Hontomín (Burgos, Spain), the study area presented here (Fig. 1.6).

The storage project site of Hontomín was chosen amongst a series of sites considered suitable for geological storage of CO_2 (GSC) scattered across the Iberian Peninsula (Prado-Pérez et al., 2008; Pérez-Estaún et al., 2009). The objective of this GSC site is the creation of a scientific laboratory that will develop the knowledge and state-of-the-art technologies needed for GSC. This research facility aims to provide a multidisciplinary understanding of the processes taking place within the reservoir and seal at the storage site. It should also demonstrate the feasibility and help to reduce the costs of its industrial application.

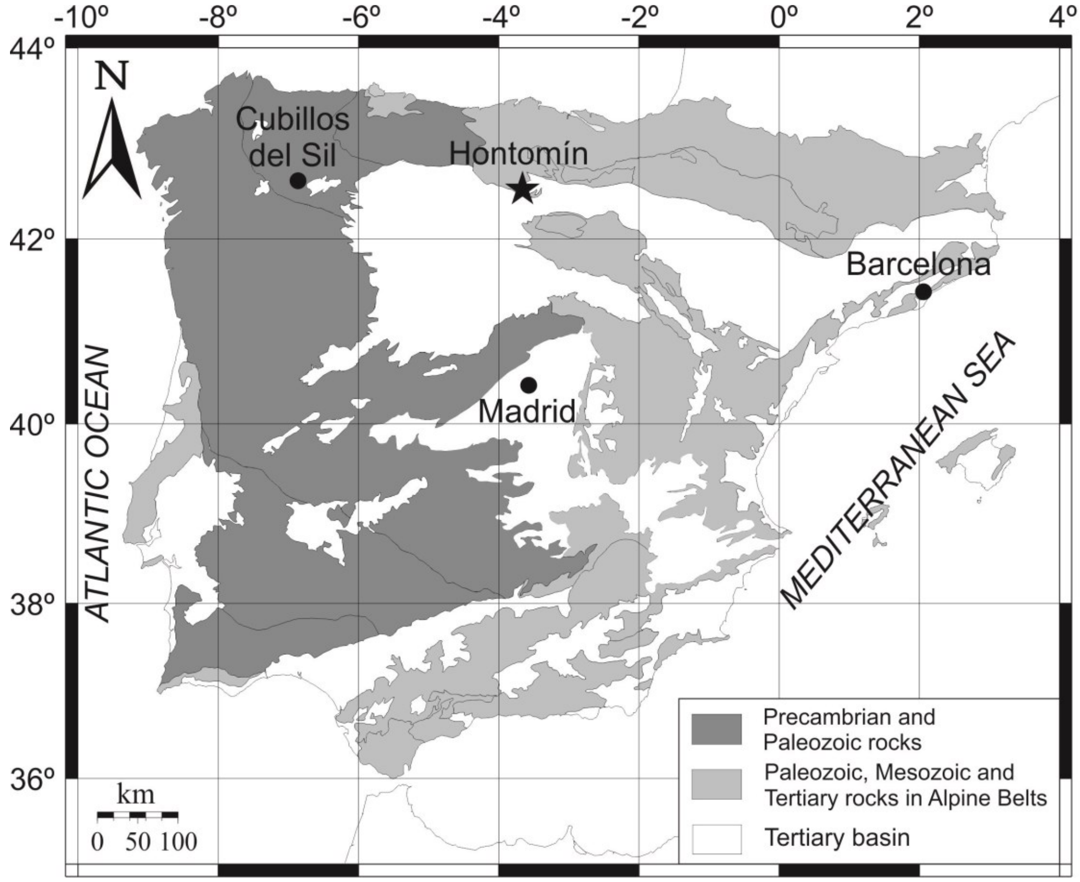

Fig. 1.6: Map of the Iberian Peninsula showing the position of the Hontomín CO_2 storage site.

The research carried out at this study site is broadly multi-disciplinary (Fig. 1.5). The challenge, during this early stage in the development of the research facility is achieving a high-resolution 3D characterization of the site. This includes the generation of a 3D coupled model, by means of the acquisition of relatively large volumes of data from within the different scientific disciplines involved: geophysics (Alcalde et al., 2013a; Alcalde et al., 2013b; Alcalde et al., 2014; Ogaya et al., 2013; 2014; Ugalde et al., 2013; Vilamajó et al., 2013), geomechanics (Canal et al., 2013), geochemistry (Elío, 2013; Elío et al., 2013; Metcalf et al., 2013; Nisi et al., 2103; Permanyer et al., 2013). This model will constitute a complete baseline, which will be used to compare with the post-injection state to monitor the evolution of the CO_2 plume and its interaction with the rock, as well as detect possible leakages into the biosphere.

Within these characterization methods, the 3D controlled seismic reflection data provides useful information for unraveling the 3D geological architecture of the reservoir-seal and overlying structures, and places constraints on the fault geometry and distribution (e.g. Thomson and Hutton, 2004; Juhlin et al., 2007; Malehmir and Bellefleur, 2009). Furthermore, the seismic technique is sensitive to some of the changes in physical properties produced by the injection of CO_2 in the storage formations (e.g., Rutqvist and Tsang, 2002; Alsuahil, 2011). Thus, the seismic method is considered a valuable technique to monitor the injected CO_2 plume (e.g., Arts et al., 2004; Chadwick et al., 2010).

1.1.5. Aims of the thesis

The aims of this thesis include the seismic baseline modeling and geological characterization of the Hontomín CO_2 storage site, by means of the 3D seismic reflection and well-log data. The resulting geological model is used to assess the suitability of the site for GSC purposes.

The aims related to the seismic baseline modeling are:

a) Develop and implement a processing sequence aimed at obtaining a 3D seismic image of the subsurface that is suitable for geological interpretation.
b) Study, characterize and understand the main geological features affecting the quality of the final image.

c) Identify the key processing steps with a higher impact on the quality of the final image.
d) Analyze the suitability of the processed dataset for the monitoring of CO_2.

The aims related to the geological characterization at the Hontomín storage site are:

a) Obtain a 3D structural model of the Hontomín subsurface through seismic interpretation, including the geometry and detailed distribution of the main geological layers and faults.
b) Provide a geodynamical, tectonic and stratigraphic model of the Hontomín structure within its regional geological frame.

The aims related to the assessment of the suitability of Hontomín for GSC purposes are:

a) Analize the site characteristics to ensure the safety, security and suitability of the Hontomín site for GSC, based on the resulting geological model.
b) Identify the most suitable position for the projected injection and monitoring boreholes.
c) Provide the scale of the Hontomín structure in terms of maximum CO_2 storage capacity and calculate the maximum capacity of the selected storage structure.

1.2. REFLECTION SEISMICS

1.2.1. The reflection seismic method

Seismic reflection surveys started to be used in oil exploration in the 1930s (Sheriff and Geldart, 1995). Since then, the data acquisition evolved from 2D, single-fold surveys to 2D multi-fold surveys, accompanied by the development of common-depth-point and migration techniques, and by advances in energy sources, sensors, processors, and processing approaches. However, the 2D technique still offered little information when characterizing structures with a strong 3D aspect (French, 1974;

Yilmaz, 2001). This weakness began to be resolved with the arrival of 3D reflection surveying in the 1980s, when 3D seismic images allowed the detailed subsurface structural and stratigraphic characterization that was missing or not discernable from previous types of data (Sheriff and Geldart, 1995; Yilmaz, 2001). Today underground structures are imaged in three dimensions, which allow seismic interpreters to view the data in cross-sections along 360° of azimuth, in depth (or time) slices parallel to the ground surface, and along planes that cut arbitrarily through the data volume. Information such as faulting and fracturing, bedding plane direction, the presence of pore fluids, complex geologic structures, and detailed stratigraphy can be interpreted from 3D seismic data sets.

The seismic reflection method is a geophysical method that consists of recording the Earth's response to a controlled seismic source of energy. The energy propagates through the subsurface and the back-scattered acoustic energy reflected by subsurface interfaces is recorded with sensors (geophones) deployed at the surface of the study area (Fig. 1.7) or in boreholes. The way these acoustic waves propagate is defined by the characteristics of the source waveform (frequency, wavelength and amplitude), as well as the characteristics of the medium (density, propagation velocity, structure etc.), which conform its reflectivity function. At each layer boundary (i.e., where the physical properties change), a proportion of the energy pulse is reflected back to the geophones, where it is recorded in the form of a seismic trace (Fig. 1.8). The travel times of these waves can be measured with geophones and converted to estimates of depths to the interfaces (Kearey et al., 2002). The objective of the reflection seismic method is to obtain a zero-offset seismic section of the subsurface where the different reflections represent changes in the acoustic impedance.

The recorded seismic traces contain the convolved information of the input energy pulse and the reflectivity function of the subsurface, as well as noise (Fig. 1.9) (Partyka et al., 1999). This noise can have multiple superimposed origins (Kearey et al., 2002): multiple reflections, direct and refracted body waves, surface waves (ground roll), airwaves and coherent and incoherent noise from the source or anthropogenic origin.

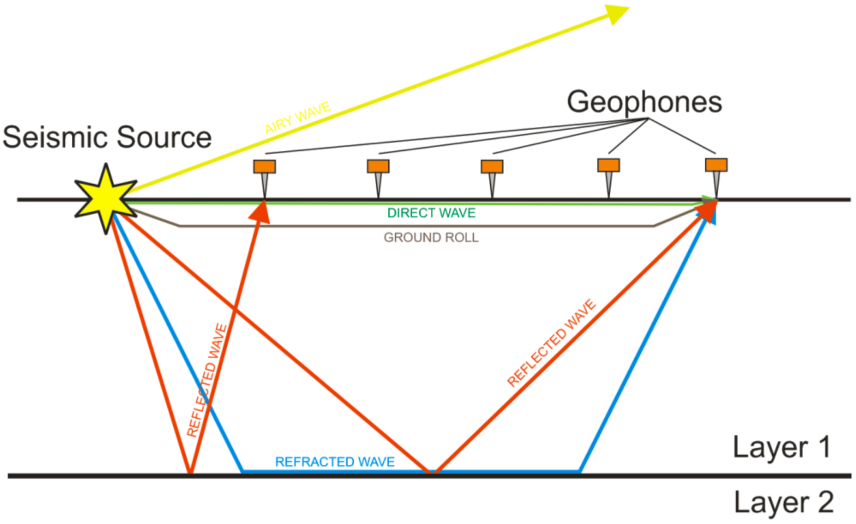

Fig.1.7: Scheme of the seismic reflection method. The energy is emitted by a source (yellow star) and propagated through the subsurface, in the form of different waves; the back-scattered acoustic energy is recorded with geophones. Modified from ISGS (http://crystal.isgs.uiuc.edu).

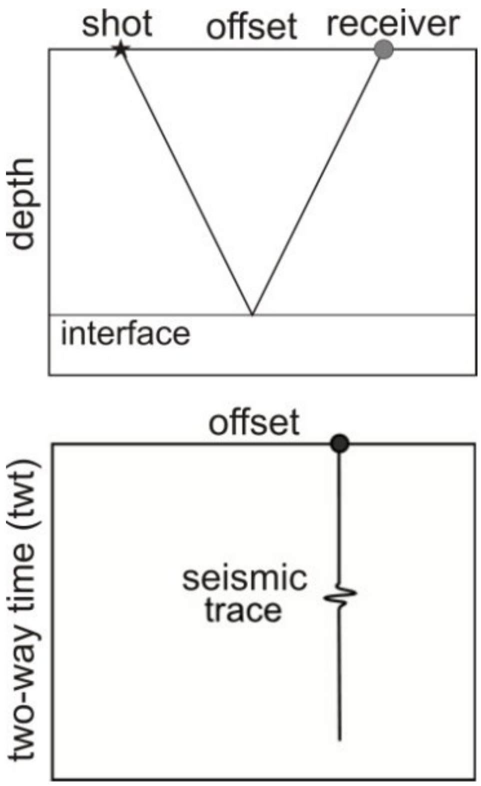

Fig. 1.8: Diagram showing the reflection of a ray in a given interface (above) and the resulting seismic trace recorded by the receiver (below). Modified from Bianco, 2011 (http://www.agilegeoscience.com).

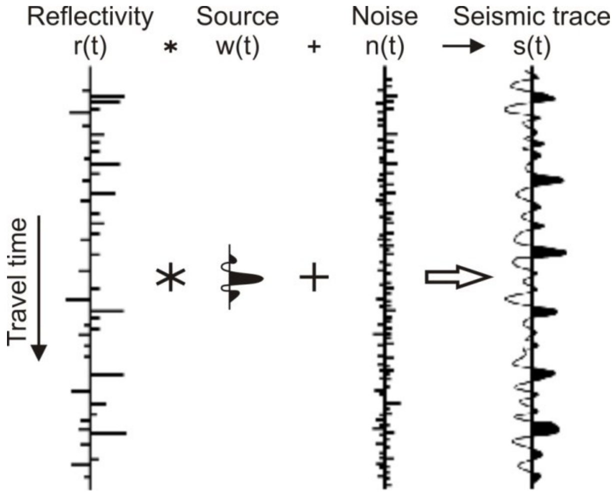

Fig. 1.9: Convolutional model of a seismic trace. The seismic trace -s(t)- is the result of the convolution of the reflectivity model of the subsurface -r(t)- with the source wavelet -w(t)- and noise -n(t)-. Modified from Partyka et al., 1999.

1.2.2. Seismic data processing

The seismic data processing aims to reconstruct the reflectivity and source functions using the seismic trace as input, and therefore provide a seismic image suitable for geological interpretation. Below, a brief and simple outline of the main steps of the seismic data processing is presented. More information about data acquisition and processing, as well as other related topics can be found in the literature (e.g., Sheriff and Geldart, 1995; Cordsen et al., 2000; Graebner et al., 2001; Kennett, 2001; Yilmaz, 2001; Aki and Richards, 2002; Kearey et al., 2002; and Červený, 2005, amongst others).

The seismic data processing can be divided in three major stages: pre-stack, stack and post-stack. The pre-stack stage begins with the implementation of the geometry of the experiment into the trace headers. The seismic signal corresponding to a given interface (e.g., Fig. 1.10) is recorded at different times in the different receptors. These times will be determined by the distance between the source and the receiver ("offset") and the propagation velocity of the seismic waves. For a simple vertical wave, the travel time from the surface to the reflector and back is called the two-way time (twt) and is given by the formula:

$$t = 2\frac{d}{V}, \qquad (1)$$

where d is the depth of the reflector and V is the wave velocity in the rock. The vertical axis in all the reflection seismic profiles shown in this thesis is given in twt. The seismic traces are commonly acquired and ordered in first place as a function of the source position ("shot gathers"), each shot gather being a compilation of seismic traces with a common source point (Fig. 1.10). The geometry calculation allows reordering the seismic traces as a function of its common midpoint in depth or "CDP" (Fig. 1.10). This CDP sorting enables us to have multiple traces per midpoint, favoring redundancy among source-receiver pairs and enhancing the quality of the seismic data when stacked.

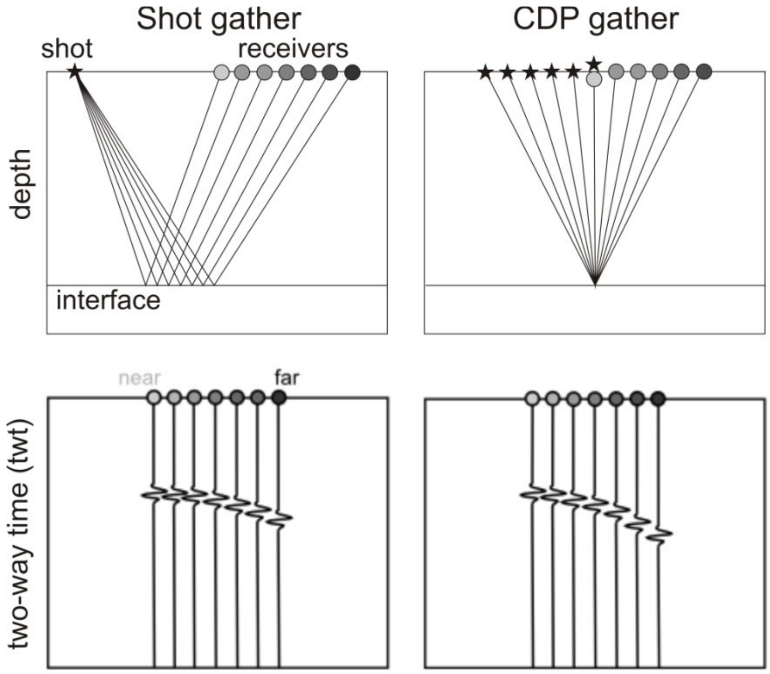

Fig. 1.10: Differences between data sorted in shot gathers (left) and CDP gathers (right). Modified from Bianco, 2011 (http://www.agilegeoscience.com).

Once the geometry has been calculated and implemented, the data is edited (abnormal traces are removed) and several gains (e.g., amplitude balance, spherical divergence corrections) and filters (e.g., mutes, bandpass filters, notch filters, deconvolution processes, coherency (F-K) filtering) are applied. The parameters of these processes are selected with the aim of enhancing the signal-to-noise ratio (S/N), as well as improving the equalization of the data and the lateral coherency of the reflections. Onshore data also requires a number of static corrections in order to remove the effect of the topography and the weathering layers in the travel times. In this sense, the determination of a precise static model is a critical step for obtaining high-quality seismic images (Juhlin et al 2007; Malehmir and Bellefleur 2009; Malehmir and Juhlin 2010; Alcalde et al., 2013b).

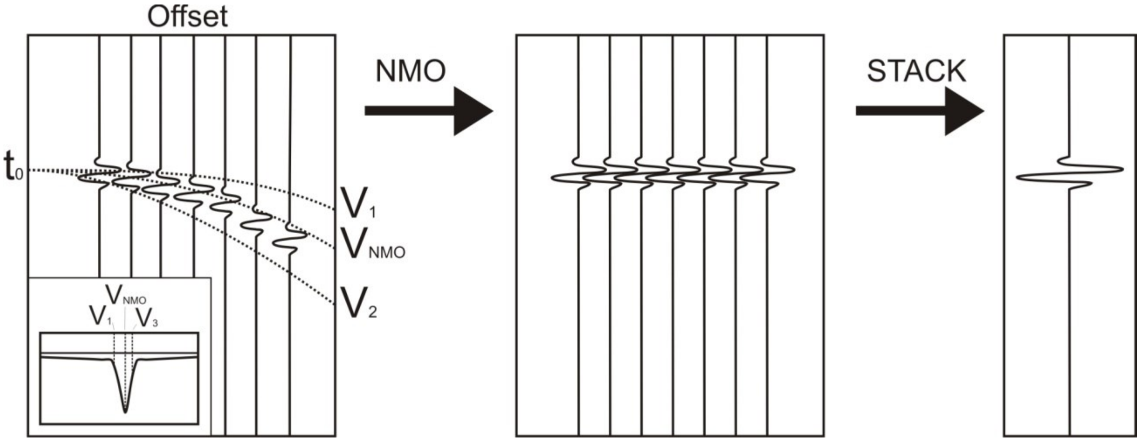

Fig. 1.11: Traces within a CDP gather are NMO-corrected by selecting the most appropriate velocity (V_{NMO}) among the others (V_1 and V_2, left); after the NMO correction is applied, the reflections are aligned horizontally (center), and the resulting stacked trace shows the maximum possible amplitude (right).

Prior to the stack phase, a velocity analysis is performed over the filtered and CDP sorted data to correct for the offset effect in the reflection times (Fig. 1.11). The stack phase sums up the seismic traces of the same CDP, sample by sample, in order to enhance the S/N ratio. Because the different traces within a CDP gather are deployed at different offsets from the source, the same event/reflection will be recorded in the geophones at different arrival times, featuring a hyperbolic shape. The normal move-out (NMO) correction is used to correct and horizontally align the events, so that the reflections produce the maximum amplitude when stacked. It is therefore necessary to select the most accurate velocities (NMO velocities) that correct for this effect; this is done by means of the velocity analysis. Assuming a medium with a single flat interface, these differences are a function of the source-receiver offset and the propagation velocity of the media. This can be calculated by:

$$t^2 = t_0^2 + \frac{x^2}{v_{NMO}^2}, \qquad (2)$$

Where t denotes the time difference, t_0 denotes the travel time for zero-offset distance (i.e., source and receiver at the same position), x denotes the given offset and v_{NMO} is the velocity value which produces peak cross-power from the stacked events (Kearey et al., 2002). A second process, the dip move-out (DMO) correction, is applied to address the problem of multiple dipping interfaces. After calculating the velocities and DMO-correcting the traces, the CDPs are stacked and the seismic image is obtained (Fig. 1.12).

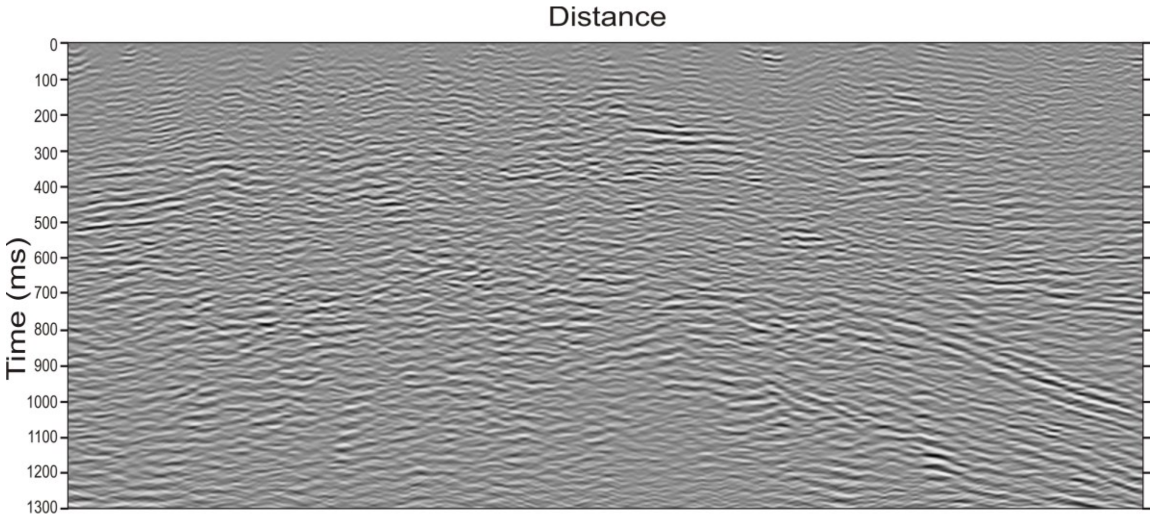

Fig. 1.12: Example of stacked seismic section.

The post-stack stage includes the application of new filtering and gain corrections (e.g., deconvolution, bandpass, coherency filters), in order to improve the quality of the seismic image. Stacked images are suitable for interpretation, but the reflection points can be displaced from their original positions when the subsurface reflectors are not horizontal. The migration process is applied to the data in order to reconstruct the seismic section so that reflection events are repositioned under their correct surface location and at the corrected vertical reflection time (Kearey et al., 2002). The seismic migration can relocate the events in time (time migration) or in depth (depth migration), resulting in a change in the domain of the vertical axis. It also improves the spatial resolution by collapsing the diffractions produced by faults and point reflections.

1.2.3. Seismic interpretation

After obtaining the migrated seismic section, it is necessary to establish the geologic significance of the seismic data. This is accomplished during the interpretation stage (Sheriff and Geldart., 2005). More information about the interpretation process, as well as other related topics can be found in the literature (e.g., McQuillin et al., 1984; Yilmaz, 2001; Kearey et al., 2002; Sheriff and Geldart, 2005; Chopra and Marfurt, 2007; Asveth et al., 2010; Brown, 2011, among others).

First, it is necessary to gather the available data relevant to the interpretation. These data can include regional geological data, well-log data, geophysical data etc., and is key to narrowing down the seismic interpretation from the multiple interpretations that can be achieved from the same seismic dataset. Within them, well data is especially important, because it allows matching the seismic data with the geology. The quality of the seismic to well tie is therefore a requisite in order to obtain an accurate geological interpretation of the seismic data. The velocity logs and checkshots (i.e., seismic campaigns with zero-offset surface sources and downhole receivers at different depths) acquired during well drilling are also very useful in constraining the velocity model of the subsurface.

After the data gathering, it is necessary to perform an analysis of the seismic characteristics. These characteristics must include analysis of the seismic sequence, seismic facies and the reflection character (Lin, University of Taiwan, http://basin.earth.ncu.edu.tw). The analysis of the seismic sequences aims to unravel depositional units by detecting unconformities or changes in seismic patterns. A seismic facies unit is a sedimentary unit with differential seismic characteristics. These include (Roksandić, 1978): reflection amplitude, dominant reflection frequency, reflection polarity, interval velocity, reflection continuity, reflection configuration, abundance of reflections, geometry of seismic facies unit and relationship with other units. The seismic facies analysis aims to determine the depositional environment and the geological causes responsible for the seismic characteristics observed. The analysis of the reflection character examines the lateral variation of individual reflection events, or series of events. It aims to locate stratigraphic changes and identify their nature. This method should be accompanied by synthetic modeling of the seismograms and seismic logs (Lin, University of

Taiwan, http://basin.earth.ncu.edu.tw). To summarize, the final interpretation should contain the structural and stratigraphical analysis, assisted by the seismic modeling (Kearey et al., 2002). After these analyses are completed and the well-log data has been integrated, the reflections are picked in 2D profiles and reflecting horizons are mapped. This includes the identification and depiction of potential faults and other interesting structures.

Once the main horizons and structures have been identified, the geological history of the study area can be inferred. These deductions are often aimed at determining the tectonic, geodynamics, sedimentary events etc. that occurred at the study area. The obtained geological model should fit or propose a robust and coherent alternative to the previous geological models of the study area, if existent, at all scales.

1.2.4. Reflection seismics and CO_2

Geophysics in general and seismic methods in particular are used in two phases of the GSC: (1) in the selection of the most suitable location for the GSC prior to the CO_2 injection ('characterization' phase); and (2) during and after the injection, to monitor the injected CO2 for environmental and economic purposes ('monitoring' phase) (Lumley, 2001; IPCC, 2005; Lumley et al., 2008; Sayers and Wilson, 2010). The present thesis is framed within the entire characterization process, which also includes providing a seismic baseline model for the monitoring stage.

1.2.4.1. Seismic characterization of CO_2 reservoirs

3D reflection seismic is broadly used for subsurface characterization and for a wide variety of purposes, including mineral (e.g., Malehmir and Bellefleur, 2009; Malehmir et al., 2012a and references therein; White et al., 2012) and hydrocarbon (e.g., Praeg, 2003, MacDonald et al., 2003; Jackson et al., 2013) exploration, radioactive waste disposal sites (e.g., Bergman et al., 2002; Schmelzbach et al., 2007), subterranean infrastructures (Malehmir et al., 2012b., Tzavaras et al., 2012) and general reservoir characterization, including CO_2 storage complexes (e.g., Förster et al., 2004; Juhlin et al., 2007; White, 2013a). In fact, high-quality seismic (2D and 3D) characterization is a requirement for the characterization and storage volume assessment of a potential CO_2 storage site (Chadwick et al., 2008; CO2CRC, 2008; IEA GHG, 2009). Among other data needs, Chadwick et al. (2008) indicate that the key datasets for a robust characterization of reservoir and overburden are:

- A regular grid of 2D seismic data to characterize broad reservoir structure and the surrounding areas;
- A high-quality 3D seismic volume at the injection site and the adjacent area, designed if possible to provide adequate resolution to the reservoir and overburden;
- Sufficient well data to characterize the reservoir and seal petrophysical properties.

A suitable storage reservoir geological characterization aims to investigate the storage potential, in terms of capacity, feasibility and security of a storage site (Chadwick et al., 2008, IEA GHG, 2009). These investigations must include a comprehensive analysis of the storage subsurface structure and an analysis of the reservoir, seal and overburden properties. The reservoir structure analysis should provide insights on the structure and stratigraphic properties at a regional and storage site scales, which will be used as input for the capacity calculations, trapping mechanisms identification etc. (Chadwick et al., 2008). The resulting structural/stratigraphic model must provide the geometry of the major horizons, including reservoir and seal depth maps, and fault system identification.

Mapping of the subsurface stratigraphy, thickness of the target formations and lateral variations in facies is necessary for the calculation of the bulk storage capacity and for elucidating the potential migration patterns (Chadwick et al., 2008). These factors will be used to confirm the suitability of the storage site, and are essential for the design of the different operations involved in CO_2 storage (e.g., drilling operations, CO_2 injection, design of monitoring, etc.). Open faults and fractures, together with abandoned drill holes or wells, form the most immediate natural pathways for CO_2 leakages and therefore constitute main risk factors for leakages at CO_2 storage sites (IPCC, 2005; Rutqvist et al., 2007; Pasala et al., 2013).

Small displacement faults may cause significant perturbation of a reservoir flow structure (Caine et al., 1996), so the fault system description must be as accurate as possible.

1.2.4.2. Seismic Time-lapse Seismic Monitoring

The monitoring of the injected CO_2 is a critical step in the GSC process in order to make sure that the CO_2 has been permanently removed from the atmosphere under strict safety conditions (Chen, 2006; Hannis, 2013). This technique, as well as the seismic technique itself, was adapted from the oil industry, where it was used in reservoir management tasks (e.g., Lumley, 2001; Calvert, 2005 and references therein). According to White (2013a), 4D seismics for monitoring geological storage of CO_2 has successfully been applied at the Sleipner field in the North Sea (e.g., Arts et al., 2004), the Weyburn-Midale field (Davis et al., 2003) in Canada, In Salah and Snøhvit in Algeria and Barents sea respectively (Eiken et al., 2011), and also in pilot-scale CO_2 injection sites, such as Cranfield (Zhang et al., 2012) in the US, Otway (Urosevic et al., 2010) in Australia, Nagaoka (Sato et al., 2011) in Japan, and Ketzin (Lüth et al., 2011) in Germany.

The injection of CO_2 in a reservoir site, including deep saline aquifers, has a number of effects on the thermal, hydrological, mechanical and chemical properties of the reservoir-seal formations and embedded fluids (e.g., Rutqvist and Tsang, 2002; Kaszuba et al., 2005; Kharaka et al., 2006; Mito et al., 2008; Huq et al., 2012; Rutqvist, 2012). Some of these changes have a direct effect on seismic signature and petrophysical properties, and therefore are detectable with the seismic reflection method (Carcione et al., 2006; Alshuhail, 2011); these include effects on the elastic properties (density, P- and S-wave velocity) (Batzel and Wang, 1992; Avseth et al., 2010), saturation (Vanorio et al., 2010), wave attenuation (Blanchard, 2011), stiffness (Avseth et al., 2010), pore pressure (Wang et al., 1998), anisotropy (MacBeth, 1999) and others.

The time-lapse seismic reservoir monitoring of a CO_2 storage site consists of acquiring and analyzing different seismic surveys repeated at the same location over time, in order to image the effects caused by the CO_2 injection in the reservoir. The method uses changes in the trace amplitudes and velocity to track the differences between the baseline and the repeated seismic images. This is why it is critically important to provide the most accurate seismic baseline model for the monitoring.

1.3. GEOLOGICAL SETTING OF HONTOMÍN

1.3.1 Regional geology

The target structure in this work, the Hontomín structure, is an elongated dome Jurassic in age. It belongs to the 'Platoforma Burgalesa' (Serrano and Martínez del Olmo, 1990; Vera, 2004; Tavani, 2012), which is enclosed in the southern section of the Basque-Cantabrian Basin (Fig. 1.13). This domain is located at the northern junction of the Cenozoic Duero and Ebro basins, forming an ESE-dipping monocline bounded by the Sierra de Cantabria Thrust to the North and the Ubierna Fault System to the South (Tavani, 2012).

This area was affected by three main deformation stages during the Mesozoic and Cenozoic (Tavani, 2012; Tavani et al., 2013). An initial extensional stage, which occurred during the Permian-Triassic, led to the development of WNW-ESE and E-W trending faults (Ziegler, 1989; García-Mondéjar et al., 1996). A second major extensional event, developed as result of the opening of the North Atlantic margin and the Bay of Biscay, occurred during the Late Jurassic and Early Cretaceous periods (e.g., Le Pichon and Sibuet 1971; Montadert et al. 1979; Ziegler 1988; García-Mondéjar et al., 1996). The Basque-Cantabrian basin and its Plataforma Burgalesa sub-unit formed at this stage. The former Permian-Triassic WNW-ESE faults were reactivated, and new NNE-SSW extensional faults developed at an angle of 75-80º with the previous faults (Tavani and Muñoz, 2012; Tavani et al., 2013).

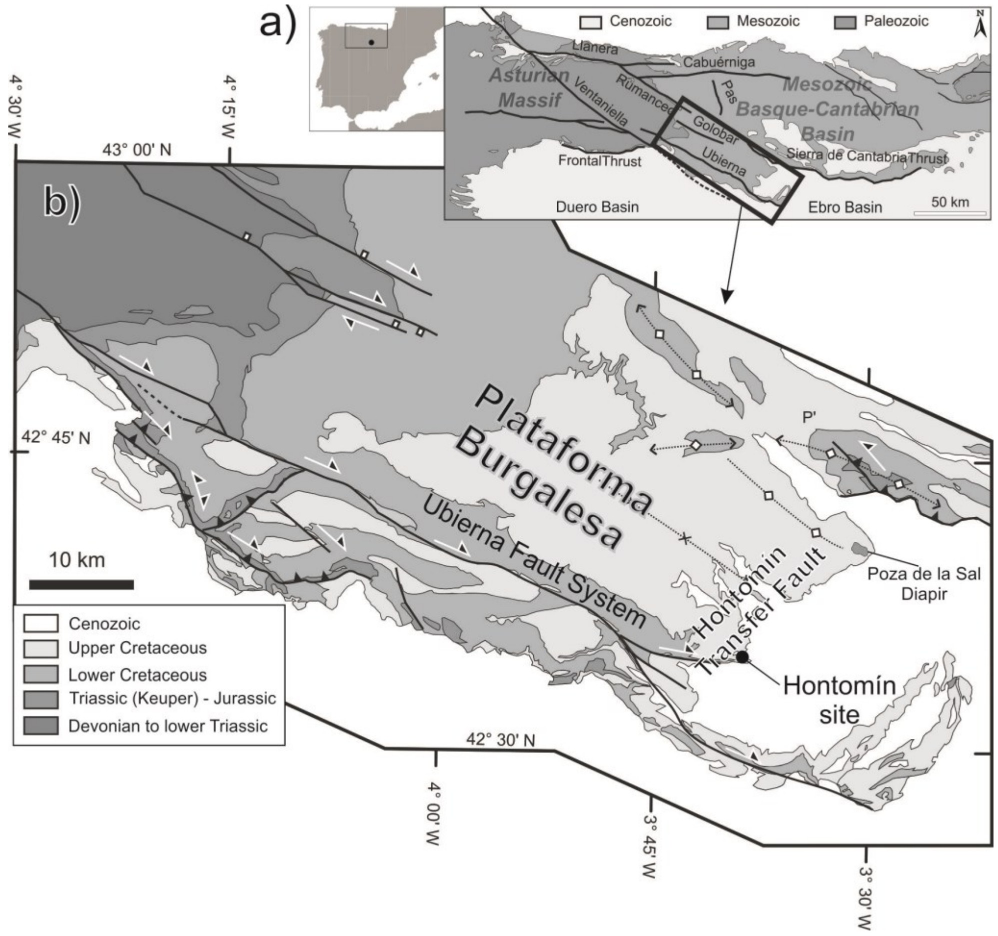

Fig. 1.13: (a) Location of the study area within the Iberian Peninsula and geological map of the Basque-Cantabrian Basin and Asturian Massif area, with labels of the main features (modified from Tavani et al., 2013); (b) geological map of the southern portion of the Basque-Cantabrian Basin, with detail of the Plataforma Burgalesa and the Hontomín location (modified from Tavani et al. 2011).

This extensional period generated a synformal domain in the study area (Pujalte et al., 2004; Quintà and Tavani, 2012), characterized by a thick Mesozoic sedimentary sequence (Quesada et al., 2012, Robles et al., 2004). The evaporite sediments deposited during the Upper Triassic (Keuper) acted as a major decoupling zone, separating the deformation of the cover sequences from the Paleozoic basement (Tavani et al., 2011; Carola et al., 2013; Tavani et al., 2013). Furthermore, evaporite migration produced by basement faulting enabled the development of extensional forced folding in the cover (Tavani et al., 2013). Finally, the latter Pyrenean orogeny originated a compressional setting in which the inherited faults were inverted, originating reverse, right-lateral and left-lateral reactivations (Tavani et al., 2011; Quintà and Tavani, 2012; Tavani et al., 2013).

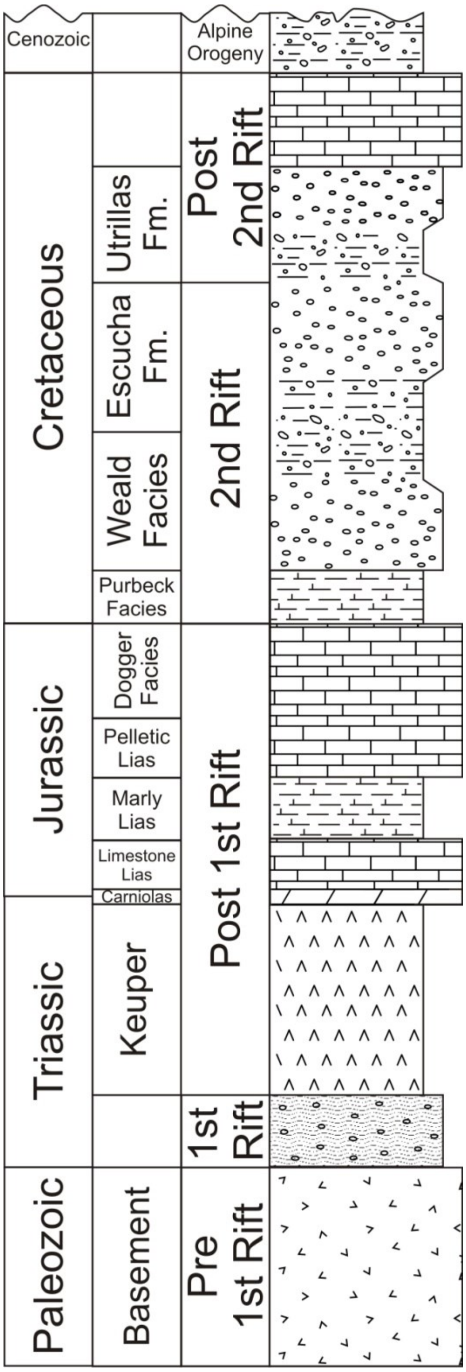

Fig. 1.14: Synthetic stratigraphic log based on regional data.

From a stratigraphic perspective (Fig. 1.14), the Mesozoic succession starts with the Triassic clastic sediments - Buntsandstein facies - lying over the Paleozoic metamorphic basement, which were deposited during the first rifting stage. On top of these materials, a Middle-Upper Triassic evaporitic unit, Keuper facies, was deposited. This unit composed of evaporites, dolomites and marls (Pujalte et al., 2004; Quesada et al., 2005) is currently forming the core of the target dome. The

Lower-Middle Jurassic series is constituted by a thick sequence of shallow marine carbonate and hemipelagic ramp sediments, set in four units: Limestone, Marly and Pelletic Lias units and a carbonate Dogger unit. The Purbeck Facies (Late Jurassic–Early Cretaceous in age) are placed uncomformably on top of the Jurassic marine rocks. They are formed by clays, sandstone and carbonate rocks, with a marine-continental transitional origin, and mark the onset of the second rifting stage. The Lower Cretaceous succession is completed by siliclastic sediments of the Weald Facies and the Escucha and Utrillas formations, also deposited during the second rift stage. They contain fluvial facies that alternate channel filling sandstones and flood plain shale sediments. The uppermost rocks outcropping in the Hontomín area are Upper Cretaceous carbonates and Cenozoic rocks (lacustrine and detritic), lying uncomformably over the Mesozoic successions and recording the transition from post-rift to compression.

The Mesozoic structure of the Hontomín dome has been described as an example of a forced fold-related dome structure (Tavani et al., 2013). These types of structures are generally associated with extensional fault systems (Schlische, 1995; Cosgrove and Ameen, 2000; Tavani et al 2011; 2013). They can develop under varying conditions (Braun et al, 1993; Jin et al., 2006) and their presence has been proposed for the Mesozoic Basque-Cantabrian Basin of Northern Iberia (Soto et al., 2011; Tavani et al., 2011; 2013). The formation prerequisite for these structures involves the existence of a ductile layer, which acts as a major decoupling zone capable of separating the deformation of the sedimentary cover from that occurring at the basement level. In the Hontomín site, this decoupling level is formed by the Triassic evaporite sediments, which separate the pre-rift Upper Triassic to Middle Jurassic folded sediments from the Paleozoic to Lower Triassic faulted rocks of the basement. The current geometry of the Hontomín dome is interpreted as having been generated by the reactivation during the Pyrenean orogenic stage of the pre-existing Mesozoic architecture. During this compressive stage, the Mesozoic sequence overrode the Cenozoic Ebro Foreland Basin (Martínez-Torres, 1993).

1.3.2. Reservoir Geology

The Hontomín structure, along with the Ayoluengo structure, has been targeted for hydrocarbon exploration in the Northern Iberian Peninsula since the early 1970s (Alvarez, 1994; Merten, 2006; Beroiz and Permanyer, 2011, Permanyer et al., 2013). A number of 2D seismic reflection transects were acquired with the aim of unraveling the regional structure (Beroiz and Permanyer, 2011; Tavani, 2012; Tavani et al., 2013). The stratigraphy of Hontomín motivated a renewed interest in the area, as the structure could be considered suitable for geological storage of CO_2 (Alcalde et al., 2013a). The available geophysical and geological data (vintage 2D seismic reflection data, well-logs, borehole core samples, etc.) indicate that the subsurface stratigraphy includes a carbonate Lower Jurassic sequence at approximately 1500 m depth that hosts a deep saline aquifer and a high-quality seal formation. This Lower Jurassic sequence outcrops to the NW of the Hontomín site (Fig. 1.15). The target reservoir formations include the upper part of the Carniolas unit and the Limestone Lias unit, with average thickness of 100 m and a porosity of 8.5 % (Alcalde et al., 2014). The salinity of the brine is 31.99 g/l, which is characteristic of stagnant formation conditions, with little or no hydrodynamic movement (Permanyer et al., 2013). The target seal comprises hemipelagic marlstones, marly limestones and black shales from the Marly and Pelletic Lias units, with an average thickness of 270 m. Other formations included in the Upper Jurassic and Lower Cretaceous also show suitable reservoir or seal properties in the overlying layers. It is therefore imperative that we comprehend the characteristics of these formations (Directive 2009/31/EC), as they form the upper part of the storage complex and are expected to provide a secondary containment barrier above the storage site caprock.

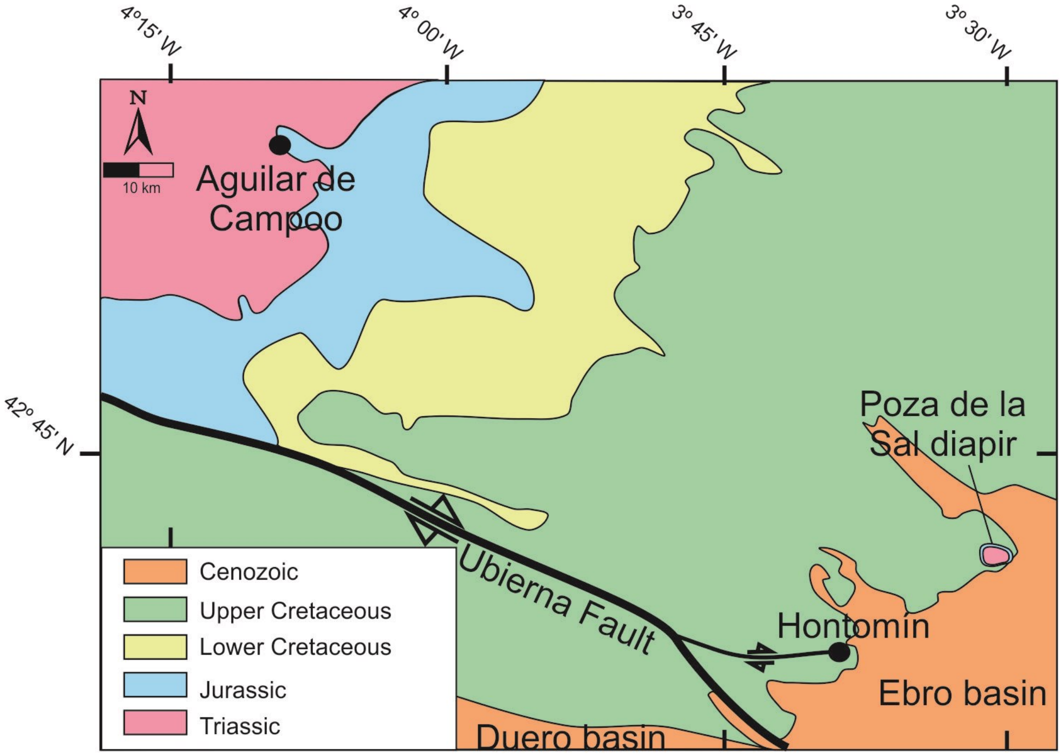

Fig. 1.15: Regional-scale geological map of the study area with the position of the Hontomín site and the main geological features.

CHAPTER II

Active seismic characterization experiments of the Hontomín research facility for geological storage of CO2, Spain.

Alcalde, J., Martí, D., Calahorrano, A., Marzán, I., Ayarza, P., Carbonell, R., Juhlin, C. and Pérez-Estaún, A. 2013a.. International Journal of Greenhouse Gas Control, 19, 785-795.

International Journal of Greenhouse Gas Control 19 (2013) 785–795

Contents lists available at ScienceDirect

International Journal of Greenhouse Gas Control

journal homepage: www.elsevier.com/locate/ijggc

Active seismic characterization experiments of the Hontomín research facility for geological storage of CO_2, Spain

J. Alcalde[a,b,*], D. Martí[b], A. Calahorrano[c], I. Marzan[b], P. Ayarza[d], R. Carbonell[b], C. Juhlin[e], A. Pérez-Estaún[a,b]

[a] Fundación Ciudad de la Energía (CIUDEN), Avenida Segunda 2 (Compostilla), n°2, 24404, Ponferrada, Spain
[b] Institute of Earth Sciences Jaume Almera (ICTJA – CSIC), Department of Earth's Structure and Dynamics, C/Lluís Solé i Sabarís s/n, 08028, Barcelona, Spain
[c] Institute of Marine Sciences – CSIC, Passeig Marítim de la Barceloneta, 37-49, 08003, Barcelona, Spain
[d] University of Salamanca, Department of Geology, Plaza de los Caídos, s/n, 37008, Salamanca, Spain
[e] Uppsala University, Department of Earth Sciences, Villavägen 16, SE-75236, Uppsala, Sweden

ARTICLE INFO

Article history:
Received 16 July 2012
Received in revised form
13 December 2012
Accepted 30 January 2013
Available online 1 March 2013

Keywords:
3D seismic reflection
Reservoir characterization
CO_2 storage
High resolution
Three-component seismic

ABSTRACT

An active source seismic experiment was carried out as part of the subsurface characterization study of the first Spanish Underground Research Facility for Geological Storage of CO_2 in Hontomín (Burgos, Spain). The characterization experiment included a 36 km^2 3D seismic reflection survey and two three-component seismic profiles. The target reservoir is a saline aquifer located at 1450 m depth within Lower Jurassic carbonates (Lias). The main seal is formed by interlayered marlstones and marly limestones of Early to Middle Jurassic age (Dogger and Lias). The seismic images obtained allow defining the 3D underground architecture of the reservoir site. The structure consists of an asymmetric dome crosscut by a relatively complex fault system. The detailed characterization of the fracture system is currently under study to unravel the geometric distribution of the faults and their extent within the different formations that form the structure. The constrained model has guided the design of the injection and monitoring boreholes and provided the data for the baseline study. The resultant high resolution seismic model will be used as a reference in future monitoring stages.

1. Introduction

The amount of CO_2 liberated by the use of fossil fuels is leading policy makers toward a sensible management of CO_2 emissions. The European Union (EU) strategy for handling CO_2 emissions includes a directive aiming to a 20% reduction of CO_2 emissions by 2020. In this context, carbon capture and storage (CCS) represents an adequate short-to-middle term solution. The EU has granted financial support to 6 demonstration projects for CCS. Within these projects, the Ciudad de la Energía (CIUDEN) foundation is leading the Spanish efforts in this topic by promoting an underground research facility (URF) for geological storage of CO_2 in Hontomín (Fig. 1). The CIUDEN foundation is dependent on the Energy State Department. The two main goals behind this URF are (1) to have a better understanding of the different processes (physical, geochemical, hydrogeological, etc.) involved in CCS; and (2) to test and develop different storage and monitoring techniques, in order to improve the methodologies and reduce the costs derived from its application.

During the feasibility phase of the URF, several locations within the Iberian Peninsula were carefully evaluated (Prado et al., 2008). The Hontomín site was selected due to the good geological and structural knowledge of the region, extensively studied because of the existence of oil traps. Thus, the existence of a saline aquifer and formations feasible for geological storage of CO_2 were identified. The area also features very low seismicity. Oil exploration activities since the 1970s provided valuable 2D seismic profiles and well-log data of the area. These data were used within the feasibility study for a first characterization of the main geological structures of the area, and were an asset for the final decision on the location of the URF in Hontomín. The available information was reprocessed in order to obtain a regional preliminary geological model of the area. The target reservoir consists of a saline aquifer placed at around 1450 m depth within a marine carbonate reservoir-seal system. If developed, this research facility will become one of the first storage sites in the world with these characteristics.

Seismic techniques constitute one of the key geophysical tools for the characterization of reservoir complexes (Arts et al., 2001; Juhlin et al., 2007). High resolution seismic images have been also used by industry for monitoring at enhanced oil recovery (EOR)

---

* Corresponding author at: Institute of Earth Sciences Jaume Almera (ICTJA) – CSIC, Department of Earth's Structure and Dynamics, C/Lluís Solé i Sabarís s/n, 08028, Barcelona, Spain. Tel.: +34 93 409 54 10; fax: +34 93 411 00 12.
E-mail addresses: jalcalde@ictja.csic.es, juan.alcalde.martin@gmail.com (J. Alcalde).

1750-5836/$ – see front matter © 2013 Elsevier Ltd. All rights reserved.
http://dx.doi.org/10.1016/j.ijggc.2013.01.039

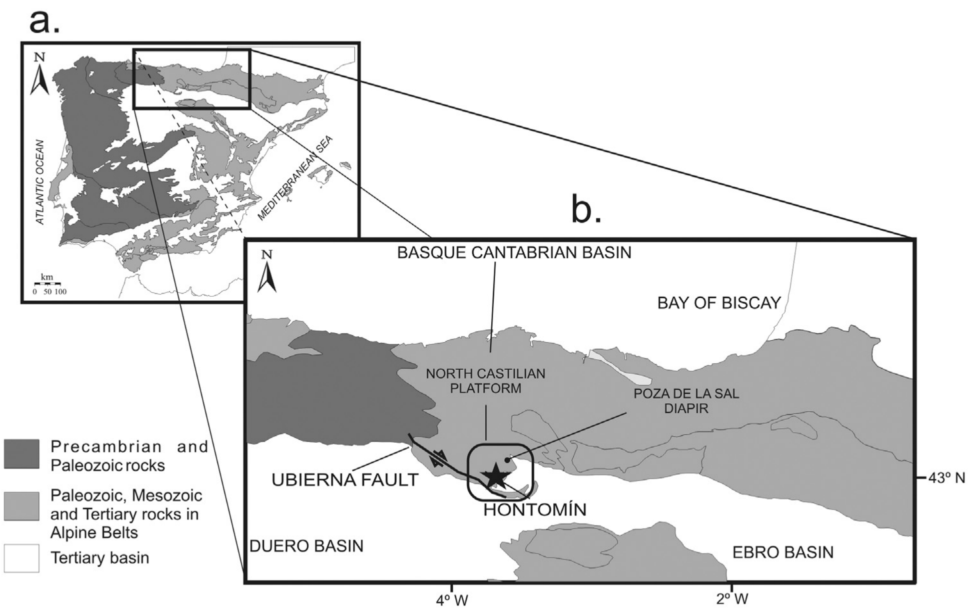

Fig. 1. Simplified geological maps (a) showing the location of the study area within the Iberian Peninsula and (b) an enlarged detailed view of the main geological features around Hontomín. The Hontomín URF is located in the North Castilian Platform (south of the Basque-Cantabrian Basin), bounded by the Ubierna fault to the south-west, the Poza de la Sal diapir to the north and the Ebro basin to the east.

sites and for tracking the migration of CO_2 and/or other fluids with time-lapse techniques (Arts et al., 2004; Lumley, 2010; Preston et al., 2005). Because of the high potential of seismic techniques for subsurface imaging and its resolution, an extensive seismic data acquisition research program was design to accomplish a seismic characterization of the site and estimate the potential and characteristics of the reservoir and seal.

This paper focuses on the description and preliminary results of the active source seismic experiments carried out at Hontomín. The data acquired include: (1) a 3D seismic reflection survey; (2) two three-component (3C) normal incidence seismic reflection transects; and (3) a multi-azimuth tomographic 3-component data volume. The surveys were designed to cover the whole storage structure, allowing a characterization of the complete volumetric architecture of the reservoir site and the fault geometry and distribution. The resulting seismic image is used to propose the most favorable location for the injection and monitoring boreholes, by estimating the possible migration paths of the CO_2, conditioned by the structure. All this information, together with the future characterization of the distribution of the physical properties, will be combined to generate a baseline model which will be used in the monitoring stage.

2. Geological setting

The URF is located in Hontomín (Burgos, northern Spain, Fig. 1). The Hontomín site borders with the Ubierna fault (NW–SE direction) to the south-west (Tavani et al., 2011), the Poza de la Sal diapir to the north (Quintá et al., 2012) and the Ebro basin to the east.

From a geological perspective, Hontomín belongs to the Basque-Cantabrian Domain, north of the Ebro and Duero basins (Fig. 1). It is part of the North Castilian Platform (Serrano and Martínez del Olmo, 1990; Quintà and Tavani, 2012) which was generated in the context of the opening of the North Atlantic and Bay of Biscay during Mesozoic times. During the Mesozoic extension, a regional synformal domain was developed (Pujalte et al., 2004); as a result, a thick sedimentary sequence was deposited in this area (Quesada et al., 2005). Subsequently, the Alpine compression produced small-scale inversion structures which are detached along the Triassic evaporites. According to the available geological and geophysical data (2D seismic reflection images and borehole logs, borehole sample descriptions, etc.), the reservoir and seal formations are Jurassic in age and form a dome-like structure with an overall extent of 5 km × 3 km.

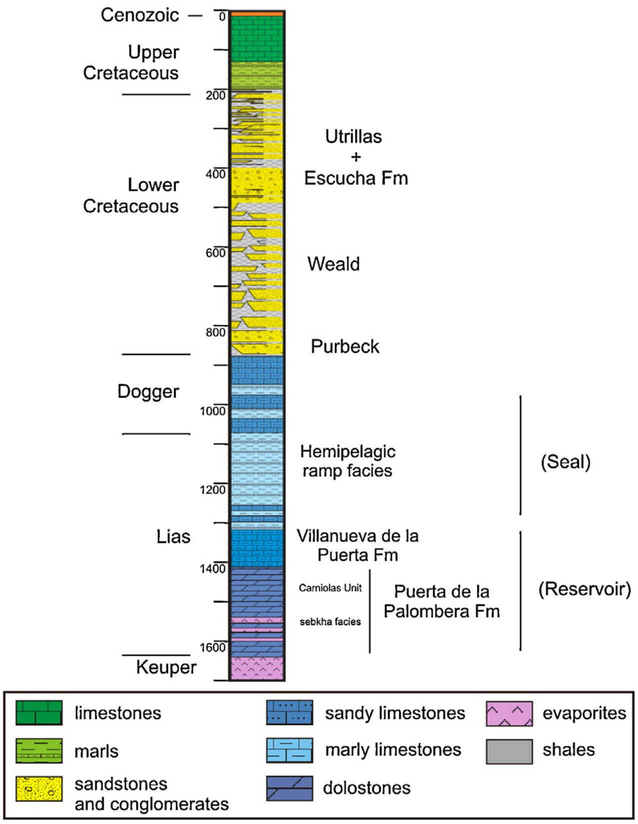

Fig. 2. Stratigraphic column. Shown is the expected stratigraphy in the injection zone derived from the available seismic and borehole data.

Source: Geomodels – UB.

The Mesozoic succession (Fig. 2) starts with Keuper Facies, which formed the core of the Hontomín dome. The Puerto de la Palombera Fm is composed of evaporites, dolomites and marls (sebkha facies), and overlies the Keuper Facies, forming the boundary between the Triassic and Lower Jurassic (Pujalte et al., 2004; Quesada et al., 2005). The Lower Jurassic is constituted by the deposits of a shallow marine carbonate ramp and the rest of the Jurassic succession is completed with carbonate and marls of a hemipelagic ramp. The Purbeck Facies of Upper Jurassic and Lower Cretaceous age (clays, sandstone and carbonate rocks) are placed unconformably on top of the marine Jurassic rocks. The rest of the Lower Cretaceous is composed of Weald, Escucha, and Utrillas Facies which essentially are siliciclastic rocks. The rocks cropping out in the Hontomín area are carbonates of the Upper Cretaceous and the detritic and lacustrine Cenozoic rocks that lay unconformably over the Mesozoic succession. The rocks of the Mesozoic succession of the Hontomín dome structure have been sampled by four preexisting boreholes which reached depths between 900 and 1832 m (Vera, 2004). The analysis of the stratigraphy of the reservoir shows a dolostone unit, known as "Carniolas", with a porosity over 12% and high salinity. The relatively high porosity of the dolostone is a result of a secondary dolomitization and overprinted fracturing. It belongs to the shallow marine carbonate ramp of Lias (Raethian-Sinemurian). The minimum thickness of the Carniolas Unit is 100 m. The succession of the reservoir is completed with oolitic grainstones called Villanueva de Puerta Fm. The unit which, most probably, will act as a seal is composed of marls and black shales from a hemipelagic ramp (Pliensbachian and Toarcian). The thickness of these units (reservoir and seal) is between 314 and 545 m (CIUDEN, 2011). The Hontomín structure is delimited by a normal fault to the north, which was active only during the Purbeck sedimentation. To the south, the structure is bounded by a strike slip fault associated with the Ubierna Fault (Tavani et al., 2011).

The topography in the study area is relatively variable, with elevations ranging from 816 to 1066 m over sea level. Three main zones can be described from a topographical/geomorphological point of view (Fig. 3): (1) a mountainous area to the west, corresponding to the Upper Cretaceous carbonates, that contains unevenly spread karstic voids; (2) a relatively flat area consisting of farming lands in the center, which mainly corresponds to the Cenozoic cover, denoting poorly compacted sediments; and (3) a cliffy area to the east, characterized by rough topography and forested vegetation.

3. Active source seismic data acquisition

A consortium of research groups (academic and industry) designed a series of scientific projects aiming to generate a multidisciplinary baseline dataset. Within this characterization phase, an extensive active seismic acquisition program was carried out. In summer 2010, two active seismic experiments were performed at Hontomín (Fig. 4): a 3D seismic reflection survey and two three-component 2D seismic profiles were acquired using digital

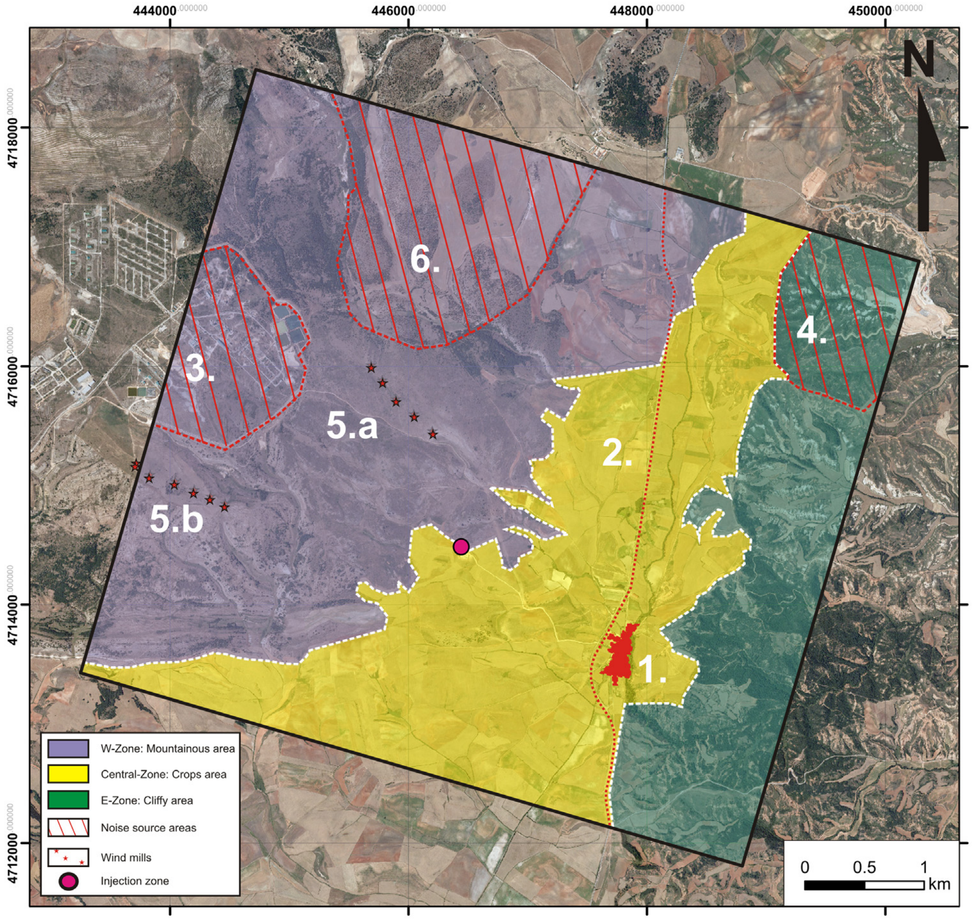

Fig. 3. Detailed map of the study area showing the different characteristic zones and sources of noise discussed in the text: the mountainous area (purple); the crops area (yellow); and cliffy area (green). Different sources of noise that have been identified in the area are marked in red: zone 1: town of Hontomín; zone 2 (dotted line): road CL-627; zone 3: explosives; zone 4: waste dump facility; zones 5.a and 5.b wind mills; zone 6: bullfighting bull farm. The theoretical injection borehole position is marked by a magenta circle. (For interpretation of the references to color in this figure legend, the reader is referred to the web version of the article.)

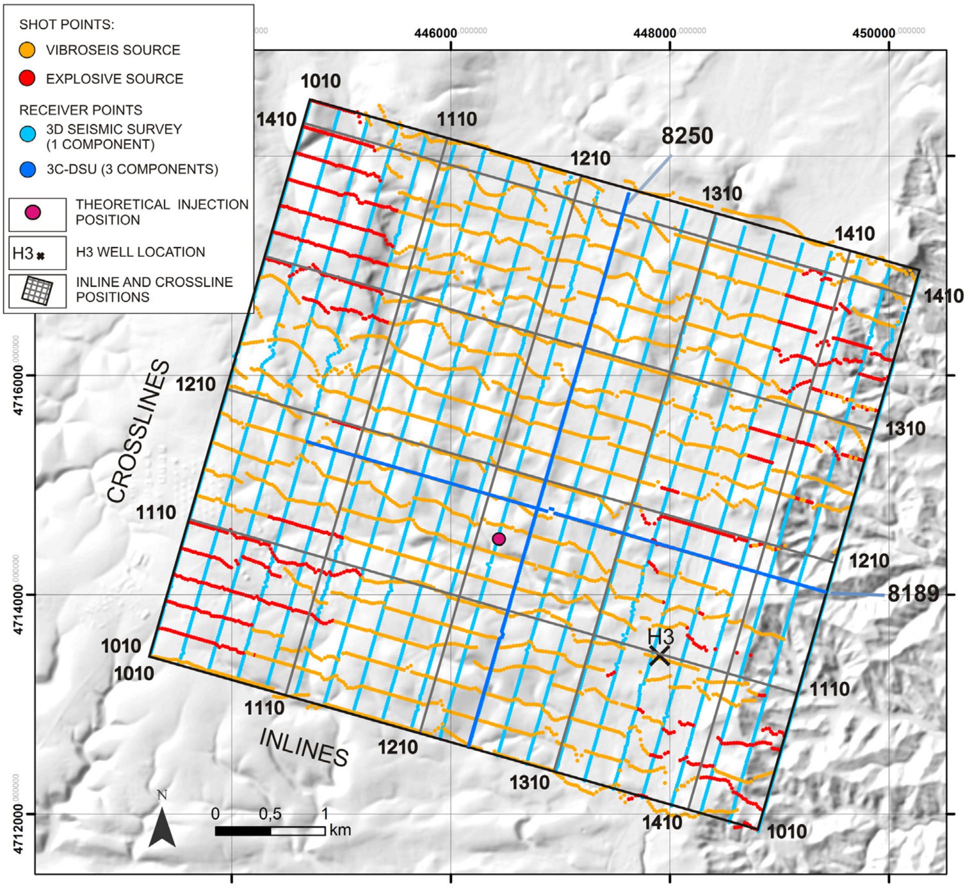

Fig. 4. The acquisition geometry of the active source seismic reflection data. The map shows the position of the elements of the active seismic experiments acquired at Hontomín. Orange points mark the position of source points acquired with the Vibroseis source. Red points mark the position of shot points acquired with the explosive source. Light blue points mark the position of the 3D survey receivers. The two 3C profiles are marked in dark blue. The magenta circle marks the proposed position for the injection borehole. The black cross marks the position of the H3 borehole. (For interpretation of the references to color in this figure legend, the reader is referred to the web version of the article.)

sensor units (DSU) instruments (3C-DSU). These experiments were designed by academics, and the company CGGVeritas was contracted for the acquisition. The 2D seismic experiment consisted of two perpendicular lines centered at the expected apex of the underground dome structure. All these experiments focused on different, but complementary, objectives in the characterization of the reservoir complex. The acquisition parameters of both experiments (Table 1), including position, size and geometry of the surveys, were chosen taking into account the information provided by studies of the feasibility phase. The final selected parameters allowed us to obtain relatively high resolution at the estimated target depth at a reasonable cost for an experiment with academic goals.

Several noise sources/types were identified in the study area (Fig. 3) during the acquisition. These included: (1) the village of Hontomín (50 inhabitants) is located inside the study area, at about 1.5 km away from the proposed injection point (Fig. 3, zone 1). (2) The whole survey is crossed by a north–south road with relatively little traffic (Fig. 3, zone 2). (3) A factory is located in the central-west edge of the survey (Fig. 3, zone 3); because this factory manufactured explosives, an agreement with the owners was reached to perform the seismic acquisition during their summer vacation period. (4) Another odd zone is located in the north-east corner of the survey (Fig. 3, zone 4). It houses a regional waste dump facility. In the shallow subsurface, the weathering layer is very loose (not compacted) and it causes coupling problems which results in severe distortions in the energy transmission. (5) The area is subject to medium level winds, making it adequate for wind power generation, and nine wind mills are installed and currently working in the study area (Fig. 3, zones 5.a and 5.b). (6) The survey passes through a bullfighting bull farm, located in the northwestern part of the study area (Fig. 3, zone 6). (7) The acquisition started during the harvest season. Therefore, noise produced by farming equipment was also identified in the shot records.

Table 1
Template acquisition parameters for the 3D survey and the 3C-DSU profiles.

Parameter	3D survey	3C-DSU
Receiver spacing	25 m	25 m
Receiver line spacing	275 m	–
Source spacing	25 m	25 m
Source line spacing	250 m	–
CDP bin size	12.5 m × 12.5 m	12.5 m × 12.5 m
Nominal fold	36 traces/CDP	105 traces/CDP
Source	Vibroseis (4 × 15-Tn M22) + explosives (450 g/shot point)	Vibroseis (4 × 15-Tn M22) + explosives (450 g/shot point)
Instrument	SG-10 (Sercel)	DSU-3 C (Sercel)

3.1. 3D seismic reflection survey

The 3D seismic reflection survey covered 36 km^2. The acquisition area was selected to illuminate/image the target structure in all its extension. The receivers were deployed along approximately N–S oriented lines (inlines), with a distance of 275 m between them. Along these inlines, receivers were deployed every 25 m.

The source lines (crosslines) were oriented approximately E–W, perpendicular to the inlines. The distance between crosslines was of 250 m. The distance between sources along the crosslines was 25 m. The complete survey consisted of 22 inlines and 22 crosslines. Each receiver station consisted of 6 vertical component geophones (10 Hz) deployed in line.

The data were acquired in 5 stages or swaths. The swaths located on the edges of the survey included six active inlines (720 active channels) (Fig. 4) whilst the inner three swaths included ten (1200 active channels). The swaths overlapped so that some of the inlines were recorded along twice until the whole study area was covered. In total, 4818 shot-points were shot and 4.5 million traces were recorded. This geometry resulted in an average fold of 36 traces/CDP.

The diversity in sedimentary media present in the near-surface of Hontomín added complexity to the data acquisition and processing, due to the differences in source coupling and in source and receiver performances. The survey was designed to use Vibroseis sources. However, due to the access difficulties in the easternmost part of the study area (cliffy area) and in other specific zones, 24% of the survey was acquired using explosive sources. The Vibroseis source consisted of a double 16 s sweep of 8–80 Hz bandwidth; the energy was generated by four Vibroseis trucks (15-Tn M22) vibrating simultaneously at each source point. The explosive energy consisted in 450 g of dynamite distributed in three 1.5 m deep boreholes per shot-point.

3.2. DSU-3C profiles

An academic crew deployed two orthogonal lines with 3C instruments (DSU). The lines were centered in the study area, with the geometry displayed in Fig. 4. One transect is oriented, approximately, N–S (line labeled 8250) and the second is oriented E–W (line labeled 8189). The main innovation of this survey was the use of the 3-component DSU3 sensors (Hons et al., 2008). These instruments, developed by Sercel, represent a new generation in solid state receivers (MEMS), and were used for the first time in Spain. The main advantages of employing receivers with these characteristics includes their broad frequency band of recording (0–800 Hz) and, more importantly, measuring the horizontal components of motion. The two perpendicular lines recorded all the shots of the 3D acquisition. Also, 2D data were acquired along lines 8250 and 8189, using the Vibroseis source along 100% of the former and along 97% of the latter.

A total of 211 receiver points (line 8250) and 198 receiver points (line 8189) were deployed along each profile (Fig. 2). The spacing between receivers was 25 m, giving a length of 5275 and 4950 m, respectively. The spacing between sources was of 25 m, the same as for the 3D. The given geometry allows a maximum CDP fold of 105. Data were acquired with a sampling rate of 1 ms and a total record length of 4 s. This sampling rate ensures the minimum resolution needed for the characterization of the target at the estimated depth to be achieved. Furthermore, P and S wave stacks can be obtained, providing key constraints for the baseline study. Since the shots fired for the 3D acquisition were also recorded by the DSU-3C array, a large data set is available for tomographic traveltime inversion, which will help constrain the physical properties (P and S-wave velocities) of the study area. This data set will be referred to as the tomographic database.

The objective of the 3C data acquisition was to obtain high resolution seismic images of the longitudinal and horizontal components (P- and S-waves). The seismic velocity of the S-waves is lower than the P-waves; thus for the same range of frequencies, the wavelength of the S-waves is shorter than the P-waves. Therefore, although S-wave data usually show poorer quality than P-wave data, they could provide information of higher resolution than the P-wave data. Furthermore, P- and S-wave information can be used together in order to obtain information on porosity, pore fluid and lithology (Castagna et al., 1985).

4. Data processing

Each of the data sets was acquired with different objectives, and they require careful signal processing in order to obtain quality images of the subsurface. The heterogeneous near surface geology, combined with the relatively rough topography (maximum elevation difference of 200 m) implies that static corrections are a key factor in the processing flow. The use of two different sources also produces a more complex processing challenge when merging both data sets. Both sources feature different frequency content, phase and amplitude composition, and also distinct interaction with the earth (coupling). Furthermore, both sources are distributed unevenly within the survey.

Specific issues that processing needed to address were: (1) The Vibroseis shot gathers show a reverberative character at near offsets; this has been attributed to coupling, being most probably related to the fields that feature crops and agricultural activities. (2) Disappearance of first breaks at offsets longer than 700 m, revealing a jump of approximately 300 ms between expected first breaks and the actual first arrival. (3) Other specific noise patterns, such as traffic noise, windmill noise, ground roll, air waves etc. were attenuated by noise attenuation steps and/or direct muting.

A key issue clearly observed in the data, especially in the 3C-DSU records is the disappearance of first breaks (black arrows in Fig. 5) at an average offset of 700 m. This "shadow zone" is consistent throughout the survey and can generally be attributed to the presence of velocity inversions (Krishna et al., 1999). In the study area the velocity inversion occurs at the Upper-Lower Cretaceous boundary. The change from carbonates to siliciclastic sediments produces a reduction of the propagation velocities. Furthermore, the siliciclastic Utrillas and Escucha formations in the Lower Cretaceous have a high porosity (14–24%) and hence, a relatively low density; confirmed by the existence of very large aquifers within these formations. The velocity inversion corresponding to this boundary can be recognized in the existing well logs of the area (example of the H3 sonic log in Fig. 7a, location in Fig. 4). In order to study this velocity inversion a 1D model was generated. This model was derived from sonic logs, in particular from borehole H3 (Fig. 7a). The simplified model consisted of three layers set at 0, 211 and 506 m depth. The physical properties assigned to each layer were: *Vp* velocities of 3000, 2000 and 4000 m/s (red dashed line in Fig. 7b); Vs velocities of 1500, 1000 and 2000 m/s (blue dashed line in Fig. 7b); and an attenuation factor of 5, 20 and 100 (green line in Fig. 7b). This model was then input into a 2D finite difference forward modeling code (SeismicUnix, after Juhlin, 1995) to generate synthetic shot gathers (Fig. 7c). The synthetic modeling exercise source gathers that are of a similar nature as the observed ones, i.e. a shadow zone at 300 m offset. This shadow zone is characterized by the disappearance of the first arrival and the shallow reflection and refraction. The reflection from the base of the low velocity layer (with a zero-offset arrival time of about 0.3 s in Fig. 7c) may be misinterpreted as a first arrival. In the synthetic data the time jump at the offset where the first arrival fades out to the later arriving reflection is 200 ms. In the real data set, the offset location and time jump varies considerably throughout the survey, but the time jump may be up to 700 ms at certain places. The existence of this shadow zone decreases the quality of the final images by restricting use of the far offset (>700 m) information for imaging the uppermost 500 m.

A processing flow (Table 2) up to post-stack time migration was applied to the entire 3D data set. It included: static correction calculations, amplitude compensation, time-variant frequency filtering

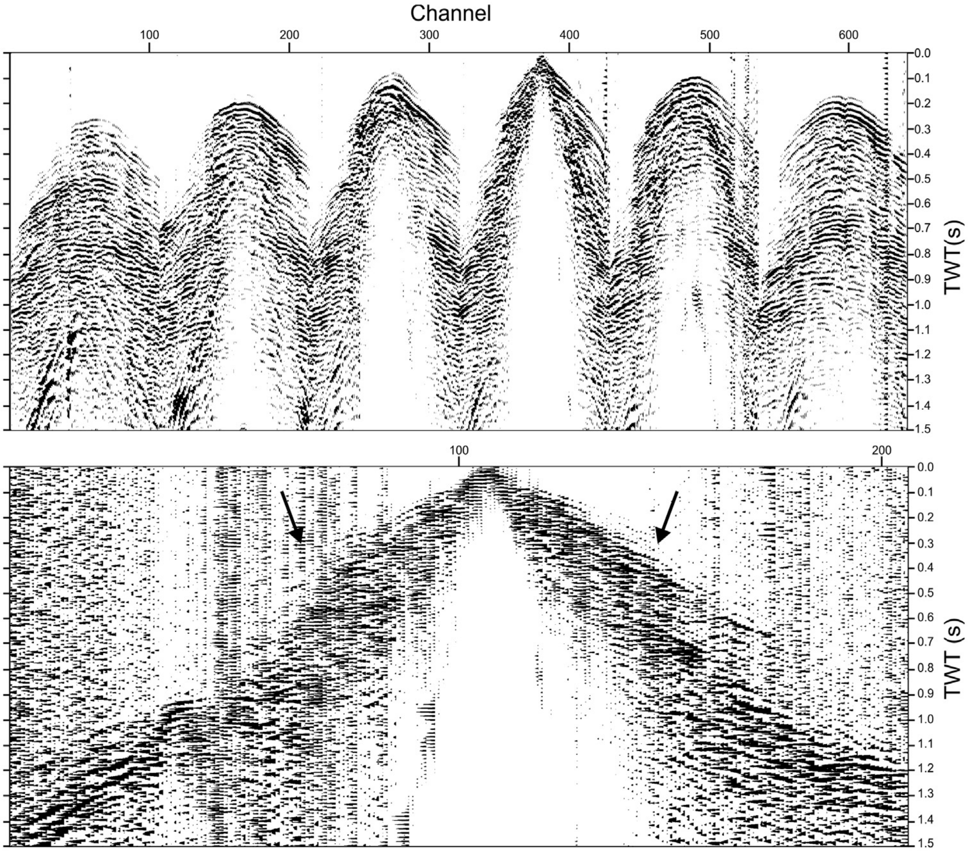

Fig. 5. Example of raw source gathers acquired in the 3D seismic reflection survey. Top, corresponds to 6 inlines from one of the swaths. Bottom, the shot gather recorded by the 3C-DSU (vertical component). The two black arrows mark the beginning of the shadow zone.

Table 2
Processing steps applied to the seismic data sets.

Step	Parameters
1	Read raw SEGY data
2	Geometry calculation and application
3	Trace edition
4	First break picking (offset range: 0–500 m)
5	90° phase shift applied to Vibroseis source data (source matching)
6	Spherical divergence correction (v^2t)
7	Time variant frequency filtering: 0–200 ms: 30–45–90–140 Hz 300–600 ms: 25–40–90–120 Hz 700–1500 ms: 20–30–70–90 Hz
8	Surface consistent deconvolution (shot and receiver domain): filter 100 ms, gap 14 ms, white noise 0.1%
9	Refraction statics: datum 1070 m, replacement velocity 3500 m/s
10	Trace balance (0–1500 ms) and surface consistent balance
11	Velocity analysis
12	Residual statics
13	Normal move-out correction: 70% stretch mute
14	Stack
15	Trace balance (0–1500 ms)
16	F_{XY}-deconvolution
17	DMO correction
18	Stack
19	Finite-difference 2.5 D migration
20	Trace balance (0–1500 ms)
21	F_{XY}-deconvolution

and surface consistent deconvolution. The results of the application of this processing (Fig. 6) show a clear improvement in the signal to noise (S/N) ratio, and most noise events have been removed or attenuated. The resulting migrated images (Figs. 8 and 9) allowed us to perform a preliminary interpretation.

Out of the applied processing steps, the ones that had the highest impact in the quality of the migrated images were the static corrections and the 3D-DMO correction. There are a number of examples in the literature showing that static corrections are key processing steps in for obtaining high quality images in similar characterization experiments (e.g. Juhlin et al., 2007; Malehmir and Bellefleur, 2009). The large topographic changes and heterogeneous geology present at Hontomín accentuates the importance of static corrections at the site. The accumulated correction (refraction + elevation) applied to the data was up to 130 ms at certain problematic locations. The application of the static corrections allowed us to obtain a moderate resolution image (and therefore subject to interpretation) in the early stages of processing. The 3D-DMO correction applied to the data increased the coherency of the reflections, especially on the flanks of the target structure.

Another important matter that arises in seismic surveys with dual sources (like Hontomín) is the matching of the wavelet properties. At Hontomín, both Vibroseis and explosive sources were utilized. As well as having a different frequency and amplitude content (addressed in the processing flow by filtering and balancing), these two source types have a different phase: zero phase in the case of the Vibroseis source and minimum phase in the case of the explosive source (Steer et al., 1996). Therefore it becomes necessary to attempt to match the zero phase Vibroseis wavelet to the minimum phase dynamite wavelet. As this work only aims to show preliminary images, a fast solution to the source matching

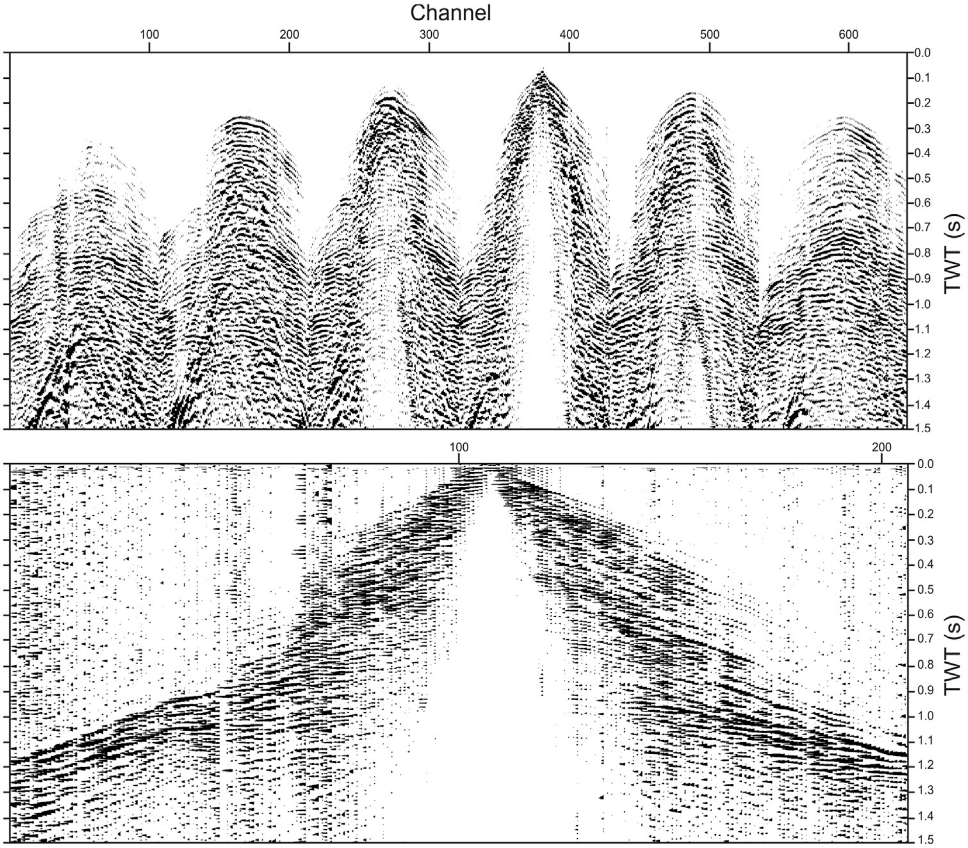

Fig. 6. The same shot gathers as Fig. 5 after the processing discussed in the text was applied (up to step 8 in Table 2).

problem was necessary. A 90° phase shift was applied to the traces acquired with the Vibroseis source, in order to approximate a minimum phase wavelet (Yilmaz, 2001). However, further work to optimize the match between dynamite and Vibroseis wavelets is ongoing; this includes applying bulk time and phase shifts, as well as convolutional match filters.

5. Seismic images description

The resulting 3D cube (Fig. 8) and 2D profiles show several common patterns. The target structure is recognized as a dome-shaped high amplitude reflection package (B in Fig. 8), observed at 700–1100 ms. This structure is asymmetric, with the south and east flanks containing steeper dips than the north and the west ones (blue line in Figs. 8 and 9). The shallowest part is culminated by a relatively flat area of about 2 km^2. Within this structure, amplitudes are irregularly distributed, suggesting a relatively high degree of internal heterogeneity. The area below the target structure shows a heterogeneous, non-continuous reflectivity (A in Fig. 8).

Another characteristic reflection fabric which suggests internal layering can be identified at 250–600 ms (D in Fig. 8). It is separated from the target structure by a heterogeneous reflection package (reflection zone C in Fig. 8). Package C is highly variable, being characterized by a lack of lateral continuity of the reflections in certain areas. The southernmost part of the survey contains structures with dips which are consistent with the estimated dips of the structure. The middle and northern parts reveal planar bedding instead, revealing an unconformity relationship with the underlying structures.

The shallowest part of the survey is highly heterogeneous, but a high amplitude reflection is observed in the southern half (reflection E in Fig. 8). This reflection, present in the south quarter of the study area, is related to high acoustic impedance, suggesting a sudden increase in velocities and/or density compared with the underlying layer. The first 250 ms have a very low S/N ratio, mainly due to artifacts generated by the migration.

6. Interpretation and discussion

6.1. The target structure

A first general interpretation of the seismic images defines the general structural geometries of the study area (Figs. 8 and 9). An anticlinal dome with asymmetric flanks dominates the center of the study area at the target depth (blue line in Fig. 8), with an approximate thickness of 300–400 ms. The total extent of this structure is about 17 km^2, and is entirely covered by the 3D survey. The apex of the anticlinal dome is found approximately in the intersection of the 2D 3C perpendicular profiles (intersection of inline 1180 and crossline 1240 in the 3D data set, α in Fig. 8). The dome is elongated in the NE–SW direction, with the SW flank being steeper than the NE one. The characteristics of the dome, including depth, shape, seismic attributes and physical properties (the latter obtained from the well-logs) indicates that the structure includes the target reservoir and seal systems. The rise in the velocities due to the marine-land Jurassic (Dogger-Purbeck) boundary produces an increase in amplitudes, that is observed as a relatively sharp change in the reflections. Well log and surface geology records indicate that the transition from Jurassic carbonates to Triassic anhydrites and other evaporitic formations is large and that is developed irregularly. This feature can explain the heterogeneous and discontinuous reflectivity of package A, and the lack of clear transition between package A and B (Fig. 8). Furthermore, these anhydrites seem to reflect a large portion of the propagating energy.

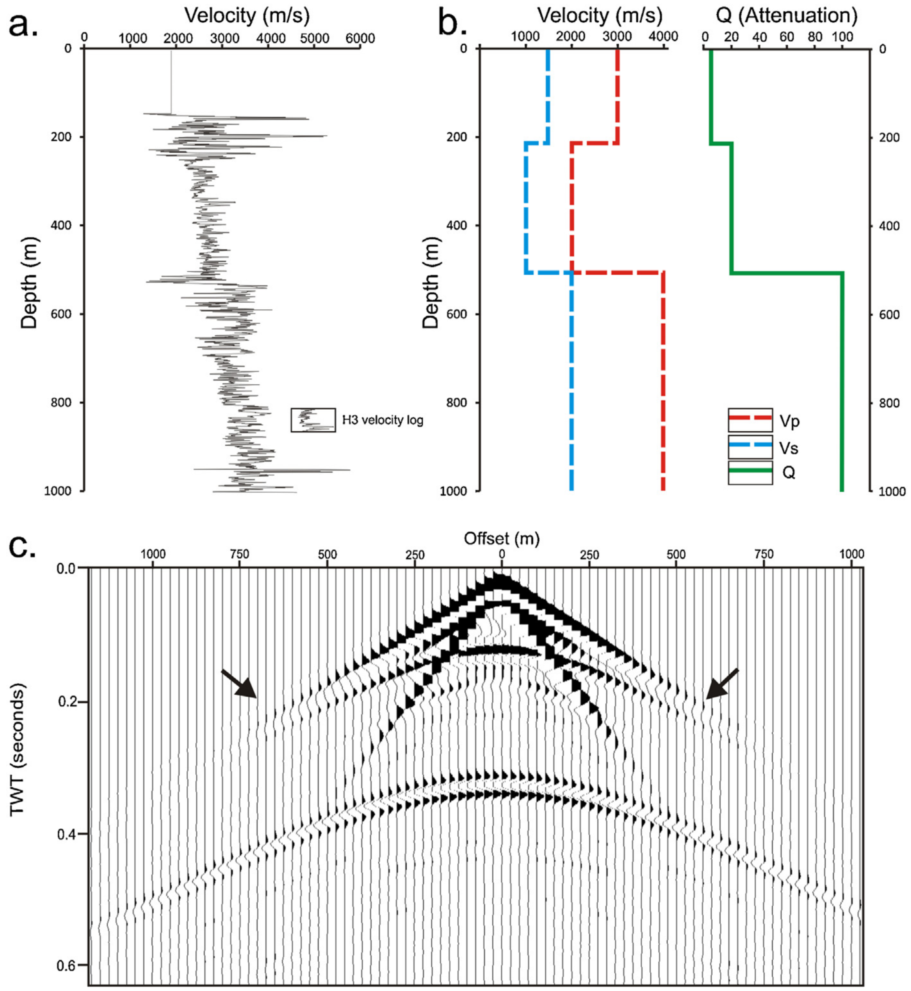

Fig. 7. Generation of a synthetic seismogram to explain the fading out of first arrivals due to the velocity inversion observed in sonic logs in the study area. (a) Sonic log extracted from H3 well (location in Fig. 2). (b) Simplified 1D models derived from the sonic log, including *Vp* (red dashed line), *Vs* (blue dashed line) and attenuation (green line). (c) Synthetic seismogram obtained from the propagation of elastic waves through the velocity model in b. The black arrows indicate the point where first arrivals and the reflection become very weak due to the low velocity zone. (For interpretation of the references to color in this figure legend, the reader is referred to the web version of the article.)

There is a lack of continuity in the reflections in this area, so there appears to be an absence of well defined internal structure within these sediments.

The package C (Figs. 8 and 9) is interpreted as the lower part of the Lower Cretaceous, probably comprised of the terrigenous Weald and Utrillas/Escucha formations. Geologically, it could represent a secondary reservoir-seal system, as these formations feature a relatively high porosity and permeability, key characteristics of these terrigenous sediments. However, the depth of these sediments and their complex lateral continuity makes them less suitable than the marine Jurassic reservoir-seal system for storage of CO_2. On top of package C, in the southern part of the survey, the Cenozoic cover (E in Fig. 8) produces a clear contrast with the Upper Cretaceous sediments. This boundary outcrops in the study area, being correlated with the mountainous/crop boundary outlined in Fig. 3.

The images show the main structures present in the study area. However, further processing (in particular pre-stack migration) should improve the seismic image and help constrain in higher detail, and in depth, the internal architecture of the individual structures. The ongoing processing steps include pre-stack depth migration that will be combined with the velocity knowledge obtained from the inversion of the tomographic data set. These processing efforts are aimed at better constraining the images, the fault extent and distribution, changes in the internal reflectivity of the seal and reservoir and the generation of a high resolution grid model which will be useful for the other research groups (hydrogeology, geochemistry, etc.) working in the URF.

6.2. Fault system identification

The study area has been subjected to different phases of extension and compression through its geological history (Quintà and Tavani, 2012). The South Fault can be observed in the entire data set (red line in Figs. 8 and 9). It has an E-W orientation, and crosses approximately the southern third of the study area. It is a strike slip fault and is related to the western Ubierna Fault (Fig. 1) (Tavani et al., 2011). A more regional study than that offered by the present seismic data set is required to assess the existence and/or size of the vertical offset for the South fault. At depth, the fault surface fluctuates, with several splits and reunifications. It is easily identifiable because it coincides with a sharp change in dips, and with the lateral change between the Cenozoic and the Upper Cretaceous formations. The injection point and the expected migration pathway of the CO_2 are located northwards of the South fault; thus, there should be no interaction between the fault and the CO_2 plume.

Several other minor faults can be observed in the study area (black thin lines in Fig. 8). None of them are large enough to be

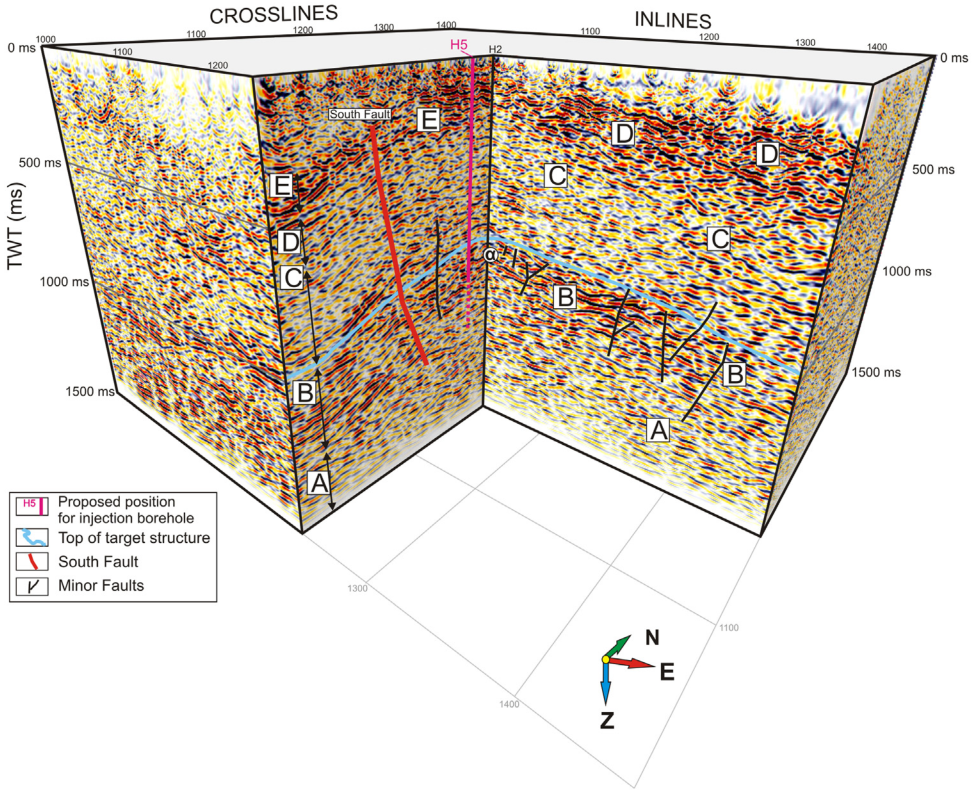

Fig. 8. Migrated 3D seismic volume obtained from the 3D survey. Main reflection packages are marked as A, B C, D and E (see text for further explanation). The blue line marks the top of the target structure. The red line marks the position of the South fault. The magenta line marks the proposed location of the injection borehole. Some minor faults are marked with black lines. The α symbol marks the position of the apex of the dome structure. (For interpretation of the references to color in this figure legend, the reader is referred to the web version of the article.)

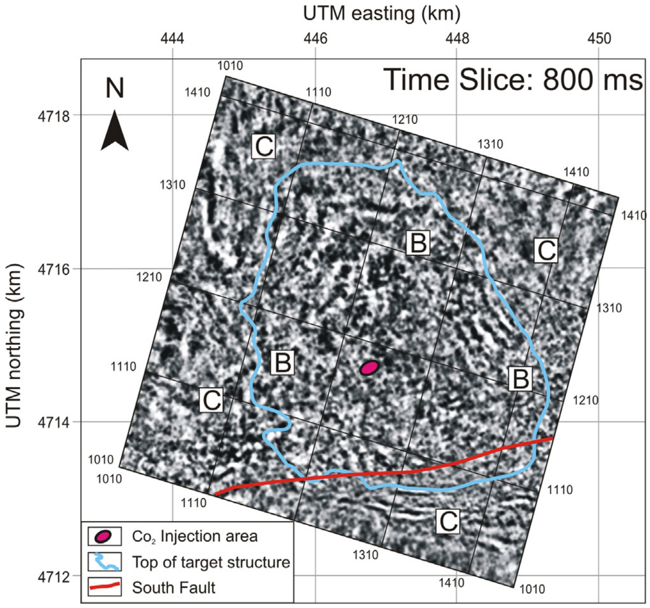

Fig. 9. Time slice at 800 ms of the migrated 3D volume. The contact between the time slice and the top of the target structure is marked in blue. B and C mark the reflection packages corresponding to Jurassic and Lower Cretaceous respectively (same as in Fig. 8). The red line marks the position of the South fault. The magenta oval marks the proposed position of the injection borehole. The time slice covers the whole area of the 3D survey. (For interpretation of the references to color in this figure legend, the reader is referred to the web version of the article.)

studied separately. All of them seem to be isolated by layers above, and, therefore, do not reach the surface. Further study is still needed to achieve definite conclusions regarding this matter, but the current images show that the small faults are unlikely to represent possible leakage pathways.

6.3. *Proposed borehole geometry*

The 3D images provide the key information to propose the location and geometry of the injection and monitoring boreholes (design of the storage facility). The seismic images allow the identification of the apex of the dome (α) structure at approximately 20 m away of the intersection of the 3C-DSU profiles (Fig. 10a). With the identification of the apex and the major fault structures, the design and location of the injection and monitoring borehole were made. Two monitoring boreholes, called H6 and H7, will be drilled together with the injection borehole (H5). The H6 well will be dedicated to geophysical monitoring and the H7 well to multi-disciplinary monitoring (hydrogeology, geochemistry, fluid sampling etc.) (Fig. 10b). Based on the geometry of the reservoir structure revealed by the 3D seismic images, if the CO_2 is injected in one flank close to the base of the slope of the reservoir structure, then the CO_2 plume will migrate from the injection borehole toward the northwest. The proposed location for the injection borehole is approximately 500 m south from the apex of the dome. The proposed distances from the injection point to the monitoring boreholes (H6 and H7) are 74 m and 40 m, respectively. A non-linear location geometry is being used to guarantee the lack of interference between the techniques that will be utilized in the geophysical and multi-disciplinary boreholes. These short distances from the injection to the monitoring points ensure that the monitoring boreholes will be able to sample the CO_2 plume, its movement and the

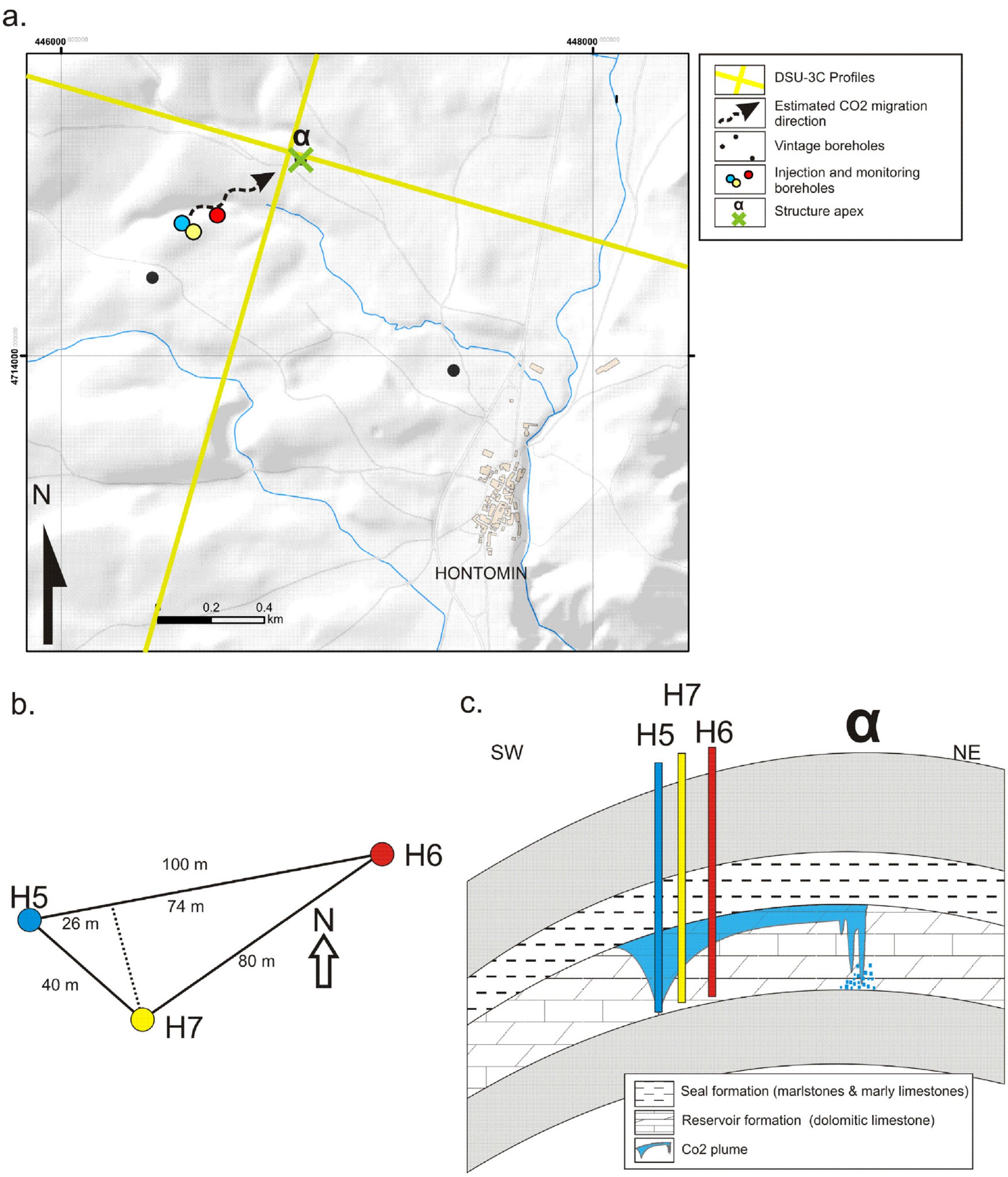

Fig. 10. Proposed injection and monitoring borehole locations and expected CO_2 plume migration. (a) Map with the position of the injection and monitoring boreholes with respect to the apex of the dome structure (α). The yellow lines mark the position of the 3C-DSU profiles. The dashed arrow marks the hypothetical migration path of the CO_2 plume. The green cross marks the calculated position of the apex of the dome. (b) Geometry of the injection (H5, blue circle) and monitoring (H6 and H7, yellow and red circle) boreholes. (c) Sketch of the migration of the plume and its relation with the position of the injection and monitoring boreholes. (For interpretation of the references to color in this figure legend, the reader is referred to the web version of the article.)

physical and geochemical processes that take place in a CO_2 storage site (Fig. 10c) from the early stages of injection, even with a reduced amount of CO_2 injected in a short period of time. Nevertheless, these distances are large enough so that the CO_2 can evolve inside the reservoir, and the different stages of interaction within the reservoir can be monitored.

7. Conclusions

A 3D survey plus two three-component 2D profiles were acquired in order to seismically characterize the URF complex of Hontomín, Spain. These seismic data were used (1) to obtain 3D images of the shallow subsurface structures of the proposed reservoir; (2) to assess the feasibility of the geological structures to be used as a storage facility for CO_2; (3) to obtain a baseline model for future monitoring studies and (4) to design a suitable location and depth geometry for the injection and monitoring boreholes. A standard processing flow up to post-stack migration was applied to the acquired 3D seismic reflection data. The migrated images allow the identification of the main structures in the area: the reservoir structure is a 17 km^2, NW–SE asymmetric carbonate dome, bounded by four main faults. This structure is onlapped by Lower Cretaceous sediments. These sediments contain an inversion in the velocity depth profile compared with the layers immediately above them. The faults observed are distributed mainly perpendicular to the reservoir structure. The seismic images in the present state suggest that these faults will not affect the injection area, or the integrity of the reservoir complex. Further processing of the seismic data is required to understand the internal characteristics of the structures. The migrated seismic images allowed us to locate the position of the apex of the dome and enabled the identification of the possible CO_2 plume migration path, which is most probably toward the northwest from the injection point. The structural model derived from the 3D seismic images helped to design the optimum locations for the injection and monitoring boreholes.

Acknowledgements

The authors sincerely thank the Managing Guest Editor Michael Kühn, Guest Editor Stefan Lueth and the anonymous reviewers for their useful comments. Funding for this Project has been partially provided by the Spanish Ministry of Industry, Tourism and Trade, through the CIUDEN-CSIC-Inst. Jaume Almera agreement (Characterization, Development and Validation of Seismic Techniques applied to CO_2 Geological Storage Sites) and by the European Union through the Technology Demonstration Plant of Compostilla OXYCFB300 Project (European Energy Programme for Recovery). Additional support has been provided by Spanish Ministry of Education and Science and Generalitat de Catalunya through grants: CSD2006-00041 and 2009SGR006, respectively. The sole responsibility of this publication lies with the author. The European Union is not responsible for any use that may be made of the information contained herein. Juan Alcalde is being currently supported by the Fundación Ciudad de la Energía (CIUDEN) Research training program. We sincerely thank CGGVeritas for their assistance during the acquisition. Processing has been carried out using GLOBE Claritas^{TM}, under license from the Institute of Geological and Nuclear Sciences Limited, Lowre Hutt, New Zealand and SeismicUnix from CWP (Center for the Wave phenomena, Colorado School of Mines). We thank all the people involved directly or indirectly in the elaboration of this work.

References

Arts, R., Brevik, I., Eiken, O., Sollie, R., Causse, E., Van Der Meer, B.,2001. Geophysical methods for monitoring marine aquifer CO_2 storage – Sleipner experiences. In: Proceedings of the 5th International Conference on Greenhouse Gas Control Technologies. CSIRO Publishing.

Arts, R., Eiken, O., Chadwick, A., Zweigel, P., van der Meer, L., Zinszner, B., 2004. Monitoring of CO_2 injected at Sleipner using time-lapse seismic data. Energy 29 (9–10), 1383–1392.

Castagna, J.P., Batzle, M.L., Eastwood, R.L., 1985. Relationships between compressional-wave and shear-wave velocities in elastic silicate rocks. Geophysics 50 (4), 571–581, April.

Hons, M., Stewart, R., Lawton, D., Bertram, M., Hauer, G., 2008. Field data comparisons of MEMS accelerometers and analog geophones. The Leading Edge 27 (7), 896–903.

Juhlin, C., 1995. Finite difference elastic wave propagation in 2-D heterogeneous transversely isotropic media. Geophysical Prospecting 43 (6), 843–858.

Juhlin, C., Giese, R., Zinck-Jørgensen, K., Cosma, C., Kazemeini, H., Juhojuntti, N., Lüth, S., Norden, B., Förster, A., 2007. 3D baseline seismics at Ketzin, Germany: the CO_2SINK project. Energy Procedia 1 (2007), 2029–2035.

Krishna, V.G., Rao, N.M., Sarkar, D., 1999. The problem of velocity inversion in refraction seismics: some observations from modeling results. Geophysical Prospecting 47, 341–357.

Lumley, D., 2010. 4D seismic monitoring of CO_2 sequestration. The Leading Edge 29 (2), 150–155.

Malehmir, A., Bellefleur, B., 2009. 3D seismic reflection imaging of volcanic-hosted massive sulfide deposits: Insights from reprocessing Halfmile Lake data, New Brunswick, Canada. Geophysics 74 (6), 209–213.

Prado, A.J., Campos, R., Ruiz, C., Pelayo, Recreo, F., Lomba, L., Hurtado, A., Eguilior, S., Pérez del Villar, M.L., 2008. Almacenamiento geológico de CO_2: selección de formaciones favorables. In: IX Congreso Nacional de Medio Ambiente, Madrid.

Preston, C., Monea, M., Jazrawi, W., Brown, K., Whittaker, S., White, D., Law, D., Chalaturnyk, R., Rostron, B., 2005. Fuel Processing Technology 86, 1547–1568.

Pujalte, V., Robles, S., García-Ramos, J.C., Hernández, J.M., 2004. El Malm-Barremiense no marinos de la Cordillera Cantábrica. In: Vera, J.A. (Ed.), Geología de España. SGE-IGME, Madrid, pp. 288–291.

Quesada, S., Robles, S., Rosales, I., 2005. Depositional architecture and transgressive–regressive cycles within Liassic backstepping carbonate ramps in the Basque-Cantabrian basin, northern Spain. Journal of the Geological Society 162 (3), 531–538.

Quintà, A., Tavani, S., 2012. The foreland deformation in the south-western Basque-Cantabrian Belt (Spain). Tectonophysics 576–577 (2012), 4–19.

Quintá, A., Tavani, S., Roca, E., 2012. Fracture Pattern Analysis as a Tool for Constraining the Interaction Between Regional and Diapir-related Stress Fields: Poza de la Sal Diapir (Basque Pyrenees, Spain), vol. 363. Geological Society, London, Special Publications 2012, pp. 521–532.

Serrano, A., Martínez del Olmo, W., 1990. Tectónica salina en el Dominio Cántabro-Navarro: evolución edad y origen de las estructuras salinas. In: Fedrico Ortí, C., Salvany, M. (Eds.), Formaciones Evaporíticas de la Cuenca del Ebro y Cadenas Periféricas, y de la Zona de Levante. Universidad de Barcelona–ENRESA, pp. 39–53.

Steer, D., Brow, L., Knapp, J., Baird, D., 1996. Comparison of explosive and Vibroseis source energy penetration during COCORP deep seismic reflection profiling in the Williston Basin. Geophysics 61 (1), 211–221.

Tavani, S., Quintà, A., Granado, P., 2011. Cenozoic right-lateral wrench tectonics in the Western Pyrenees (Spain): the Ubierna Fault System. Tectonophysics 509, 238–253.

Vera, J.A., 2004. Geología de España. SGE-IGME, Madrid, p. 890.

Yilmaz, O., 2001. Seismic Data Analysis – Processing, Inversion and Interpretation of Seismic Data. SEG, Tulsa, OK, p. 2027.

CHAPTER III

3D Reflection Seismic Imaging of the Hontomín structure in the Basque-Cantabrian Basin (Spain).

Alcalde, J., Martí, D., Juhlin, C., Malehmir, A., Sopher, D., Saura, E., Marzán, I., Ayarza, P., Calahorrano, A., Pérez-Estaún, A., and Carbonell, R. 2013b. Solid Earth 4, pp. 481-496.

Solid Earth, 4, 481–496, 2013
www.solid-earth.net/4/481/2013/
doi:10.5194/se-4-481-2013

Solid Earth
Open Access

3-D reflection seismic imaging of the Hontomín structure in the Basque–Cantabrian Basin (Spain)

J. Alcalde[1,2], **D. Martí**[1], **C. Juhlin**[3], **A. Malehmir**[3], **D. Sopher**[3], **E. Saura**[1], **I. Marzán**[1], **P. Ayarza**[4], **A. Calahorrano**[5], **A. Pérez-Estaún**[1,2], **and R. Carbonell**[1]

[1]Institute of Earth Sciences Jaume Almera CSIC, Barcelona, Spain
[2]CIUDEN Foundation, Ponferrada, Spain
[3]Department of Earth sciences, Uppsala University, Uppsala, Sweden
[4]University of Salamanca, Geology Department, Salamanca, Spain
[5]Barcelona Center for Subsurface Imaging, Barcelona, Spain

Correspondence to: J. Alcalde (juan.alcalde.martin@gmail.com)

Received: 26 August 2013 – Published in Solid Earth Discuss.: 13 September 2013
Revised: 5 November 2013 – Accepted: 10 November 2013 – Published: 9 December 2013

Abstract. The Basque–Cantabrian Basin of the northern Iberia Peninsula constitutes a unique example of a major deformation system, featuring a dome structure developed by extensional tectonics followed by compressional reactivation. The occurrence of natural resources in the area and the possibility of establishing a geological storage site for carbon dioxide motivated the acquisition of a 3-D seismic reflection survey in 2010, centered on the Jurassic Hontomín dome. The objectives of this survey were to obtain a geological model of the overall structure and to establish a baseline model for a possible geological CO_2 storage site. The 36 km^2 survey included approximately 5000 mixed (Vibroseis and explosives) source points recorded with a 25 m inline source and receiver spacing. The target reservoir is a saline aquifer, at approximately 1450 m depth, encased and sealed by carbonate formations. Acquisition and processing parameters were influenced by the rough topography and relatively complex geology. A strong near-surface velocity inversion is evident in the data, affecting the quality of the data. The resulting 3-D image provides constraints on the key features of the geologic model. The Hontomín structure is interpreted to consist of an approximately 10^7 m^2 large elongated dome with two major (W–E and NW–SE) striking faults bounding it. Preliminary capacity estimates indicate that about 1.2 Gt of CO_2 can be stored in the target reservoir.

1 Introduction

The Hontomín structure has been classified as an example of a forced fold-related dome structure (Tavani et al., 2013). This type of folding is generally closely related to the development of extensional fault systems (Schlische, 1995; Cosgrove and Ameen, 2000; Tavani et al., 2011, 2013). They can develop under varying conditions (Braun et al., 1993; Jin et al., 2006) and their presence has been proposed in the Mesozoic Basque–Cantabrian Basin of northern Iberia (Soto et al., 2011; Tavani et al., 2011, 2013). The formation prerequisite for these structures involves the existence of a ductile layer which acts as a major decoupling zone that is able to separate the deformation of the sedimentary cover from the deformation and faulting occurring at the basement. The decoupling level in this area is formed by Triassic evaporites, which separate the pre-rift Upper Triassic–Middle Jurassic folded sediments from the Paleozoic–Lower Triassic faulted rocks of the basement. The structure appears to have been generated by reactivation of the pre-existing extensional basin architecture during a compressional phase associated with Cenozoic tectonics affecting the Pyrenees. During this compressive stage the overlying Mesozoic sequence overrides the Cenozoic Ebro foreland Basin (Martínez-Torres, 1993). Thus, the area constitutes a unique case study of a major deformation system within the Basque–Cantabrian Basin in the northern Iberian Peninsula.

Published by Copernicus Publications on behalf of the European Geosciences Union.

The Hontomín structure, along with the Ayoluengo structure, has been targeted for hydrocarbon exploration in the northern Iberian Peninsula (Alvarez, 1994; Merten, 2006; Beroiz and Permanyer, 2011). Thus, the area has been extensively studied since the early 1970s. A number of 2-D seismic reflection transects were acquired with the aim to unravel the regional structure (Beroiz and Permanyer, 2011). The subsurface stratigraphy includes a carbonate Jurassic sequence that hosts a deep saline aquifer and a high-quality seal formation. This stratigraphy motivated new interest in the area as the structure could be considered feasible for geological storage of CO_2 (Orr, 2004; Baines and Worden, 2004; Alcalde et al., 2013).

Geophysical methods have been broadly used for the characterization of geological structures (Martí et al., 2002; Preston et al., 2005; Förster et al., 2006). Amongst these, seismic methods provide high-resolution images and baseline models of hydrocarbon producing and/or storage reservoirs (Juhlin et al., 2007; White, 2009). The interest in the Hontomín structure motivated the acquisition of a number of multidisciplinary data sets intended to characterize the Hontomín site (e.g., Alcalde et al., Elío et al., 2013, 2013; Ogaya et al., 2013; Ugalde et al., 2013). The active seismic experiments carried out in the area were initially discussed in Alcalde et al. (2013). These included a 3-D seismic reflection data set, acquired with the aim of obtaining a 3-D image of the Hontomín structure. Constraining the tectonic framework of the area and providing a geological and seismic baseline model were the main aims of the survey.

The study area is geologically complex and, at the surface, topographically irregular. One of the difficulties encountered during processing is the existence of velocity inversions at relatively shallow depths which complicate the determination of optimum static corrections. In general terms, the Hontomín area comprises a very heterogeneous folded structure, composed of mixed sedimentary marine carbonate and continental siliciclastic sediments. According to well-log data, the reservoir-seal system within the Hontomín structure is a carbonate sequence located at approximately 1500 m depth. Reflection seismic methods often encounter difficulties when attempting to image carbonate reservoirs. Suggested reasons behind this are the absence of distinct layering during the deposition and diagenetic alterations of the carbonate sediments (Masaferro et al., 2003; Braaksma et al., 2006; Von Hartmann et al., 2012), abrupt impedance and velocity changes (Rudolph et al., 1989; Janson et al., 2007), and more generally, high structural complexity (Phipps 1989; Rudolph et al., 1989; Erlich et al., 1990; Kenter et al., 2001). This was an important issue during velocity analysis. Other problems encountered related to acquisition and processing are presented and discussed in this work.

The revised processing scheme used in the present study was adapted to the characteristics of the Hontomín subsurface. The resulting final image features higher coherency than that presented in Alcalde et al. (2013) throughout the entire seismic volume. The improvement is mainly due to the calculation of a more precise static model, the improved noise reduction and the source wavelet matching method applied. This enables a better analysis and identification of the subsurface structures, providing a definitive seismic reference model of the study area. Although the focus of this paper is the acquisition and processing of the 3-D data set, a preliminary interpretation is also presented.

2 Geological setting

The Hontomín structure (Fig. 1) is bordered by the NW–SE Ubierna fault to the southwest (Tavani et al., 2011), the Poza de la Sal diapir to the north (Quintà et al., 2012) and the Ebro and Duero basins to the east and southwest, respectively. The study area is located within in the North Castilian Platform, a Mesozoic sub-unit on the western part of the Basque–Cantabrian basin (Serrano and Martinez del Olmo, 1990) that developed during the opening of the Atlantic Ocean and the Bay of Biscay (Ziegler, 1989). This Mesozoic extensional regime generated a synformal domain in the region (Pujalte et al., 2004; Quintà and Tavani, 2012), characterized by a thick sedimentary sequence (Quesada et al., 2005). Due to the subsequent Alpine compressional regime, small-scale inversion structures were produced, leading to reverse, right-lateral and left-lateral reactivation of the pre-existing faults (Tavani et al., 2011; Quintà and Tavani, 2012; Tavani et al., 2013).

The extensive exploration for natural resources within the area (Alvarez, 1994; Merten, 2006; Beroiz and Permanyer, 2011) produced a relatively large amount of geophysical and geological data. This includes vintage 2-D seismic reflection data, well-logs, borehole core samples, etc. The existing data indicate that the reservoir and seal formations are Jurassic in age, and form a slightly elongated dome-like structure with an overall aerial extent of 5 km × 3 km. The area features low natural seismicity as stated in Ugalde et al., (2013). From a stratigraphic perspective, the lowest Mesozoic succession (Fig. 1b) is the Keuper facies, which forms the core of the target dome. The “Carniolas” unit is composed of evaporites, dolomites and marls (sabkha facies) and lies over the Keuper facies, representing the boundary between the Triassic and Lower Jurassic (Quesada et al., 2005; Pujalte et al., 2004). The Lower Jurassic sediments can be described with four units: Limestone Lias and Marly Lias, and Pelletic dogger and Limestone dogger. They are characterized by shallow marine carbonate ramp sediments and hemipelagic ramp sediments. The Upper Jurassic–Lower Cretaceous transition is constituted by the Purbeck facies, formed by clays, sandstone and carbonate rocks. The remainder of the Lower Cretaceous succession consists of siliciclastic sediments from Weald, Escucha and Utrillas facies, mainly composed of a series of sandstones and shales, and occasionally microconglomerates. The uppermost rocks (outcropping in the

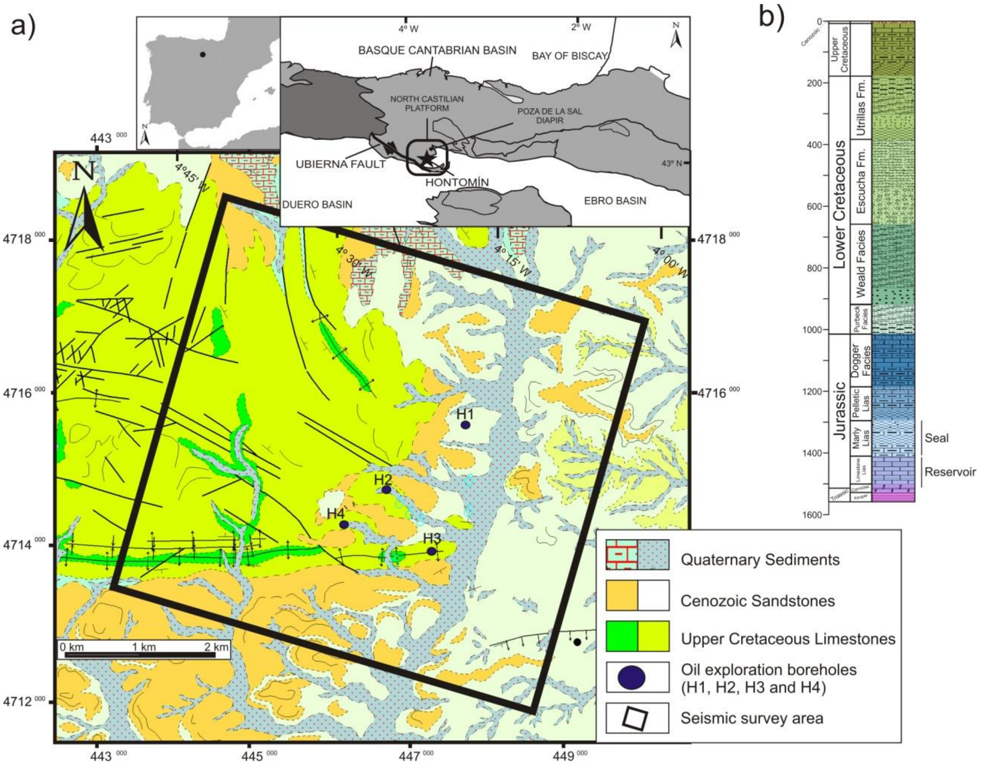

Fig. 1. (a) Location of the study area within the Iberian Peninsula and detail of the main geological features and **(b)** expected stratigraphy in the injection zone based on available seismic and borehole data.

Hontomín area) are Upper Cretaceous carbonates and Cenozoic rocks (lacustrine and detritic) lying unconformably over the Mesozoic successions. The structure is bounded to the south by a strike-slip fault associated to the Ubierna Fault (Tavani et al., 2011).

Four pre-existing boreholes (H1, H2, H3 and H4 in Fig. 2), reaching depths between 900 and 1832 m, sampled the Mesozoic succession. These boreholes were drilled between the 1970s and the 1990s for oil exploration purposes and some were still producing in 2009. Beneath the producing level, a saline aquifer formation is present. It is located at approximately 1500 m depth, within Early Jurassic (Raethian–Sinemurian) shallow marine carbonate ramp sediments. This potential CO_2 storage formation is composed of a dolostone unit (upper part of the Carniolas unit), overlain by an oolitic limestone formation (Limestone Lias), with an average thickness of approximately 80 m. This reservoir level is fairly porous (between 9 and 17 %, Ogaya et al., 2013) and contains saline water with more than 20 g l^{-1} of NaCl. The porosity of the Carniolas is believed to be the result of secondary dolomitization and different fracturing events. There is no available information on its permeability. The potential upper seal unit is comprised of marlstones and black shales from the hemipelagic ramp, corresponding to the Marly Lias unit (Pliensbachian and Toarcian in age).

Table 1. Acquisition parameters of the Hontomín 3-D survey.

Number of shotpoints	4936 (69–5005)
Shotpoint spacing	25 m
Source type	Vibroseis & explosives
Sweep length	16 s
Sweeps per source point	2
Frequency range (Vibroseis)	8–80 Hz
Explosive charge per source point	450 g (3 boreholes)
Number of receiver points (traces)	4 333 605
Sample rate	1 ms
Receiver spacing	25 m
Maximum channels per shot	1200
Number of inlines	463 (1000 : 1462)
Inline spacing	275 m (11 shots)
Number of crosslines	431 (1000 : 1430)
Crossline spacing	250 m (10 receivers)
Number of CDPs	199 559
Bin size	$12.5 \times 12.5\ \text{m} = 156.25\ \text{m}^2$
Maximum CDP fold (max traces/CDP)	36

3 Seismic data acquisition

The acquisition parameters (Table 1) were selected based on the knowledge derived from previous studies in the area (Gemodels/UB 2011, internal report). These previous studies included surface geological mapping, reprocessing of vintage 2-D seismic exploration surveys and correlation with the

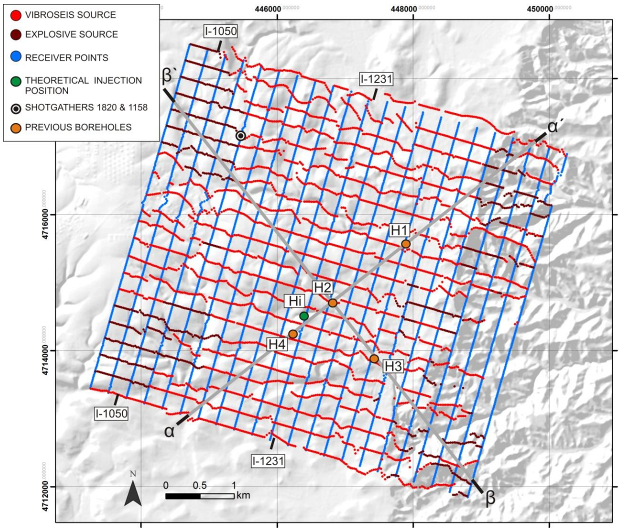

Fig. 2. Map with the position of the elements of the 3-D seismic reflection experiment acquired in Hontomín. Light red points mark the position of Vibroseis source shot points. Deep red points mark the position of the explosive source shot points. Blue points mark the receiver positions. The green circle marks the proposed position for the CO_2 injection borehole. The orange circles mark the position of previous boreholes (drilled for oil exploration).

exploration boreholes, which provided overall information of the subsurface structures. The survey size was designed to cover the entire Hontomín structure.

The 3-D seismic survey geometry included 22 source lines perpendicular to 22 receiver lines, with intervals of 25 m between sources and receivers (Fig. 2). The distance between receiver lines was 250 m, and source lines 275 m. The survey was acquired in five stages corresponding to different patches (swaths), with patches at the edge of the survey consisting of six active receiver lines, and the inner patches consisting of 10 receiver lines. A maximum of 120 channels were active per receiver line, resulting in a maximum of 1200 traces per shot gather.

The survey was originally designed to be fully acquired with a Vibroseis source (M22 vibrators). However, logistical issues (mainly due to the rough topography in the eastern part) forced the use of explosives in about 24 % of the acquired data. The selected parameters for the Vibroseis source were two 16 s sweeps, with an 8–80 Hz bandwidth. The explosive source consisted of 450 g of explosives, deployed in three 1.5 m deep holes for each shot point. The total number of source points was 4818, resulting in 4 333 605 traces.

The use of two different sources during the acquisition resulted in different seismic signatures in the shot gathers depending upon what type of source was used (Fig. 3). The explosive shot records are more strongly contaminated with ground roll and low-frequency guided waves than the Vibroseis shot records. The frequency content of the Vibroseis shots was determined by the sweep bandwidth of the source (i.e., 8–80 Hz), whereas the explosive data, which feature lower amplitude, resulted in a broader bandwidth, up to 100 Hz (Fig. 4).

4 Seismic data processing

The relatively regular pattern of the acquisition geometry (Fig. 2) gives a natural bin size of 12.5 m × 12.5 m for the CDP bins, resulting in a maximum CDP fold of 36 traces/CDP (Fig. 5a). This fold value is relatively conventional in land surveys and for reservoir characterization (Ashton et al., 1994; Roche, 1997) and affordable from the academic point of view. According to previous information of the study area (Geomodels/UB 2011, internal report; Ogaya et al., 2013), dipping events steeper than 16° are rather unexpected, and therefore, quasi-horizontal dips were assumed in the processing. Source-receiver offsets of up to 2500 m (Fig. 5b) were enough to constrain reflections from a depth of 1500 m (1150 ms two-way travel time (twt), assuming an average velocity of 3500 $m\,s^{-1}$). Furthermore, at travel times corresponding to this target depth, surface-wave energy is considerably decreased. The swath acquisition provided a well-sampled azimuthal coverage (Fig. 5c), which assures the three-dimensionality of the data. The available well-log data indicate that the lithologies with higher impedance contrast are located above 1400 ms twt in most cases. Taking this into account the data were processed down to 1500 ms. The processing flow (Table 2) was designed and implemented in order to enhance the S/N ratio and image the target structures.

Alcalde et al. (2013) applied a standard processing to the 3-D data set. A review of this preliminary processing was conducted to identify some key data/noise issues associated with the data set. These issues included the identification of the noise sources present during the acquisition, the shadow zone related to a near-surface velocity inversion and the source wavelet matching issue. The new processing workflow presented in this paper and described below addresses these issues and takes a more detailed look at the signal processing in order to obtain a final image suitable for subsequent detailed interpretation.

5 Source matching

The use of multiple sources in seismic data acquisition introduces additional complexity to the processing, due to the need to homogenize their phase characteristics (Steer et al 1996; Feroci et al 2000). Since both Vibroseis and dynamite sources were utilized in the survey (Fig. 2), efforts were made to match source wavelets and bulk time shifts between the dynamite and Vibroseis traces, in order to improve the lateral continuity of the final stacked volume. Although the conventional approach is to convert the Vibroseis source data to minimum phase, given that most of the survey consisted of

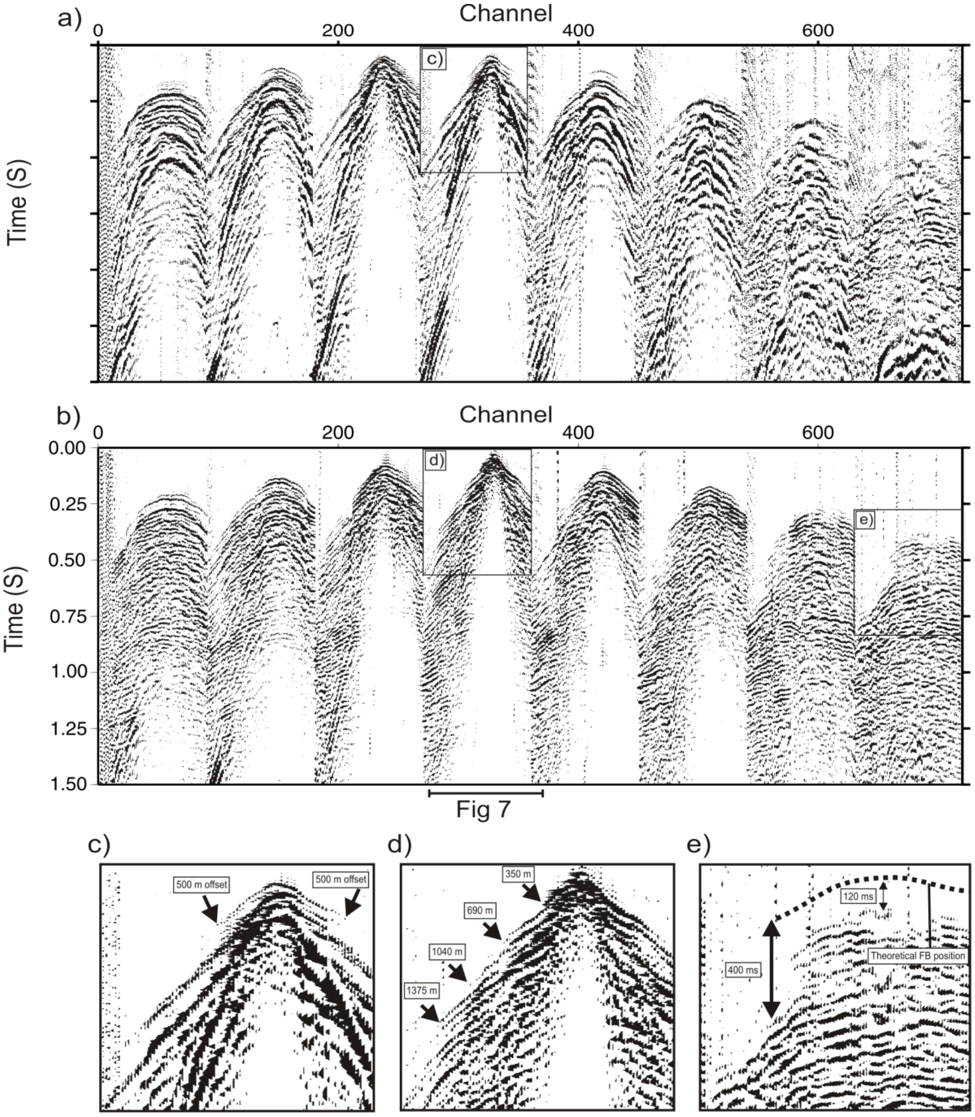

Fig. 3. Raw shot gather 1158, acquired with explosive source **(a)**, and the co-located shot gather 1820, acquired with Vibroseis source **(b)**. Three zooms from different zones of the two shots are shown in **(c)**, **(d)** and **(e)**, with black arrows indicating the observed loss of first arrivals and the resultant shadow zone. The location of shot gathers 1158 and 1820 is marked in Fig. 2.

Vibroseis shots, with the dynamite shots confined to the survey edges, the minimum phase dynamite wavelet was converted to zero-phase to match the cross-correlated Vibroseis wavelet. In order to do this, two wavelet matching processes were tested: (1) applying trace wide time and phase shifts and (2) a convolutional match filter and time shift. The match filter used to convert the dynamite wavelets to zero-phase was based on a wavelet extracted from 10 dynamite shots from different parts of the survey.

In order to assess the best parameters for each different wavelet matching method, co-located dynamite and Vibroseis trace pairs were selected. For the time and phase-shift wavelet matching method, a range of different values of both were applied to the dynamite trace. Thus, the correlation coefficient between the two traces in a given time window was assessed. This analysis was also performed in the same time window after applying the match filter and variable time shift. The optimum parameters were selected based on those which gave the highest correlation coefficient. It was observed that, based on tests performed with synthetic data, the effects of environmental noise could be overcome by stacking the correlation coefficients across many dynamite-Vibroseis trace pairs.

Figure 6 shows the stacked correlation coefficients for 1080 pairs of dynamite and Vibroseis traces, located within 25 m of each other, taken from 10 different shots. The best match between the dynamite and the Vibroseis traces is obtained at time and phase shifts of 12 ms and −150°,

Table 2. Processing steps applied to the seismic data set.

Step	Parameters
1	Read 1.5 s SEG-Y data Trace edition: 140 000 traces First break picking (manual): 500 m offset range, 670 000 times picked
2	Spherical divergence correction
3	Source matching: $-150°$ phase shift, 20 ms time shift applied to the explosive data
4	Surface consistent deconvolution: filter 100 ms, gap 14 ms, white noise 0.1 %
5	Elevation statics: datum 1070 m, replacement velocity 3500 m s^{-1}
5	Refraction static corrections
8	Air wave mute
9	Spectral equalization: 20 Hz window length, 20–30–90–120 Hz bandpass filter
10	Time-variant bandpass Filter: 35–50–100–140 Hz at 0–300 ms 27–40–85–120 Hz at 500–800 ms 20–30–70–100 Hz at 900–1500 ms
11	Residual statics (iterative)
12	Velocity Analysis
13	AGC: 250 ms
14	NMO: 50 % stretch mute
15	3-D DMO correction
16	Stack
17	Trace balance: window 300–1300 ms
18	Butterworth bandpass filter: 20–30–100–135 Hz (0.5–0.95–0.95–0.5)
19	Post-stack deconvolution: gap = 20 ms
20	Spectral equalization: 20 Hz window length, BP = 20–30–80–100 Hz
21	F_{XY}-deconvolution: inline and crossline directions
22	2.5 Finite-difference time migration, 45° algorithm
23	Top mute

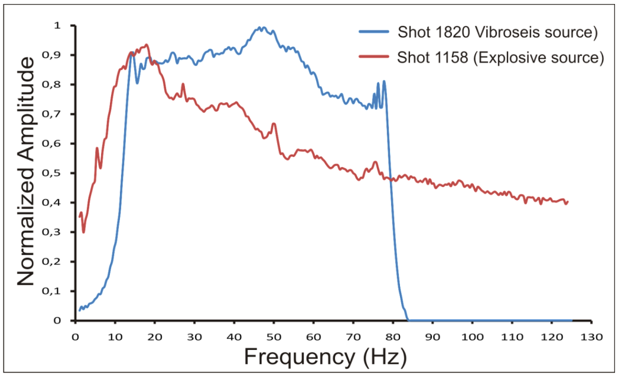

Fig. 4. Frequency spectra of the shot gathers shown in Fig. 3: shot gather 1820, acquired with Vibroseis source (dark grey) and shot gather 1158, acquired with explosive source (light grey). The high-cut filter in the spectrum of the Vibroseis data was applied in the field.

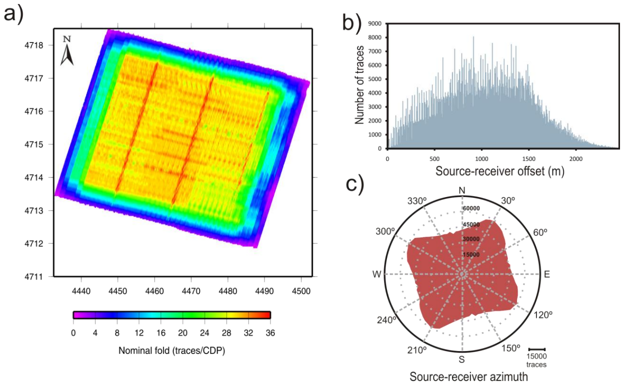

Fig. 5. (a) CDP fold coverage calculated from a CDP bin size of 13 m. **(b)** Source-receiver offset distribution. **(c)** Azimuthal coverage of the survey.

respectively. For the match filter method, the optimum time shift to use in addition to the match filter was 24 ms.

Certain corrections were performed in order to diminish the disparity in the amplitudes and frequency content of the shot-gathers (Fig. 4). The frequency contents were equalized by the use of combined bandpass filtering and spectral equalization in the pre- and post-stack stages. The high-amplitude contrast forced the use of AGC and trace balancing (250 and 300–1300 ms time windows, respectively), since the spherical divergence correction did not completely equalize the amplitudes.

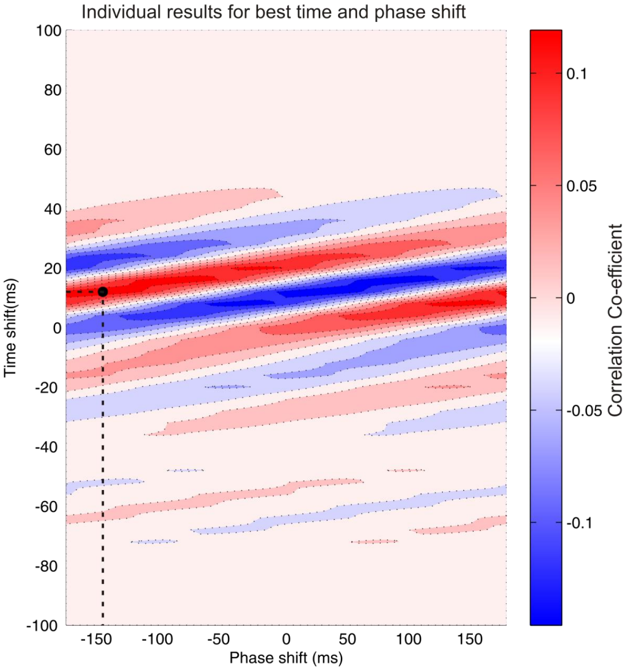

Fig. 6. Plot of the correlation coefficient vs. time and phase shift applied to the dynamite traces. The color scale shows the stacked correlation coefficient values for 1080 trace pairs, with red colors indicating strong positive values and blue indicating strong negative values. The optimum parameters of −150° phase shift and 12 ms time shift were chosen based on the stacked correlation coefficients.

6 Static corrections

Elevation and refraction statics are key processes for obtaining a high-quality final seismic image (Juhlin et al., 2007; Malehmir and Bellefleur, 2009; Malehmir and Juhlin, 2010). In our case, they were essential for improving the final image due to the large topographic changes (up to 200 m) and heterogeneous geology present in the study area. The entire data set was referenced to a datum of 1070 m a.m.s.l., just above the highest altitude of the survey. The replacement velocity, based upon apparent velocities in the shot-records, was 3500 m s^{-1}. The resultant elevation static model adjusted the data by 67 ms on average, with maximum corrections of 10 ms.

The refraction static modeling was an arduous process due to the heterogeneous characteristics of the subsurface. One of the most interesting features observed is the lack of clear first arrivals in the data at offsets greater than 300 m (black arrows in Fig. 3c, d). This signal disappearance is observed as a sharp (black arrows in Fig. 3c) or as gradual loss of amplitude (black arrows in Fig. 3d) with increasing offset. This phenomenon is observed in the whole survey for both source types. At far offsets, this results in a lack of signal in the upper 500 ms (Fig. 3e), i.e., a “shadow zone”. The existence of this shadow zone added difficulty to the picking of first arrivals in the near-offset traces, and impossible at offsets larger than about 700 m. In spite of this difficulty, more than 670 000 first breaks, ranging from 0 to 500 m offsets, were manually picked. The refraction statics were calculated using a two-layer model, with an input-fixed upper-layer velocity (at 1070 m m.s.l.) of 1900 m s^{-1}, and a lower half-space velocity (at a starting depth of 40 m below the surface) of 3500 m s^{-1}. The resulting model refraction statics ranged from 0 to 40 ms (RMS of approximately 8 ms), whereas the residual refraction statics were always below 4 ms. Static corrections, particularly the refraction static corrections, increased the quality of the final image and improved the coherency of the reflections in the data (Figs. 7c and 8c).

7 Stack, post-stack processing and migration

Velocity analysis after static corrections provided further support for the existence of a velocity inversion between 200 to 500 ms. The NMO-velocity reduction in this interval ranged from 300 to 600 ms. The CDP gathers show disrupted reflections before and after NMO corrections (Fig. 9). An example of a stacked section (up to step 14 in Table 2) is shown in Fig. 10a. After a satisfactory NMO model had been obtained, a 3-D Kirchhoff DMO code (based on Hale and Artley, 1993) was applied to the pre-stack data, using the NMO velocities as initial input (Fig. 10b). Although the Hontomín structures are not steeply dipping, the 3-D DMO processed volume shows increased coherency and improved definition of the flanks of the dome, as well as improvement in the continuity of reflections, as compared to the stacked data without DMO applied (black arrows in Fig. 10a, b). Post-stack F_{XY}-deconvolution in the inline and crossline directions was implemented to remove random noise and further increase coherency. Different finite-difference and phase-shift time migration codes were tested. We chose a 45° finite-difference post-stack algorithm, due to the spatial variation of the velocities present in the study area.

8 Processing results and interpretation

Analysis of the seismic image

A section comparing the preliminary image obtained by Alcalde et al. (2013), and the same section obtained in this work can be found in Fig. 11. In the revised work flow, the subsurface is well imaged in the migrated volume from approximately 75 ms down to 1350 ms, completely covering the target structure. Significant differences between the two volumes can be observed. In general, the revised work flow exhibits less low-frequency background noise and an overall increase of the signal-to-noise ratio. The northern part shows clearer reflections and improved identifiability of the defining structures. The revised work flow also has lower

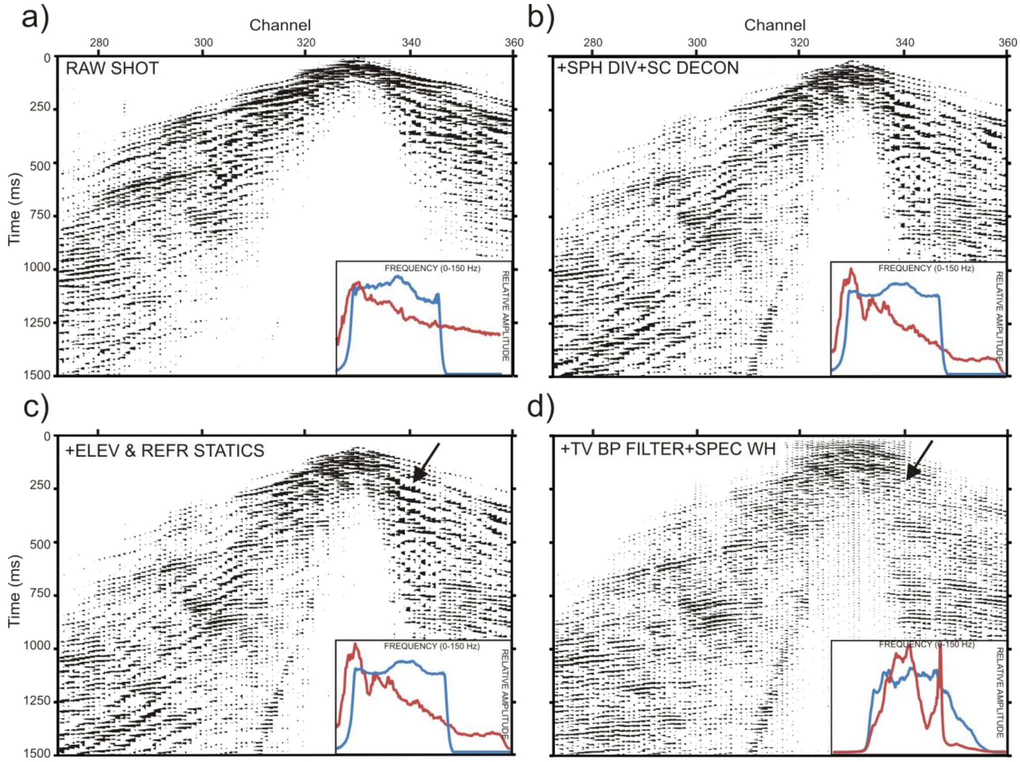

Fig. 7. Closeup of the shot gather 1820 (see also Fig. 3) after different steps in the data processing: **(a)** raw shot; **(b)** same as **(a)** plus spherical divergence and surface consistent deconvolution; **(c)** same as **(b)** plus elevation and refraction statics; and **(d)** same as **(c)** plus time-variant frequency filter and spectral whitening. Each plot also contains a frequency spectrum graph (similar to that of Fig. 4) comparing the amplitudes and frequencies of the shot 1820 (Vibroseis source, dark grey) and 1158 (explosive source, light grey). Note that frequency graphs are shown only for qualitative comparison (values of the frequency graphs are the same as in Fig. 4, not shown here for display purposes).

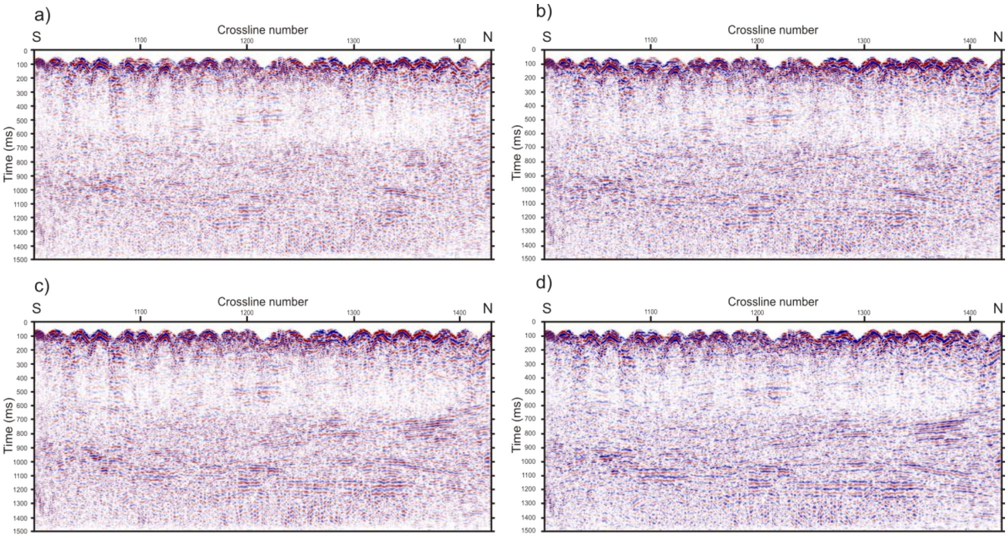

Fig. 8. **(a)** Raw inline 1050; **(b)** same as **(a)** with the source wavelet matching based on time and phase shifting applied; **(c)** same as **(a)** with elevation and refraction statics applied; **(d)** same as **(a)** with source wavelet matching, elevation and refraction statics applied. The location of inline 1050 is marked in Fig. 2.

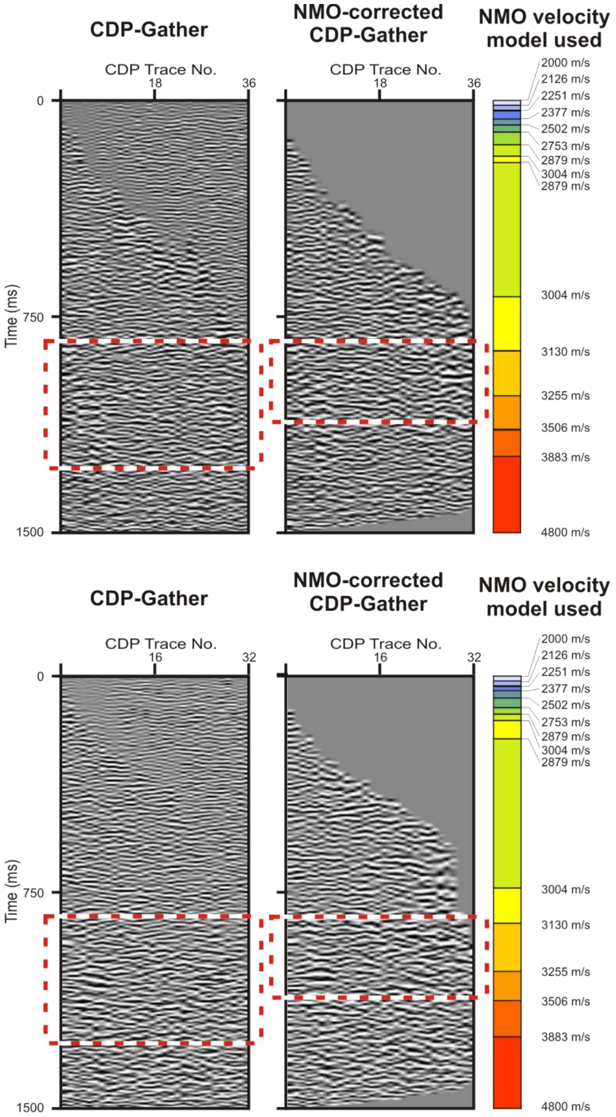

Fig. 9. Example of two CDP gathers from different areas before and after NMO correction, and the two NMO velocity models applied in each case. The highlighted boxes mark a reflectivity area whose reflections are not continuous even after a correct NMO correction.

migration-related artifacts, especially in the edges of the section.

The lateral continuity of the reflections is limited in the whole seismic volume (e.g., sets E and F in Fig. 12). This could be due to the influence of the shallow velocity inversion, as well as to the existence of heterogeneities associated with small-scale fracture zones. However, the quality of the processed data is enough to allow us to perform a detailed analysis of key seismic events/facies and their distribution within the migrated seismic volume (Figs. 12a and Fig. 13). Line α-α' (location in Fig. 2) crossing boreholes H4, H2 and H1 is used in this section to analyze the seismic image and correlate it with the main geological units (Fig. 12). This characterization is applicable to the whole seismic volume.

Three domains were identified by the analysis of the seismic facies in the seismic data set. The first domain generally contains low-amplitude, discontinuous reflections (A). It is located at the bottom of the seismic volume, below approximately 1100 ms. It shows a reduction in amplitudes compared to the interval immediately above, and less continuity in the reflections. Within this domain, a brighter set of parallel reflections (B) is found between inlines 1305 and 1340. Overlying the A and B facies sets, the second domain is composed of a sequence of more continuous, high-amplitude reflections (C). They show an asymmetric dome-shaped geometry with an average thickness of 300 ms (Fig. 12). The boundary between the A and C reflection packages is chaotic across most of the seismic volume. The C set is characterized by higher amplitudes compared to the surrounding seismic facies, with dominant frequencies around 30 to 40 Hz. Its amplitudes decrease towards the end of the second domain.

Over the dome flanks, the third domain begins with a set of reflections (D) overlying the C set. Set D is characterized by very high amplitudes and a 80–120 ms^{-1} thickness. However, the D package is only observed in the northern portion of the study area. The overlying E set is characterized by variable amplitude and non-planar reflections. A high-amplitude reflection at approximately 575 ms bounds the E set. Above this, a set of higher amplitudes and more continuous parallel reflections appear (F). This package has an approximately constant thickness of 400 ms. In Fig. 12, set F shows an important lateral change of the seismic properties (at inline 1260, approximately), where a more continuous character to the north becomes less continuous to the south. At the top of the seismic volume, another set of discontinuous reflections (G), nearly 200 ms thick, covers the whole area and generally extends to the surface. In the southern part, a set of south-dipping reflections (H) with high-coherency overlies set G near the surface.

9 Correlation between seismic data and geology

The subsurface structure of the Hontomín CO_2 storage site described below is based on the seismic data, information from borehole data and previously presented information of the underground and surface geology. The available well-log data lack velocity and/or density information in approximately the first 400 m, and totally lack check-shot information. This makes it extremely difficult to obtain a precise seismic to well tie. An example of the calculation of a synthetic trace for the H3 well using the available well-log information is shown in Fig. 14. The time–depth relationship of the synthetic was set manually, thus featuring a limited accuracy.

The seismic domains previously described represent the three main subsurface geometries found in Hontomín. Within them, five different units have been interpreted within the

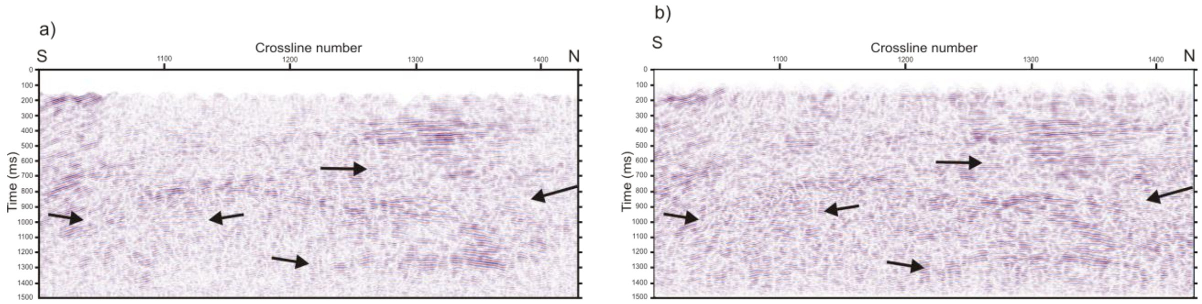

Fig. 10. Unmigrated seismic section from inline 1231 with **(a)** up to processing step 14 (Table 2) applied, and **(b)** same as **(a)** with DMO corrections applied. Note the enhancement of coherency after the application of the DMO (black arrows). The location of inline 1231 is marked in Fig. 2.

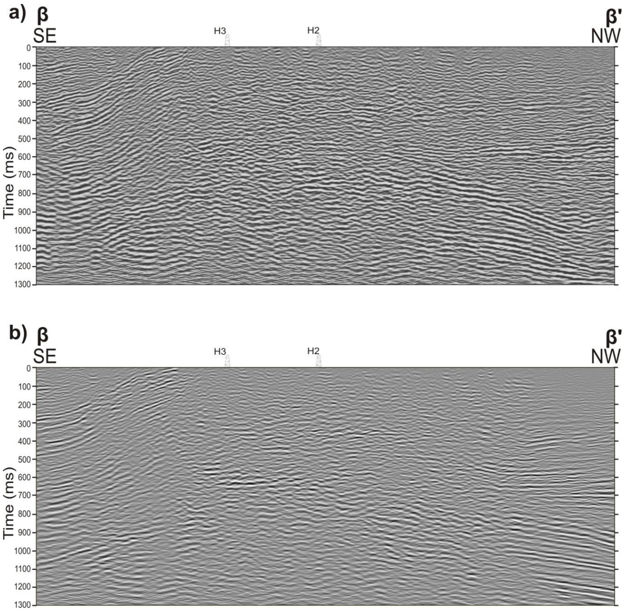

Fig. 11. (a) Migrated section (up to processing step 25 in Table 2) from α-α' section (location in Fig. 2) showing the main seismic facies (A to H) identified, arranged in three domains; and **(b)** interpretation of section **(a)**, in which five main units have been recognized: Triassic, Jurassic, Lower Cretaceous, Upper Cretaceous and Cenozoic units. Three faults affecting the Jurassic structure have also been interpreted in this section: the Southern fault (red line), the Central fault (dark blue line) and the Eastern fault (magenta line), at inlines 1180, 1225 and 1305, respectively.

study area (from bottom to top): (1) Triassic, (2) Jurassic, (3) Lower Cretaceous, (4) Upper Cretaceous, and (5) Cenozoic (Fig. 12b).

The Triassic package (Fig. 12b) generally has an inhomogeneous seismic pattern. It includes reflection sets A and B. The presence of a variable quantity of anhydrite layers, together with the associated increase in velocity of these layers, could explain the lack of clear seismic events. Only in specific locations, such as B (Fig. 12a), can clear sub-horizontal layering be defined by high-amplitude reflections. Surface and borehole data show a non-uniform, gradual change from anhydrite to carbonate. This could be linked to the diffuse seismic response observed near the surface. The overlying Jurassic unit (Fig. 12b) is characterized by a high-amplitude reflective body observed from 750 to 1200 ms, corresponding to seismic set C. It includes the target aquifer and an overlying seal layer. The Jurassic unit is overlain by the Lower Cretaceous unit, which includes seismic sets D, E and F. Set D probably corresponds to a transitional sedimentary package, which could explain why it only appears in the northern portion of the seismic volume. The upper part of the Lower Cretaceous is formed by the Weald, Utrillas and Escucha Fm sediments (Fig. 1). Their boundaries are unclear, but they all feature high-amplitudes and gently dipping plane-parallel layering. The shadow zone is probably contained within the boundary between sets F and G (150 ms TWT, approximately). This boundary divides the Lower and Upper Cretaceous. It is especially visible in the areas where the shadow zone is more noticeable (e.g., inline 1200 to 1250 in Fig. 12a). The Upper Cretaceous carbonates outcrop across the entire study area except on its southern and eastern ends, where the Upper Cretaceous beds drop and are overlain by the Cenozoic unit (set H). This package exhibits high coherency and an approximate dip of the reflections of 16° to the south. In the eastern part, this package is subhorizontal, displaying less coherency than in the southern end.

Three main faults were identified in the seismic data set: the southern, the eastern and the central faults (Figs. 12, 13 and 15). The Southern fault is an approximately E–W striking fault zone that crosses the entire data set. It is not purely vertical, and shows some bifurcation. The Eastern fault is a major NNW–SSE reverse fault that abuts the Southern fault. A third set of small-scale faults are observed only in a few sections. One of them is the Central fault, a reverse fault mapped only in the α-α' section (Fig. 12b).

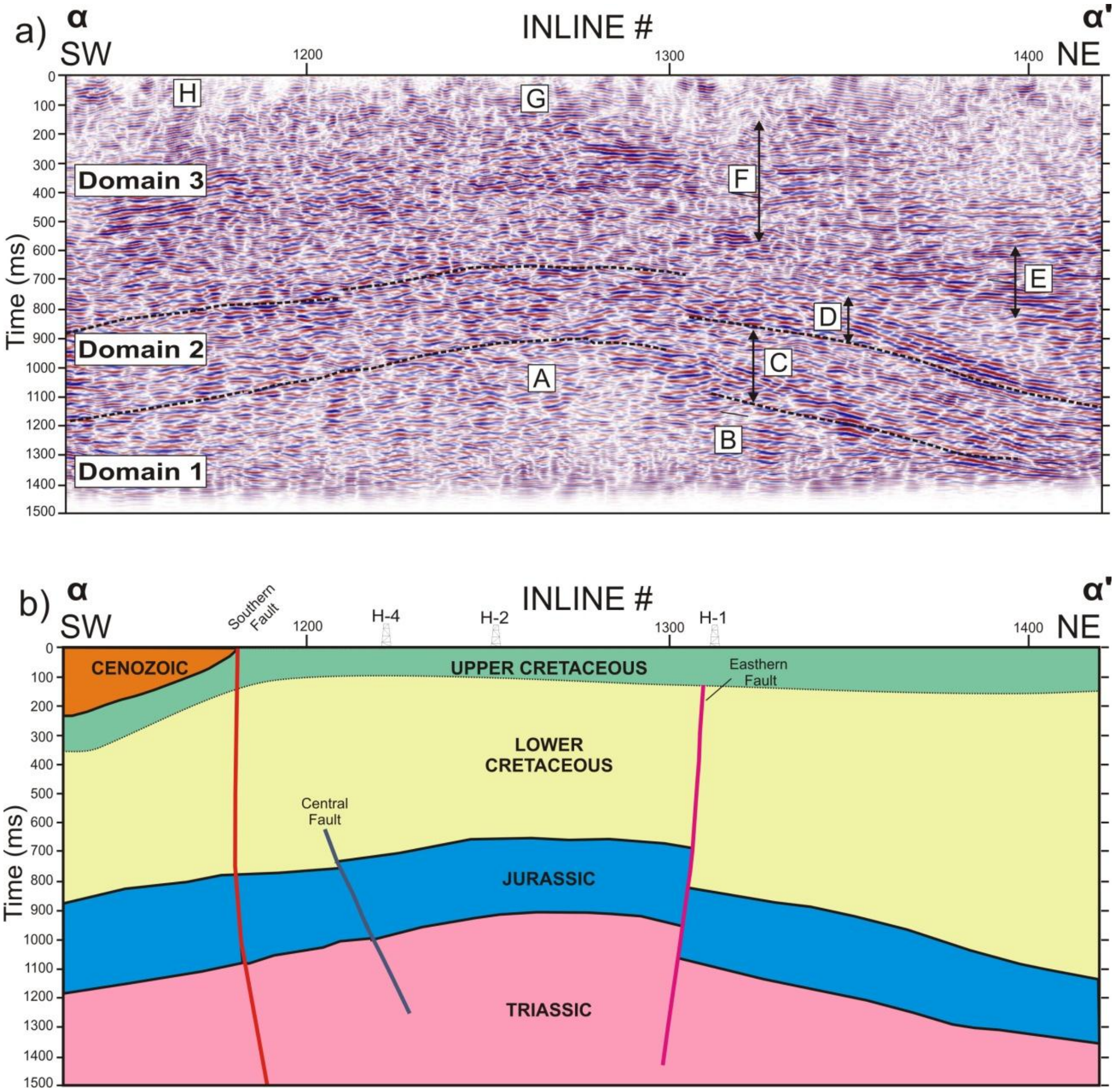

Fig. 12. Section β-β' of the Hontomín data set, **(a)** processed with Alcalde et al. (2013) processing flow, and **(b)** with the processing flow outlined in Table 2. Location of the β-β' section in Fig. 2.

10 Discussion

Data acquisition and processing

Three-dimensional seismic experiments, especially in complex environments, generally require a reasonable fold in order to obtain high-quality images of the subsurface structures. The acquisition approach used in Hontomín (Fig. 2) assured that the target could be properly imaged, with long offsets and 3-D sampling across the whole survey area (Fig. 5) and with a reasonable fold (Ashton, et al., 1994; Roche, 1997). However, it was unexpected to find a sharp velocity inversion so close to the surface. The velocity inversion is associated with the Upper–Lower Cretaceous boundary (i.e., the transition from high-velocity carbonates to low-velocity, water-saturated siliciclastic sediments). According to Fermat's principle, the seismic energy reaching the velocity inversion point tends to travel preferentially through deeper (higher velocity) formations, avoiding the shallower (lower velocity) layers. This results in a complete loss of amplitudes that severely affected the quality of the data by reducing the information in the traces corresponding to the position of the shadow zone at offsets larger than 500 m (Fig. 3). Besides, the deep reflections show a severe lack of coherency across the data set (Fig. 9). The conventional NMO correction processing thus fails to some extent since reflective zones are correctly aligned horizontally, but single reflections are disrupted and the signals do not sum constructively in the stacking process (Fig. 9). This feature could be a product of the interaction of the backscattered shear-wave energy with

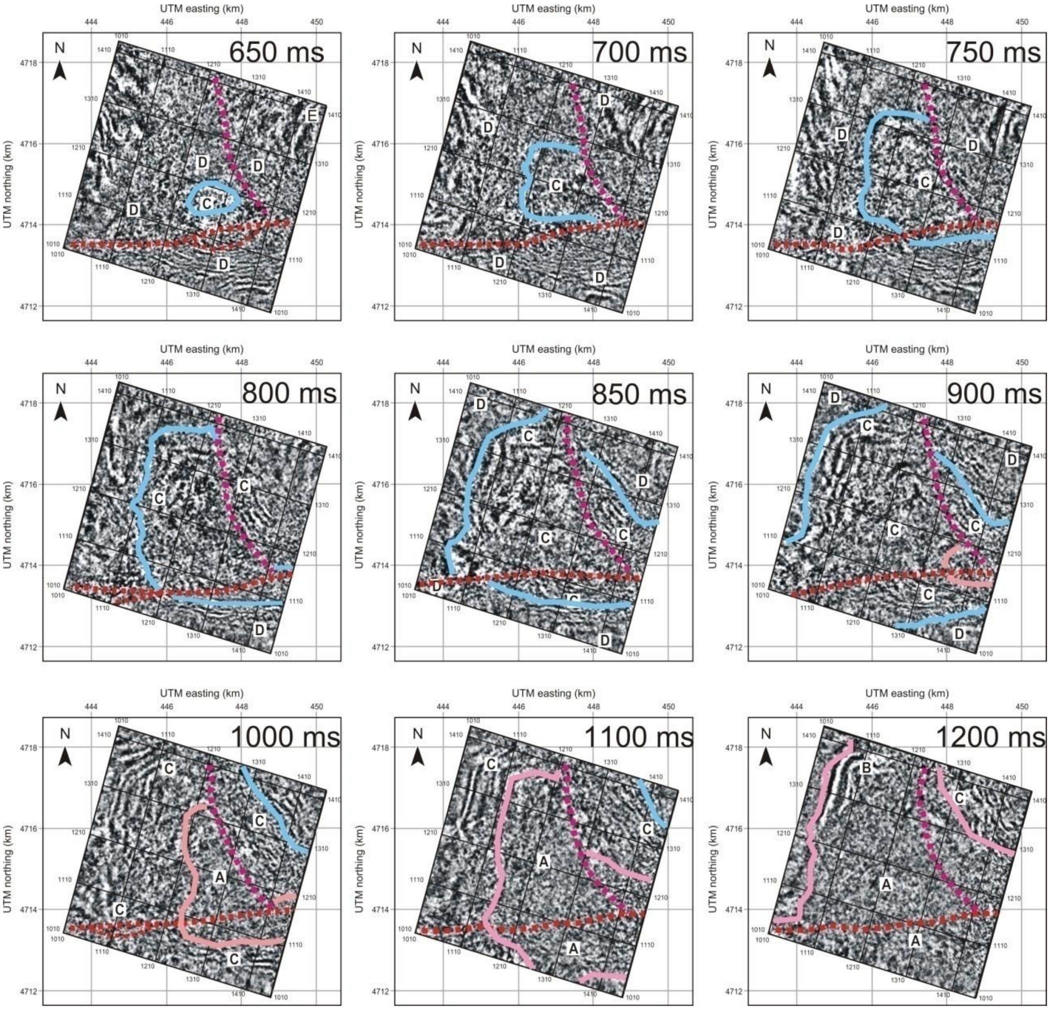

Fig. 13. Time slices from the migrated seismic volume with the different seismic reflection sets (A to H) recognized. The blue line (observed from time slice 900 to 650 ms) represents the top of the Jurassic dome structure (probably the top of the Purbeck Fm.). The pink line represents the base of the Jurassic dome (observed from time slice 1200 to 900 ms). Two faults have been interpreted: the Southern fault (red dashed line) and the Eastern fault (magenta dashed line). Note that certain splits of the Eastern fault have been marked in time slices 1000 and 650 ms.

the deep reflections, although further studies should be performed to elucidate this aspect.

Additional difficulties arose during the data processing due to physical property changes related to the carbonate composition of the subsurface. In this sense, the carbonate sediments behave similarly to crystalline media, containing sharp velocity variations which produce a blurred seismic signature. As observed in similarly difficult reservoir imaging experiments, the most relevant processing steps for reaching a good final image were the elevation and refraction static corrections (e.g., Juhlin 1995; Malehmir et al., 2012). Although first break picking was hindered by the “shadow zone” (Fig. 3), the resultant static model was very successful in improving the seismic image (Fig. 8), which is in accordance with the heterogeneous surface geology. However, there is still room for improvement in the statics calculation. New information about the near-surface velocity field (e.g., sonic-log data, shallow refraction seismic data, surface wave tomography etc.) could help to constrain and refine the near-surface velocity model.

For the source wavelet matching, the two wavelet matching methods (match filtering and phase and time shift) were applied to a subset of the data which was then stacked and qualitatively assessed. Both methods improved the data and when compared to each other, both were very similar in overall performance. As the phase and time shift method was simpler to apply, this method was chosen and applied to the data in the final workflow. This resulted in enhanced reflector continuity and strength in areas of the stacked section, which contained both dynamite, and Vibroseis traces in the

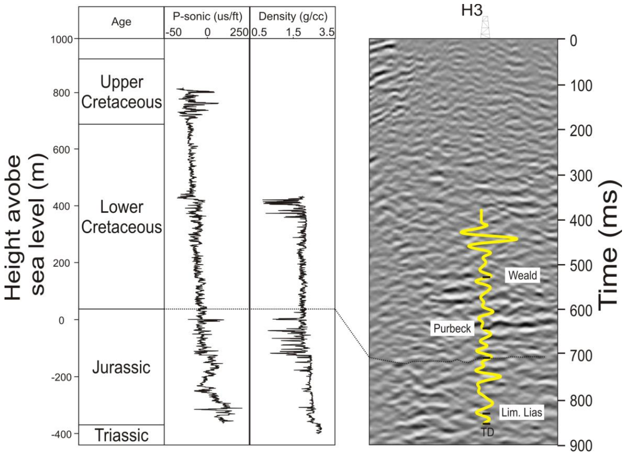

Fig. 14. Sonic and density logs of the H3 well in depth, with their interpreted age. A zero offset synthetic trace, calculated assuming a Ricker wavelet with a peak frequency of 30 Hz is shown (yellow). The time–depth relationship for the synthetic was set manually, due to the lack of check shot data and velocity information of the shallow subsurface. The synthetic is overlain on a portion of the β-β' section (location in Fig. 2). The Jurassic–Lower Cretaceous boundary is correlated with a dotted line. Main seismic events are also labeled in the seismic section.

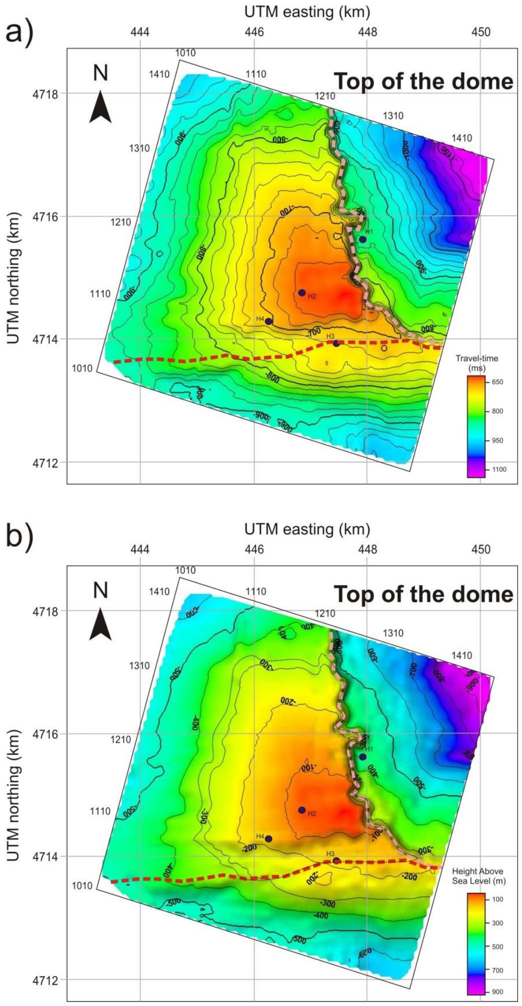

Fig. 15. (a) Time and **(b)** depth surface (replacement velocity of 3500 m s^{-1}) of the top of the Jurassic featuring the target dome structure, with the approximate position of southern (red dashed line) and eastern (pink dashed line) faults. The black dotted line indicates the area of the dome considered for the capacity estimation.

pre-stack gathers (Fig. 8). Due to the unequal distribution of the explosive source points throughout the Hontomín survey (Fig. 2), the source matching effects are only observed at the edges of the survey, where the explosive source concentration is higher.

The use of AGC within the workflow helped to obtain a good quality final image. However, it does not preserve the original amplitude character of the data set. This could jeopardize the use of amplitude variation methods for monitoring. Modifications to the processing flow should therefore be made before this data set can be used as a baseline to a repeat survey as part of a time-lapse seismic monitoring study.

11 Geometry of the deep structures

In general, the work flow outlined in Table 2 provides an improved image compared to the previous preliminary image presented in Alcalde et al. (2013) (Fig. 11). Our final processed seismic volume allows an interpretation of the five main geological units present in the study area (Fig. 12). The target Jurassic dome structure has been mapped from 650 ms to 1200 ms twt (Fig. 15a). The horizons corresponding to the top and the base of this structure have been mapped throughout the volume (Fig. 13). The top surface appears first just below 1050 ms and reaches its crest above 650 ms. The base surface appears at 1350 ms in the northern part of the data set, and peaks at 880 ms TWT. They define an elongated dome like structure. The geometry of the dome is almost symmetric up to 850 ms. From this point, the dome develops into an elongated shape in the NW–SE direction. It maintains this geometry until ~ 725 ms. The crest of the dome (at 650 ms) is found at the eastern side of the H2 well, in an area between inlines 1270–1300 and crosslines 1130–1160 (Fig. 15). The Jurassic dome resembles a pseudo-triangle in plan view, with the two main faults, eastern and southern faults, representing two of the sides. The third side was determined subjectively at the two-way time that the dome changes from symmetric to elongated (i.e., approximately 850 ms). The calculated area of the dome is 9.4×10^6 m^2.

The Hontomín structure is faulted at different scales. The southern and Eastern fault mark the southern and eastern limit of the dome, respectively. The Southern fault crosses the entire processed volume, separating the southern third of the study area from the remainder (Fig. 12 and Fig. 13). It has been related to the Ubierna fault (Tavani et al., 2013) and described as a dextral strike-slip fault that outcrops within the study area. It is easily recognizable because it coincides with a change in the dip of the reflections (i.e., increased dips to the south side of the fault coupled with a loss of lateral continuity of the events). It is difficult to assess whether a vertical offset across it is present or not, since the fault cuts through dome-shape structures and different sections give varying interpretations of the offset. The fault also contains branches that are only observable in certain sections of the seismic cube (Fig. 13). This fault could be an important conduit for fluid circulation, as observed by Ogaya et al. (2013). In addition, hydrochemistry studies in fluids derived from surface springs conducted by Nisi et al. (2013) in the eastern part of the Southern fault suggest that these fluids could have a deep origin, supporting the idea of the fluid circulation and, thus, a leaky fault. The Eastern fault presents the largest vertical offset of the study area (up to 380 m, Fig. 15b). It is nearly vertical near the surface and slightly dipping at depth. It has been mapped up to the Lower–Upper Cretaceous boundary. It marks a sharp seismic facies contrast. Other minor faults (e.g., the Central fault, Fig. 12b) with small offsets (less than ~ 20 ms) have been identified, but not included in this preliminary interpretation.

12 Internal architecture

The frequency range at the target time (700–1200 ms) is from 30 to 70 Hz. This frequency range is wide enough to ensure a reasonable resolution at the aquifer level. The dominant frequency of the data ranges from 20 to 75 Hz. Thus, assuming an average velocity of 3900 $\mathrm{m\,s^{-1}}$, the vertical resolution ranges between 13 to 50 m, based on the 1/4 wavelength criterion (Widess 1973; Sheriff and Geldart 1995). Based on the Fresnel zone criterion (Sheriff and Geldart 1995; Yilmaz 2001), the lateral resolution for the deepest structures at depths of 1200 and 1500 m (approximately) range from 180 to 320 m. Migration tends to collapse the Fresnel zone (and therefore increase the spatial resolution) to approximately the dominant wavelength (Yilmaz, 2001). However, the presence of noise and migration–velocity related errors could degrade the lateral resolution significantly.

A limited definition of the internal architecture was achieved in the interpretation stage. First, the carbonate units show subtle acoustic impedance changes (determined from the existing logs) and significant scattering. This makes the identification of the internal structures very difficult. Second, to date, the available velocity information from well logs is incomplete for the first 400 m. The latter issue does not allow us to tie the seismic data to the available boreholes. In this respect, new boreholes geared to hydrogeological modeling should cover this lack of information; nevertheless, these are not currently available. New processing steps should be performed in order to carry out the detailed geological interpretation of the 3-D volume, including a time to depth conversion of the data with the velocity information derived from logging tools, wave-equation datuming and, if possible, prestack depth migration.

In spite of this lack of internal definition, we have calculated a theoretical CO_2 capacity of the reservoir unit within the Jurassic structure. We will not take in consideration the possible interactions of the CO_2 with the reservoir formation, since this is outside of the scope of this article. Further information about geochemical and rock physics interactions, conducted inside the Hontomín project, can be found in García-Ríos et al. (2013) and Canal et al. (2012), respectively. The outcrop data indicates that Jurassic units are relatively homogeneous and their thicknesses are relatively constant. The calculation takes into account the characteristics of the top of the interpreted dome, and extrapolates it downwards. Assuming an average thickness and effective porosity of the reservoir unit of 80 m and 8.5 % (obtained from the well-log data), respectively, the calculated total pore volume in the dome reservoir is $1.6 \times 10^6\,\mathrm{m^3}$. At the expected average reservoir conditions (41 °C and 15.3 MPa), the density of CO_2 is 745 558 $\mathrm{kg\,m^{-3}}$. Thus, a maximum CO_2 storage capacity of 1.2 Gt of CO_2 is expected in the Hontomín Jurassic structure. This value is a rough estimate, but provides an overall idea of the scale and potential of the Hontomín site for CO_2 storage.

13 Conclusions

The data processing applied to the Hontomín 3-D seismic reflection data set allowed a preliminary interpretation of the main underground structure of the Hontomín area to be made. The data also characterize the Jurassic structure, which contains a potential reservoir-seal system for the storage of CO_2 in a deep saline aquifer. The structure includes a near-surface layer characterized by a velocity inversion. This generated unexpected complications in the static correction calculations, and reduced the overall quality of the data. In spite of this, the processing steps applied to the data resulted in relatively good images that show an elongated, faulted dome structure. Static corrections proved to be the most important step within the data processing flow. Other key processing steps included the DMO correction, frequency filtering and amplitude equalization. The two source wavelets used in the acquisition were matched using a self-developed code that gave similar results to that of the standard match filtering, with an easier implementation.

Five main geological units were interpreted from the migrated volume, including the target dome corresponding to the Jurassic package. The shape of the target structure is an asymmetric dome, with a steeper flank facing southwest. Two major faults, the Southern fault and the Eastern fault have been successfully interpreted as crossing the entire volume W–E and NNW. The total area of the dome structure is

$9.4 \times 10^6\,m^2$. The calculated pore volume for the reservoir structures within the Hontomín dome is $1.6 \times 10^6\,m^3$, giving a maximum theoretical storage capacity of 1.2 Gt of CO_2. A refined interpretation of internal structures and small-scale fracture zones, as well as time to depth conversion using the forthcoming well-log information are the next logical steps to be carried out. The processed data set represents the 3-D seismic model that could be used as a baseline model within a CO_2 storage scenario.

Acknowledgements. The authors sincerely thank the Editor Hans Thybo, Peter Bergmann and the anonymous reviewer for their useful comments. Funding for this Project has been partially provided by the Spanish Ministry of Industry, Tourism and Trade, through the CIUDEN-CSIC-Inst. Jaume Almera agreement (Characterization, Development and Validation of Seismic Techniques applied to CO_2 Geological Storage Sites) and by the European Union through the Technology Demonstration Plant of Compostilla OXYCFB300 project (European Energy Programme for 534 Recovery). Additional support has been provided by Spanish Ministry of Education Science (CSD2006-00041), Generalitat de Catalunya (2009SGR006) and CSIC JAE-Doc postdoctoral research contract (E.S.). The sole responsibility of this publication lies with the authors. The European Union is not responsible for any use that may be made of the information contained herein. Juan Alcalde is being currently supported by the Fundación Ciudad de la Energía (CIUDEN) research training program. We sincerely thank CGGVeritas for their assistance during the acquisition. Processing has been carried out using GLOBE ClaritasTM, under license from the Institute of Geological and Nuclear Sciences Limited, Lower Hutt, New Zealand and SeismicUnix from CWP (Center for the Wave phenomena, Colorado School of Mines). We thank all the people involved directly or indirectly in the elaboration of this work.

Edited by: H. Thybo

References

Alcalde, J., Martí, D., Calahorrano, A., Marzán, I., Ayarza, P., Carbonell, R., Juhlin, C., and Pérez-Estaún, A.: Active seismic characterization experiments of the Hontomín research facility for geological storage of CO_2, Spain, Int. J. Greenh. Gas Con., in press, doi:10.1016/j.ijggc.2013.01.039, 2013.

Alvarez, C.: Hydrocarbons in Spain – exploration and production, First Break, 12, 1994.

Arts, R., Eiken, O., Chadwick, A., Zweigel, P., van der Meer, L., and Zinszner, B.: Monitoring of CO_2 injected at Sleipner using time-lapse seismic data, Energy, 29, 1383–1392, 2004.

Ashton, P., Bacon, B., Deplante, C., Sinclair, D. T., and Redekop, G.: 3-D seismic survey design, Oilfield Review, 19–32, 1994.

Braaksma, H., Proust, J. N., Kenter, J. A. M., Drijkoningen, G. G., and Filippidou, N.: Sedimentological, Petrophysical, and Seismic Characterization of an Upper Jurassic Shoreface-Dominated Shelf Margin (the Boulonnais, Northern France), J. Sediment. Res., 76, 175–199, 2006.

Baines, S. J. and Worden, R. H.: Geological Storage of Carbon Dioxide, Geol. Soc. Lond., Special Publications, 233, 1–6, 2004.

Braun, J., Batt, G. E, Scott, D. J., McQueen, H., and Beaseley, R.: A simple kinematic model for crustal deformation along two- and three- dimensional listric normal faults derived from scaled laboratory experiments, J. Struct. Geol., 16, 1477–1490, 1994.

Beroiz, C. and Permanyer, A.: Hydrocarbon habitat of the Sedano trough, Basque-Cantabrian Basin, Spain, J. Pet. Geol., 34, 387–410, doi:10.1111/j.1747-5457.2011.00511.x, 2011.

Canal, J., Falcón, I., Barrientos, V., Juncosa, R., and Delgado, J.: Injection of reactive fluids in geological reservoirs: The coupling between rock reactivity, hydrodynamics and petrophysics, DHI/Fluid Consortium Meeting Fall 2012, Colorado School of Mines, Abstract paper, 2012.

Cosgrove, J. W. and Ameen, M. S.: Forced Folds and Fractures. Geological Society, London, Special Publications, 169, The Geol. Soc. Lond., 2000.

Elío, J, Nisi, B, Ortega, M. F., Mazadiego, L. F, Vaselli, O., and Grandia, F.: CO_2 soil flux baseline at the Technological Development Plant for CO_2 Injection at Hontomin (Burgos, Spain), Int. J. Greenh. Gas Con., 18, 224–236, 2013.

Erlich, R. N., Barrett, S. F., and Bai Ju Guo: Seismic and geologic characteristics of drowning events on carbonate platforms, AAPG Bulletin, 74 1523–1537, 1990.

Feroci, F., Orlando, L., Balia, R., Bosman, C., Cardarelli, E., and Deidda, G.: Some considerations on shallow seismic reflection surveys, J. Appl. Geophys., 45, 127–139, 2000.

Förster, A., Norden, B., Zinck-Jørgensen, K., Frykman, P., Kulenkampss, J., Spangerberg, E., Erzinger, J., Zimmer, M., Kopp, J., Borm, G., Julin, C., Cosma, C., and Hurter, S.: Baseline characterization of the CO_2SINK geological storage site at Ketzin, Germany, Environ. Geosci., 13, 145–161, 2006.

García-Ríos, M., Luquot, L., Soler, J. M., and Cama, J.: Laboratory-scale interaction between CO2-rich brine and reservoir rocks (limestone and sandstone), Procedia Earth and Planetary Science, 7, 109–112, 2013.

Hale, D. and Artley, C.: Squeezing dip moveout for depth-variable velocity, Geophysics, 58, 257–264, 1993.

Jin, G. and Groshong, R. H.: Trishear kinematic modeling of extensional fault-propagation folding, J. Struct. Geol., 28 170–183, 2006.

Juhlin, C.: Imaging of fracture zones in the Finnsjön area, central Sweden, using the seismic reflection method, Geophysics 60, 66–75, 1995.

Juhlin, C., Giese, R., Zinck-Jørgensen, K., Cosma, C., Kazemeini, H., Juhojuntti, N., Lüth, S., Norden, B., and Förster, A.: 3-D baseline seismics at Ketzin, Germany: The CO_2SINK project, Geophysics, 72, B121–B132, 2007.

Janson, X., Eberli, G. P., Bonnaffe, F., Gaumet, F., and de Casanove, V.: Seismic expressions of a Miocene prograding carbonate margin, Mut Basin, Turkey, AAPG Bulletin, 91, 685–713, 2007.

Kenter, J. A. M., Bracco Gartner, G. L., and Schlager, W.: Seismic models of a mixed carbonate-siliciclastic shelf margin: Permian upper San Andres Formation, Last Chance Canyon, New Mexico, Geophysics, 66, 1744–1748, 2001.

Malehmir, A. and Bellefleur, B.: 3-D seismic reflection imaging of volcanic-hosted massive sulfide deposits: Insights from reprocessing Halfmile Lake data, New Brunswick, Canada, Geophysics, 74, 209–213, 2009.

Malehmir, A. and Juhlin, C.: An investigation of the effects of the choice of stacking velocities on residual statics for hardrock reflection seismic processing, J. Appl. Geophys., 72, 28–38, doi:10.1016/j.jappgeo.2010.06.008, 2010.

Malehmir, A., Juhlin, C., Wijns, C., Urosevic, M., Valasti, P., and Koivisto, E.: 3-D reflection seismic investigation for open-pit mine planning and exploration in the Kevitsa Ni-Cu-PGE deposit, Northern Finland, Geophysics, 77, WC95–WC108, 2012.

Martí, D., Carbonell, R., Tryggvason, Escuder-Viruete, J., and Pérez-Estaún, A.: Mapping brittle fracture zones in three dimensions: high resolution traveltime seismic tomography in a granitic pluton, Geophys. J. Int., 149, 95–105, 2002.

Martínez-Torres, L. M.: Corte balanceado de la Sierra Cantabria (cabalgamiento de la Cuenca Vasco- Cantábrica sobre la Cuenca del Ebro), Geogaceta, 14, 113–115, 1993.

Masaferro, J., Bourne, R., and Jauffred, J.: 3-D visualization of carbonate reservoirs, The Leading Edge, 22, 18–25, doi:10.1190/1.1542751, 2003.

Merten, R.: Petroleum exploration and production in Spain, Z. Dtsch. Ges. Geowiss., 157, 717–732, 2006.

Nisi, B., Vaselli, O., Tassi, F., Elío, J., Delgado Huertas, A., Mazadiego, L. P., and Ortega, M. F.: Hydrogeochemistry of surface and spring waters in the surroundings of the CO_2 injection site at Hontomín-Huermeces (Burgos, Spain), Int. J. Greenh. Gas Con., 14, 151–168, doi:10.1016/j.ijggc.2013.01.012, 2013.

Ogaya, X., Ledo, J., Queralt, P., Marcuello, A., and Quintà, A.: First geoelectrical image of the subsurface of the Hontomín site (Spain) for CO_2 geological storage: A magnetotelluric 2D characterization, Int. J. Greenh. Gas Con., 13, 168–179, 2013.

Orr, F.: Storage of Carbon Dioxide in geologic Formations, J. Petrol. Technol., 56, 90–97, 2004.

Phipps, G. G.: Exploring for dolomitized Slave Point carbonates in northeastern British Columbia, Geophysics, 54, 806–814, 1989.

Preston, C., Monea, M., Jazrawi, W., Brown, K., Whittaker, S., White, D., Law, D., Chalaturnyk, R., and Rostron, B.: IEA GHG Weyburn CO_2 monitoring and storage project, Fuel Process. Technol., 86, 1547–1568, 2005.

Pujalte, V., Robles, S., García-Ramos, J. C., and Hernández, J. M.: El Malm-Barremiense no marinos de la Cordillera Cantábrica, in: Geología de España, edited by: Vera, J. A., SGE-IGME, Madrid, 288–291, 2004.

Quesada, S., Robles, S., and Rosales, I.: Depositional architecture and transgressive-regressive cycles within Liassic backstepping carbonate ramps in the Basque-Cantabrian basin, northern Spain, J. Geol. Soc., 162, 531–538, 2005.

Quintà, A. and Tavani, S.: The foreland deformation in the southwestern Basque-Cantabrian Belt (Spain), Tectonophysics, 576–577, 4–19, 2012.

Quintá, A., Tavani, S., and Roca, E.: Fracture pattern analysis as a tool for constraining the interaction between regional and diapir-related stress fields: Poza de la Sal Diapir (Basque Pyrenees, Spain), Geol. Soc. Lond. SP, 363, 521–532, doi:10.1144/SP363.25, 2012.

Rudolph, K. W., Schlager, W., and Biddle, K. T.: Seismic models of a carbonate foreslope-to-basin transition, Picco di Vallandro, Dolomite Alps, northern Italy, Geology, 17, 453–456, 1989.

Roche, S. L.: Time-lapse, multicomponent, three-dimensional seismic characterization of San Andres shallow shelf carbonate reservoir, vacuum field, lea county, New Mexico, Ph.D. Thesis, Colorado School of Mines, 1997.

Schlische, R. W.: Geometry and Origin of Fault-related Folds in Extensional Settings, AAPG Bulletin, 79, 11-1661-1678, Ph.D. Thesis, Colorado School of Mines, 1995.

Serrano, A. and Martínez del Olmo, W.: Tectónica salina en el Dominio Cántabro-Navarro: evolución, edad y origen de las estructuras salinas, in: Formaciones Evaporíticas de la Cuenca del Ebro y Cadenas Periféricas, y de la Zona de Levante, edited by: Fedrico Ortí, C. and Salvany, M., Universidad de Barcelona – ENRESA, 39–53, 1990.

Sheriff, R. E. and Geldart, L. P.: Exploration seismology. History, Theory, and Data Acquisition, vol. 1., Cambridge University Press, New York, 1985.

Steer, D., Brow, L., Knapp, J., and Baird, D.: Comparison of explosive and Vibroseis source energy penetration during COCORP deep seismic reflection profiling in the Williston Basin, Geophysics, 61, 211–221, 1996.

Soto, R., Casas-Sainz, M., and Villalaín, J. J.: Widespread Cretaceous inversión event in norhtern Spain: evidence from subsurface and palaeomagnetic data, J. Geol. Soc., 168, 899–912, doi:10.1144/0016-76492010-072, 2011.

Tavani, S., Quintà, A., and Granado, P.: Cenozoic right-lateral wrench tectonics in the Western Pyrenees (Spain): The Ubierna Fault System, Tectonophysics, 509, 238–253, doi:10.1016/j.tecto.2011.06.013, 2011.

Tavani, S., Carola, C., Granado, P., Quintà, A., and Muñoz, J. A.: Transpressive inversion of a Mesozoic extensional forced fold system with an intermediate décollement level in the Basque-Cantabrian Basin (Spain), Tectonics, 32, doi:10.1002/tect.20019, 2013.

Ugalde, A., Villaseñor, A., Gaite, B., Casquero, S., Martí, D., Calahorrano, A., Marzán, I., Carbonell, R., and Estaún, A. P.: Passive seismic monitoring of an experimental CO_2 geological storage site in Hontomín (Northern Spain), Seismol. Res. Lett., 84, 75–84, 2013.

Von Hartmann, H., Buness, H., Krawczyk, C. M., and Schulz, R.: 3-D seismic analysis of a carbonate platform in the Molasse Basin – reef distribution and internal separation with seismic attributes, Tectonophysics, 572–573, 16–25, 2012.

White, D.: Monitoring CO_2 storage during EOR at the Weyburn-Midale Field, SEG, The leading Edge, 28, 838–842, doi:10.1190/1.3167786, 2009.

Widess, M. B.: How thin is a thin bed?, Geophysics, 38, 1176–1180, 1973.

Yilmaz, O.: Seismic Data Analysis – Processing, Inversion, and Interpretation of Seismic Data, Soc. of Expl. Geophys., Tulsa, OK, 2001.

Ziegler, P. A.: Evolution of the North Atlantic: An Overview, AAPG Memoir, 46, in: Extensional Tectonics and Stratigraphy of the North Atlantic Margins, edited by: Tankard, A. J. and Balkwill, H. R., 111–129, 1989.

CHAPTER IV

3D geological characterization of the Hontomín CO2 storage site, Spain: multidisciplinary approach from seismics, well-logging and regional data.

Alcalde, J., Marzán, I., Saura, E., Martí, D., Ayarza, P., Juhlin, C., Pérez-Estaún, A., and Carbonell, R. 2014. Tectonophysics (accepted).

ARTICLE IN PRESS
TECTO-126279; No of Pages 20

Tectonophysics xxx (2014) xxx–xxx

Contents lists available at ScienceDirect

Tectonophysics

journal homepage: www.elsevier.com/locate/tecto

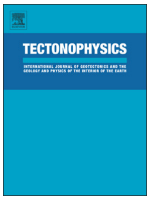

3D geological characterization of the Hontomín CO_2 storage site, Spain: Multidisciplinary approach from seismic, well-log and regional data

Juan Alcalde [a,b,*], Ignacio Marzán [a,1], Eduard Saura [a,1], David Martí [a,1], Puy Ayarza [c,2], Christopher Juhlin [d,3], Andrés Pérez-Estaún [a,1], Ramon Carbonell [a,1]

[a] *Institute of Earth Sciences Jaume Almera ICTJA-CSIC, Barcelona, Spain*
[b] *CIUDEN Foundation, Ponferrada, Spain*
[c] *University of Salamanca, Salamanca, Spain*
[d] *Uppsala University, Uppsala, Sweden*

A R T I C L E   I N F O

Article history:
Received 19 August 2013
Received in revised form 14 April 2014
Accepted 17 April 2014
Available online xxxx

Keywords:
3D geological modeling
3D reflection seismics
Well-log correlation
CO_2 storage
Maximum capacity estimation

A B S T R A C T

The first Spanish Technological Development plant for CO_2 storage is currently under development in Hontomín (Spain), in a fractured carbonate reservoir. The subsurface 3D geological structures of the Hontomín site were interpreted using well-log and 3D seismic reflection data. A shallow low velocity zone affects the wave propagation and decreases the coherency of the underlying seismic reflections, deteriorating the quality of the seismic data, and thus preventing a straightforward seismic interpretation. In order to provide a fully constrained model, a geologically supervised interpretation was carried out. In particular, a conceptual geological model was derived from an exhaustive well-logging analysis. This conceptual model was then improved throughout a detailed seismic facies analysis on selected seismic sections crossing the seismic wells and in consistency with the regional geology, leading to the interpretation of the entire 3D seismic volume. This procedure allowed characterizing nine main geological levels and four main fault sets. Thus, the stratigraphic sequence of the area and the geometries of the subsurface structures were defined. The resulting depth-converted 3D geological model allowed us to estimate a maximum CO_2 storage capacity of 5.85 Mt. This work provides a 3D geological model of the Hontomín subsurface, which is a challenging case study of CO_2 storage in a complex fractured carbonate reservoir.

1. Introduction

Storage of CO_2 in saline aquifers is considered one of the most promising actions for stabilization of atmospheric CO_2 concentrations (Bachu, 2000; IPCC, 2005). The geological storage of CO_2 (GSC) aims to inject this greenhouse gas in an appropriate reservoir site, which requires a suitable reservoir formation (i.e. high porosity and permeability), sealed by a proved competent seal formation (i.e. low porosity and permeability, lack of conductive faults, etc.), placed at a suitable depth to ensure profitability (e.g. Bachu, 2000; Chadwick et al., 2006; IPCC, 2005; Pérez-Estaún et al., 2009) (Fig. 1). The first Spanish CO_2 storage Technology Development Plant is currently being developed in Hontomín, Spain (Fig. 2), led by the CIUDEN Foundation. The project is carried out in a research and development (R&D) basis, whose objectives focus on the knowledge of strategies for CO_2 injection, testing of monitoring techniques and methodologies and the understanding of the physico-chemical processes associated with CO_2 storage in a deep saline aquifer, through real experiments at the facility.

A number of characteristics determined the suitability of the Hontomín reservoir for GSC (Prado et al., 2008). These included: (1) the existence of a deep saline aquifer, filled with brine (20 g/l of NaCl, Ogaya et al., 2013) and very low oil content; (2) the location of this aquifer within a carbonate reservoir–seal system, allowing mineral trapping-related studies; (3) the acquaintance of a dipping structure, which allows to accelerate the CO_2 migration processes; (4) the relatively small size of the target structure, making it tractable for research purposes; (5) the low seismicity of the area; and (6) the availability of previous information (2D seismic datasets, well-log data) acquired with oil exploration goals.

At the Hontomín site, the target reservoir and seal formations consist of Upper Jurassic marine carbonates, arranged in an asymmetric dome-like structure and located at approximately 1485 m of depth (Alcalde et al., 2013a; Ogaya et al., 2013). The relatively small size of the target

---

* Corresponding author at: Institut of Earth Sciences Jaume Almera ICTJA-CSIC, C/ Lluís Solé i Sabarís s/n, 08028 Barcelona, Spain. Tel.: +34 646874631.
E-mail addresses: juan.alcalde.martin@gmail.com (J. Alcalde), imarzan@ictja.csic.es (I. Marzán), esaura@ictja.csic.es (E. Saura), dmarti@ictja.csic.es (D. Martí), puy@usal.es (P. Ayarza), christopher.juhlin@geo.uu.se (C. Juhlin), andres@ictja.csic.es (A. Pérez-Estaún), ramon.carbonell@csic.es (R. Carbonell).
[1] Tel.: +34 934095410.
[2] Tel.: +34 923294488.
[3] Tel.: +46 18 471 2392.

http://dx.doi.org/10.1016/j.tecto.2014.04.025
0040-1951/© 2014 Elsevier B.V. All rights reserved.

Please cite this article as: Alcalde, J., et al., 3D geological characterization of the Hontomín CO_2 storage site, Spain: Multidisciplinary approach from seismic, well-log and regional data, Tectonophysics (2014), http://dx.doi.org/10.1016/j.tecto.2014.04.025

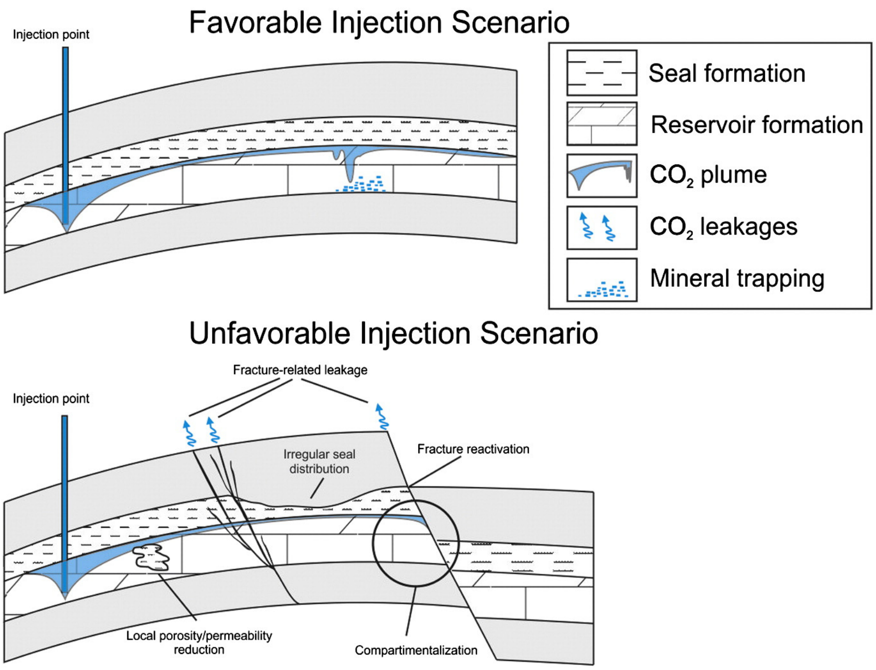

Fig. 1. Scheme of favorable and unfavorable scenarios for geological storage of CO_2.

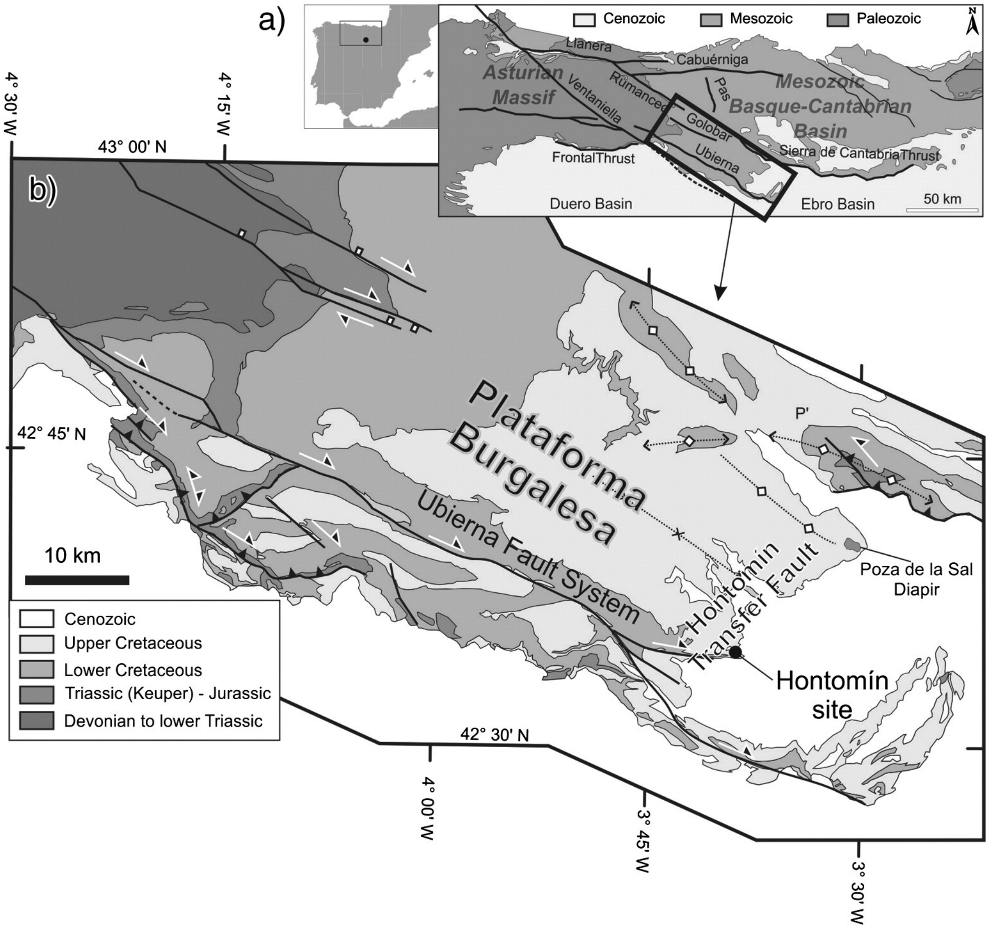

Fig. 2. (a) Location of the study area within the Iberian Peninsula, and geological map of the Basque–Cantabrian Basin and Asturian Massif area with labels of the main features (modified from Tavani et al., 2013); (b) geological map of the southern portion of the Basque–Cantabrian Basin, with detail of the Plataforma Burgalesa and the Hontomín location (modified Tavani et al., 2011).

Please cite this article as: Alcalde, J., et al., 3D geological characterization of the Hontomín CO_2 storage site, Spain: Multidisciplinary approach from seismic, well-log and regional data, Tectonophysics (2014), http://dx.doi.org/10.1016/j.tecto.2014.04.025

structure (approximately 5 × 3 km^2) facilitates CO_2 monitoring processes. Besides, the existence of structural complexities enables the experimentation related to faults, controlled leakages and remediation techniques.

The Hontomín site presents three main scientific and technical challenges from a GSC point of view. First, it represents one of the first GSC pilot plants implemented in carbonate formations. Carbonate reservoirs possess very interesting attributes for GSC (Bachu et al., 1994): after injection, CO_2 partly dissolves the carbonate rocks (increasing the porosity and permeability, and improving the injectivity), whereas in a long term, the CO_2-saturated brine reacts with the carbonate rocks forcing the precipitation of new minerals and thus ensuring the fixation of the CO_2 in the subsurface (mineral trapping) (Fig. 1).

The second challenge is related to the geological complexity of the study area (Fig. 2), which has undergone a very complex and tectono-sedimentary evolution (e.g. García-Mondéjar, 1996; Pujalte et al., 2004; Quintà and Tavani, 2012; Tavani, 2012; Tavani et al., 2011; Tavani et al., 2013). This issue is especially important in Hontomín's reservoir and seal formations, which developed fractures under successive deformation stages. In fact, fracturing can have a significant impact on the characteristics of the reservoir system, either increasing or decreasing its secondary porosity and permeability (e.g. Nelson, 2001). Whereas fracturing may enhance secondary porosity and improve the injectivity and capacity of the reservoir, fine fracture filling and, above all, low-permeability fault cores may compartmentalize the reservoir, reducing drastically the reservoir's suitability. Besides, open fractures and highly permeable fault damage zones in the seal formation may significantly reduce its sealing capacity, thus jeopardizing the integrity of the reservoir complex.

Several multidisciplinary experiments have been carried out in the Hontomín site in order to elaborate a 3D Thermo-, Hydro-, Mechanical- and Chemical (THMC) coupled model (e.g. Alcalde et al., 2013a, 2013b; Canal et al., 2013; Elío et al., 2013; Nisi et al., 2012; Martinez-Landa et al., 2013; Ogaya et al., 2013; Ugalde et al., 2013; Vilamajó et al., 2013). Within them, a 3D seismic reflection dataset was acquired, aiming to obtain a 3D structural and seismic baseline model of the study area (Alcalde et al., 2013b). Carbonate reservoirs may be difficult targets for reflection seismic methods, mainly due to the possible lack of layering during the deposition, diagenetic alterations and other structural complexity-related problems (e.g. Kenter et al., 2001; Masaferro et al., 2003; Phipps, 1989; Rudolph et al., 1989; Von Hartmann et al., 2012). These features can frustrate the attempts to characterize the internal structure with seismic reflection methods. In the case of the Hontomín dataset, this issue is stressed by the existence of a near-surface velocity inversion, studied in detail by Alcalde et al. (2013a; 2013b). This velocity inversion generates a "shadow zone" that interrupts the lateral coherency of the reflections in the whole 3D volume.

The complex geology present in Hontomín and the limited quality of the seismic data prevent the application of a conventional straightforward horizon picking in the seismic volume. Therefore, we present an interpretation approach in which seismic facies analysis, well-log correlation and surface geology studies are complemented by a conceptual geological model (Fig. 3). Interactive development of the seismic interpretation and the conceptual model leads to the presented geological model. The results obtained by this work enable the understanding of the sedimentary and tectonic history of the Hontomín area, as well as the determination of the feasibility of the reservoir formations for GSC.

2. Geological setting

The CO_2 storage site of Hontomín is enclosed in the southern section of the Mesozoic Basque–Cantabrian Basin, named "Plataforma Burgalesa" (Serrano and Martinez del Olmo, 1990; Tavani, 2012) (Fig. 2). This domain is located in the northern junction of the Cenozoic Duero and Ebro basins, forming an ESE-dipping monocline bounded by the Sierra de Cantabria Thrust to the North and the Ubierna Fault System to the South (Tavani, 2012).

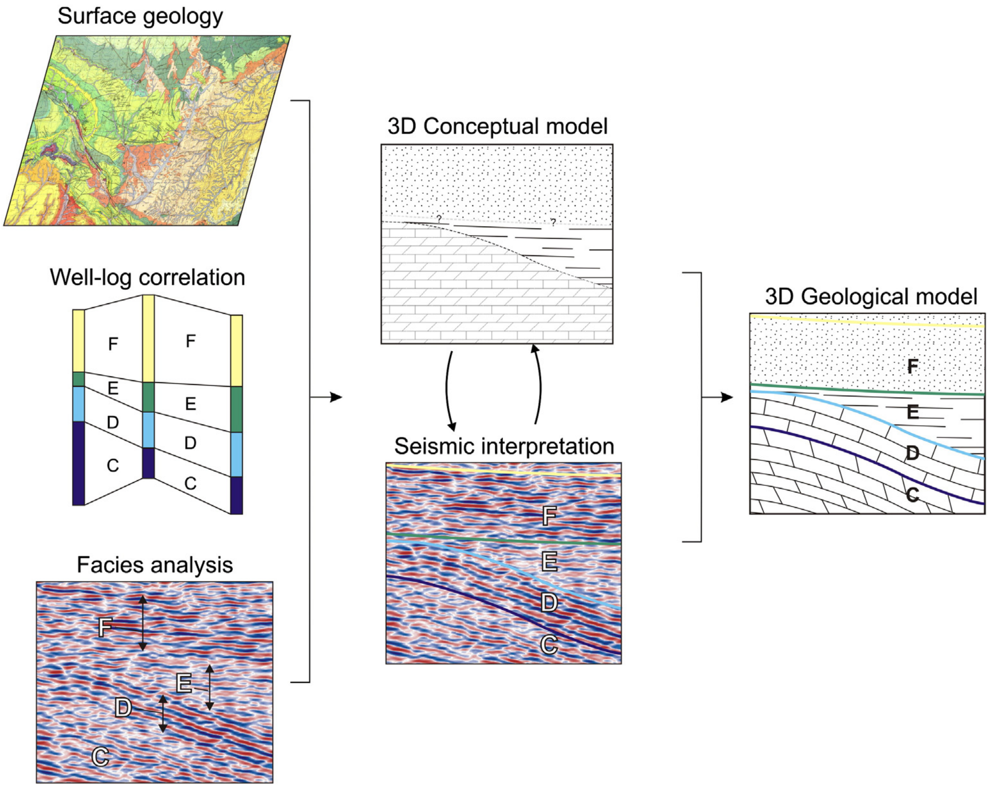

Fig. 3. Strategy for the generation of the 3D geological model. The well-log data was used as starting point for the conceptual modeling, which was then combined with the 3D seismic data and complemented with surface and regional geology.

Please cite this article as: Alcalde, J., et al., 3D geological characterization of the Hontomín CO_2 storage site, Spain: Multidisciplinary approach from seismic, well-log and regional data, Tectonophysics (2014), http://dx.doi.org/10.1016/j.tecto.2014.04.025

Three main deformation stages, affected the study area during the Mesozoic and Cenozoic (Tavani, 2012; Tavani et al., 2013). First, a Permian–Triassic extensional stage led to the development of ESE–WNW and E–W trending faults (Ziegler, 1989; García-Mondéjar, 1996). The second rifting event, linked to the opening of the North Atlantic and Bay of Biscay (Le Pichon and Sibuet, 1971; Montadert et al., 1979; Ziegler, 1989; García-Mondéjar, 1996) generated the Plataforma Burgalesa along with the Basque–Cantabrian basin. This event inherited ESE–WNW striking faults and generated NNE–SSW striking extensional faults, oriented at an angle of 75–80° with the previous faults (Tavani and Muñoz, 2012; Tavani et al., 2013). During this second rifting event, Upper Triassic Keuper evaporites acted as a major decoupling zone, imposing different deformation styles in the cover sequences and in the Paleozoic basement (Alcalde et al., 2013b; Tavani et al., 2011; Tavani et al., 2013). In particular, this decoupling enabled the development of extensional forced folds in the supra-salt cover, led by coeval evaporite migration and faulting in the sub-salt basement (Tavani et al., 2013). Finally, the latter Pyrenean orogeny originated a compressional environment which caused reverse, right-lateral and left-lateral reactivations of inherited faults (Quintá et al., 2012; Quintà and Tavani, 2012; Tavani et al., 2011; Tavani et al., 2013).

From a stratigraphic perspective, the Mesozoic succession in the Hontomín structure (Fig. 4b) starts with the evaporites and clays of the Triassic Keuper Facies, which forms the core of the target dome. The Lower Jurassic is composed of evaporites, dolomites and marls, and lies over the Keuper Facies (Pujalte et al., 2004; Quesada et al., 2005). The upper part of the Lower Jurassic and the Middle Jurassic series is constituted by shallow marine carbonates and hemipelagic ramp sediments which can be divided in four units: Lower Jurassic (1) Carbonate, (2) Marly and (3) Pelletic Lias units and a Middle Jurassic carbonate (4) Dogger unit. The Purbeck Facies (Late Jurassic–Early Cretaceous in age) is formed by clays, sandstone and carbonate rocks, placed uncomformably on top of the Jurassic marine rocks. The Lower Cretaceous succession is completed by siliclastic sediments of the Weald Facies, and the Escucha and Utrillas formations. They are made of fluvial deposits that alternate channel filling sandstones and flood plain shale sediments. The uppermost rocks exposed in the Hontomín area are Upper Cretaceous carbonates and Cenozoic rocks (lacustrine and detritic) lying uncomformably over the Mesozoic successions (Vera, 2004).

The reservoir and seal formations were selected based on the available geophysical and geological data (vintage 2D seismic reflection data, well-logs, borehole core samples, etc.). These formations are Jurassic in age, and form in the Hontomín area a dome-like structure with an overall extent of 5 × 3 km^2. The target CO_2 injection point is a saline aquifer included in the carbonate reservoir–seal system at about 1500 m deep. The target Jurassic formations meet the requirements considered suitable for CO_2 Geological Storage, including physical properties (i.e., porosity, permeability and brine salinity), effective sealing capacity, and depth (Bachu, 2000; Chadwick et al., 2006; Pérez-Estaún et al., 2009). They are formed by a dolostone unit known as “Carniolas” and an oolitic limestone. The estimated porosity of the Carniolas reaches over 12% (Ogaya et al., 2013) and is slightly lower at the Carbonate Lias level (8.5% in average). The reservoir levels contain saline water with more than 20 g/l of NaCl. The high porosity of the lower part of the reservoir (i.e., the Carniolas level) is the result of secondary dolomitization and different fracturing events. The minimum thickness of the reservoir units is 100 m. The potential upper seal unit comprises marlstones and black shales from a hemipelagic ramp (Pliensbachian and Toarcian; Vera, 2004).

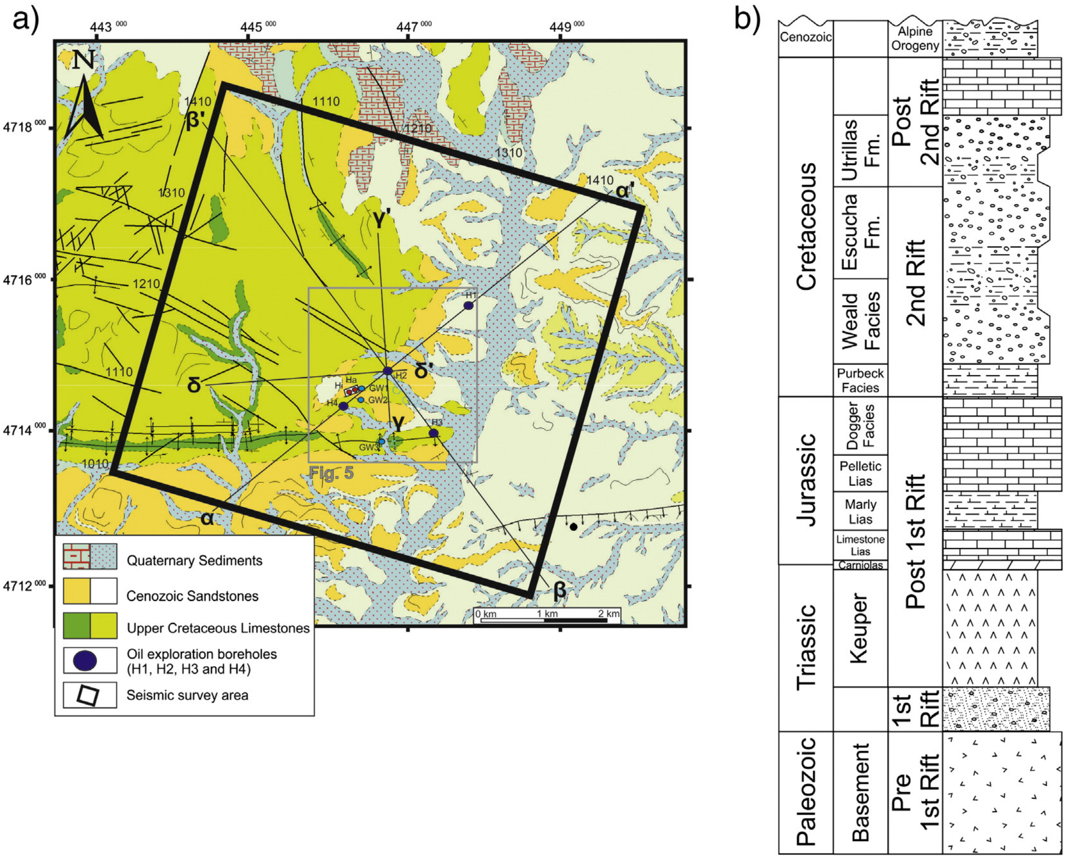

Fig. 4. (a) Detail of the main geological features of the study area, with the position of the 3D seismic survey (black square), the location of the wells used in the modelling and the injection (Hi) and monitoring (Ha) wells; (b) Synthetic stratigraphic log based on available seismic and well data.

Please cite this article as: Alcalde, J., et al., 3D geological characterization of the Hontomín CO_2 storage site, Spain: Multidisciplinary approach from seismic, well-log and regional data, Tectonophysics (2014), http://dx.doi.org/10.1016/j.tecto.2014.04.025

Table 1
Main characteristics of the 39 interpreted well-tops. The five last columns are mean values for the main logs: gamma ray (GR), sonic (DT), bulk density (RHOB), neutron porosity (shale volume corrected; Nφ-Vsh) and deep resistivity (Res_D).

Period	Age	Litostratigraphic units		Paleoenvironment	Code	CO2	GR (gAPI)	DT (μs/f)	RHOB (g/c3)	NΦ–Vsh (PU)	Res_D (Ω.m)
Tertiary	Tertiary	Bureba Facies		Fluvial / lacustrine	T		47.03	127.00	–	–	82.78
Cretaceous	Cenomanian–Maastrichtian			Carbonatic continental margin	KS6		26.34	67.56	–	–	193.37
					KS5		41.88	87.67	–	–	90.40
					KS4		50.68	101.88	–	–	64.51
					KS3		100.25	150.87	–	–	24.64
					KS2		68.51	109.45	–	–	28.91
					KS1		70.39	110.44	–	–	35.51
	Early Cenomanian	Utrillas Fm.		Fluvial: braided rivers with abrupt topography	KU5	Seal	90.90	161.50	–	–	32.66
					KU4		100.37	129.16	–	–	43.27
					KU3		66.72	122.31	–	–	61.75
					KU2		69.33	126.50	–	–	59.79
					KU1		102.58	123.26	–	–	57.32
	Aptian–Albian	Escucha Fm.		Fluvial: braided rivers with smooth topography	KE2		43.85	112.60	–	–	103.93
					KE1		24.45	93.05	2.38	14.42	230.06
	Late Valanginian–Barremian	Weald Facies–Pas Group		Fluvial: Meandering rivers, fining upsequence channel fills	KW3		39.83	96.55	2.34	18.87	133.62
					KW2		40.00	89.15	2.37	14.22	171.38
					KW1		28.74	84.08	2.37	15.28	200.48
	Oxfordian–Early Valanginian	Purbeck Facies	Cabuerniga Group	Transgressive–regressive cycle	JKP2	Seal	62.52	86.42	2.32	14.04	142.99
Jurassic			Campoo Group	Deltaic	JKP1	Reservoir	73.47	81.36	2.34	20.74	42.32
	Callovian	Dogger		Hemipelagic ramp	JD4		42.95	64.46	2.58	5.80	74.94
					JD3		45.00	63.26	2.66	2.23	122.03
	Bathonian				JD2	Reservoir	30.11	56.82	2.67	0.27	190.00
					JD1		33.77	69.25	2.61	7.61	25.51
	Late Bajocian	Pelletic Limestone Unit			Jpllt5		16.94	57.61	2.66	4.82	78.80
	Early Bajocian				Jpllt4	Seal	48.17	65.25	2.63	4.47	28.61
					Jpllt3		36.25	61.76	2.65	4.98	34.82
					Jpllt2		58.38	69.41	2.57	6.77	20.13
					Jpllt1		46.11	67.17	2.66	5.35	23.90
	Toarcian	Marly Lias	Castillo Pedroso Fm.		LM5	Main Seal	66.51	76.13	2.62	8.13	11.65
					LM4		90.00	82.53	2.60	4.78	9.65
	Pliensbachian		Camino Fm.		LM3		65.00	68.72	2.61	1.50	19.62
					LM2		90.00	80.07	2.56	2.88	15.66
	Late Sinemurian		P. Pozazal Fm.		LM1	Seal	44.71	61.71	2.69	1.19	35.31
	Early Sinemurian	Limestone Lias	Rio Polla Fm.	Inner ramp	LC4	Main Resevoir	21.85	54.42	2.69	3.04	51.87
			Sopeña Fm.		LC3		24.33	71.03	2.60	12.83	11.78
					LC2		17.00	53.95	2.67	4.85	48.76
					LC1		16.93	53.90	2.74	5.15	30.76
Triassic–Jurassic	Triassic–Jurassic	Carnioles–P. Palombera Fm.	Villanueva P. Fm.	Tidal	Dol2		26.30	59.96	2.61	18.00	16.84
					Dol1		23.92	52.22	2.74	10.00	82.14
			Anhidrites Unit		UA		21.26	50.63	2.89	0.03	500.00

Please cite this article as: Alcalde, J., et al., 3D geological characterization of the Hontomín CO_2 storage site, Spain: Multidisciplinary approach from seismic, well-log and regional data, Tectonophysics (2014), http://dx.doi.org/10.1016/j.tecto.2014.04.025

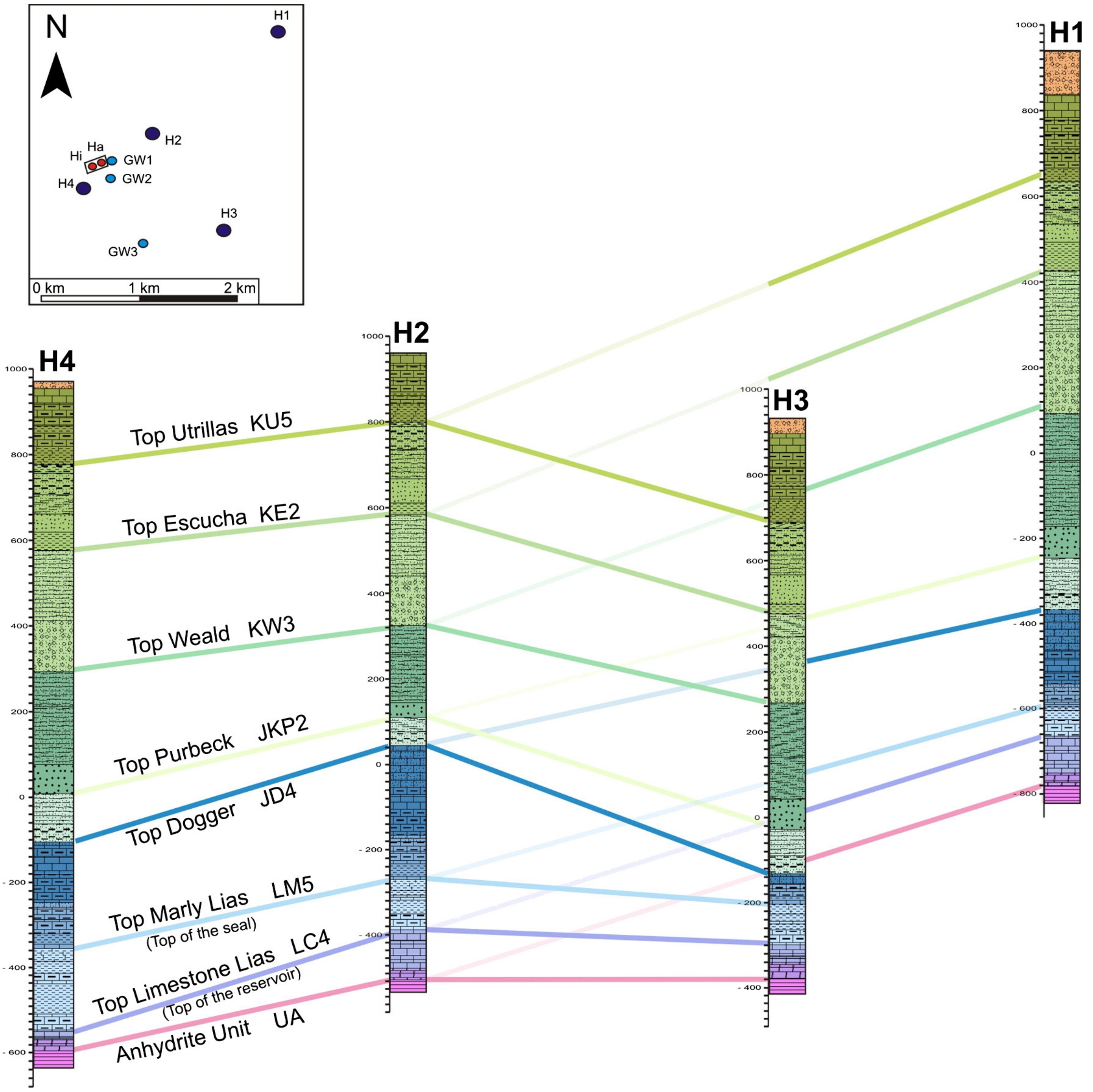

Fig. 5. 3D stratigraphic correlation of exploration wells H1, H2, H3 and H4, based on the sonic, GR, resistivity and bulk density logs. The well interpretation is referenced to the top of the Purbeck Fm.

3. Available data

3.1. 3D seismic reflection data

The reflection seismic method constitutes one of the main techniques for the characterization of geological reservoir complexes (e.g., Arts et al., 2001; Martí et al., 2002; Förster et al., 2006). A correct seismic characterization is essential to determine the most suitable position for the CO_2 injection (e.g., Alcalde et al., 2013a; Juhlin et al., 2007) and to be used as a baseline in order to track the underground migration of the CO_2 with time-lapse techniques (e.g., Arts et al., 2004; Ivanova et al., 2012; Lumley, 2010; White, 2013).

To accomplish these objectives, a 3D seismic reflection survey was acquired in Hontomín in summer of 2010 (Alcalde et al., 2013a; 2013b) (Fig. 4). The acquisition parameters included 22 source lines (crosslines), deployed E–W, perpendicular to 22 receiver lines (inlines) deployed N–S, with intervals of 25 m between sources and between receivers; the inline and crossline spacing was 250 m and 275 m, respectively, covering a total extent of 36 km^2. A maximum of 120 channels were active per inline, giving a maximum of 1200 traces per shot gather. This acquisition geometry gave a maximum common depth point (CDP) fold of 36 traces/CDP. Two sources were used in Hontomín: a Vibroseis source (16 s sweep of 8–80 Hz bandwidth), used in 76% of the source points, and an explosive source (450 g of dynamite distributed in three 1.5 m deep boreholes) used in the remaining 24% source points.

The acquired seismic data was processed down to 1500 ms (Alcalde et al., 2013b). The main applied processing steps include source wavelet matching, static corrections, 3D dip move-out corrections and post stack time migration. A significant effort was made to match the phases of the two used sources. That included the use of trace wide time and phase shifts, which resulted in enhanced reflector continuity and strength. Static corrections resulted to be one of the key processes for obtaining a seismic image suitable for geological interpretation. In the Hontomín dataset, the large topographic changes (up to 200 m) and heterogeneous geology resulted in shifts of over 70 ms per trace on average (Alcalde et al., 2013b).

The existence of an unexpected sharp velocity inversion near the surface, associated with the Upper–Lower Cretaceous contact, severely affected the quality of the data (Alcalde et al., 2013b). This feature

Please cite this article as: Alcalde, J., et al., 3D geological characterization of the Hontomín CO_2 storage site, Spain: Multidisciplinary approach from seismic, well-log and regional data, Tectonophysics (2014), http://dx.doi.org/10.1016/j.tecto.2014.04.025

reduced the information on the traces corresponding to the position of the shadow zone at offsets larger than 500 m, and decreased the efficacy of the NMO correction. The final migrated volume, however, provided good quality images of the Hontomín site from 75 to 1350 ms.

3.2. Well-log correlation

The well-log correlation was the starting point for the 3D geological modeling of the Hontomín's underground structure. Four oil exploration boreholes lie within the study area (H1, H2, H3 and H4) (Figs. 4a, 5). They were acquired in the late 1960s (H1 and H2), 1991 (H3) and 2007 (H4). The available log data and sampled depths are very uneven, and although they reach the target depths, there is an important lack of data in the upper part of the main logs.

A correlation between the well lithologies and the seismic reflections as accurate as possible is crucial for the interpretation of the seismic data. None of the four wells originally contained a complete sonic log: wells H1, H3 and H4 lack the first 400 m of sonic data, approximately; and well H2, a key well located nearby the expected crest of the Mesozoic structure, lacks it completely. Furthermore, check-shots in these wells were missing or unavailable. This made impossible a preliminary seismic to well tie of the data.

At the beginning of 2012 three new wells were drilled for monitoring shallow aquifers (GW1, GW2 and GW3, of 400 m, 400 m and 150 m depth, respectively) (Figs. 4a, 5). These wells provided information on the uppermost layers of the study area, which was especially useful for the incomplete logs. Firstly, a careful interpretation was performed in all the wells, resulting in the identification of 39 well-tops and 12 main levels from the Triassic up to the Cenozoic (Table 1). This interpretation consisted of the identification of stratigraphic intervals based on all available well-logs. Well-log correlation allowed a better and more accurate characterization of the stratigraphic intervals and delimitation of well-tops (Fig. 5). Prioritizing modern logs, we then calculated the sonic value averages for the 39 sections delimited by the main well-tops. This 1D velocity model was then used to complete the missing sonic log information, allowing a full depth-to-time domain conversion of the wells. With the aim of improving model characterization, we also calculated the average values for 4 additional main logs: gamma ray, deep resistivity, bulk density and neutron porosity (shale volume corrected) (Table 1). Unfortunately, the available density and porosity logs lack the first 400 m, and therefore they could not be completed. The domain conversion of the wells enabled an adequate interpretation of the seismic data. Besides, the data was used to elaborate a lithological and petrophysical prognosis of the injection area, which will be useful for the drilling operations (Fig. 6).

The well-log correlation showed a number of features that conditioned the subsequent seismic interpretation and modeling (Figs. 5 and 6). There were found remarkable thickness variations in the Dogger and Marly Lias sequences between H4 and H2 wells, which are located only 700 m away. The Dogger thickness variation could be caused by differential erosion, whereas the Marly Lias thickness variation was interpreted as associated with faulting, as discussed below. The H3 well, drilled right on top of a fault, shows a very complex sequence arrangement, cut by 2 main faults and with significant drilling mud losses along the Jurassic sequence.

The shallow, high velocity layer responsible for signal degradation (Alcalde et al., 2013a, 2013b) is clearly identifiable in the sonic logs of the GW wells. It has been interpreted as the uppermost layer of the Late Cretaceous (KS6, Fig. 6). It is a limestone layer with velocities up to 4500 m/s (Table 1). We believe that this, together with the underlying Utrillas low velocity layer (KU5, Fig. 6), is the main cause of seismic signal degradation (Alcalde et al., 2013a; 2013b). The available logs also allowed us to identify and locate the potential reservoirs and seals in the subsurface of Hontomín, according to their porosity and distribution properties (Table 1).

4. Seismic interpretation

A conventional approach to seismic data interpretation usually includes an appropriate seismic to well tie and the picking of the most interesting reflections through the dataset (e.g. McQuillin et al., 1984; Sheriff and Geldart, 1985; Sopher and Juhlin, 2013). In the Hontomín survey, however, the seismic dataset is characterized by a limited lateral continuity of the reflections, due to the strong influence of the shallow velocity inversion in the wave propagation (Alcalde et al., 2013b). This effect generates disappearances, splits and displacements of the reflections, making complicate or preventing the tracking of a single reflection through different sections. Hence, a different approach to the interpretation was designed (Fig. 3) to take advantage of the available datasets and bias the interpretation in the areas with sparse constrains. This approach begun with the generation of a conceptual 3D model, in which the general structure was outlined from the well-log correlation and regional studies, such as those included in Tavani et al. (2011), Quintà and Tavani (2012) and Tavani et al. (2013), and references therein. Special care was taken in the seismic to well tie. This step was very important due to the relative quality of the seismic dataset. The seismic interpretation process was then performed, using the conceptual model as a reference. The advances in the interpretation were progressively used to readjust the conceptual model and vice versa, in an iterative way. The final interpretation is a compromise between the seismic and well-log data and regional geology, which supplies in our opinion the best fit solution. However, we are aware that different approaches could provide another interpretation.

4.1. Seismic facies analysis

The subsurface is well imaged in the migrated volume from ~75 ms down to ~1350 ms of two-way travel-time (twt) (Figs. 7 and 8). The analysis of the seismic features allowed us to characterize up to 8 different seismic facies, named “A” to “I” from bottom to top (Figs. 7, 8 and 9a, b and c). These facies appear arranged in three domains. The lowermost domain (A and B), is characterized by a section of discontinuous, low amplitude reflections (A), enclosing a brighter set of parallel reflections (B). The A set ranges from 900 ms down to the lower limit of the image. The B set appears unevenly distributed, normally in blocks of less than 50 × 50 CDP and always below 1100 ms twt throughout the whole dataset. The second domain (C and D) shows a characteristic dome-shape structure. It begins with a 200 ms twt thick set of bright reflections (C). It is characterized by an increase of the lateral coherency with respect to the underlying domain, but the boundary between these first two domains is not neat. Set C is roofed by a discontinuous, high amplitude package (D) of approximately 120–200 ms. An abrupt vertical offset, along with an increment in the dip of sets C and D is observed at the NE of the H1 well (Fig. 7). The third domain (E–I) contains reflections dipping at a very low angle in the central and northern parts of the study area. A set of bright reflections (E) onlaps the D package in the northern edge of the study area. This E package ranges from 700 ms down to 900 ms twt, and gently dips towards the N–NE (<3°). This package is overlain by a plane-parallel set of reflections (F) that completely covers the E package and fossilizes the dome structure of the lower domains. The thickness of this package is approximately uniform (~200 ms) at the southern and central part of the cube, and constantly increases towards the north. Above the F set, a low amplitude, occasionally scattered set (G) is observed from 500 ms to the surface. It contains reflection packages with high amplitude and coherency (H) unevenly distributed. Finally, another high amplitude, coherent set (I) can be observed at the SE part of the seismic volume (Fig. 8a). This set is approximately 100 ms thick and displays an overall south-dipping attitude on the southern part of the seismic cube.

Age attribution to the described seismic facies was based on well-log data. The first domain includes the lowermost sets, A and B, and was interpreted to contain the basal Triassic and older rocks. The available

Please cite this article as: Alcalde, J., et al., 3D geological characterization of the Hontomín CO_2 storage site, Spain: Multidisciplinary approach from seismic, well-log and regional data, Tectonophysics (2014), http://dx.doi.org/10.1016/j.tecto.2014.04.025

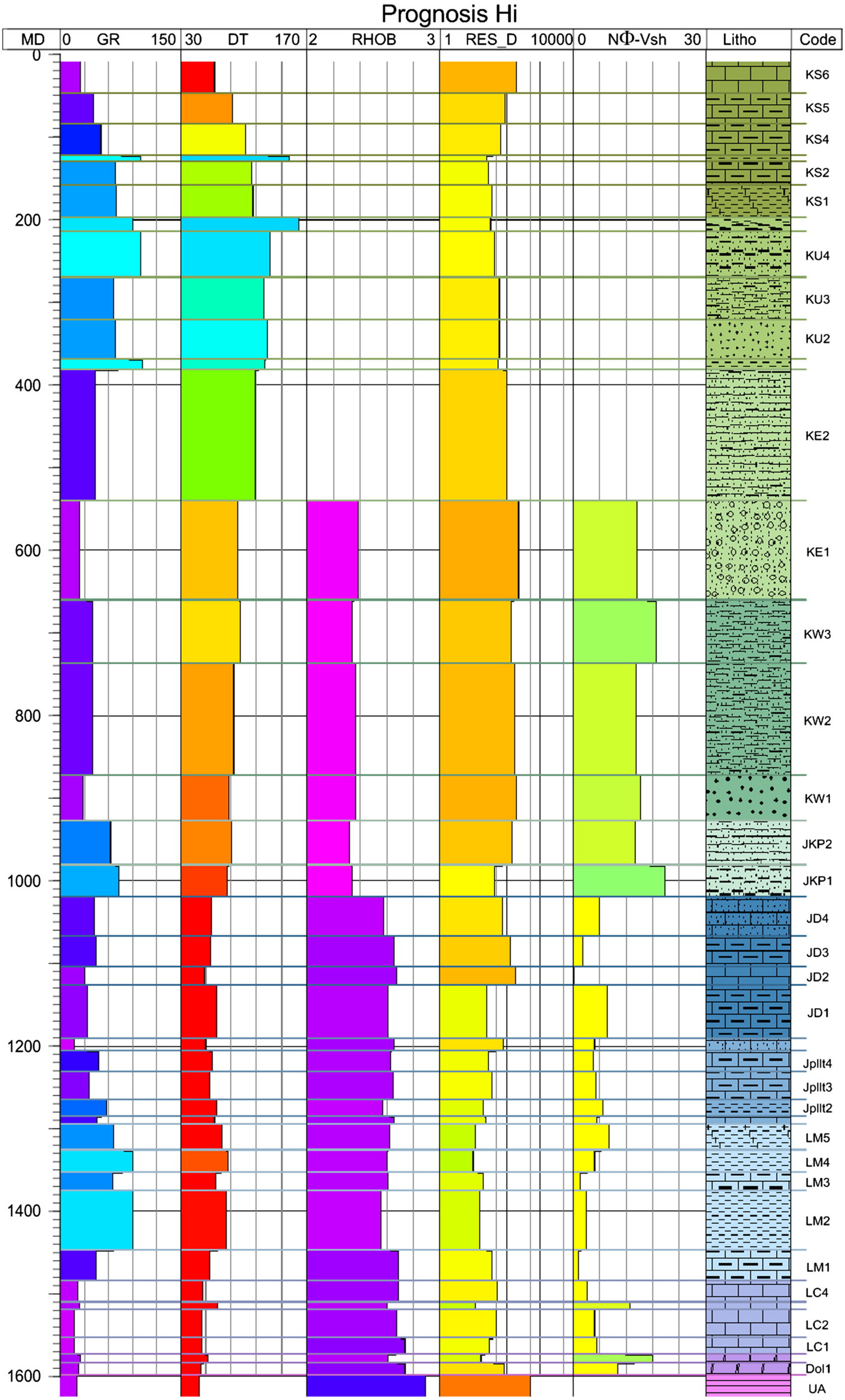
Prognosis Hi
MD
0
GR
150
30
DT
170
2
RHOB
3
1
RES_D
10000
0
NΦ-Vsh
30
Litho
Code
0
200
400
600
800
1000
1200
1400
1600
KS6
KS5
KS4
KS2
KS1
KU4
KU3
KU2
KE2
KE1
KW3
KW2
KW1
JKP2
JKP1
JD4
JD3
JD2
JD1
Jpllt4
Jpllt3
Jpllt2
LM5
LM4
LM3
LM2
LM1
LC4
LC2
LC1
Dol1
UA

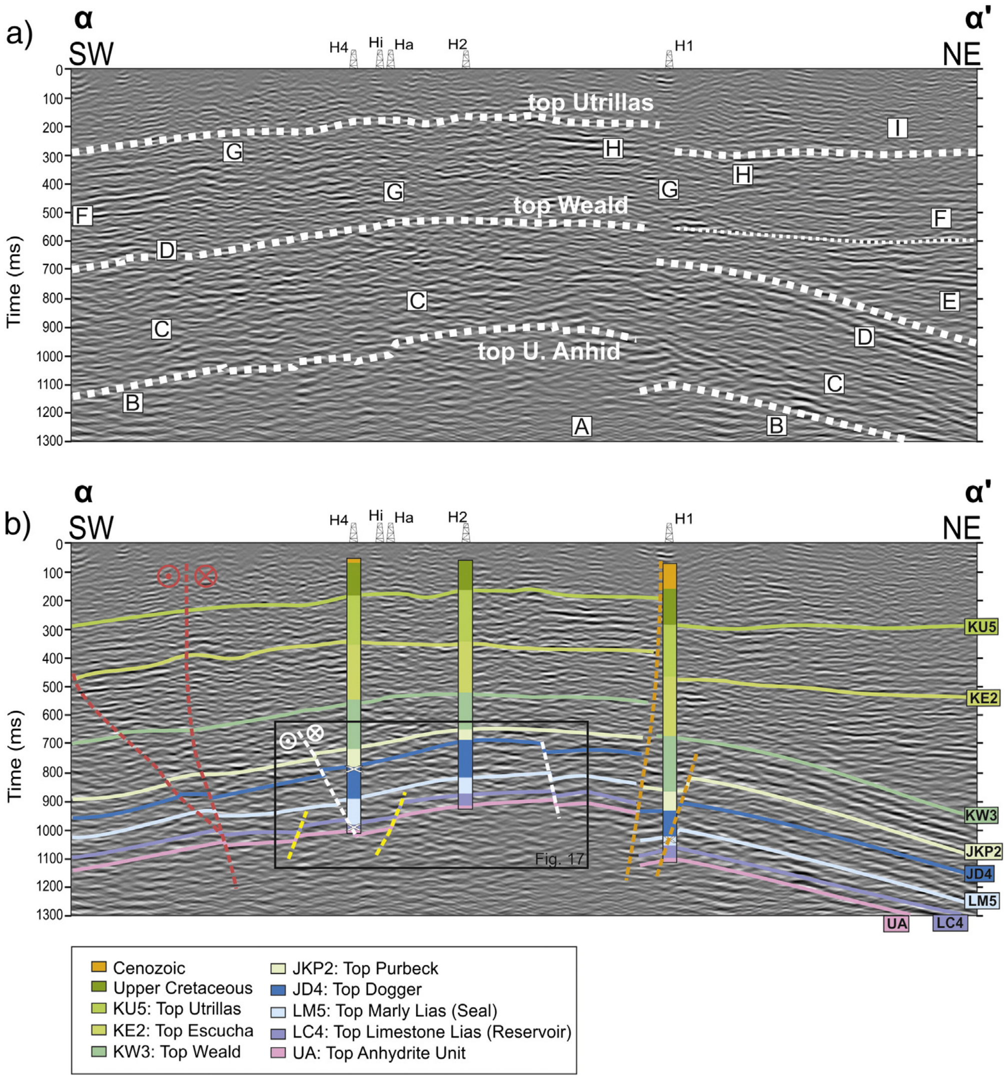

Fig. 7. First 1300 ms of the migrated section α–α′ (location marked in Fig. 3a) with (a) an analysis of the main seismic facies observed, and (b) the final interpretation of the main horizons (continuous lines) and faults (dashed lines). The well-tops from wells H4, H2 and H1 are included. The white crosses mark the well positions intersected by faults (from well-logs).

wells, however, do not reach these depths. Therefore, these data do not provide constraints for either the internal structure within the Triassic sediments, or the depth of the Palaeozoic basement. These Upper Triassic sediments are overlain by the second domain including Jurassic–Lower Cretaceous sediments. It is formed by facies C and D, and the target reservoir and seal formations should be found within this domain. The third domain contains the remainder of the Lower Cretaceous sequence at its bottom (facies E, F, the lower portion of facies G and facies H) and the Late Cretaceous and Cenozoic sediments (Upper part of facies G and facies I).

4.2. Seismic cube interpretation

To interpret the seismic cube, horizon picking was first performed in profiles “α” (Fig. 7b) and “β” (Fig. 8b), with approximate SW–NE and SE–NW orientations, respectively (Fig. 9d). They are the best constrained profiles in the seismic cube, crossing the oil exploration boreholes: profile α–α′ crosses wells H4, H2 and H1, and profile β–β′, wells H3 and H2. Within these two sections, 8 main layers were interpreted (Figs. 7b, 8b and Table 2), corresponding to the main units obtained from the well-log correlation (Fig. 5). The three lowermost horizons are of special interest from the point of view of the CO_2 injection site since they correspond to the base of the reservoir (top of the Anhydrite Unit, UA), the top of the reservoir (top of the Lias Limestone, LC4) and the top of the seal (top of the Marly Lias, LM5). Five additional overlying layers were also interpreted corresponding to the tops of Dogger, Purbeck, Weald, Escucha and Utrillas formations (JD4, JKP2, KW3, KE2 and KU5, respectively). The seismic interpretation was limited down to the anhydrite unit because of the low signal to noise ratio and the lack of well-log data below this level.

The interpreted α and β profiles were then used as reference for horizon picking following a grid of sections parallel to α and β with an approximate spacing of 250 m, to complete the entire dataset interpretation. This gridding distance, however, was intentionally kept variable, making it denser in the vicinity of conflictive areas (e.g. fault zones, low reflectivity zones, steep horizon changes, etc.).

Four types of faults were identified in the seismic cube. An overall scheme of them, with the labeling used during the interpretation can be found in Fig. 9d. The “S-faults” (S-1 to S-3, red dashed lines in Fig. 9d), are located in the southern portion of the study area. Faults S2 and S3 branch from fault S1 and they have a limited along-strike length, compared with the other faults having a similar orientation

Fig. 6. Lythological and petrophisical prognosis of the injection position (Hi). It includes well-log interpolations for GR, sonic, bulk density, neutron porosity (shale volume corrected), resistivity and lythology. Location of Hi in Fig. 3a; details of the variables and values in Table 1.

Please cite this article as: Alcalde, J., et al., 3D geological characterization of the Hontomín CO_2 storage site, Spain: Multidisciplinary approach from seismic, well-log and regional data, Tectonophysics (2014), http://dx.doi.org/10.1016/j.tecto.2014.04.025

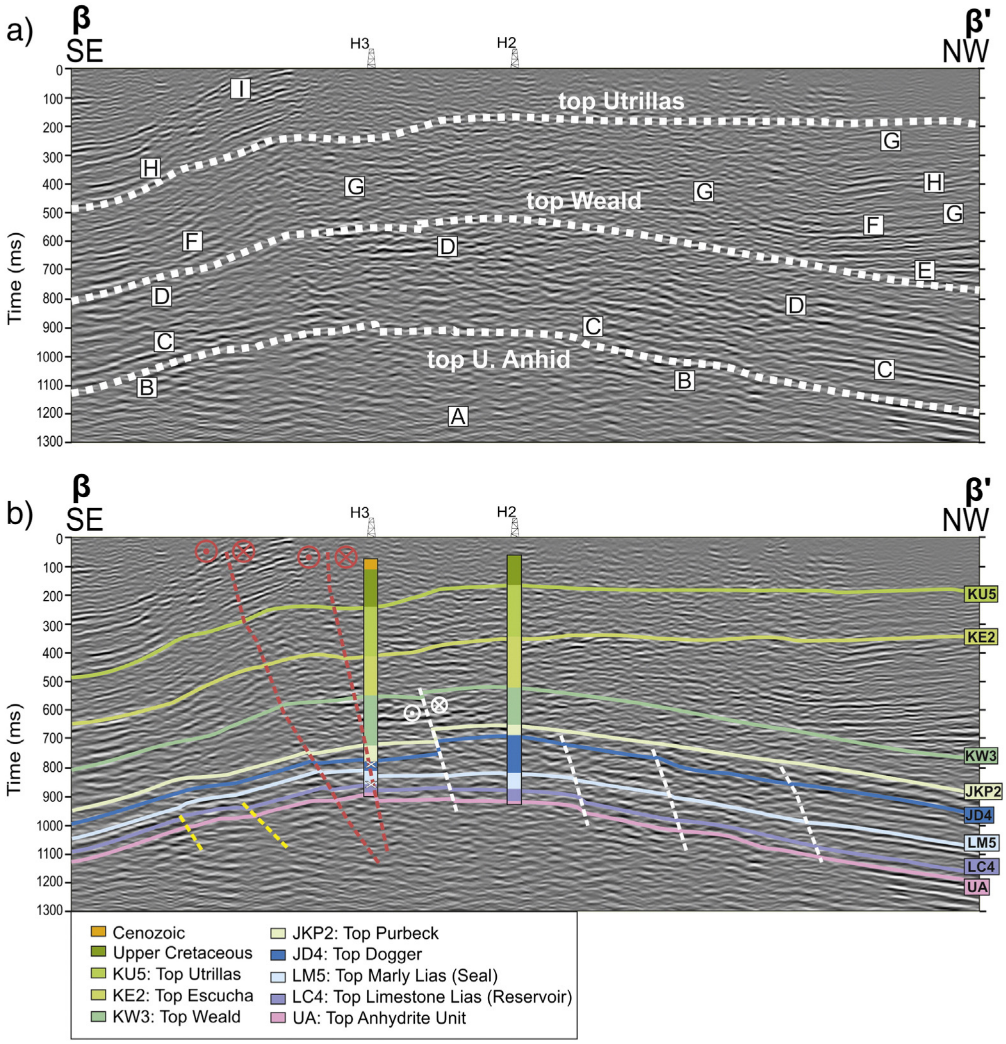

Fig. 8. First 1300 ms of the migrated section β–β′ (location marked in Fig. 4a) with (a) an analysis of the main seismic facies observed, and (b) the final interpretation of the main horizons (continuous lines) and faults (dashed lines). The well-tops from wells H3 and H2 are included. The white crosses mark the well positions intersected by faults (from well-logs).

(i.e. faults N-1 to N-5). This, coupled with the well-known strike-slip kinematics of fault S1 (that is a splay of the Ubierna right-lateral fault) (Quintà and Tavani, 2012; Tavani et al., 2011), indicates a flower-like assemblage associated with the strike-slip movement of the Ubierna fault. The kinematics of these faults is recorded by wells H3 and H2. These wells show thicker Jurassic–Lower Cretaceous successions (UA-JKP2) on the NW than on the SE fault block, suggesting downward displacement of the northern block during the deposition of these units (Fig. 8). Besides, the JKP2–KW3 interval is thicker in H3 than in H2 and the interval KW3–KU5 shows roughly similar thicknesses on both wells and the Cenozoic succession is about 35 m thick in H3, whereas it is not present in H2. Finally, the KE2–Cenozoic interval is ~110 m higher on the NW wall of these faults, indicating a late uplift of this wall. The “E-faults” (E-1 and E-2, orange dashed lines in Fig. 9d) are located in the eastern portion. Vertical motions along this fault are nicely constraint by wells H1 and H2 on both limbs of this structure. The lower part of the section, from UA to KW3 (Fig. 7), is characterized by a thicker succession on the SW than on the NE wall, indicating a downward displacement of the SW wall during the Jurassic. Besides, the intermediate part (from KW3 to KU5) shows rather homogeneous thicknesses on wells H1 and H2, although the well-tops are about ~170 m shallower on the SW than on the NE of the fault, which indicates a post-depositional uplift of the SW fault wall. Finally, the Cenozoic succession is much thicker in well H1. However, since the top of this succession is eroded in H2, time relationship between fault activity and the sedimentation of this unit cannot be established with the available data (Fig. 7b). The “N-faults” (N-1 to N-5, white dashed lines in Fig. 9d) are small scale E–W striking and N-dipping normal faults located in the central, northern and western part of the study area. The “X faults” (X-1 to X-6, yellow dashed lines in Fig. 9d) are small scale normal faults placed perpendicularly to the N-faults. Finally, two sets of small scale faults located at the eastern edge of the study area were identified (XE and XS, yellow dashed lines in Fig. 9d). They both lie near the limits of the seismic dataset resolution and far away from well constraints, and therefore the information about their nature and offset cannot be anticipated. However, they show similarities in orientation and development with the X faults, and therefore they have been considered as possible members of this group.

The final interpretation result is an 8-layered, 3D geological model of the entire study volume (Fig. 10 and supplementary material SM1). The depth conversion was performed using the 8-layered velocity model derived from the well-log correlation (Fig. 5). It is a noticeable division of the study area in three blocks delimited by the two major faults, S-1 and E-1 (hereafter “Southern Fault” and “Eastern Fault”, respectively): the Eastern, the Central and the Southern-block (Fig. 9d). This division is observed in all the interpreted layers (Fig. 10 and supplementary material SM1). Table 2 summarizes the details of heights and thicknesses of all the modeled layers. We will now focus on the four layers that condense the overall underground structure: UA, JD4, KW3 and KU5 (Figs. 11, 12, 13 and 14, respectively). Note that all the depth values

Please cite this article as: Alcalde, J., et al., 3D geological characterization of the Hontomín CO_2 storage site, Spain: Multidisciplinary approach from seismic, well-log and regional data, Tectonophysics (2014), http://dx.doi.org/10.1016/j.tecto.2014.04.025

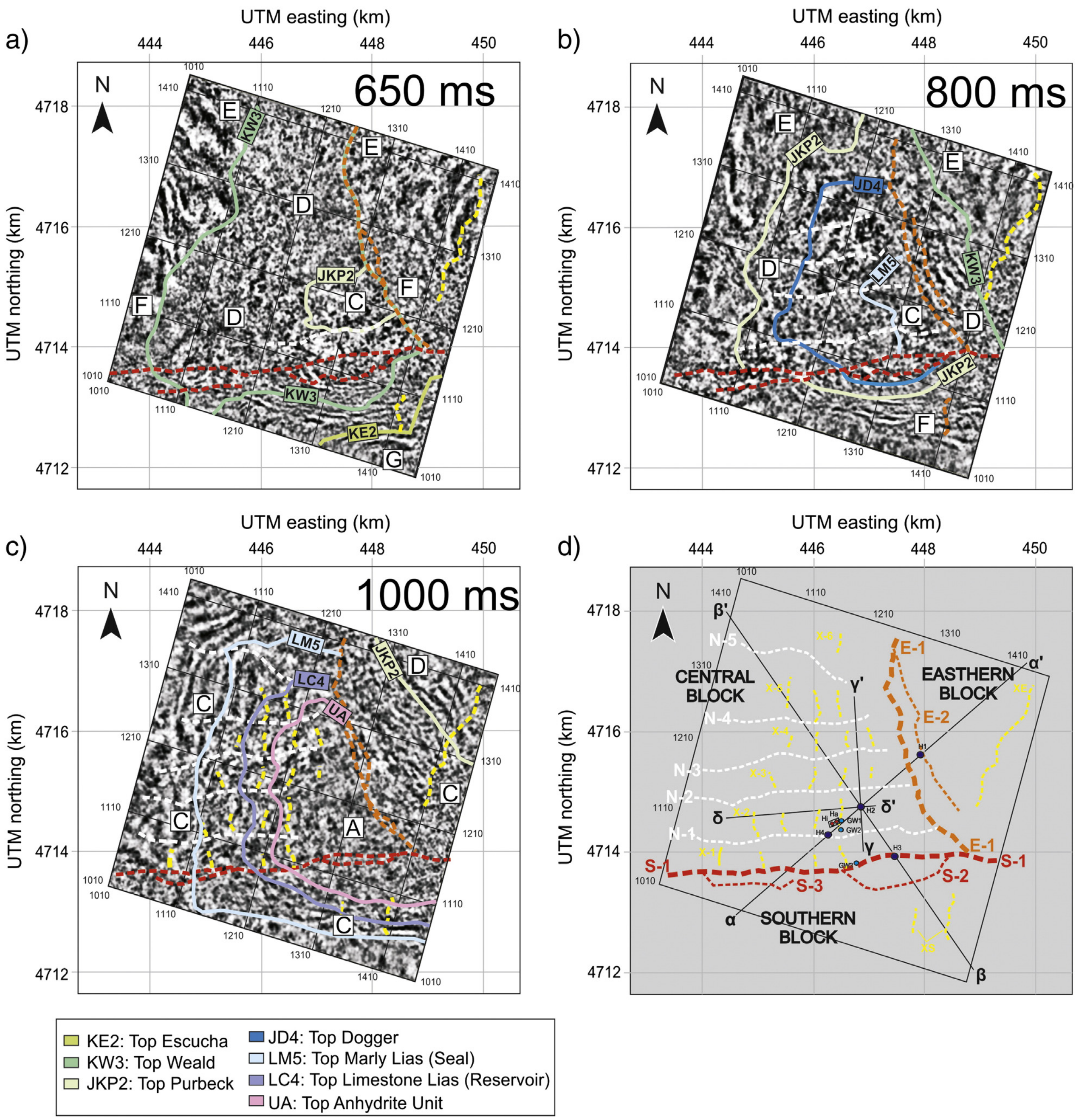

Fig. 9. Time slices with the main horizons (continuous lines) and fault distribution (dashed lines) interpreted at (a) 650 ms; (b) 800 ms; and (c) 1000 ms twt; and (d) general distribution and labeling of the main faults interpreted in the study area. The position of profiles α–α′, β–β′, γ–γ′, δ–δ′ and of the wells is shown.

indicated in this work are given in meters relative to mean sea level (msl). The UA layer (Fig. 11) ranges from −1085 m to −232 m msl. It defines the top of the Triassic units and the core of the overlying Jurassic structure. It is thoroughly affected by all the described faults (S-, E-, N-, and X faults), and the result is a staggered shape, especially in the Central-block. In UA, the Central-, Eastern-, and Southern-blocks dip

Table 2
Main position values for the 8 layers interpreted. *: Relative to sea level, in meters.

Layer	Maximum depth*	Minimum depth*	Mean value*	Average layer thickness
KU5	+191 m	+822 m	+631 m	194 m
KE2	+14 m	+706 m	+482 m	410 m
KW3	−384 m	+328 m	+72 m	364 m
JKP2	−656 m	+120 m	−185 m	108 m
JD4	−773 m	+52 m	−293 m	209 m
LM5	−976 m	−128 m	−494 m	129.5 m
LC4	−1032 m	−195 m	−627 m	80.19 m
UA	−1085 m	−232 m	−703 m	–

Please cite this article as: Alcalde, J., et al., 3D geological characterization of the Hontomín CO_2 storage site, Spain: Multidisciplinary approach from seismic, well-log and regional data, Tectonophysics (2014), http://dx.doi.org/10.1016/j.tecto.2014.04.025

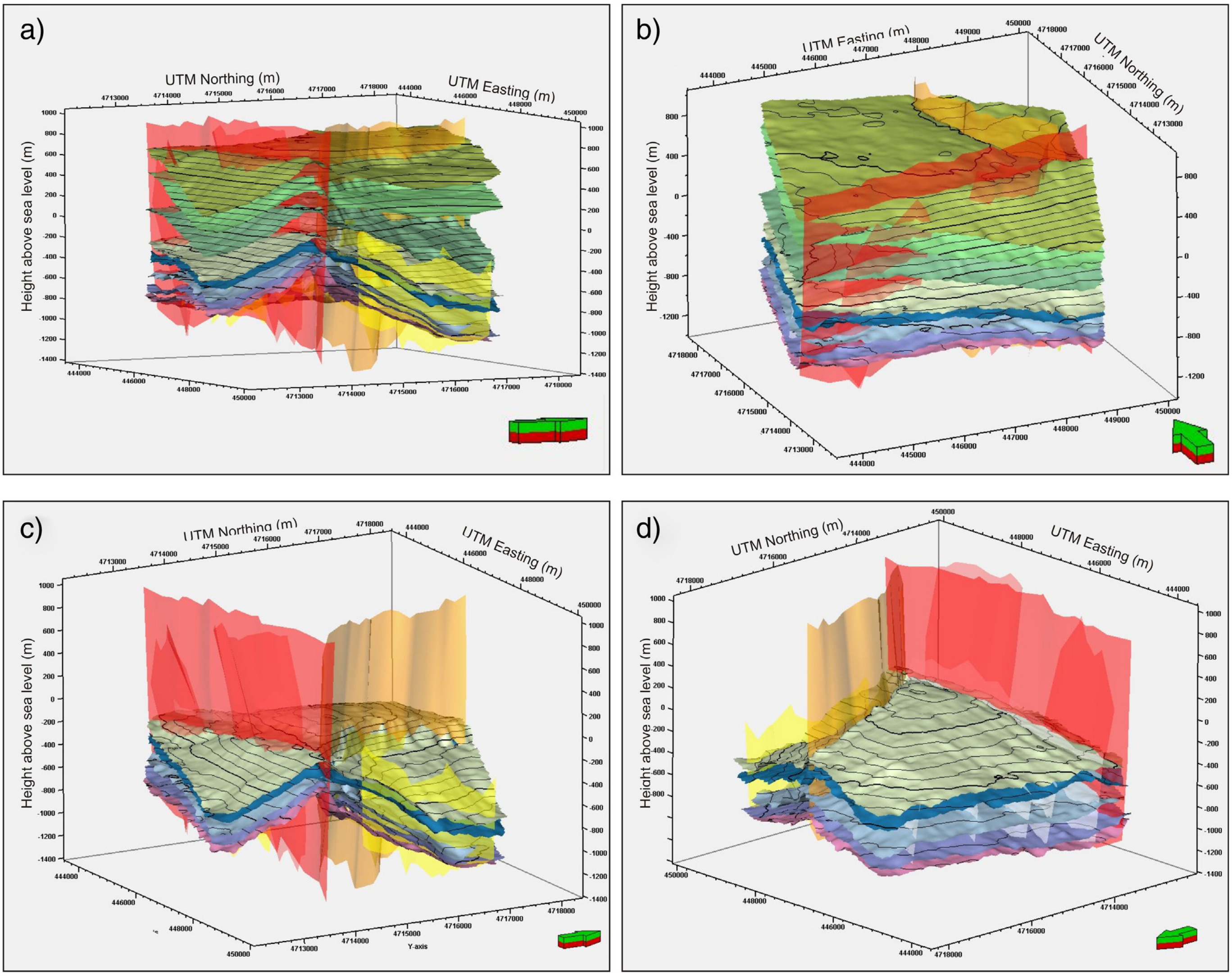

Fig. 10. 3D visualization of the resulting 8-layered geological model (a and b) and detail of the target dome structure (Jurassic) (c and d).

towards the NE (~5–18°), NW (~8–25°) and SSW (~5–30°), respectively. The crest of the dome is located near the junction of the South- and East faults. The JD4 (Fig. 12) depth ranges from −773 m to +52 m msl. It is the last purely Jurassic layer, and utterly delineates the Jurassic dome-like geometry. It is important to remark on the steep vertical offset (up to 140 m) of JD4 across N-1 fault. This offset has a reverse displacement, in clear disagreement with the rest of the N-faults that have a normal displacement. In this layer, the crest of the dome is located near the H2 well, 2 km to the NE of the culmination of the underlying UA layer. The KW3 layer (Fig. 13) ranges from −384 to 328 m msl. It is only affected by S- and E-faults, and presents an intermediate geometry between the Jurassic and the Cretaceous structure. This geometry is characterized by a reduction in the dips of the Eastern- (~5–20°) and more especially Central-block (~0–8°). On the contrary, the Southern-block increases its dip to 15–30°. The crest of the dome has a small displacement to the N with respect to the underlying JD4, and shows a plateau-like shape. The KU5 (Fig. 14) is theuppermost interpreted layer; it ranges from 191 m to 822 m msl. It still shows a gentle dome structure, which covers the Central-block, and displays clear structural steps associated with the Eastern and Southern faults. The Eastern-block lays about 150 deeper than the Central-block and reduces its dip to 2–10°, while the Southern-block defines a monocline dipping fairly constantly 30–35° to the SW.

5. Discussion

5.1. Conceptual modeling and fault timing

The quality of the seismic volume together with the relative geological complexity of the study area prevented a conventional straightforward horizon picking during the interpretation stage. This presents a major practical problem, because the interpretations are not unique. To address this problem, a reference model was set up by using well-log and seismic data complemented with surface and regional geology as starting points. Certain tectono-sedimentary events were inferred by studying the thickness differences between the 39 interpreted well-tops (Table 1). The criteria used to date these events were based on the distribution of thickness variations for a given interval. When thickness variations were observed along a set of successive formations, these were interpreted as recording an event of differential vertical motions, which given the short distance between wells was assumed to correspond to faulting. Besides, when thickness variation was observed on a single formation, differential erosion was envisaged. These events were checked and correlated with the events outlined in regional works carried out in the study area (e.g., García-Mondéjar, 1996; Quintà and Tavani, 2012; Serrano and Martinez del Olmo, 1990; Tavani and Muñoz, 2012; Tavani et al., 2011, 2013).

Please cite this article as: Alcalde, J., et al., 3D geological characterization of the Hontomín CO_2 storage site, Spain: Multidisciplinary approach from seismic, well-log and regional data, Tectonophysics (2014), http://dx.doi.org/10.1016/j.tecto.2014.04.025

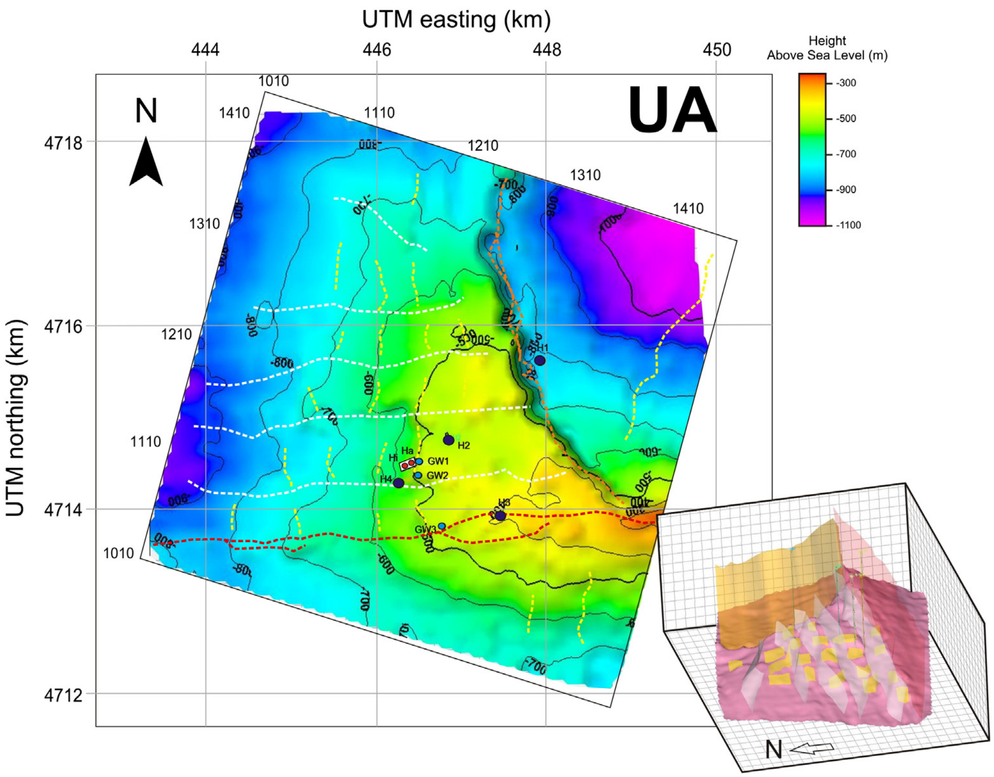

Fig. 11. Depth map and 3D perspective view of the interpreted UA layer (top of the Anhydrite Unit). The dashed lines in the map represent the faults affecting this layer (description and labeling in Fig. 9d).

Significant thickness variations were observed within the Liassic (Limestone and Marly) sediments. The α profile (Fig. 7) shows a significant discrepancy in thicknesses between the H4 and H2 wells at the Limestone and Marly Lias levels (Limestone Lias in H2 is twice as thick as in H4). A mud loss, reported in the H4 drilling report in the middle of this level was matched in the seismic volume with the E–W oriented,

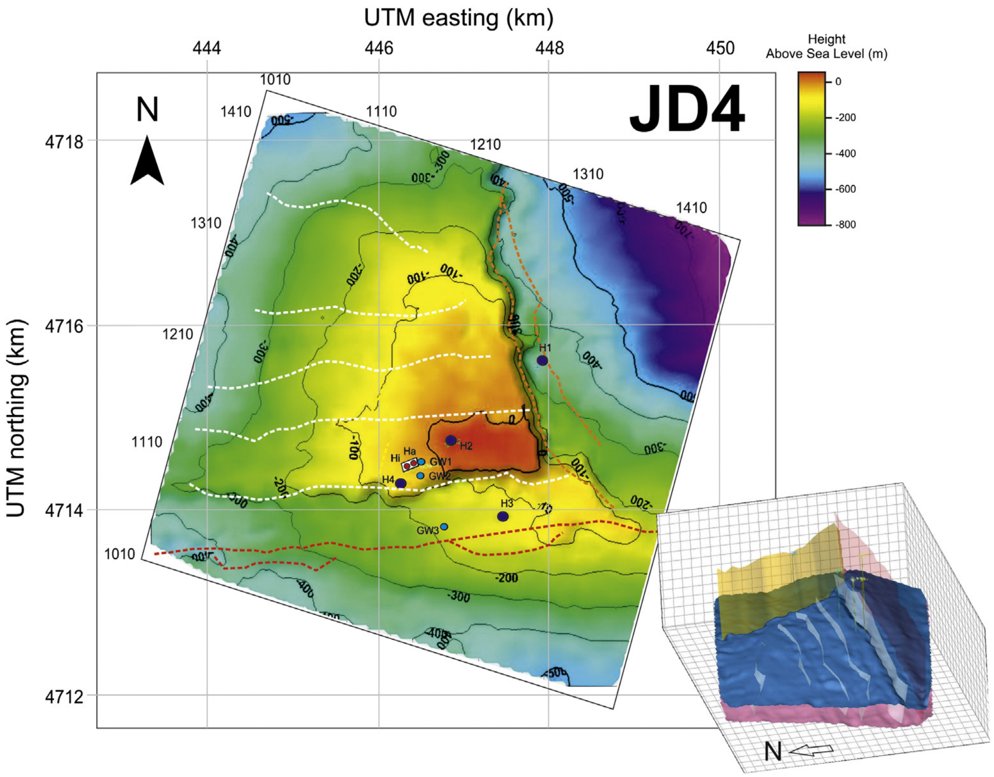

Fig. 12. Depth map and 3D perspective view of the interpreted JD4 layer (top of the Dogger Unit). The dashed lines in the map represent the faults affecting this layer (description and labeling in Fig. 9d).

Please cite this article as: Alcalde, J., et al., 3D geological characterization of the Hontomín CO_2 storage site, Spain: Multidisciplinary approach from seismic, well-log and regional data, Tectonophysics (2014), http://dx.doi.org/10.1016/j.tecto.2014.04.025

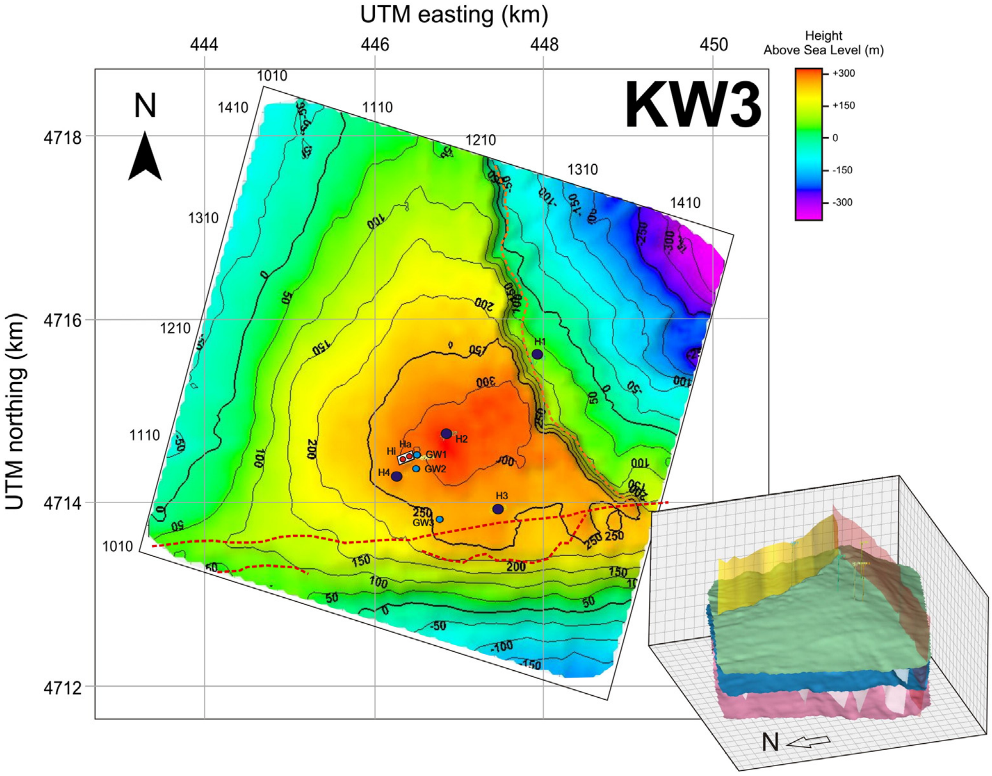

Fig. 13. Depth map and 3D perspective view of the interpreted KW3 layer (top of the Weald Unit). The dashed lines in the map represent the faults affecting this layer (description and labeling in Fig. 9d).

N-dipping “N-1” fault (Fig. 7b). Several parallel faults with similar characteristics (set N) have been identified, which are fossilized by the top of the Purbeck sediments and separating blocks with varying thicknesses of the underlying Jurassic succession (Figs, 9d and 15a). These thickness variations suggest that faults of set N were active during the Late Jurassic. Fault N1, however, shows a thicker Weald succession on the

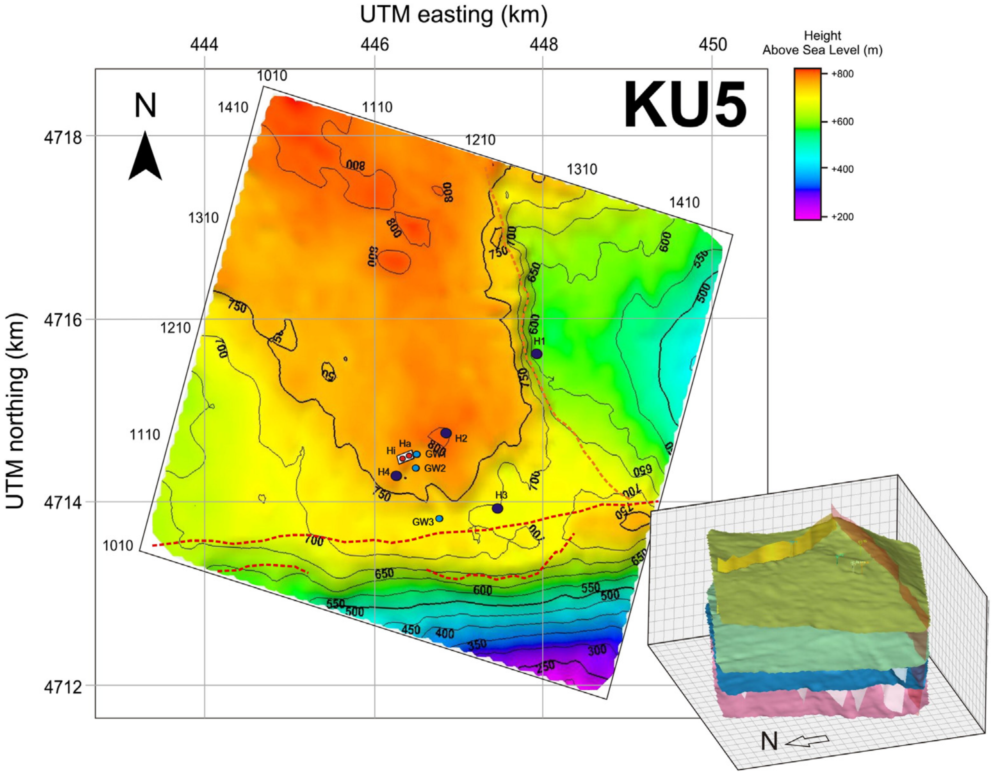

Fig. 14. Depth map and 3D perspective view of the interpreted KU5 layer (top of the Utrillas Unit). The dashed lines in the map represent the faults affecting this layer (description and labeling in Fig. 9d).

Please cite this article as: Alcalde, J., et al., 3D geological characterization of the Hontomín CO_2 storage site, Spain: Multidisciplinary approach from seismic, well-log and regional data, Tectonophysics (2014), http://dx.doi.org/10.1016/j.tecto.2014.04.025

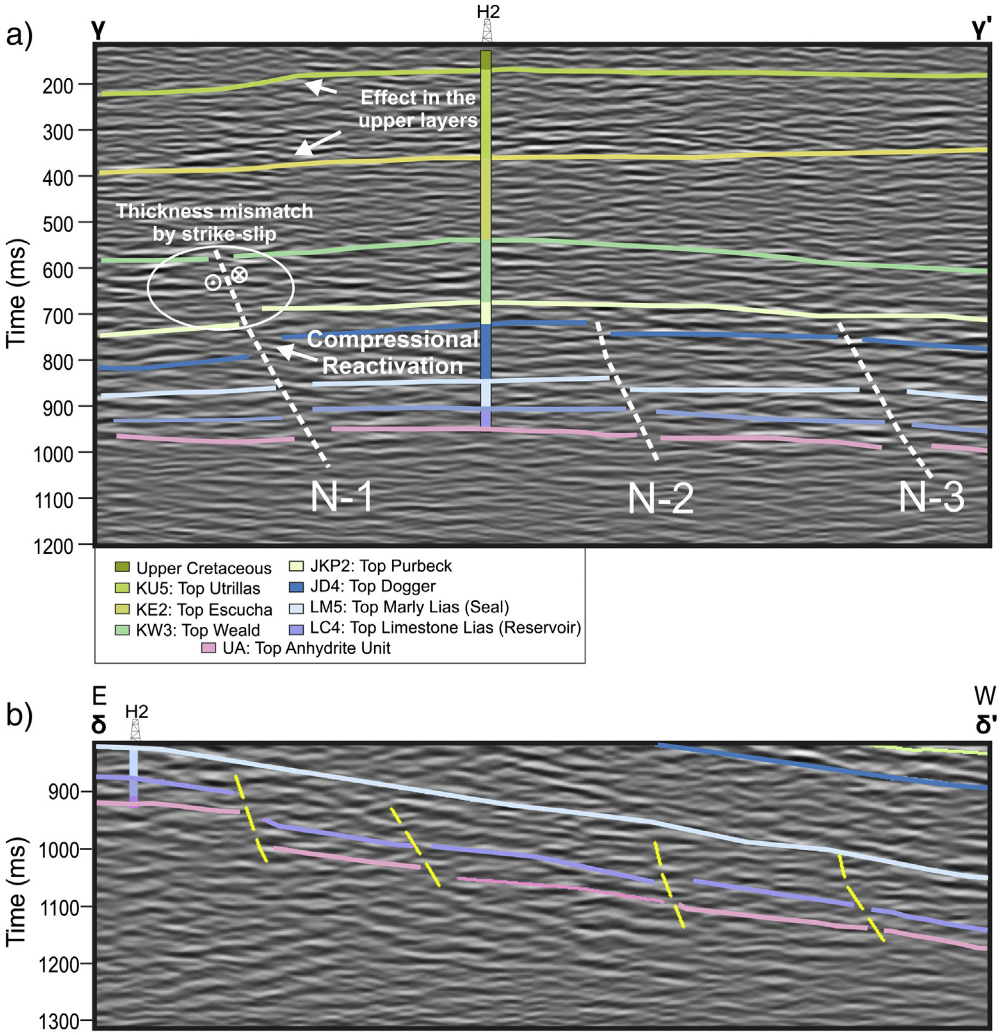

Fig. 15. Portion of profiles a) δ–δ′ and b) γ–γ′ with the final interpretation of the main horizons (continuous lines) and the detail of the geometry of set X- (yellow dashed lines in a) and N-faults (white dashed lines in b).

southern than on the northern wall, recording that vertical movements on both sides of this fault extended in time for a longer period than in the remaining faults of set N. The implications of this change in thickness are discussed below.

Fig. 15a shows a portion of profile γ–γ′ in which a detail of the geometry and activity of set N is observed. Set N faults are much more developed than Set X faults, which results in a significant structural step, with a drop of ~250 m of the Central-block with respect to the Southern-Block (Fig. 12). The Marly Lias presents an opposite pattern in terms of thickness: it is 190 m thick in H4 and only 110 m thick in H2. This difference in thicknesses within the relatively short distance between H4 and H2 wells (715 m approximately) suggests the occurrence of an extensional fault that explains the differential sedimentation. This extensional fault was observed as dipping to the S, with an E–W orientation (yellow dashed line in Fig. 7b), and was later identified as a set X fault. This X-fault pattern (small vertical offset, with same orientation and dip) was observed in the entire volume in disconnected faults affecting sediments up to the Marly Lias (Fig. 15b). Thickness variations of the lower part of the Marly Lias succession across set X faults, record their activity during the Late Sinemurian–Pliensbachian. Moreover, there is no seismic evidence of movements of these faults after the sedimentation of the Marly Lias.

The β profile (Fig. 8) also shows a difference in thicknesses between H3 and H2 in the Lias levels. Since H3 well is reported to be located just on top of the Southern fault, we believe that thickness reduction in this well is actually the effect of this fault.

Thickness variations across the Southern and Eastern faults suggest a multistage evolution of these structures. Whereas changes in thickness of the lower part record higher subsidence of the Central-block with respect to the Eastern- and Southern-blocks, seismic, well and surface data indicate that the Central-block is currently structurally higher than the bounding blocks. We interpret these characteristics as indicating that the Eastern and Southern faults acted as normal faults during the Mesozoic and were later inverted as high angle lateral-reverse faults during the Cenozoic compressional stage. However, the exposure level of the Central-block below the Cenozoic horizon does not permit a more accurate age constraint for the timing of fault inversion. The attitude of these faults in the Jurassic interval, suggests that the Southern fault was part of Set N, whereas the Eastern fault was part of set X.

5.2. Geological evolution of the Hontomín area

The analysis of the seismic facies helped constraining the conceptual model of the evolution of the Hontomín area. The final conceptual model used in the interpretation (Fig. 16-2 and 16-3) includes two main regional deformation stages. The first one occurred during the main Late Jurassic–Early Cretaceous extensional stage (e.g. Tavani and

Please cite this article as: Alcalde, J., et al., 3D geological characterization of the Hontomín CO_2 storage site, Spain: Multidisciplinary approach from seismic, well-log and regional data, Tectonophysics (2014), http://dx.doi.org/10.1016/j.tecto.2014.04.025

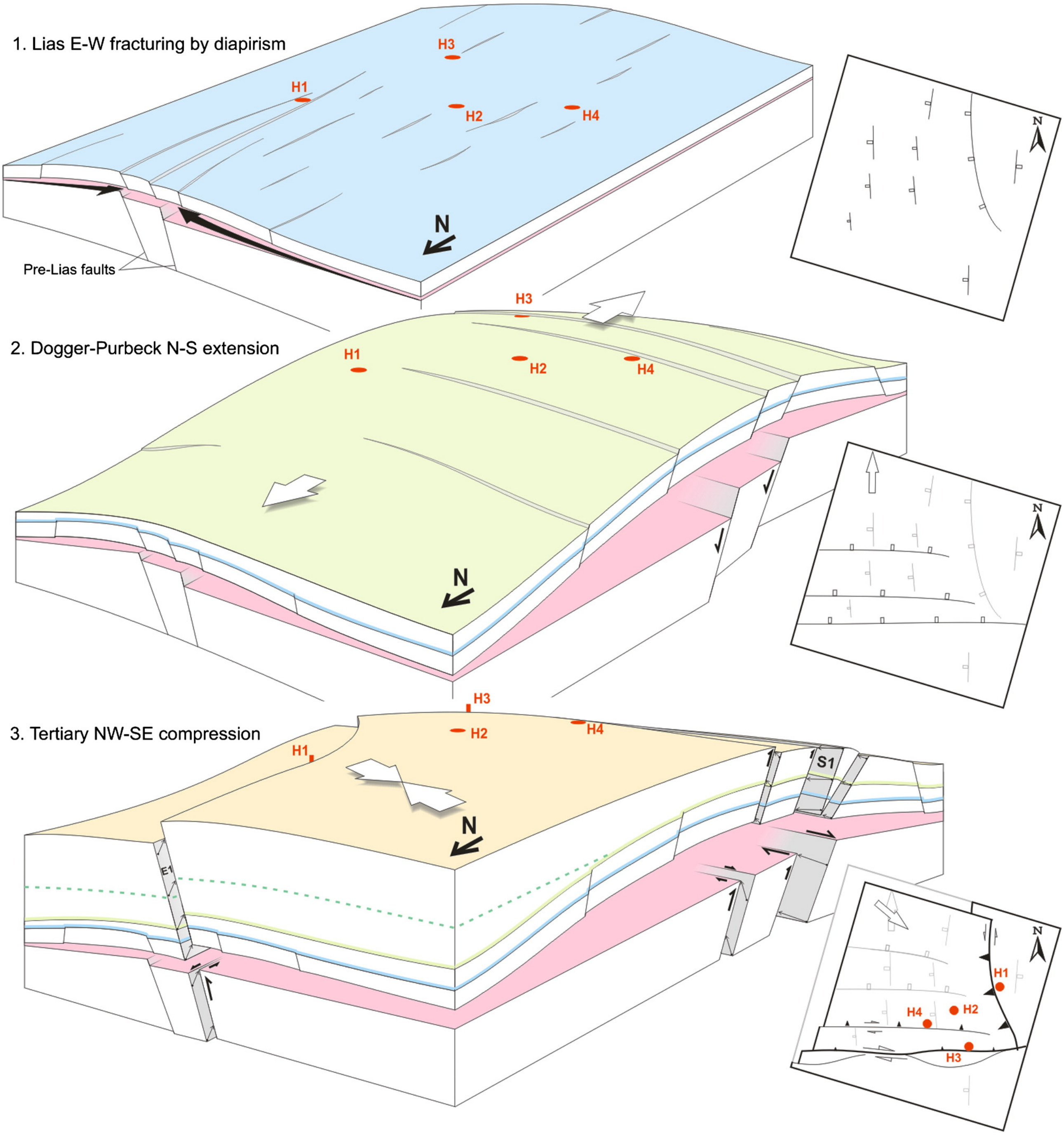

Fig. 16. The sequence of the three main geological events for the zone. Pink color represents the Keuper detachment level. 1) E–W Triassic evaporites migration during deposition of Marly Lias produces a slight accommodation folding of the Trias-Lias cover and poor development if normal faults, shaping a N–S oriented anticline. 2) N–S extension during deposition of Purbeck produces faulting on the basement and covers and triggers N–S salt migration and shapes a dome-like structure. 3) NW–SE Cenozoic compression breaks the structure reactivating and inverting the mains east (E1) and south (S1) faults produces a wedge-thrusting of the NW block. The green dashed line represents a Cretaceous layer onlapping the dome-like structure.

Muñoz, 2012; Ziegler, 1989), and generated E–W trending normal faults. These faults probably triggered or amplified the migration of the Triassic materials towards the dome core and generated associated minor normal faulting affecting the Jurassic–Lower Cretaceous succession, as proposed by Tavani et al. (2013). The second stage of deformation corresponds to the Alpine Orogeny (Late Cretaceous–Cenozoic), which inverted some of the previous faults within a transpressive regime (Tavani and Muñoz, 2012; Tavani et al., 2013).

Surface geometries and fault configuration of the built geological model allow us to propose a geological evolution of the Hontomín dome, which can to some extent be integrated in the regional framework (Fig. 16). This local evolution model focuses on the structures with good age constrain based on exploration wells, and therefore will only refer to the Post-Triassic evolution of the Hontomín dome. In this model, we propose three main stages affecting the Hontomín structure, according to the identified fault systems (Fig. 16): (1) a local, small scale fracturing stage during Late Lias; (2) a regional fracturing stage during the Late Jurassic–Early Cretaceous extension; and (3) a regional tectonic shortening stage associated with fault inversion, occurring during the Alpine compressional stage.

Please cite this article as: Alcalde, J., et al., 3D geological characterization of the Hontomín CO_2 storage site, Spain: Multidisciplinary approach from seismic, well-log and regional data, Tectonophysics (2014), http://dx.doi.org/10.1016/j.tecto.2014.04.025

The Set X faults (Fig. 9d) were described as active during the Liassic period, being confined within the Marly Lias sediments. The overlying Pelletic Limestone unit's thickness is more or less the same in H4 and H2 wells, which suggests that faulting is held below this level. According to previous works, there is an absence of extensional events in the area between the Triassic and the Late Jurassic–Early Cretaceous rifting periods (e.g., García-Mondéjar, 1996; Quintà and Tavani, 2012; Tavani, 2012; Tavani et al., 2013; Ziegler, 1989). A possible origin for these normal faults is that they are associated with normal faults in the basement, originated during the Triassic rifting. These Triassic basement normal faults could produce halokinetic processes associated with differential loading, related to the contrast in thicknesses of the Triassic evaporite sediments on both walls of the basement faults. The salt migration could produce a gentle dome growth and generate normal faults on the flanks (Fig. 16-1). The East fault was probably originated during this stage, either as an important normal fault or, most probably, as a set of aligned N–S faults, which eventually merged during a later reactivation. Although available non-migrated data below 1.5 s supply some local evidences of faulting at the basement level below the eastern fault, a detailed and accurate geophysical study including the processing of the lower interval of the acquired seismic cube would be necessary for a better comprehension the basement structure. This would enhance the validation of the halokinetic origin of the Set X faults.

A regional extensional period occurred during the Late Jurassic–Early Cretaceous (Fig. 16-2). During this stage, the E–W north-dipping faults of Set N (Fig. 9d) were formed. Set N is fossilized by the upper Purbeck beds, with the exception of N-1, which as mentioned above was apparently active during the deposition of the Weald materials. Paradoxically, thickness variations of these materials across N-1 suggest a reverse activity of this fault during this period. Possible explanations could be a local inversion related to underlying salt doming, thickness variations associated with strike-slip reactivation, the occurrence of an unidentified, south-dipping normal fault south of N1 or a wrong interpretation of the top Weald horizon. Finally, this fault was also reactivated in a later compressional stage.

During the Late Jurassic–Early Cretaceous extensional stage, the Hontomín dome started a major development by a forced fold mechanism generated by the WNW–ESE Ubierna Fault and the oblique NNE–SSW Hontomín Fault (Tavani et al., 2013). Another basement normal fault, W–E oriented in this case, forced the folding and the halokinetic growth of the Hontomín dome structure. The Southern Fault, which we attribute to this set, would have originally formed as several minor segments located above a structurally weak zone, which were subsequently merged. The combination of Set N development and salt accumulation below the dome crest is associated with block tilting and differential sedimentation and erosion, which would be the reason for the thickness variation of the Purbeck beds between wells H4 and H2 (Fig. 17).

The third deformation stage took place during the Alpine compression (Fig. 16-3). This stage is characterized by the inversion of previous structures, mostly focused on the Southern and Eastern faults. At a regional scale, this stage corresponds to the formation of the Ubierna Fault (Fig. 2), a right-lateral fault with reverse component located on the western part of the study zone (Tavani et al., 2011). The location of the Hontomín structure on the SE tip of the Ubierna fault resulted in a significant control by this fault on the final geometry of the Hontomín dome. As a consequence, the Southern fault was mostly inverted as a right-lateral strike-slip fault with a small vertical component, whereas the Eastern fault was mostly inverted as a reverse fault with a gentle left-lateral component (Fig. 16-3). The area near the fault N-1 was also reactivated during this process, although some of the resulting deformation was in the form of folding in the uppermost layers, as recorded by the fossilization of this fault by the Purbeck Fm. A slight buckling of the uppermost beds on top of this fault, records mild activity during the successive stages. During Alpine inversion the Triassic materials stacked against the Southern and Eastern faults, increasing the structural relief of the Dome, and the set X faults where passively rotated at the proximities of the main inverted faults. The inversion stage is recorded by the uppermost sediments, deposited during the Late Cretaceous–Cenozoic, defining a step of >450 m across the Southern and N-1 faults, and >250 m across the Eastern fault (Fig. 14).

5.3. Theoretical capacity calculation

Several formations have been identified as potential reservoirs and seals throughout the Hontomín site (Table 1). Within them, the Lias Limestone and the Marly Lias were respectively selected as the target reservoir and seal formations, according to Alcalde et al. (2013a). At the reservoir level, the crest of the dome structure is located near the H2 well. The position of the injection (HI) and monitoring (HA) wells (Fig. 4) was selected aiming to find the maximum gradient direction, which is contained approximately in the H4–H2 direction (Fig. 7; location in Figs. 4 and 9). This geometry will produce a faster migration of the injected CO_2, benefiting the monitoring experiments (Alcalde et al., 2013a).

The detailed 3D model anticipates the existence of an X-set fault between the injection and monitoring boreholes affecting the injection level (Fig. 18). This fault separates two zones suitable for CO_2 injection: one in the W side of the fault ("H4 block" hereafter) and one in the E side of the fault ("H2 block" hereafter) (Fig. 18). The average vertical offset of this fault is 130 m, higher than the total thickness of the reservoir

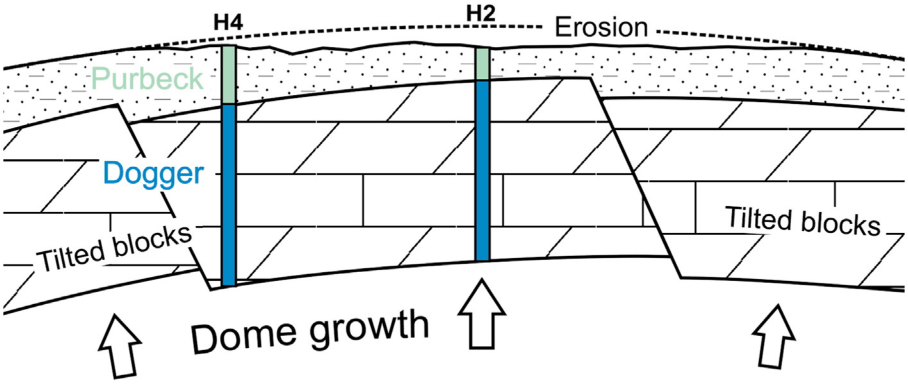

Fig. 17. Scheme of the tilting of the Dogger blocks forced by the normal faulting and the dome growth, and resultant differential sedimentation in the covering Purbeck layer (also observed in the well interpretations).

Please cite this article as: Alcalde, J., et al., 3D geological characterization of the Hontomín CO_2 storage site, Spain: Multidisciplinary approach from seismic, well-log and regional data, Tectonophysics (2014), http://dx.doi.org/10.1016/j.tecto.2014.04.025

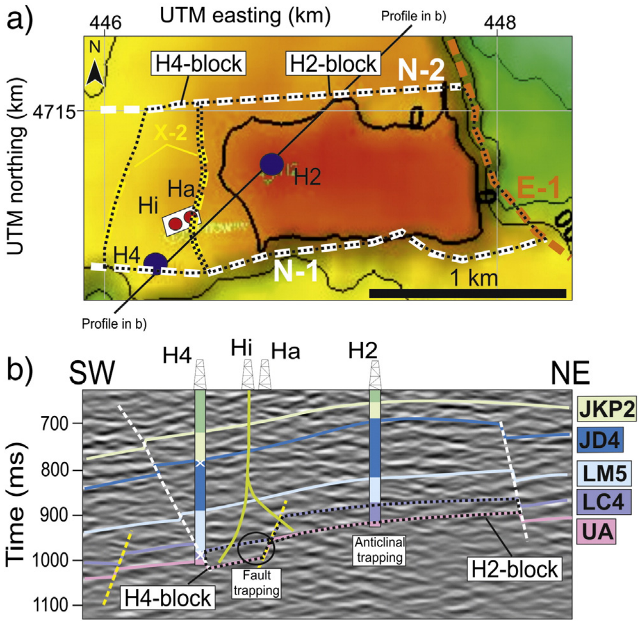

Fig. 18. a) Position of the two potential CO_2 reservoirs, the H4-block and H2-block, limited by N-1, N-2, E-1, and two X-2 faults at S, N, E and W, respectively. b) Zoom of the potential reservoirs with the two trapping mechanisms available: fault trapping for the H4-block and anticlinal trapping for the H2-block.

layer and therefore will compartmentalize the reservoir, forming a barrier to the pass of the injected CO_2 between the two blocks. These two potential reservoir blocks are furthermore delimited by the Eastern fault in the E, the N-1 and N-2 in the S and N respectively, and by another X-like fault in the W (Fig. 18a). Far from considering this compartmentalisation a problem, the presence of this fault adds an interesting challenge in terms of well design and monitoring capacity. By underground deviation of the injection well, the two blocks are accessible from the same position in surface. The H2 block is larger than block H4 (Fig. 18a). However, this does not necessarily mean that the H2 block is more suitable for holding the injection. The amount of CO_2 to be injected is also a fundamental factor in this issue. If only a few tones of CO_2 are to be injected (as is the case of an R&D demonstration plant), it may be of interest to inject CO_2 in a steep zone, which could accelerate the migration of the plume. This could speed up the physical and geochemical processes that take place in the reservoir and seal levels, from the early stages of injection, even with a reduced amount of CO_2 injected in a short period of time. Additionally, injection of CO_2 in block H4 would also supply assessment on the sealing capacity of the fault separating the blocks. The eventual arrival of the CO_2 plume to the monitoring borehole would allow inferring the porosity-permeability parameters of the fault, which can be used in further developments of the storage site.

We have made a broad estimation of the maximum storage capacity of the two blocks, in order to provide a primary evaluation of the two potential scenarios. The H4 block has a total area of $2.366 \cdot 10^6$ m^2. The H2 block's area is larger ($1.076 \cdot 10^7$ m^2), but its dip is slightly lower, which would affect the migration velocity of the CO_2 plume (Alcalde et al., 2013a, 2013b). The total volume of these two blocks ranges from $1.695 \cdot 10^7$ m^3 in the H4 block, to $9.275 \cdot 10^7$ m^3 in the H2 block. We have also calculated pore volume (PV) of the reservoir formation for the two blocks. Assuming an average formation porosity of 8.5%, obtained from the well-log data, the total PV are $9.94 \cdot 10^5$ m^3 for the H4 block reservoir, and $7.884 \cdot 10^6$ m^3 for the H2 block reservoir.

We have also calculated the maximum theoretical CO_2 storage capacity, assuming a short term storage, and thus considering only the existence of structural and stratigraphic trapping (Bachu et al., 2007; Welkenhuysen et al., 2013), as well as an isotropic distribution of the porosity. This maximum CO_2 storage capacity is calculated as a function of the available storage volume and the density of the CO_2 at the storage conditions:

$$M_{CO_2} = PV \times (1 - S_{wi}) \times \rho_{CO_2} \tag{1}$$

where M_{CO2} is the theoretical storage capacity (kg), PV is the total pore volume (m^3), S_{wi} is the irreducible water (brine in this case) saturation (0–1) and ρ_{CO2} is the density of CO_2 at reservoir conditions (kg/m^3).

The S_{wi} values are usually determined from drainage experiments, which are not yet available in Hontomín. Recent experiments determine that S_{wi} values derived from empirical relationships between porosity, permeability and water saturation (Schlumberger, 1989) are more imprecise and more optimistic compared to the experimental data (Bennion and Bachu, 2010; Torskaya et al., 2007). However, since the experimental data is also unavailable in Hontomín, we used the empirical relationships given in Schlumberger (1989) and calculated an approximate S_{wi} value of 0.123, using the porosity values as a reference. We calculated the ρ_{CO2} using the average temperature and pressure conditions at the target depth, obtained from H1 to H4 wells. By solving the equation of state formulated in Peng and Robinson (1976), the resulting ρ_{CO2} is 745.558 kg/m^3, at average reservoir conditions of 41 °C and 15.3 MPa. With these input values, the calculated maximum theoretical storage capacity is 0.65 Mt of CO_2 for the H4 block reservoir, and 5.2 Mt of CO_2 for the H2 block reservoir. Furthermore, the connectivity of both reservoirs would imply an increase of the overall M_{CO2}, which would be of 5.85 Mt of CO_2.

6. Conclusions

A geologically supervised interpretation is used to interpret the subsurface structure of the Hontomín dome. This approach is supported by a starting conceptual model that benefits from well-log correlation as first input, and is constrained by a detailed seismic facies analysis and the surface and regional geology This approach allowed detailed delineation of 8 surfaces from Jurassic to Cenozoic and 4 sets of faults, in spite of the limited resolution of a 3D reflection seismic dataset compromised by the existence of a shallow velocity inversion and a complex underground geology.

The geometry of the Hontomín structure is characterized by a central culmination with a continuous domal geometry towards the N and W, but bounded by two major faults in the S and E associated with vertical steps of >450 m and >250 m, respectively. Surface culminations are not vertically stacked and the dip of the dome flanks decreases upsequence, which suggests a protracted although discontinuous growth of the structure. Additionally, two sets of faults have been differentiated, which trend N and E and are associated with the main Southern and Eastern faults.

Detailed analysis of thickness variations across the Hontomín structure and especially across the main faults, allowed differentiating three main stages in the evolution of the dome. The first stage corresponds to the development of N-trending faults and is recorded by differential deposition of the lowermost Jurassic (Marly Lias) units. These faults could have been originated by salt movements produced by differential loading related to W–E oriented basement faults, originated in the Triassic rifting event. These movements could have produced a forced folding and the halokinetic growth of the Hontomín dome structure. The second stage corresponds to the development of the East-trending faults and is recorded by the deposition of the Purbeck deposits. This stage occurred within a regional extensional regime related to the opening of the Bay of Biscay, and is related to the migration of the Triassic materials towards the dome core, which enhanced its growth. The third and final stage occurred during the Pyrenean orogeny and was mainly characterised by the reactivation and inversion of the South and East faults and the further development of the domal structure, as recorded by the syn-kinematic Cenozoic sediments.

The 3D model of the Hontomín structure provides a challenging scenario for the testing of CO_2 storage. With a maximum theoretical CO_2 storage capacity of 5.85 Mt and the occurrence of early faults compartmentalising the reservoir, monitoring of the evolution of an injected CO_2 plume is expected to supply a high quality model of the behavior of CO_2 in fractured carbonate reservoirs to be used in the development of future CO_2 storage sites.

Supplementary data to this article can be found online at http://dx.doi.org/10.1016/j.tecto.2014.04.025.

Acknowledgments

The authors sincerely thank the Guest Editor Irina Artemieva and the two anonymous reviewers for their useful comments. Funding for this Project has been partially provided by the Spanish Ministry of Industry, Tourism and Trade, through the CIUDEN-CSIC-Inst. Jaume Almera agreement (ALM-09-027: Characterization, Development and Validation of Seismic Techniques applied to CO_2 Geological Storage Sites) and by the European Union through the Technology Demonstration Plant of Compostilla OXYCFB300 Project (European Energy Programme for Recovery). Additional support has been provided by Spanish Ministry of Education Science (CSD2006-00041), Generalitat de Catalunya (2009SGR006) and CSIC JAE-Doc postdoctoral research contract (E.S.). The sole responsibility of this publication lies with the authors. The European Union is not responsible for any use that may be made of the information contained herein. Juan Alcalde is being currently supported by the Fundación Ciudad de la Energía (CIUDEN) Research training program. The authors would like to sincerely thank Javier Elío for his kind help with the capacity estimation calculations, Institut Geològic de Catalunya for their useful work with the GWs, GEMODELS/UB and to all the people involved directly or indirectly in the elaboration of this work.

References

Alcalde, J., Martí, D., Calahorrano, A., Marzán, I., Ayarza, P., Carbonell, R., Juhlin, C., Pérez-Estaún, A., 2013a. Active seismic characterization experiments of the Hontomín research facility for geological storage of CO_2, Spain. Int. J. Greenhouse Gas Control 19, 785–795. http://dx.doi.org/10.1016/j.ijggc.2013.01.039.

Alcalde, J., Martí, D., Juhlin, C., Malehmir, A., Sopher, D., Saura, E., Marzán, I., Ayarza, P., Calahorrano, A., Pérez-Estaún, A., Carbonell, R., 2013b. 3-D reflection seismic imaging of the Hontomín structure in the Basque–Cantabrian Basin (Spain). Solid Earth 4, 481–496. http://dx.doi.org/10.5194/se-4-481-2013.

Arts, R., Brevik, I., Eiken, O., Sollie, R., Causse, E., Van Der Meer, B., 2001. Geophysical methods for monitoring marine aquifer CO_2 storage Sleipner experiences. Proceedings of the 5th International Conference on Greenhouse Gas Control Technologies. CSIRO Publishing.

Arts, R., Eiken, O., Chadwick, A., Zweigel, P., van der Meer, L., Zinszner, B., 2004. Monitoring of CO_2 injected at Sleipner using time-lapse seismic data. Energy 29 (9-10), 1383–1392.

Bachu, S., 2000. Sequestration of CO_2 in geological media: criteria and approach for site selection in response to climate change. Energy Convers. Manag. 41 (9), 953–970. http://dx.doi.org/10.1016/S0196-8904(99)00149-1 (1 June 2000).

Bachu, S., Gunter, W.D., Perkins, E.H., 1994. Aquifer disposal of CO_2: hydrodynamic and mineral trapping. Energy Convers. Manag. 35, 269–279.

Bachu, S., Bonijoli, D., Bradshaw, J., Burruss, R., Holloway, S., Christensen, N.P., Mathiassen, O.M., 2007. CO_2 storage capacity estimation: methodology and gaps. Int. J. Greenhouse Gas Control 1, 430–443.

Bennion, D.B., Bachu, S., 2010. Drainage and imbibition CO2/brine relative permeability curves at reservoir conditions for carbonate formations. SPE Paper 134028, SPE Annual Conference and Exhibition, Florence, Italy.

Canal, J., Delgado, J., Falcón, I., Yang, Q., Juncosa, R., Barrientos, V., 2013. Injection of CO_2-saturated water through a siliceous sandstone plug from the Hontomín Test Site (Spain): experiments and modeling. Environ. Sci. Technol. 47, 159–167.

Chadwick, A., Arts, R., Bernstone, C., May, F., Thibeau, S., Zweigel, P., 2006. Best practice for the storage of CO_2 in saline aquifers. Keyworth, Nottingham: British Geological Survey Occasional Publication, No. 14 978-0-85272-610-5.

Elío, J., Nisi, B., Ortega, M.F., Mazadiego, L.F., Vaselli, O., Grandia, F., 2013. CO2 soil flux baseline at the Technological Development Plant for CO2 Injection at Hontomin (Burgos, Spain), Int. J. Greenhouse Gas Control 18, 224–236.

Förster, A., Norden, B., Zinck-Jørgensen, K., Frykman, P., Kulenkampss, J., Spangerberg, E., Erzinger, J., Zimmer, M., Kopp, J., Borm, G., Julin, C., Cosma, C., Hurter, S., 2006. Baseline characterization of the CO2SINK geological storage site at Ketzin, Germany. Environ. Geosci. 13 (3), 145–161.

García-Mondéjar, J., 1996. Plate reconstruction of the Bay of Biscay. Geology 24, 635–638.

IPCC — Intergovernmental Panel on Climate Change, 2005. IPCC Special Report on Carbon Dioxide Capture and Storage. Cambridge University Press, Cambridge, UK pp. 195–276 (Chapter 5).

Ivanova, A., Kashubin, A., Juhojuntti, N., Kummerow, J., Henninges, J., Juhlin, C., Lüth, S., Ivandic, M., 2012. Monitoring and volumetric estimation of injected CO_2 using 4D seismic, petrophysical data, core measurements and well logging: a case study at Ketzin, Germany. Geophys. Prospect. 60, 957–973. http://dx.doi.org/10.1111/j.1365-2478.2012.01045.x.

Juhlin, C., Giese, R., Zinck-Jørgensen, K., Cosma, C., Kazemeini, H., Juhojuntti, N., Lüth, S., Norden, B., Förster, A., 2007. 3D baseline seismics at Ketzin, Germany: The CO2SINK project. Energy Procedia 1, 2029–2035.

Kenter, J.A.M., Bracco Gartner, G.L., Schlager, W., 2001. Seismic models of a mixed carbonate–siliciclastic shelf margin: Permian upper San Andres Formation, Last Chance Canyon, New Mexico. Geophysics 66 (6), 1744–1748.

Le Pichon, X., Sibuet, J.C., 1971. Western extension of boundary between European and Iberian plates during the Pyrenean orogeny. Earth Planet. Sci. Lett. 12, 83–88.

Lumley, D., 2010. 4D seismic monitoring of CO_2 sequestration. Lead. Edge (Tulsa, OK) 29 (2), 150–155.

Martí, D., Carbonell, R., Tryggvason, A., Escuder-Viruete, J., Pérez-Estaún, A., 2002. Mapping brittle fracture zones in three dimensions: High resolution traveltime seismic tomography in a granitic pluton. Geophys. J. Int. 149 (1), 95–105.

Martinez-Landa, L., Rötting, T., Carrera, J., Russian, A., Dentz, M., Cubillo, B., 2013. Use of hydraulic tests to identify the residual CO2saturation at a geological storage site. Int. J. Greenhouse Gas Control. http://dx.doi.org/10.1016/j.ijggc.2013.01.043.

Masaferro, J., Bourne, R., Jauffred, J., 2003. 3D visualization of carbonate reservoirs. Lead. Edge 22 (1), 18–25. http://dx.doi.org/10.1190/1.1542751.

McQuillin, R., Bacon, M., Barclay, W., 1984. An introduction to seismic interpretation: reflection seismics in petroleum exploration, Second edition. (287 pp.).

Montadert, L., de Charpal, O., Roberts, D., Guennoc, P., Sibuet, J.C., 1979. Northeast Atlantic passive continental margins: rifting and subsidence processes. In: Talwani, M., Hay, W., Ryan, W.B.F. (Eds.), Deep Drilling Results in the Atlantic Ocean: Continental Margins and Paleoenvironment. Maurice Ewing Ser., vol. 3. AGU, Washington, DC, pp. 154–186. http://dx.doi.org/10.1029/ME003p0154.

Nelson, R.A., 2001. Geologic Analysis of Naturally Fractured Reservoirs, Second edition. Gulf Professional Publishing, Woburn 9780884153177.

Ogaya, X., Ledo, J., Queralt, P., Marcuello, A., Quintà, A., 2013. First geoelectrical image of the subsurface of the Hontomín site (Spain) for CO_2geological storage: A magnetotelluric 2D characterization. Int. J. Greenhouse Gas Control 13, 168–179.

Peng, D.-Y., Robinson, D.B., 1976. A New Two-Constant Equation of State. Ind. Eng. Chem. Fundam. 15, 59–64.

Pérez-Estaún, A., Gómez, M., Carrera, J., 2009. El almacenamiento geológico de CO_2, una de las soluciones al efecto invernadero. Enseñanza Cienc. Tierra (17.2), 179–189.

Phipps, G.G., 1989. Exploring for dolomitized Slave Point carbonates in northeastern British Columbia. Geophysics 54 (7), 806–814.

Prado, Pérez J.A., Campos, R., Ruiz, C., Pelayo, M., Recreo, F., Lomba, L., Hurtado, A., Eguilior, S., Pérez, del Villar L., 2008. Almacenamiento geológico de CO_2: Selección de formaciones favorables. Comunicación técnica, Congreso Nacional del Medio Ambiente. Cumbre del Desarrollo Sostenible, Madrid.

Pujalte, V., Robles, S., García-Ramos, J.C., Hernández, J.M., 2004. El Malm-Barremiense no marinos de la Cordillera Cantábrica. In: Vera, J.A. (Ed.), Geología de España. SGE-IGME, Madrid, pp. 288–291.

Quesada, S., Robles, S., Rosales, I., 2005. Depositional architecture and transgressive–regressive cycles within Liassic backstepping carbonate ramps in the Basque–Cantabrian basin, northern Spain. J. Geol. Soc. 162 (3), 531–538.

Quintà, A., Tavani, S., 2012. The foreland deformation in the south-western Basque–Cantabrian Belt (Spain). Tectonophysics 576-577, 4–19.

Quintá, A., Tavani, S., Roca, E., 2012. Fracture pattern analysis as a tool for constraining the interaction between regional and diapir-related stress fields: Poza de la Sal Diapir (Basque Pyrenees, Spain). Geol. Soc. Lond., Spec. Publ. 363, 521–532. http://dx.doi.org/10.1144/SP363.25.

Rudolph, K.W., Schlager, W., Biddle, K.T., 1989. Seismic models of a carbonate foreslope-to-basin transition, Picco di Vallandro, Dolomite Alps, northern Italy. Geology (ISSN: 00917613) 17 (5), 453–456.

Schlumberger, 1989. Log interpretation Principles/Applications. Schlumberger Wireline & Testing, Sugar Land, Texas, USA.

Serrano, A., Martinez del Olmo, W., 1990. Tectonicasalina en el Dominio Cantabro–Navarro: evolucion,edad y origen de las estructuras salinas. In: Orti, F., Salvany, J.M. (Eds.), Formaciones evaporiticas dela Cuenca del Ebro y cadenas perifericas, y de lazona de Levante. Nuevas Aportaciones y GuiadeSuperficie. Empresa Nacional De Residuos RadiactivosS.A, ENRESA-GPPG, Barcelona, pp. 39–53.

Sheriff, R.E., Geldart, L.P., 1985. Exploration seismology. Data-processing and interpretation, vol. 2. Cambridge University Press, New York.

Sopher, D., Juhlin, C., 2013. Processing and Interpretation of vintage 2D marine seismic data from the outer Hanö Bay Area, Baltic Sea. J. Appl. Geophys. http://dx.doi.org/10.1016/j.jappgeo.2013.04.011.

Tavani, S., 2012. Plate kinematics in the Cantabrian domain of the Pyrenean orogen. Solid Earth 3, 265–292.

Tavani, S., Muñoz, J.A., 2012. Mesozoic rifting in the Basque–Cantabrian Basin (Spain): Inherited faults, transversal structures and stress perturbation. Terra Nova 24, 70–76.

Tavani, S., Quintà, A., Granado, P., 2011. Cenozoic right-lateral wrench tectonics in the Western Pyrenees (Spain): The Ubierna Fault System. Tectonophysics 509, 238–253.

Tavani, S., Carola, C., Granado, P., Quintà, A., Muñoz, J.A., 2013. Transpressive inversion of a Mesozoic extensional forced fold system with an intermediate décollement level in the Basque–Cantabrian Basin (Spain). Tectonics 32. http://dx.doi.org/10.1002/tect.20019.

Please cite this article as: Alcalde, J., et al., 3D geological characterization of the Hontomín CO_2 storage site, Spain: Multidisciplinary approach from seismic, well-log and regional data, Tectonophysics (2014), http://dx.doi.org/10.1016/j.tecto.2014.04.025

Torskaya, T., Jin, G., Torres-Verdin, C., 2007. Pore-level analysis of the relationship between porosity, irreducible water saturation, and permeability of clastic rocks. Proceedings — SPE Annual Technical Conference and Exhibition, 2, pp. 1331–1339.

Ugalde, A., Villaseñor, A., Gaite, B., Casquero, S., Martí, D., Calahorrano, A., Marzán, I., Carbonell, R., Estaún, A.P., 2013. Passive seismic monitoring of an experimental CO_2 geological storage site in Hontomín (Northern Spain). Seismol. Res. Lett. 84 (1), 75–84.

Vera, J.A., 2004. Geología de España. SGE-IGME, Madrid p. 890.

Vilamajó, E., Queralt, P., Ledo, J., Marcuello, A., 2013. Feasibility of Monitoring the Hontomín (Burgos, Spain) CO_2 Storage Site Using a Deep EM Source. Surv. Geophys. 34 (4), 441–461.

Von Hartmann, H., Buness, H., Krawczyk, C.M., Schulz, R., 2012. 3-D seismic analysis of a carbonate platform in the Molasse Basin — reef distribution and internal separation with seismic attributes. Tectonophysics 572-573, 16–25. http://dx.doi.org/10.1016/j.tecto.2012.06.033.

Welkenhuysen, K., Ramírez, A., Swennen, R., Piessens, K., 2013. Strategy for ranking potential CO_2 storage reservoirs: A case study for Belgium. Int. J. Greenhouse Gas Control 17, 431–449. http://dx.doi.org/10.1016/j.ijggc.2013.05.025.

White, D., 2013. Seismic characterization and time-lapse imaging during seven years of CO2 flood in the Weyburn field, Saskatchewan, Canada. Int. J. Greenhouse Gas Control 16 (Suppl. 1), S78–S94. http://dx.doi.org/10.1016/j.ijggc.2013.02.006.

Ziegler, P.A., 1989. Evolution of the North Atlantic: An Overview. AAPG Memoir, 46 In: Tankard, A.J., Balkwill, H.R. (Eds.), Extensional Tectonics and Stratigraphy of the North Atlantic Margins, 111-129.

Please cite this article as: Alcalde, J., et al., 3D geological characterization of the Hontomín CO_2 storage site, Spain: Multidisciplinary approach from seismic, well-log and regional data, Tectonophysics (2014), http://dx.doi.org/10.1016/j.tecto.2014.04.025

CHAPTER V

DISCUSSION

5.1 3D SEISMIC MODELING

5.1.1. Suitability of the survey design

The acquisition parameters used in the 3D seismic campaign (Table 1 in Alcalde et al., 2013b) were chosen based on previous studies in the region, such as regional geology, vintage 2D seismic profiles and well-log correlation (Alvarez-Marrón and Brown, 2008; Prado-Pérez et al., 2008; Quintá, 2013). The main aims in the design of the seismic survey were: (a) full coverage of the target subsurface structures; (b) have enough fold (traces/CDP) to ensure a high redundancy of information at each CDP position; and (c) provide a wide range of frequencies (with an emphasis on high frequencies), to obtain adequate vertical resolution at the target depth.

In order to image the entire target dome structure, including the injection area, a 36 km^2 area was covered by the 3D survey. The bin size used (12.5 x 12.5 m), determined by the receiver spacing resulted in a CDP fold of 36 traces/CDP, which is a standard value in onshore reservoir characterization surveys (Ashton et al. 1994; Roche, 1997; Juhlin et al., 2007). The recorded frequency at the target depth (700-1200 ms twt) ranges from 30 to 70 Hz, providing a vertical and lateral resolution of 13-50 m and 180-320 m, respectively. These resolution ranges enabled the elaboration of detailed maps of the target levels, including the reservoir and seal units (Alcalde et al., 2014).

5.1.2. Features affecting the data acquisition, quality and processing

The acquired data were deeply influenced by the intricate near surface geology and the mixed sedimentary media present in the study area (Alcalde et al., 2013a and 2103b). These features produced three major effects with regard to the data: (1) the alternation of siliciclastic and carbonate sediments caused steep changes in properties, which blurred the seismic signature; (2) one of these changes, a near surface velocity inversion, resulted in a loss of first arrivals and a shadow zone in the traces (Fig. 3 in Alcalde et al., 2013b); and (3) the rough topography of the study area, especially abrupt in the eastern part, prevented the access of the Vibroseis source and required the use of a second source (i.e. explosives) in 24% of the survey, resulting in a mixed source acquisition (Figs. 3 and 4 in Alcalde et al., 2013a).

The behavior of the carbonate sediments at the target depths in Hontomín can be compared to that of crystalline media: sharp variations in seismic properties, particularly in velocity, producing a blurred and incoherent seismic signature. In such difficult environments, elevation and refraction static corrections are considered to be the most relevant processing steps for reaching a good final image (e.g. Juhlin 1995; Malehmir and Bellefleur 2009). At the time of the seismic data acquisition (i.e., summer 2010), the subsurface velocity and density information available from well-logs was incomplete for the first 400 m. Thus, it was unexpected to find a sharp velocity inversion so close to the surface and this was not taken into account during the design of the seismic acquisition campaign. The velocity inversion severely affected the quality of the data by reducing the information of the traces corresponding to the position of the shadow zone at offsets larger than 500 m (Fig. 3 in Alcalde et al., 2013b). In addition to the loss of signal, this velocity inversion affected the first-break picking and the subsequent static corrections calculation. However, the static corrections produced one of the biggest improvements in data quality (Fig. 8c in Alcalde et al., 2013b). Nonetheless, there is still room for improvement in the coherence of the reflections in the shot gathers that could be achieved through a more detailed static corrections or the application of other processing techniques such as wave equation datuming (Beryhill, 1979, 1984; Schneider et al., 2005; Flecha et. al, 2004).

Given that a mixed source was employed in the survey it was necessary to perform source wavelet matching. Match filtering and phase and time shift methods were tested on synthetic and real data, and the overall performance of the two methods was similar. Because the phase and time shift method was simpler to apply, this method was selected for the final processing sequence. This source matching enhanced the reflector continuity and strength in the stacked areas where CDPs contained both dynamite and Vibroseis traces (Fig. 8 in Alcalde et al., 2013b). These areas correspond to the edges of the survey, where the explosive source points are located.

5.1.3 Analysis of the seismic model

The time-lapse monitoring of injected CO_2 requires that changes in the reservoir properties (i.e., saturation, pressure and temperature) caused by the injection of the CO_2 produce a detectable change in the seismic parameters (i.e., P and S-wave velocity and density) (Urosevic et al., 2010; Dixit et al., 2012). The Sleipner and Weyburn experiments constitute the most well-known examples of CO_2 monitoring with seismic techniques (Arts et al., 2004; Chadwick et al., 2010; Meadows and Cole, 2013; White, 2013a, 2013b). Among other properties, seismic monitoring commonly examines the variations in two characteristics of the reflections in order to map the spatial extent of the injected CO_2: travel time (i.e., changes in velocity) and amplitude (i.e., changes in impedance). Below, the consistency of the velocity model and the suitability of the amplitude equalization processes used are qualitatively assessed.

The processing flow applied to the Hontomín dataset (Table 2 in Alcalde et al., 2013b) allowed obtaining a final 3D image in which a number of sedimentary units were identified and mapped, including the target reservoir and seal levels (Alcalde et al., 2014). The velocity model used to convert these maps to depth was extracted from the sonic logs, adapted to the 3D structures mapped and finally checked against the NMO-velocity model to ensure its consistency. The resulting velocity model is therefore coherent with the interpreted horizons and well constrained around the injection area and, thus, could be considered an appropriate baseline velocity model.

The use of AGC within the workflow helped to obtain a good quality final image, which is essential for the interpretation process. However, AGC can impair the suitability of the seismic baseline model because it overprints the amplitude character of the dataset. The AGC could be replaced by true amplitude recovery processes (e.g., spherical divergence and linear gains) in the processing sequence, before the dataset is used as a reference in a time-lapse monitoring study based on amplitude variations. A detailed test on the parameters of these processes could provide an effective tool for equalizing the amplitudes without losing the “amplitude character” of the traces, which AGC erases (Maslen, 2014).

5.2 3D GEOLOGICAL MODELING

5.2.1 Interpretation through conceptual modeling

The interpretation of the Hontomín seismic volume is challenging due to the relatively complex geology of the area and the quality of the resultant migrated data. These factors result in multiple possible interpretations of the seismic dataset and, thus, other constraints should be set to reduce the uncertainty. To address this issue, a geologically supervised interpretation was carried out based on a pre-defined conceptual model (Fig. 3 in Alcalde et al., 2014). This interpretation approach benefited from well-log, seismic and regional geology; however, the well-log correlation was the starting point of the conceptual modeling. The 39 interpreted well-tops (Table 5.1) were analyzed to identify possible tecto-sedimentary events. The identified events were subsequently dated based on the thickness relationships of the formations with each other: when a substantial thickness variation was observed on a single formation, differential erosion was assumed; when thickness variations were observed along a set of successive formations, and thus could not be reasonably tied to erosion, they were interpreted as indicating faults. The proposed events were then checked and correlated with the events determined in regional works carried out in the study area (e.g., Serrano and Martínez del Olmo, 1990; García-Mondéjar, 1996; Tavani et al., 2011 and 2013; Quintà and Tavani, 2012; Tavani and Muñoz, 2012; Carola et al., 2013). This approach allowed detailed delineation of 8 surfaces, from Jurassic to Cenozoic, and 4 sets of faults (Fig. 5.1 and 5.2).

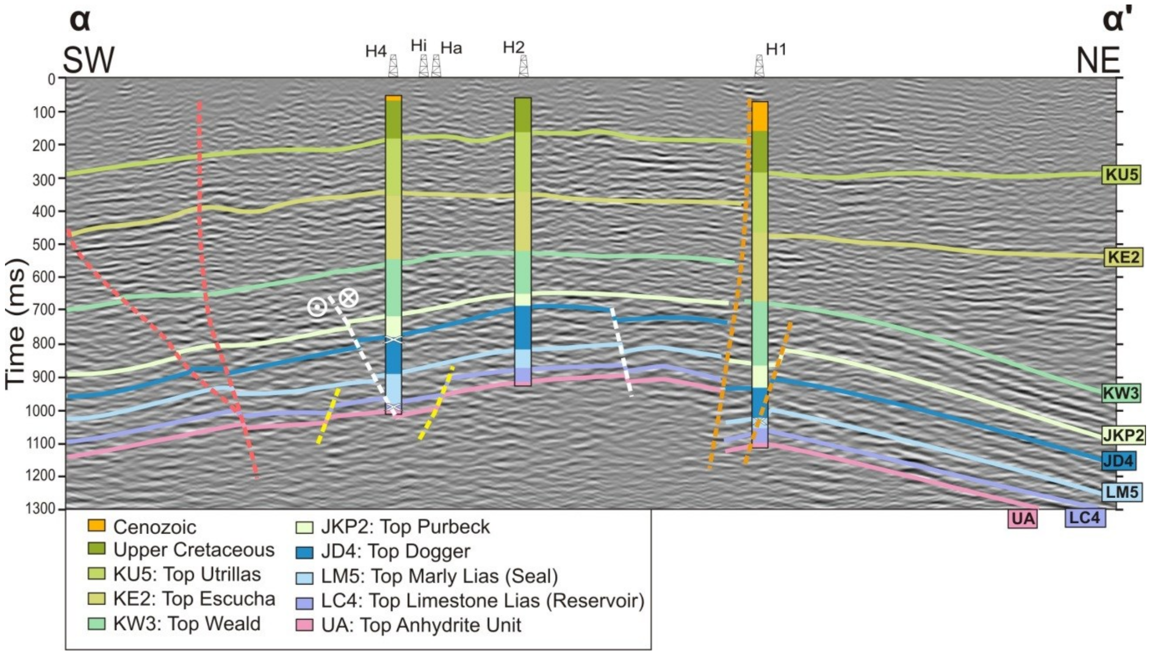

Fig. 5.1: First 1300 ms of the migrated section α-α' (location marked in Fig. S.2) with the final interpretation of the main horizons (continuous lines) and faults (dashed lines). The well-tops from wells H4, H2 and H1 are included. The white crosses mark the well positions intersected by faults (from well-logs).

5.2.2. The fault system

The analysis of the fault system was a critical step in the geological modelling process because the faults determine the main structural changes in the Hontomín subsurface and provide the major indications of the potential tecto-sedimentary events that occurred in the area. Four sets of faults were identified in the seismic cube: set "N", "X", "S" and "E" (Fig. 5.3). Sets "N" and "X" are normal faults affecting Jurassic units, whereas set "S" and "E" faults affect the entire sedimentary column. Two major faults corresponding to the latter sets ("Southern-Fault" and "Eastern-Fault", respectively) divide the study area in three structural blocks: the Eastern, the Central and the Southern block (Fig. 5.3). This division is observed in all the interpreted layers.

Period	Age	Litostratigraphic units		Paleoenvironment	Code	CO2	GR (gAPI)	DT (μs/f)	RHOB (g/c3)	Nφ-Vsh (PU)	Res_D (Ωm)
Tertiary	Tertiary	Bureba Facies		Fluvial / lacustrine	T		47.03	127.00	-	-	82.78
Cretaceous	Cenomanian-Maastrichtian			Carbonatic continental margin	KS6		26.34	67.56	-	-	193.37
					KS5		41.88	87.67	-	-	90.40
					KS4		50.68	101.88	-	-	64.51
					KS3		100.25	150.87	-	-	24.64
					KS2		68.51	109.45	-	-	28.91
					KS1		70.39	110.44	-	-	35.51
	Early Cenomanian	Utrillas Fm.		Fluvial: braided rivers with abrupt topography	KU5	Seal	90.90	161.50	-	-	32.66
					KU4		100.37	129.16	-	-	43.27
					KU3		66.72	122.31	-	-	61.75
					KU2		69.33	126.50	-	-	59.79
					KU1		102.58	123.26	-	-	57.32
	Aptian-Albian	Escucha Fm.		Fluvial: braided rivers with smooth topography	KE2		43.85	112.60	-	-	103.93
					KE1		24.45	93.05	2.38	14.42	230.06
	Late Valanginian - Barremian	Weald Facies - Pas Group		Fluvial: Meandering rivers, fining upsequence channel fills	KW3		39.83	96.55	2.34	18.87	133.62
					KW2		40.00	89.15	2.37	14.22	171.38
					KW1		28.74	84.08	2.37	15.28	200.48
	Oxfordian- Early Valanginian	Purbeck Facies	Cabuerniga Group	Transgressive-regressive cycle	JKP2	Seal	62.52	86.42	2.32	14.04	142.99
Jurassic			Campoo Group	Deltaic	JKP1	Reservoir	73.47	81.36	2.34	20.74	42.32
	Callovian	Dogger		Hemipelagic ramp	JD4		42.95	64.46	2.58	5.80	74.94
					JD3		45.00	63.26	2.66	2.23	122.03
	Bathonian				JD2	Reservoir	30.11	56.82	2.67	0.27	190.00
					JD1		33.77	69.25	2.61	7.61	25.51
	Late Bajocian	Pelletic Limestone Unit			Jpllt5		16.94	57.61	2.66	4.82	78.80
	Early Bajocian				Jpllt4	Seal	48.17	65.25	2.63	4.47	28.61
					Jpllt3		36.25	61.76	2.65	4.98	34.82
					Jpllt2		58.38	69.41	2.57	6.77	20.13
					Jpllt1		46.11	67.17	2.66	5.35	23.90
	Toarcian	Marly Lias	Castillo Pedroso Fm.		LM5	Main Seal	66.51	76.13	2.62	8.13	11.65
					LM4		90.00	82.53	2.60	4.78	9.65
	Pliensbachian		Camino Fm.		LM3		65.00	68.72	2.61	1.50	19.62
					LM2		90.00	80.07	2.56	2.88	15.66
	Late Sinemurian		P. Pozazal Fm.		LM1	Seal	44.71	61.71	2.69	1.19	35.31
	Early Sinemurian	Limestone Lias	Rio Polla Fm.	Inner ramp	LC4	Main Resevoir	21.85	54.42	2.69	3.04	51.87
			Sopeña Fm.		LC3		24.33	71.03	2.60	12.83	11.78
					LC2		17.00	53.95	2.67	4.85	48.76
					LC1		16.93	53.90	2.74	5.15	30.76
Triassic-Jurassic	Triassic-Jurassic	Carnioles - P. Palombera Fm.	Villanueva P. Fm.	Tidal	Dol2		26.30	59.96	2.61	18.00	16.84
					Dol1		23.92	52.22	2.74	10.00	82.14
			Anhidrites Unit		UA		21.26	50.63	2.89	0.03	500.00

Table 5.1: Main characteristics of the 39 interpreted well-tops. The five last columns are mean values for the main logs: gamma ray (GR), sonic (DT), bulk density (RHOB), neutron porosity (shale volume corrected; Nφ-Vsh) and deep resistivity (Res_D).

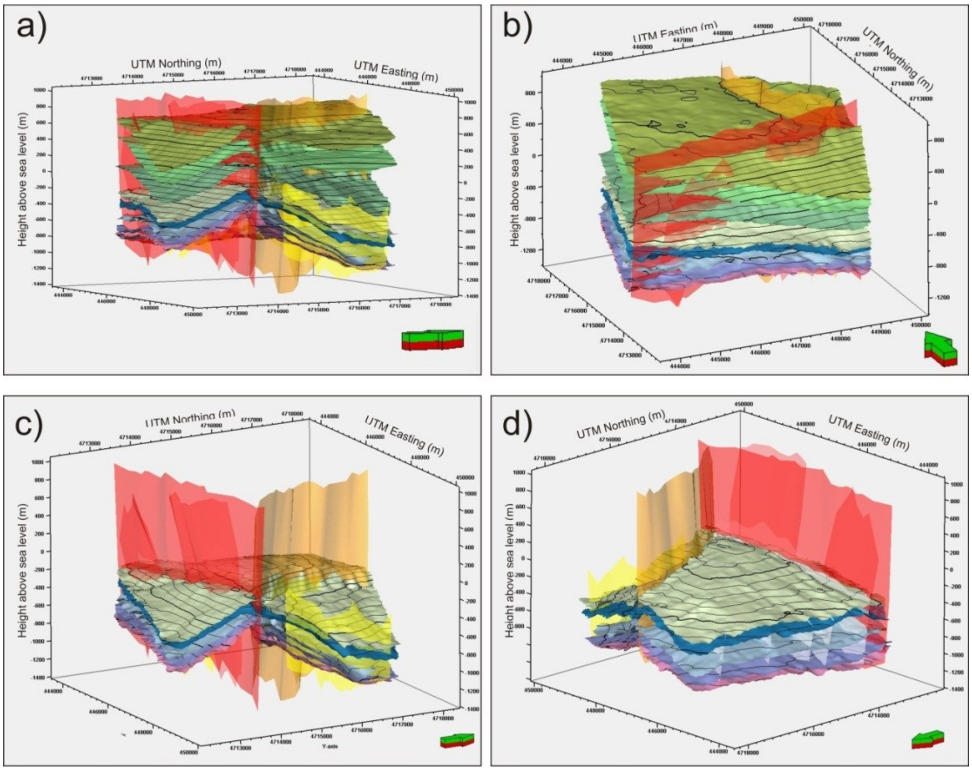

Fig. 5.2: 3D visualization of the resulting 8-layered geological model (a and b) and detail of the target dome structure (Jurassic) (c and d). In: Alcalde et al., 2014.

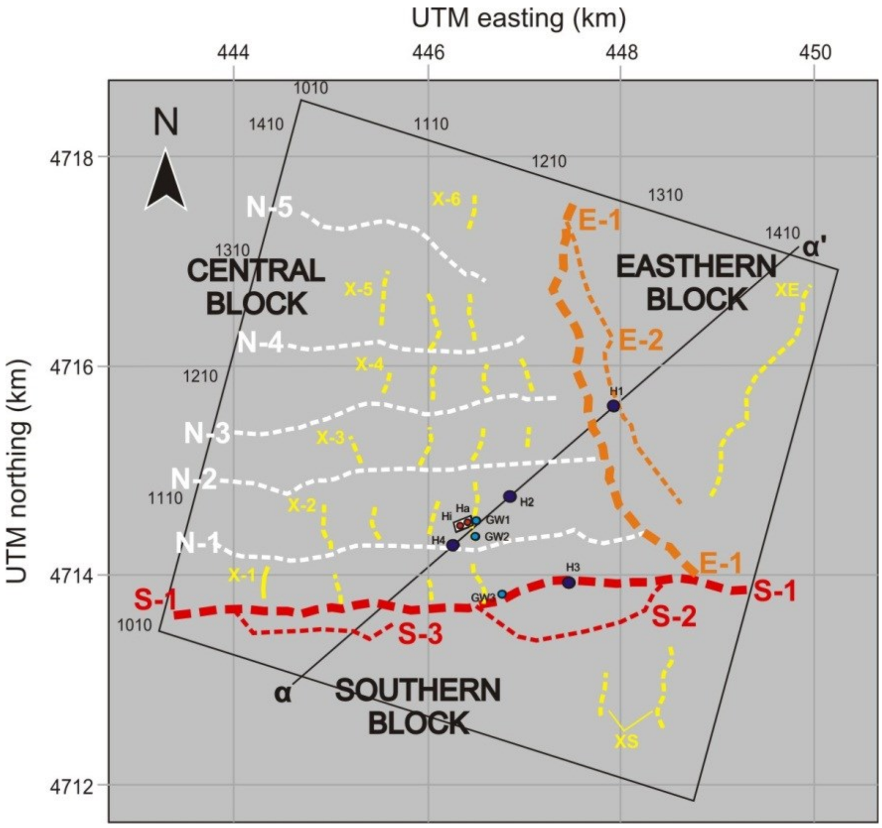

Fig. 5.3: General distribution and labelling of the main faults interpreted in the study area. The position of profile α-α' and of the wells is shown.

Set “X” and “N” are both normal displacement faults affecting the Early Jurassic Limestone and Marly Lias units (Fig. 5.1). The presence of the “N-1” fault was suggested by two observations: (a) the Limestone Lias in H2 doubles its thickness with respect to H4 (Fig. 5.1), which given the short distance between wells was assumed to correspond to faulting; (b) a mud loss was reported in the drilling report of the H4 well at the Marly Lias level. These observations were later confirmed in the seismic image in which the E-W oriented, N-dipping “N-1” fault was interpreted (Fig. 5.1). Other similar faults were identified in the seismic volume and correspond to the set N faults (Fig. 5.3). Set N faults separate blocks with varying thicknesses in the Jurassic units and are fossilized by the top of the Purbeck formation (Fig. 5.1 and Fig. 15a in Alcalde et al., 2014). The N-1 shows a thicker Weald succession on the southern than on the northern wall, suggesting that it was active for a longer period than in the remaining faults of set N.

Set “X” faults were first inferred based on observations made regarding the thicknesses of the Marly Lias unit. The thickness of this unit is 190 m in H4 and 110 m in H2, contrary to the Limestone Lias unit thickness. Given the distance between wells (715 m approximately), the occurrence of an extensional fault is suggested as an explanation for the differential sedimentation. This fault was identified in the seismic volume as a N-S oriented, S-dipping fault (yellow dashed line in Fig. 5.1), corresponding to set “X”. Other faults with the same X-fault pattern were observed in the entire volume as disconnected faults affecting sediments up to the Marly Lias (Fig. 15b in Alcalde et al., 2014). Set X faults are observed as affecting the Marly Lias succession and there is no seismic evidence of movements of these faults after the sedimentation of the Marly Lias.

The evolution of the Southern and the Eastern faults, defined by the thickness relationships of the entire sedimentary column, is interpreted to be a multi-stage evolution. The thickness variations of the Mesozoic units suggest higher subsidence of the Central block with respect to the Eastern and Southern blocks. However, the seismic, well and surface data indicate that the Central block is currently structurally higher. These apparently contradictory characteristics are interpreted as indicating that the Eastern and Southern faults were normal faults in their origin during the Mesozoic, and were later inverted as high angle lateral-reverse faults during the Cenozoic compressional stage. The attitude of these faults in the Jurassic interval, suggests that the Southern fault was part of Set N, whereas the Eastern fault was part of set X.

5.2.3. Geological Evolution of Hontomín

The conceptual model used in the interpretation includes two main regional deformation stages: (a) an initial one, which developed during the main Late Jurassic-Early Cretaceous extensional stage and which generated NE-SW and NW-SE trending normal faults (e.g. Ziegler, 1989; Tavani and Muñoz, 2012); and (b) a second stage of deformation corresponding to the Alpine Orogeny (Late Cretaceous-Cenozoic), which inverted some of the previous faults within a transpressive regime (Vera, 2004; Tavani and Muñoz, 2012; Tavani et al. 2013).

The geological model obtained from the interpretation of the 3D seismic dataset (Fig. 5.2) allowed us to infer the evolutionary history of the Hontomín structure, which is integrated into the regional framework (Fig. 5.4). Three main stages are proposed in this model (Fig. 5.4): (1) a local, small-scale fracturing stage during Late Lias; (2) a regional fracturing stage during the Late Jurassic-Early Cretaceous extension; and (3) a regional tectonic shortening stage associated with fault inversion, occurring during the Alpine compressional stage.

The first deformation stage described is related to the generation of the set X faults (Fig. 5.4-1). Their origin is puzzling, since there is no evidence of a regional extensional event between the Triassic and the Late Jurassic-Early Cretaceous rifting periods (e.g., Ziegler, 1989; García-Mondéjar, 1996; Quintà and Tavani, 2012; Tavani, 2012; Tavani et al., 2013). We propose that the possible origin for the set X faults could be traced to the early stage of development of the Hontomín dome. At that stage, salt movements by differential loading related to Triassic basement faults originated in the Triassic rifting event. The salt migration could have produced a gentle dome growth and generated normal faults on the flanks (Fig. 5.4-1). This stage could also have been the origin of the Eastern fault as a set of aligned N-S faults, which eventually merged during a later reactivation.

The second event corresponds to a regional extensional period occurring during the Late Jurassic-Early Cretaceous (Fig. 5.4-2) and is related to the generation of Set N faults. During this stage, the Hontomín dome started its major development by a forced fold mechanism generated by the WNW-ESE Ubierna Fault and the oblique NNE-SSW Hontomín Fault (Tavani et. al., 2013).

A W-E oriented basement normal fault forced the folding and the halokinetic growth of the Hontomín dome structure. The Southern fault would have originally formed as several minor set N-like segments located above a structurally weak zone, which were subsequently merged. The combination of Set N development and salt accumulation below the dome crest is associated with block tilting and differential sedimentation and erosion, which may be the reason for the thickness variation of the Purbeck beds between wells H4 and H2 (Fig. 17 in Alcalde et al., 2014).

The set N faults are fossilized by the Purbeck sediments, except the N-1, which is thought to have been active during the deposition of the Weald unit and which was also reactivated at a later compressional stage. The N-1 fault shows a relatively important vertical offset, which marks the boundary between the Central and the Southern blocks (Fig. 8 in Alcalde et al., 2014). The lower layers (i.e., Anhydrite unit and Liassic and Dogger formations) show sedimentation associated to normal faulting, whereas thickness variations in the upper layers (i.e., Upper Cretaceous and Cenozoic sediments) show reverse motion. A number of potential explanations to this intricate behavior are proposed: local inversion related to underlying salt doming, thickness variations associated to strike-slip reactivation, the existence of an unidentified, S-dipping normal fault south of N-1 or a wrong interpretation of the top Weald horizon. These explanations take into consideration the complicated sequence of events involved in the motion of this fault: extension, compression and strike-slip.

The third deformation stage took place during the Alpine compression (Fig. 5.4-3). This stage is characterized by the inversion of previous structures, mostly focused on the Southern and Eastern faults. The location of the Hontomín structure on the SE tip of the Ubierna fault, formed at this stage (Tavani et al., 2011), resulted in a decisive influence of this fault on the final geometry of the Hontomín dome. The Southern fault was mostly inverted as a right lateral strike-slip fault with a small vertical component, whereas the Eastern fault was mostly inverted as a reverse fault with a gentle left-lateral component (Fig. 5.4-3). The area near the fault N-1 was also reactivated during this process, although some of the resulting deformation took the form of folding in the uppermost layers, as recorded by the fossilization of this fault by the Purbeck Fm (Fig. 15a in Alcalde et al., 2014). A slight buckling of the uppermost beds on top of this fault suggests mild activity during the successive stages.

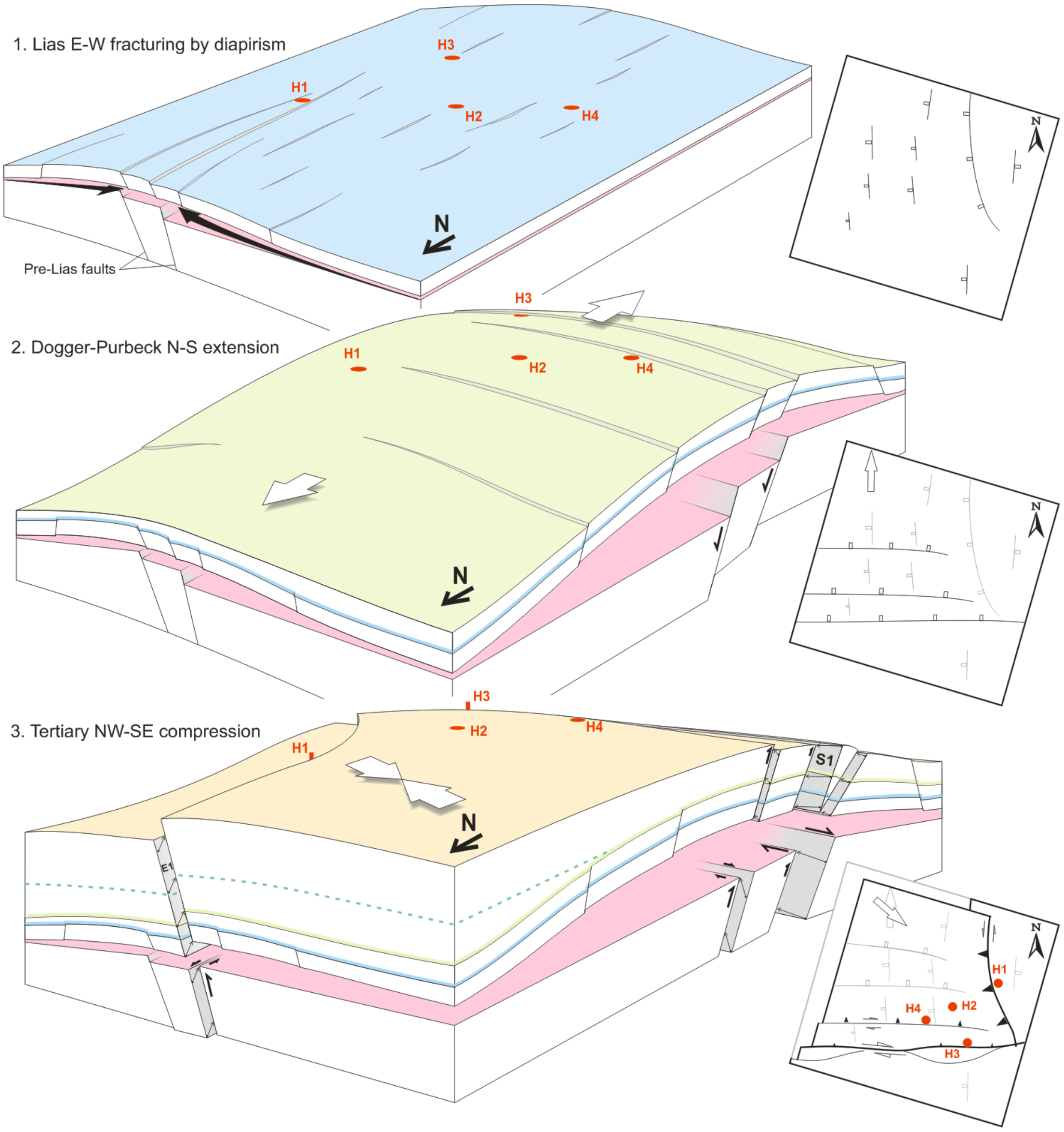

Fig. 5.4: The sequence of the three main geological events for the zone. Pink color represents the Keuper detachment level. 1) E-W Triassic migration of evaporites during deposition of Marly Lias produces a slight accommodation folding of the Trias-Lias cover and poor development of normal faults, forming a N-S oriented anticline. 2) N-S extension during deposition of Purbeck produces faulting on the basement and covers and triggers N-S salt migration and forms a dome-like structure. 3) NW-SE Cenozoic compression breaks the structure reactivating and inverting the mains east (E1) and south (S1) faults, producing a wedge-thrusting of the NW block. The green dashed line represents a Cretaceous layer onlapping the dome-like structure.

During the inversion stage the Triassic materials stacked against the Southern and Eastern faults, increasing the structural relief of the Dome. The inversion stage is recorded by the uppermost sediments, deposited during the Late Cretaceous-Cenozoic, defining a step of >450 m across the Southern and N-1 faults, and >250 m across the Eastern fault (Fig. 14 in Alcalde et al., 2014).

5.3. CONTRIBUTION TO THE CO_2 STORAGE SITE

5.3.1. Suitability of the Hontomín Site for GSC

The resulting geological model was generated from seismic, well-log and regional geological data (Alcalde et al., 2014). This model provides detailed characteristics of the structures involved in the GSC in Hontomín (including the target reservoir and seal formations, the fracture system and the overburden) and, hence, it is an essential tool for evaluating the safety, security and suitability of the Hontomín site for CO_2 storage. We have used the geological model to fill the evaluation table previously presented (Table 1.1) and ensure that the Hontomín site is suitable for GSC purposes (Table 5.2). The assessment carried out in this work includes the evaluation of critical, essential and desirable criterion levels, proposed in IEA GHG (2009).

Critical level

The well-log correlation was achieved through an exhaustive work with gamma ray, sonic, density, porosity and resistivity logs (Table 5.1). According to their properties, several formations have been identified as potential reservoirs and seals (Table 5.1), with the Lias Limestone and the Marly Lias, respectively, being selected as the target reservoir and seal formations (Alcalde et al. 2013a).

The monitoring potential with seismic methods, discussed above, is adequate. The seismic baseline modelling carried out in the study area is appropriate to the characteristics (i.e., size, depth, thickness of the target formations etc.) of the Hontomín site (Alcalde et al., 2013a and 2013b).

Essential level

The seismic model constitutes the most important tool for assessing the faulting intensity in the study area. The Hontomín area was more fractured than expected based on the previous geological and geophysical data available for the region. Intense faulted reservoirs can produce compartmentalization or, more seriously, leakage of the injected CO_2. The fault system identified at Hontomín (Fig. 5.3) could produce a certain degree of compartmentalization that, given the amount of CO_2 to be injected (which is low due to the R&D nature of this project) will not constitute a risk factor. Further hydrogeological tests should be carried out in order to evaluate the risk of leakage from the storage site but, given the fault development, leakage is not anticipated. This hydrogeological characterization of the Hontomín site is beyond the scope of this thesis. However, the 3D geological model obtained in this work forms the basis for this characterization process by providing the structural framework and several formation properties which are essential for this purpose.

Desirable level

The geological characterization carried out at the Hontomín site incorporated practical information about the desirable characteristics for a GSC site, including target formation thicknesses, target depth of injection and rock properties derived from the well-logs. The average thickness of the target reservoir and seal formations (over 80 m and 100 m in both cases) and porosity are adequate considering the capacity and injectivity requirements. Further hydrogeological tests should be carried out to obtain the permeability values.

At the reservoir level, the crest of the dome structure is located near the H2 well. The position of the injection (HI) and monitoring (HA) wells was selected with the intention of finding the maximum gradient direction, which is contained approximately in the H4-H2 direction (Fig. 5.1). This geometry will produce a faster migration of the injected CO_2, benefiting the monitoring experiments (Alcalde et al. 2013a).

Table 5.2: Site selection criteria for ensuring the safety and security of CO_2 storage and suitability of the Hontomín site. Colored cells indicate criterions assessed completely (green) or partially (yellow) in this work. Modified from IEA GHG, 2009.

Criterion Level	No.	Criterion	Eliminatory or unfavorable	Preferred or favorable	Assessment at Hontomín
Critical	1	Reservoir–seal pairs; extensive and competent barrier to vertical flow	Poor, discontinuous, faulted and/or breached	Intermediate and excellent; many pairs (multi-layered system)	🟩 ✓
	2	Pressure regime	Over-pressured: pressure gradients greater than 14 kPa/m	Pressure gradients less than 12 kPa/m	✓
	3	Monitoring potential	Absent	Present	🟩 ✓
	4	Affecting protected ground water quality	Yes	No	✓
Essential	5	Seismicity	High	Moderate or less	✓
	6	Faulting and fracturing intensity	Extensive	Limited to moderate	🟩 ✓
	7	Hydrogeology	Short flow systems, or compaction flow; Saline aquifers in communication with protected groundwater aquifers	Intermediate and regional-scale flow	🟨 ✓
Desirable	8	Depth	<750-800 m	>800 m	🟩 ✓
	9	Located within fold belts	Yes	No	✓
	10	Adverse diagenesis	Significant	Low to moderate	✓
	11	Geothermal regime	Gradients ≥ 35 ºC/km and/or high surface temperature	Gradients < 35 ºC/km and low surface temperature	—
	12	Temperature	< 35 ºC	≥ 35 ºC	✓
	13	Pressure	< 7.5 MPa	≥ 7.5 MPa	✓
	14	Thickness	< 20 m	≥ 20 m	🟩 ✓
	15	Porosity	< 10%	≥ 10%	🟩 ✓
	16	Permeability	< 20 mD	≥ 20 mD	—
	17	Caprock thickness	< 10 m	≥ 10 m	🟩 ✓
	18	Well density	High	Low to moderate	✓

✓ Suitable ✗ Unsuitable — Unknown/Non-applicable

The detailed 3D model anticipates the existence of an X-set fault between the injection and monitoring boreholes affecting the injection level (Fig. 5.5). This fault separates two zones suitable for CO_2 injection: one in the W side of the fault ("H4 block" hereafter) and one in the E side of the fault ("H2 block" hereafter) (Fig. 5.5). The average vertical offset of this fault is 130 m – greater than the total thickness of the reservoir layer – and therefore will compartmentalize the reservoir, acting as a barrier and limiting the migration of the injected CO_2 between the two blocks. These two potential reservoir blocks are furthermore delimited by the Eastern-fault in the east, the N-1 and N-2 in the south and north respectively, and by another X-like fault in the west (Fig. 5.5a). Far from considering this compartmentalization a problem, the presence of this fault adds an interesting challenge in terms of well design and monitoring capacity. By underground deviation of the injection well, the two blocks are accessible from the same position at the surface. The H2 block is larger than block H4 (Fig. 5.5a). However, this does not necessarily mean that the H2 block is more suitable for holding the injection. The amount of CO_2 to be injected is also a fundamental factor in this issue. If only a few tones of CO_2 are to be injected (as is the case of an R&D demonstration plant), it may be of interest to inject CO_2 in a steep zone, which could accelerate the migration of the plume. This could speed up the physical and geochemical processes that take place at the reservoir and seal levels, from the early stages of injection, even with a reduced amount of CO_2 injected in a short period of time. Additionally, injection of CO_2 in block H4 would also help assess the sealing capacity of the fault separating the blocks. The eventual arrival of the CO_2 plume to the Monitoring borehole would allow us to infer the porosity–permeability parameters of the fault, to be used in further developments of the storage site.

5.3.2. Injection and monitoring wells location

The 3D seismic images of this work provided key information for determining the most suitable position for locating the injection and monitoring wells. The project involved three wells (1 injection + 2 monitoring wells) in the original planning (Alcalde et al., 2013a), but was redesigned to its current state, in which only two wells (1 injection + 1 monitoring well) have been drilled (Alcalde et al., 2013b; 2014).

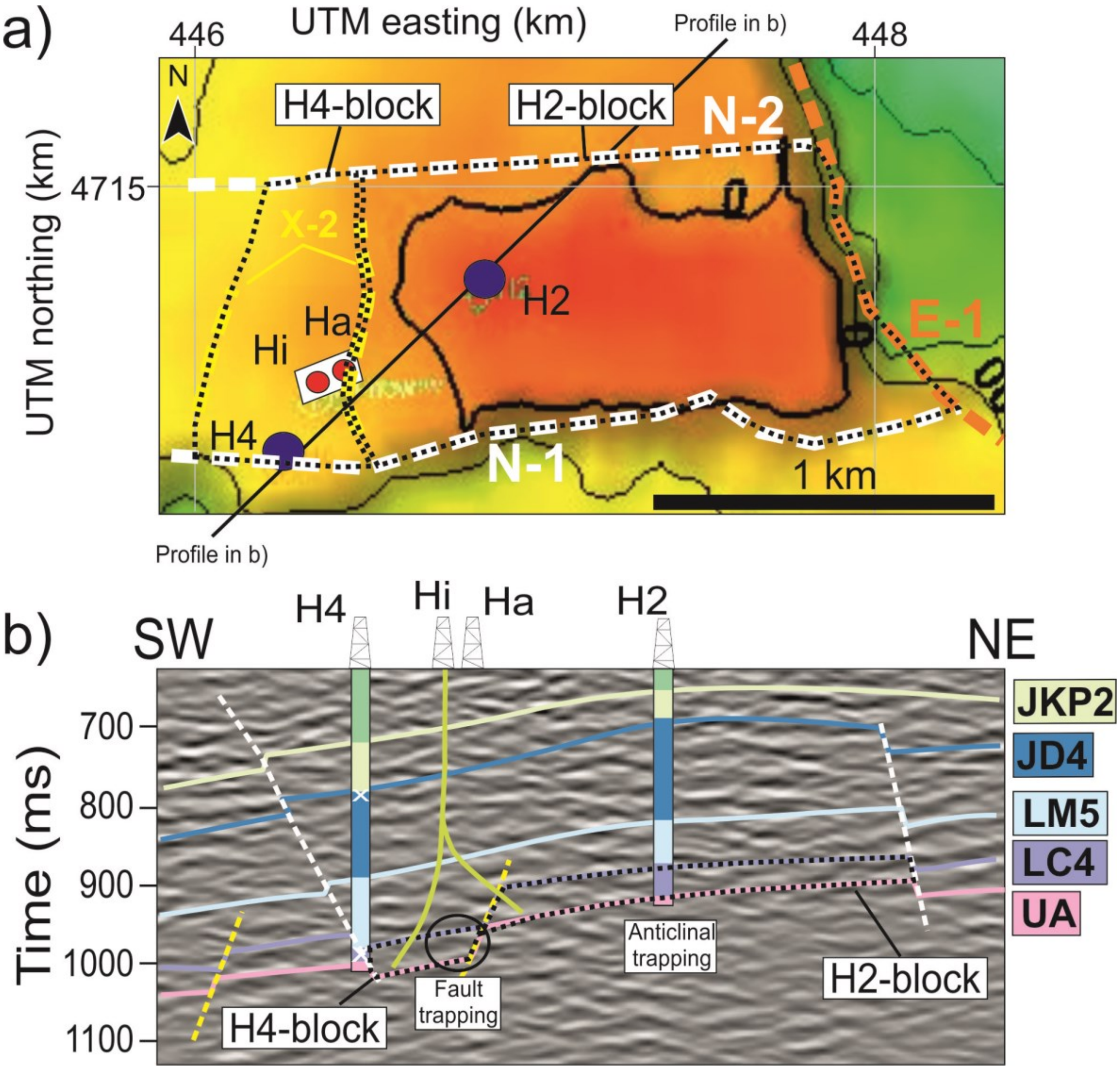

Fig. 5.5: a) Position of the two potential CO_2 reservoirs, the H4-block and H2-block, limited by N-1, N-2, E-1, and two X-2 faults at S, N, E and W, respectively. b) Zoom of the potential reservoirs with the two trapping mechanisms available: fault trapping for the H4-block and anticlinal trapping for the H2-block.

The first approach to their current location was based on the identification of the apex and the major fault structures. Based on this geometry, the position of the injection (Hi) and monitoring (Ha) wells was chosen to lie over the steepest flank of the dome, at approximately 500 m from the structural apex (Fig. 10 in Alcalde et al., 2013a), which is located near the H2 well. The position was selected with the goal of finding the maximum gradient direction, which is contained approximately in the H4-H2 direction (Fig. 7 in Alcalde et al., 2014). This geometry will produce a faster migration of the injected CO_2, benefiting the monitoring experiments (Alcalde et al. 2013a).

5.3.3. Storage capacity calculation

The Jurassic structure was identified as a pseudo-triangle dome, with the two main faults – Eastern and Southern – representing two of the sides, and a third side being determined subjectively at the two-way-time that the dome changes from symmetric to elongated (i.e., approximately 850 ms) (Fig. 15 in Alcalde et al., 2013b). The calculated area of the dome is $9.4 \cdot 10^6$ m^2.

In order to provide an estimation of the scale and potential of the Jurassic dome structure, the maximum storage capacity was calculated (Alcalde et al., 2013b). Assuming an average thickness and effective porosity of the reservoir unit of 80 m and 8.5 % (obtained from the well-log data), respectively, the calculated total pore volume (PV) in the dome reservoir is $1.6 \cdot 10^6$ m^3. We have calculated the maximum theoretical CO_2 storage capacity assuming a short-term storage, and thus considering only the existence of structural and stratigraphic trapping (Bachu et al., 2007; Welkenhuysen et al., 2013), as well as an isotropic distribution of the porosity. This maximum CO_2 storage capacity is calculated as a function of the available storage volume and the density of the CO_2 at the storage conditions provided by:

$$M_{CO_2} = PV \times (1 - S_{wi}) \times \rho_{CO_2} \quad (3)$$

Where M_{CO2} is the theoretical storage capacity (kg), PV is the total pore volume (m^3), S_{wi} is the irreducible water (brine in this case) saturation (0-1) and ρ_{CO2} is the density of CO_2 at reservoir conditions (kg/m^3).

The S_{wi} values are usually determined from drainage experiments, which are not yet available at Hontomín. Recent experiments determine that S_{wi} values derived from empirical relationships between porosity, permeability and water saturation (Schlumberger, 1989) are less precise and more optimistic compared to experimental data (Torskaya et al., 2007; Bennion and Bachu, 2010). However, since experimental data is also unavailable at the Hontomín site, we used the empirical relationships given in Schlumberger, 1989 and calculated an approximate S_{wi} value of 0.123, using the porosity values as a reference. We calculated the ρ_{CO2} using the average temperature and pressure conditions at the target depth, obtained from H1-4 wells. By solving the equation of state formulated in Peng and Robinson (1976), the resulting ρ_{CO2} is 745.558 kg/m^3, at average reservoir conditions of 41^o C and 15.3 MPa. Thus, a maximum CO_2 storage capacity of 1.2 Gt of CO_2 is expected in the Hontomín Jurassic dome structure.

The same assumptions were used to calculate the maximum storage capacities of the H2 and H4 blocks (Alcalde et al., 2014). The H4 block has a total area of $2.366 \cdot 10^6$ m^2. The H2 block's area is larger ($1.076\ 10^7$ m^2). The total volume of these two blocks ranges from $1.695 \cdot 10^7$ m^3 in the H4 block, to $9.275 \cdot 10^7$ m^3 in the H2 block. Assuming an average formation porosity of 8.5 %, obtained from the well-log data, the total PV are $9.94 \cdot 10^5$ m^3 for the H4 block reservoir, and $7.884 \cdot 10^6$ m^3 for the H2 block reservoir. Giving the S_{wi} and ρ_{CO2}values previously determined, the calculated maximum theoretical storage capacity is 0.65 Mt of CO_2 for the H4 block reservoir and 5.2 Mt of CO_2 for the H2 block reservoir. Furthermore, the connectivity of both reservoirs would imply an increase of the overall M_{CO2}, which would equal 5.85 Mt of CO_2.

CHAPTER VI

CONCLUSIONS AND FUTURE WORK

6.1 CONCLUSIONS

The principal aim of this thesis was the seismic baseline modeling and geological characterization of the Hontomín CO_2 geological storage site. 3D seismic reflection and well-log data have been have been integrated in order to obtain a multidisciplinary model of the subsurface. The most relevant results of the research work carried out are reflected in three manuscripts published in internationally recognized scientific journals included within the Scientific Citation Index (SCI). Results include the first high resolution image of the storage site. The resulting geological model is crucial to assess the suitability of the Hontomín site for GSC purposes, and an asset for the monitoring phase to be carried out during and after the CO_2 injection.

The 3D seismic survey was design to suit the imaging aims, in terms of areal coverage, data redundancy and vertical and horizontal resolution at the proposed target depths. The acquired data were deeply influenced by the intricate near surface geology and the mixed sedimentary media (carbonate and siliciclastic) present in the study area. The rough topography of the study area required the use of two sources, Vibroseis and explosive. Furthermore, the complex geology at Hontomín includes a near-surface layer characterized by a velocity inversion, which was detected and modeled. This inversion generated a shadow zone in the data, producing unexpected complications in the static correction calculations and reducing the overall quality of the data. The data processing applied to the Hontomín 3D seismic reflection data set addressed these issues and provided a seismic image of the study area suitable for interpretation. Static corrections proved to be one of the most important steps within the data processing flow. The mixed source wavelets were matched utilizing a self-developed code that performed the appropriate time and phase shift to the traces, producing a similar matching result as that of the standard match filtering, with an easier implementation. Other processing steps that were decisive in producing a quality final image included the DMO correction, frequency filtering and amplitude equalization.

The interpretation of the seismic volume was challenging due to the effects of the relatively complex geology in the image of the resultant migrated data. To reduce the uncertainty, a geologically-supervised interpretation was carried out based on a defined conceptual model. This conceptual model was built based on the available dataset (i.e., well-log, seismic and regional geology), using the well-log data as primary input. This approach allowed detailed delineation of 8 surfaces, from Jurassic to Cenozoic, and 4 sets of faults.

The geological model obtained implies three main stages in the evolution of the Hontomín structure: (1) a local, small scale N-S fracturing stage during Late Lias, possibly related to salt mobilization during early growth stages of the dome; (2) a regional fracturing stage during the Late Jurassic-Early Cretaceous extension, generating W-E normal faults; and (3) a regional tectonic shortening stage associated to fault inversion, occurring during the Alpine compressional stage inverting some of the pre-existing extensional faults.

The resulting model was used to assess the suitability of the Hontomín site for GSC by evaluating the properties of the underground structures. Several formations were identified as potential reservoirs and seals throughout the sedimentary column. Within them, limestone and marly Lias represent the most suitable reservoir and seal formations, respectively, due to their properties (e.g., porosity, permeability, depth, thickness etc.). Our resulting model shows that the Hontomín area is more fractured than it what was believed to be before the seismic characterization survey was acquired. The Hontomín site was conceive as a subsurface research facility, not a storage reservoir for production, and therefore, the existence of fracturing would provide additional research opportunities (e.g., interaction of the injected CO_2 with the fractures; influence on permeability). In spite of this fracturing, the Hontomín structure has been positively evaluated to host the GSC pilot plant.

The position of the injection and monitoring boreholes was selected based on the results of this work. They were located at the steepest flank of the dome, aiming to find the maximum gradient direction to produce a faster migration of the injected CO_2, benefiting the monitoring experiments. At this location, two potential reservoir blocks can be reached by the two boreholes. The H4 block is smaller and has a steeper dip than the H2 block. Their maximum storage capacity was calculated in order to provide an overall idea of the scale of the two blocks. This resulted in a maximum theoretical storage capacity of 0.65 Mt of CO_2 for the H4 block reservoir and 5.2 Mt of CO_2 for the H2 block reservoir, giving a combined capacity of 5.85 Mt of CO_2.

The 3D seismic model obtained can be used as a basis for a baseline reference model to detect and measure changes produced by the injected CO_2 plume during the monitoring stage. The resulting velocity model is coherent with the interpreted horizons and well constrained around the injection area, implying it is suitable for monitoring changes in velocity properties. The use of AGC within the workflow helped to obtain a good quality final image, but it should be replaced by true amplitude recovery processes in the processing sequence before the dataset can be used as a reference in a time-lapse monitoring study based on amplitude variations.

6.2 FUTURE WORK

Future work will focus on improving the seismic baseline model, the geological model, and in the further analysis and modeling for GSC purposes.

Modifications to the processing flow should be made before the Hontomín 3D seismic data set can be used as a baseline to a repeat survey as part of a time-lapse seismic monitoring study. These modifications should include:

- The coherency of the reflections within the CDPs is insufficient and this problem is probably related to the static models used for the corrections. One possible solution to this problem could be wave-equation datuming (Berryhill, 1979; 1984; Schneider et al., 1995; Flecha et al., 2004). This method partially migrates the data below the near surface to a fixed datum before proceeding with the standard processing. This could resolve static problems unachievable by the static corrections used and thus increase the coherency of the reflections in the seismic cube.
- Pre-stack migration is computationally highly demanding and therefore not often available for academic institutions. However, this type of migration enhances the

final image and it is especially useful in intensely fractured and/or highly variable velocity areas, such as in the study area.

- The use of AGC within the workflow helped to obtain a good quality final image. However, it does not preserve the original amplitude character of the data set, jeopardizing the use of amplitude variation methods for monitoring. The AGC process should be replaced by true amplitude recovery methods, such as spherical divergence and linear gains in order to achieve the amplitude balance.

There is also room for improvement in the geological interpretation and modeling. The perspective of advances in this sense includes:

- Advances in the data processing producing a better quality image will have a direct impact in the interpretation. The improvements in coherency will be especially helpful to differentiate faults from simple gaps in the reflections.
- One of the main characteristics of the Hontomín project is that the site characterization is being achieved through multiple methods. Future work will include matching and correlation of the seismic model with the results of other disciplines, such as electromagnetics, hydrogeological, geochemical, geomechanical models etc.
- The dataset was processed down to 1.5 s, but the acquired data was to 4 s. The processing of the whole dataset would allow imaging the basement faulting, which is believed to be related to the origin of the development of the dome.
- Conventional structural restoration and seismic flattening will help to constrain the fault displacements in areas where the present-day structural relief makes it difficult to visualize stratigraphic features (Gao, 2009).

Finally, future modeling will be performed regarding the GSC nature of this project:

- Synthetic seismic modeling together with fluid substitution will assess the sensibility of the seismic baseline model to changes in fluid properties, such as those produced by the CO2 injection.
- The hydrodynamic properties of the faults will be determined through fluid flow modeling. This will require petrophysical properties from core samples as well

as the geological model as inputs. The results will be used to determine the safety of the site, as well as to plan the monitoring experiments.

- The acquisition of vertical seismic profiles (VSP), would be an unique asset to the characterization of the site, because it represents a unique way to provide a direct connection between the subsurface rock stratigraphy, the well-logs data and the surface 3D seismic data. 3D VSP is usually richer in higher frequencies than surface normal incidence data, it is free of converted phases and provides a new link between the seismic image and the lithology.
- Last but not the least, during the acquisition of the 3D Hontomín experiment, 3 component seismic data was acquired (Alcalde et al., 2013a). This data set would provide a very useful high resolution Vp and Vs seismic tomographic model of the Hontomín subsurface.

REFERENCES

Aki, K., and Richards, P. 2002. Quantitative seismology: Theory and Methods (2nd ed.). San Francisco: University Science Books. Sausalito, CA, USA. 700 pp.

Alcalde, J., Martí, D., Calahorrano, A., Marzán, I., Ayarza, P., Carbonell, R., Juhlin, C. and Pérez-Estaún, A. 2013a.Active seismic characterization experiments of the Hontomín research facility for geological storage of CO2, Spain. International Journal of Greenhouse Gas Control, 19, 785-795.

Alcalde, J., Martí, D., Juhlin, C., Malehmir, A., Sopher, D., Saura, E., Marzán, I., Ayarza, P., Calahorrano, A., Pérez-Estaún, A., and Carbonell, R. 2013b.3D Reflection Seismic Imaging of the Hontomín structure in the Basque-Cantabrian Basin (Spain).Solid Earth4, pp. 481-496.

Alcalde, J., Marzán, I., Saura, E., Martí, D., Ayarza, P., Juhlin, C., Pérez-Estaún, A., and Carbonell, R. 2014. 3D geological characterization of the Hontomín CO2 storage site, Spain: multidisciplinary approach from seismics, well-logging and regional data. Tectonophysics (accepted).

Alshuhail, A. 2011. CO_2 Sequestration Site Characterization and Time-lapse Monitoring using Reflection Seismic Methods. PhD Thesis, University of Calgary, Department of Geology and Geophysics, Calgary, Canada. 481 pp.

Alvarez, C. 1994. Hydrocarbons in Spain – exploration and production. First Break, 12, Vol 1. DOI: 10.3997/1365-2397.1994004

Alvarez-Marron, J., and Brown, D. 2008. Caracterización estructural del subsuelo de las potenciales ubicaciones de una planta piloto de Almacenamiento Geológico de CO_2. Institute of Earth Sciences Jaume Almera – CSIC. 44 pp. Internal report.

Arts, R., Brevik, I., Eiken, O., Sollie, R., Causse, E., Van Der Meer, B. 2001. Geophysical methods for monitoring marine aquifer CO2 storage Sleipner experiences. Proceedings of the 5th International Conference on Greenhouse Gas Control Technologies, CSIRO Publishing.

Arts, R., Eiken, O., Chadwick, R. A., Zweigel, P., van der Meer, L., and Kirby, G. A. 2004. Monitoring of CO_2 injected at Sleipner using time-lapse seismic data. Energy, 29, pp. 1383–1393.

Ashton, P., Bacon, B, C. Deplante, D.T., Sinclair, Redekop, G. 1994. 3D seismic survey design, Oilfield Review, 19-32.

Avseth, P., Mukerji, T., and Mavko, G. 2010. Quantitative Seismic Interpretation. Cambridge University Press, Cambridge, UK. 359 pp.

Bachu, S. 2000. Sequestration of CO2 in geological media: criteria and approach for site selection in response to climate change. Energy Conversion and Management, Volume 41, Issue 9, 1,pp. 953-970, DOI: 10.1016/S0196-8904(99)00149-1.

Bachu, S, 2003. Screening and ranking of sedimentary basins for sequestration of CO2 in geological media in response to climate change. Environmental Geology, vol. 44, pp. 277-289.

Bachu, S., Bonijoli, D., Bradshaw, J., Burruss, R., Holloway, S. Christensen, N.P., Mathiassen, O.M., 2007. CO2 storage capacity estimation: methodology and gaps. International Journal on Greenhouse Gas Control, 1, 430–443.

Baines, S. J. & Worden, R. H. (eds). 2004. Geological Storage of Carbon Dioxide. Geological Society, London, Special Publications, 233, 1-6.

Batzle, M., & Wang, Z. 1992. Seismic properties of pore fluids. Geophysics , 57, pp. 1396-1408.

Bennion, D.B., Bachu, S., 2010. Drainage and imbibition CO_2/brine relative permeability curves at reservoir conditions for carbonate formations. In: SPE Paper 134028, SPE Annual Conference and Exhibition, Florence, Italy

Bergman, B., Juhlin, C. and Palm, H. 2002. High-resolution reflection seismic imaging of the upper crust at Laxemar, shoutheastern Sweden. *Tectonophysics* 355, pp. 201-213.

Beroiz, C.; Permanyer, A., (2011), Hydrocarbon habitat of the Sedano trough, Basque-Cantabrian Basin, Spain. J. Pet. Geol. 2011, 34, 387– 410, DOI: 10.1111/j.1747-5457.2011.00511.x

Berryhill, J. R., 1979, Wave-equation datuming: Geophysics, 44, pp. 1329–1344.

Berryhill, J. R., 1984, Wave-equation datuming before stack: Geophysics, 49, pp. 2064–2067.

Bianco, E. 2011. G is for Gather. Agile Geoscience. Web. http://www.agilegeoscience.com/. Last time accessed: 18 of February 2014.

Blanchard, T. D. 2011. Time-lapse seismic attenuation as a tool for monitoring hydrocarbons and CO_2 in geological materials. PhD thesis, The University of Leeds, School of Earth and Environment. 275 pp.

Braaksma, H., Proust, J. N., Kenter, J. A. M., Drijkoningen, G. G., and Filippidou, N.: Sedimentological, Petrophysical, and Seismic Characterization of an Upper Jurassic Shoreface-Dominated Shelf Margin (the Boulonnais, Northern France), J. Sediment. Res., 76, 175–199, 2006.

Braun, J., Batt, G.E, Scott, D.J., McQueen, H., Beaseley, R. 1994. A simple kinematic model for crustal deformation along two- and three- dimensional listric normal faults derived from scaled laboratory experiments, Journal of Structural Geology, 16, 10-1477-1490.

Brown, A. 2011. Interpretation of three-dimensional seismic data (7th ed.). AAPG Memoir 42. Society of Exploration Geophysicists: Investigations in Geophysics, No. 9. 663 pp.

Caine, J.S., Evans, J.P., Forster, C.B. 1996. Fault zone architecture and permeability structure. Geology, 24 (11), pp. 1025-1028.

Calvert, A. 2005. Insights and Methods for 4D Reservoir Monitoring and Characterization. Society of Exploration Geophysicists and European Association of Geoscientists and Engineers, Tulsa, OK, USA.219 pp.

Canal, J., Delgado, J., Falcón, I., Yang, Q., Juncosa, R., Barrientos, V. 2013. Injection of CO_2-saturated water through a siliceous sandstone plug from the Hontomin test site (Spain): Experiment and modeling. *Environmental Science and Technology*, 47 (1), pp. 159-167.

Carcione, J. M., Picotti, S., Gei, D., and Rossi, G. 2006. Physics and Seismic Modeling for Monitoring CO_2 Storage. Pure and Applied Geophysics. 163, Issue 1. Pp. 175-207.

Carola, E., Tavani, S., Ferrer, O., Granado, P., Quintà, A., Butillé, M., and Muñoz, J. A. 2013. Along-strike extrusion at the transition between thin- and thick-skinned domains in the Pyrenean Orogen (northern Spain). Geological Society, London, Special Publications 377, issue 1. pp. 119-140. doi 10.1144/SP377.3.

Červený, V. 2001. Seismic Ray Theory. Cambridge: Cambridge University Press, Cambridge, United Kingdom. 724 pp. ISBN 0-521-36671-2.

Chadwick, A., Arts, R., Bernstone, C., May, F., Thibeau, S., and Zweigel, P. 2008. Best practice for the storage of CO_2 in saline aquifers. Keyworth, Nottingham: *British Geological Survey Occasional Publication No. 14.* ISBN: 978-0-85272-610-5

Chadwick, A., Williams, G., Delepine, N., Clochard, V., Labat, K., Sturton, S., Buddensiek, M-L., Dillen, M., Nickel, M., Lima, A. L., Arts, R., Neele, F., and Rossi, G. 2010. Quantitative analysis of time-lapse seismic monitoring data at the Sleipner CO_2 storage operation. The Leading Edge. V 29, no. 2, pp. 170-177.

Chen, A. 2006. Interpretation of Time-lapse Surface Seismic Data at a CO2 Injection Site, Violet Grove, Alberta. MsC Thesis, University of Calgary, Department of Geology and Geophysics, Calgary, Canada. 113 pp.

Chopra, S., and Marfurt, K. J. 2007. Seismic Atributes for Prospect Identification and Reservoir Characterization. Society of Exploration Geophysicists: Geophysical Development Series no. 11. 464 pp.

CO2CRC, 2008. Storage Capacity Estimation, Site Selection and Characterisation for CO_2 Storage Projects. Cooperative Research Centre for Greenhouse Gas Technologies, Canberra. CO2CRC Report No. RPT08-1001. 52pp.

Cordsen, A., Galbraith, M., and Peirse, J. 2000. Planning Land 3-D Seismic Surveys. Geophysical Development Series No. 9. Society of Exploration Geophysicists. Tulsa, OK, USA. 205 pp.

Cosgrove, J. W. & Ameen, M. S. (eds). 2000. Forced Folds and Fractures. Geological Society, London, Special Publications, 169. 232 pp.

Davis, T. L., Terrell, M. J., Benson, R. D., Cardona, R., Kendall, R. R., and Winarsky, R. 2003. Multicomponent seismic characterization and monitoring of the CO_2 flood at Weyburn Field, Saskatchewan. The Leading Edge, 22 (7), pp. 696–697.

Directive 2009/31/EC of the European Parliament and of the Council of 23 April 2009 on the geological storage of carbon dioxide and amending Council Directive 85/337/EEC, European Parliament and Council Directives 2000/60/EC, 2001/80/EC, 2004/35/EC, 2006/12/EC, 2008/1/EC and Regulation (EC) No 1013/2006.

Dixit, H. K., Puri, A., and Rathore, R. 2012. Time-Lapse Seismic-Concept, Technology & Interpretation. Geohorizons January 2012, pp. 66-72

Dooley, J.J., Kim, S.H., Edmonds, J.A., Friedman, S.J., Wise, M.A. 2004. A first-order global geological assessment model. In: Proceedings 7th International Conference of Greenhouse Gas Control Technologies, Canada: Vancouver.

Eiken, O., Ringrose, P., Hermanrud, C.,Nazarian, B.,Torp, T. A., and Hoier, L. 2011. Lessons learned from 14 years of CCS operations: Sleipner, in Salah and Snohvit. Energy Procedia, 4, pp. 5541–5548.

Elío, J. 2013. Estrategias de Monitorización de CO2 y otros gases en los estudios de análogos naturales. PhD Thesis, Universidad Politécnica de Madrid. Edited by: E. T. S. de Ingenieros de Minas, Madrid, Spain. 416 pp.

Elío J, Nisi B, Ortega M. F., Mazadiego L.F, Vaselli O. and Grandia F. (2013).CO_2 soil flux baseline at the Technological Development Plant for CO_2 Injection at Hontomin (Burgos, Spain). International Journal of Greenhouse Gas Control, 18,pp. 224–236.

Erlich, R. N., Barrett, S. F., and Bai Ju Guo: Seismic and geologic characteristics of drowning events on carbonate platforms, AAPG Bulletin, 74 1523–1537, 1990.

Feroci, F., Orlando, L., Balia, R., Bosman, C., Cardarelli, E., and Deidda, G.: Some considerations on shallow seismic reflection surveys, J. Appl. Geophys., 45, 127–139, 2000.

Flecha, I., Martí, D., Carbonell, R., Escuder-Viruete, J., and Pérez-Estaún, A. 2004. Imaging low-velocity anomalies with the aid of seismic tomography. Tectonophysics, 388, pp. 225-238.

French, W. S. 1974. Two-dimensional and three-dimensional migration of model-experiment reflection profiles. Geophysics. Vol 39 (3), pp. 265-277.

Förster, A., Norden, B., Zinck-Jørgensen, K., Frykman, P., Kulenkampff, J., Spangenberg, E., Erzinger, J., Zimmer, M., Kopp, J., Borm, G., Juhlin, C., Cosma, C. G., and Hurter, S. 2006. Baseline characterization of the CO2SINK geological storage site at Ketzin, Germany.Environmental Geosciences, 13 (3), pp. 145-161.

García-Ríos, M., Luquot, L., Soler, J. M., and Cama, J. 2013.Laboratory scale interaction between CO2-rich brine and reservoir rocks (limestone and sandstone). Procedia Earth and Planetary Science, 7, pp. 109–112.

Global CCS Institute (GCCSI). 2012. The Global Status of CCS: 2012. Canberra, Australia. ISBN 978-0-9871863-1-7.

Graebner, R. J., Hardage, B. A., Schneider, W. A. 2001. Society of Exploration Geophysicists, Tulsa, OK, USA. 857 pp.

Hale, D. and Artley, C.: Squeezing dip moveout for depth-variable velocity, Geophysics, 58, 257–264, 1993.

Hannis, S. D. 2013. Monitoring the geological storage of CO_2. In: Geological Storage of Carbon Dioxide (CO_2): Geoscience, Technologies, Environmental Aspects and Legal Frameworks. Edited by: Guyas, J., and Mathias, S., Woodhead Publishing Limited, Cambridge, UK. Pp. 68-96.

Huq, F., Blum, P., Marks, M.A.W., Nowak, M., Haderlein, S.B., Grathwohl, P. 2012. Chemical changes in fluid composition due to CO 2 injection in the Altmark gas field: Preliminary results from batch experiments. Environmental Earth Sciences, 67 (2), pp. 385-394.

IEA Greenhouse Gas R&D Programme (IEA GHG). 2009. CCS Site Characterization Criteria, 2009/10, July 2009, 112 pp.

IEA World Energy Outlook (IEA WEO).2011.International Energy Agency. World Energy Outlook. International Energy Agency. International Energy Agency.© OECD/IEA, 2011.

IPCC 2005. Special Report on Carbon Dioxide Capture and Storage. 2005. Prepared byWorking Group III of the Intergovernmental Panel on Climate Change [Metz, B.,O. Davidson, H. C. de Coninck, M. Loos, and L. A. Meyer (eds.)]. Cambridge University Press, Cambridge, United Kingdom and New York, NY, USA, 442 pp.

IPCC 2007. Summary for Policymakers. 2007. In: Climate Change 2007: The Physical Science Basis. Contribution of Working Group I to the Fourth Assessment Report of the Intergovernmental Panel on Climate Change [Solomon, S., D. Qin, M. Manning, Z. Chen, M. Marquis, K.B. Averyt, M. Tignor and H.L. Miller (eds.)]. Cambridge University Press, Cambridge, United Kingdom and New York, NY, USA.

Ivanova, A., Kashubin, A., Juhojuntti, N., Kummerow, J., Henninges, J., Juhlin, C., Lüth, S. and Ivandic, M., 2012. Monitoring and volumetric estimation of injected CO_2 using 4D seismic, petrophysical data, core measurements and well logging: a case study at Ketzin, Germany. Geophysical Prospecting, 60, 957-973. doi: 10.1111/j.1365-2478.2012.01045.x

Janson, X., Eberli, G. P., Bonnaffe, F., Gaumet, F., and de Casanove, V. 2007. Seismic expressions of a Miocene prograding carbonate margin, Mut Basin, Turkey, AAPG Bulletin, 91, 685–713.

Jackson, C. A.-L., Chua, S.-T., Bell, R. E. and Magee, C. 2013.Structural style and early stage growth of inversion structures: 3D seismic insights from the Egersund Basin, offshore Norway. *Journal of Structural Geology* 46, 167-185.

Jin, G., and Groshong, R. H. 2006. Trishear kinematic modeling of extensional fault-propagation folding. Journal of Structural Geology 28 170–183.

Juhlin, C. 1995. Imaging of fracture zones in the Finnsjön area, central Sweden, using the seismic reflection method, Geophysics 60, 66–75,

Juhlin, C., R. Giese, K. Zinck-Jørgensen, C. Cosma, H. Kazemeini, N. Juhojuntti, S. Lüth, B. Norden, and A. Förster. 2007. 3D baseline seismics at Ketzin, Germany: The CO2SINK project, Geophysics, *72*(5), B121-B132.

Kaszuba, J.P., Janecky, D.R., and Snow, M.G. 2005. Experimental evaluation of mixed fluid reactions between supercritical carbon dioxide and NaCl brine: Relevance to the integrity of a geologic carbon repository. Chemical Geology, 217 (3-4 SPEC. ISS.), pp. 277-293.

Kharaka, Y.K., Cole, D.R., Hovorka, S.D., Gunter, W.D., Knauss, K.G., Freifeld, B.M. 2006. Gas-water-rock interactions in Frio Formation following CO_2 injection: Implications for the storage of greenhouse gases in sedimentary basins. Geology, 34 (7), pp. 577-580.

Kearey, P., Brooks, M. & Hill, I. 2002. An Introduction to Geophysical Exploration, 3rd ed. Blackwell Science, Oxford, UK, 262 pp.

Kenter, J.A.M., Bracco Gartner, G.L., Schlager, W. 2001. Seismic models of a mixed carbonate-siliciclastic shelf margin: Permian upper San Andres Formation, Last Chance Canyon, New Mexico. Geophysics, 66 (6), pp. 1744-1748.

Kiehl, J.T., Trenberth, K.E. 1997. Earth's Annual Global Mean Energy Budget.Bulletin of the American Meteorological Society, 78 (2), pp. 197-208.

Le Pichon, X., and Sibuet, J. C. 1971. Western extension of boundary between European and Iberian plates during the Pyrenean orogeny. Earth Planetary Scientific Letters, 12, 83-88.

Lin, A. T. Sequence Stratigraphy Course. Department of Earth Sciences, National Central Univ., Taiwan. http://140.115.21.141/download/courses/sequence_strat. Last accessed: 23 of February 2014.

Lovell, B. 2011. Challenged by Carbon: The Oil Industry and Climate Change. Cambridge University Press, Cambridge, UK.230 pp.

Lumley, D. 2001. Time-lapse seismic reservoir monitoring. Geophysics, 66(1), pp. 50–53.doi: 10.1190/1.1444921

Lumley, D., Adams, D., Wright, R., Markus, D., & Cole, S. 2008. Seismic monitoringof CO2 geo-sequestration: realistic capabilities and limitations. Expanded Abstract of the 78th Annual International SEG Meeting, pp. 2841-2845. Las Vegas: Society of

Exploration Geophysicists.

Lüth, S., Bergmann, P., Cosma, C.,Enescu, N., Giese, R., Götz, J., Ivanova, A., Juhlin, C., Kashubin, A., Yang, C., and Zhang, F. Time-lapse seismic surface and down-hole measurements for monitoring CO2 storage in the CO2SINK project (Ketzin, Germany). Energy Procedia, 4, pp. 3435–344.

Lupion, M., Diego, R., Loubeau, L., Navarrete, B. 2011a. CIUDEN CCS project: Status of the CO_2 capture technology development plant in power generation. Energy Procedia, 4, pp. 5639-5646

Lupion, M., Navarrete, B., Otero, P., Cortés, V.J. 2011b. Experimental programme in CIUDEN's CO_2 capture technology development plant for power generation. Chemical Engineering Research and Design, 89 (9), pp. 1494-1500

MacDonald, I.R., Sager, W.W., Peccini, M.B. 2003. Gas hydrate and chemosynthetic biota in mounded bathymetry at mid-slope hydrocarbon seeps: Northern Gulf of Mexico. *Marine Geology*, 198 (1-2), pp. 133-158.

Malehmir, A. and Bellefleur, B. 2009. 3D seismic reflection imaging of volcanic-hosted massive sulfide deposits: Insights from reprocessing Halfmile Lake data, New Brunswick, Canada, Geophysics, Vol 74, NO. 6, 209-213.

Malehmir, A., and Juhlin, C. 2010. An investigation of the effects of the choice of stacking velocities on residual statics for hardrock reflection seismic processing. Journal of Applied Geophysics, 72, 28-38. doi:10.1016/j.jappgeo.2010.06.008

Malehmir, A., Durrheim, R., Bellefleur, G., Urosevic, M., Juhlin, C., White, D., Milkereit, B., Campbell, G. 2012a. Seismic methods in mineral exploration and mine planning: a general overview of past and present case histories and a look into the future. Geophysics 77 (5), WC173–WC190. http://dx.doi.org/10.1191/GEO2012-0028.1.

Malehmir, A., Juhlin, C., Wijns, C., Urosevic, M., Valasti, P., Koivisto, E. 2012b.3D reflection seismic imaging for open-pit mine planning and deep exploration in the Kevitsa Ni-Cu-PGE deposit, northern Finland. Geophysics, 77 (5), pp. WC95-WC108.

Martí, D., Carbonell, R., Tryggvason, Escuder-Viruete, J., and Pérez-Estaún, A. 2002. Mapping brittle fracture zones in three dimensions. 2002. High resolution traveltime seismic tomography in a granitic pluton, Geophys. J. Int., 149, 95–105.

Martinez-Landa, L., Rötting, T., Carrera, J., Russian, A., Dentz, M., and Cubillo, B. 2013. Use of hydraulic tests to identify the residual CO_2 saturation at a geological storage site. International Journal of Greenhouse Gas Control.

Martínez-Torres, L. M. 1993. Corte balanceado de la Sierra Cantabria (cabalgamiento de la Cuenca Vasco- Cantábrica sobre la Cuenca del Ebro). Geogaceta, 14, 113–115.

MacBeth, C. 1999. Azimuthal variation in P-wave signatures due to fluid flow. Geophysics. 64(4), pp. 1181–1192.

Masaferro, J., Bourne, R., and Jauffred, J., 2003. 3D visualization of carbonate reservoirs. The Leading Edge, 22 (1), 18–25. doi: 10.1190/1.1542751

Maslen, G. 2014. AGC: The Equaliser. GLOBE Claritas. Web. http://seismicreflections.globeclaritas.com. Last time accessed: 04 of April 2014.

McQuillin, R., Bacon, M., and Barclay, W. 1984. An Introduction to Seismic Interpretation. Gulf Publishing Company, Book Publication Division. 287 pp.

Meadows, M. A., and Cole, S. P. 2013. 4D seismic modeling and CO_2 pressure-saturation inversion at the Weyburn Field, Saskatchewan. International Journal of Greenhouse Gas Control, 16, S103–S117.

Metcalf, A., Granados, A., and Delgado-Huertas, A., 2013. Determining seasonal natural effects over isotopic baselines for CO2 storage monitoring. Energy Procedia, Submitted.

Merten, R. 2006. Petroleum exploration and production in Spain, Zeitschrift der DeutschenGesellschaftfürGeowissenschaften, v157, 4, 717-732

Mito, S., Xue, Z., and Ohsumi, T. 2008. Case study of geochemical reactions at the Nagaoka CO_2 injection site, Japan. International Journal of Greenhouse Gas Control, 2 (3), pp. 309-318.

Montadert, L., de Charpal, O., Roberts, D., Guennoc, P., Sibuet, J.C., 1979. Northeast Atlantic passive continental margins: rifting and subsidence processes. In: Talwani, M., Hay, W., Ryan, W.B.F. (Eds.), Deep Drilling Results in the Atlantic Ocean: Continental Margins and Paleoenvironment. Maurice Ewing Ser., vol. 3. AGU, Washington, DC, pp. 154–186, http://dx.doi.org/10.1029/ME003p0154.

Nelson, R. A., 2001. Geologic Analysis of Naturally Fractured Reservoirs (Second edition), Gulf Professional Publishing, Woburn, 2001, ISBN 9780884153177

Nisi, B., Vaselli, O., Tassi, F., Elío, J., Delgado Huertas, A., Mazadiego, L.P., Ortega, M.F. (2013). Hydrogeochemistry of surface and spring waters in the surroundings of the CO_2 injection site at Hontomín-Huermeces (Burgos, Spain). International Journal of Greenhouse Gas Control 14, 151-168.

Ogaya, X., Ledo, J., Queralt, P., Marcuello, A., Quintà, A. 2013. First geoelectrical image of the subsurface of the Hontomín site (Spain) for CO_2 geological storage: A magnetotelluric 2D characterization. International Journal of Greenhouse Gas Control, 13, pp. 168-179.

Ogaya, X., Queralt, P., Ledo, J., Marcuello, Á., and Jones, A. G. 2014. Geoelectrical baseline model of the subsurface of the Hontomín site (Spain) for CO_2 geological storage in a deep saline aquifer: a 3D magnetotelluric characterization. International Journal of Greenhouse Gas Control. *–Accepted-*

Orr, F. 2004. Storage of Carbon Dioxide in geologic Formations, J. Petrol. Technol., Vol 56, Number 9, 90-97.

Partyka, G.A., Gridley, J.M., and Lopez, J. 1999. Interpretational Applications of Spectral Decomposition in Reservoir Characterization. The Leading Edge, vol. 18, No. 3, pp. 353-360.

Pasala, S.M., Forster, C.B., Deo, M., Evans, J.P. 2013. Simulation of the impact of faults on CO_2 injection into sandstone reservoirs. Geofluids, 13 (3), pp. 344-358.

Peng, D.-Y., and Robinson, D. B. 1976. A New Two-Constant Equation of State: Ind. Eng. Chem., Fundam., 15, 59-64.

Pérez-Estaún, A., Gómez, M. and Carrera, J. 2009. El almacenamiento geológico de CO_2, una de las soluciones al efecto invernadero. Enseñanza de las Ciencias de la Tierra, (17.2), 179-189.

Permanyer, A., Márquez, G., Gallego, J.R. 2013. Compositional variability in oils and formation waters from the Ayoluengo and Hontomín fields (Burgos, Spain). Implications for assessing biodegradation and reservoir compartmentalization. Organic Geochemistry, 54, pp. 125-139.

Phipps, G.G., 1989. Exploring for dolomitized Slave Point carbonates in northeastern British Columbia. Geophysics, 54 (7), 806-814.

Prado Pérez, J. A. R. Campos, C. Ruiz, M. Pelayo, F. Recreo, L. Lomba, A. Hurtado, S. Eguilior, L. Pérez del Villar. 2008. Almacenamiento geológico de CO_2: Selección de formaciones favorables. Comunicación técnica, Congreso Nacional del Medio Ambiente. Cumbre del Desarrollo Sostenible. Madrid.

Preston, C., Monea, M., Jazrawi, W., Brown, K., Whittaker, S., White, D., Law, D., Chalaturnyk, R., and Rostron, B. 2005. IEA GHG Weyburn CO2 monitoring and storage project, Fuel Process. Technol., 86, 1547–1568.

Praeg, D. 2003. Seismic imaging of mid-Pleistocene tunnel-valleys in the North Sea Basin-high resolution from low frequencies. Journal of Applied Geophysics, 53 (4), pp. 273-298.

Pujalte, V., Robles, S., García-Ramos, J. C. and Hernández, J. M. 2004.El Malm-Barremiense no marinos de la Cordillera Cantábrica. Geología de España (J.A. Vera, Ed), SGE-IGME, Madrid, pp. 288-291.

Quesada, S., Robles, S., Rosales, I., 2005. Depositional architecture and transgressive–regressive cycles within Liassic backstepping carbonate ramps in the Basque-Cantabrian basin, northern Spain. Journal of the Geological Society 162 (3), 531–538.

Quintà, A., and Tavani, S. 2012. The foreland deformation in the south-western Basque-Cantabrian Belt (Spain). Tectonophysics, 576-577 (2012) 4-19.

Quintá, A., Tavani, S. and Roca, E., 2012. Fracture pattern analysis as a tool for constraining the interaction between regional and diapir-related stress fields: Poza de la Sal Diapir (Basque Pyrenees, Spain). Geological Society, London, Special Publications. V 363,pp. 521-532. DOI: 10.1144/SP363.25

Quintà, A. 2013. El patrón de fracturación alpina en el sector suroccidental de los Pirineos Vascos. PhD Thesis, Universidad de Barcelona. 152 pp.

Robles, S., Quesada, S., Rosales, I., Aurell, M., and García-Ramos, J. C. 2004. El Jurásico marino de la Cordillera Cantábrica. Geología de España (J.A. Vera, Ed), SGE-IGME, Madrid, pp. 279-285.

Roche, S.L. 1997. Time-lapse, multicomponent, three-dimensional seismic characterization of San Andres shallow shelf carbonate reservoir, vacuum field, lea county, New Mexico, PhD Thesis, Colorado School of Mines.

Roksandić, M. M. 1978. Seismic facies analysis concepts. Geophysical Prospecting. Vol 26, No 2. pp. 383 - 398.

Rudolph, K.W., Schlager, W., Biddle, K.T., 1989. Seismic models of a carbonate foreslope-to-basin transition, Picco di Vallandro, Dolomite Alps, northern Italy, Geology, 17 (5), pp. 453-456. ISSN: 00917613

Rutqvist, J., Tsang, C.-F. 2002. A study of caprock hydromechanical changes associated with CO_2-injection into a brine formation. Environmental Geology, 42 (2-3), pp. 296-305.

Rutqvist, J., Birkholzer, J.T., Cappa, F., Tsang, C.-F., 2007. Estimating maximum sustainable injection pressure during geological sequestration of CO2 using coupled fluid flow and geomechanical fault-slip analysis. Energy Conv. Man., 47:1798-1807.

Rutqvist, J. 2012. The geomechanics of CO_2 storage in deep sedimentary formations. Geotechnical and Geological Engineering, 30 (3), pp. 525-551.

Sato, S., Mito, S.,Horie, T., Ohkuma, H., Saito, H., Watanabe, J.,and Yoshimura, T. 2011.Monitoring and simulation studies for assessing macro- and meso-scale migration of CO_2 sequestered in an onshore aquifer: experiences from the Nagaoka pilot site, Japan. International Journal of Greenhouse Gas Control, 5, pp. 215–237.

Sayers, C., and Wilson, T. 2010. An introduction to this special section: CO_2 sequestration. The Leading Edge, 29, pp. 148-149.

Schlische, R. W. 1995. Geometry and Origin of Fault-related Folds in Extensional Settings, AAPG Bulletin, 79, 11-1661-1678, PhD Thesis, Colorado School of Mines.

Schlumberger. 1989. Log interpretation Principles/Applications.Schlumberger Wireline & Testing, Sugar Land, Texas, USA.

Schneider, W. A. Jr., Phillip, L. D., and Paal, E. F., 1995, Wave-equation velocity replacement of the low-velocity layer for overthrust-belt data. Geophysics, 60, pp. 573–580.

Schmelzbach, C., Horstemeyer, H., and Juhlin, C. 2007. Shallow 3D seismic-reflection imaging of fracture zones in crystalline rock. Geophysics, 72, pp. 149-160.

Serrano, A., and Martínez del Olmo, W. 1990. Tectónica salina en el Dominio Cántabro–Navarro: evolución, edad y origen de las estructuras salinas. In: Orti, F. & Salvany, J. M. (eds) Formaciones evaporíticas dela Cuenca del Ebro y cadenas periféricas, y de lazona de Levante. Nuevas Aportaciones y Guía de Superficie. Empresa Nacional De Residuos Radiactivos S.A, ENRESA-GPPG, Barcelona, 39–53.

Sheriff, R. E. and Geldart, L. P. 1995. Exploration Seismology (Second Edition). Cambridge University Press, New York, USA. ISBN: 0-521-46826-7

Soto, R., Casas-Sainz, M., and Villalaín, J. J. 2011. Widespread Cretaceous inversion event in norhtern Spain: evidence from subsurface and palaeomagnetic data, Journal of the Geological Society 2011, v.168; p899-912. doi: 10.1144/0016-76492010-072

Sopher, D., and Juhlin, C., 2013. Processing and Interpretation of vintage 2D marine seismic data from the outer Hanö Bay Area, Baltic Sea.Journal of Applied Geophysics.doi: 10.1016/j.jappgeo.2013.04.011

Steer, D., Brow, L., Knapp, J., and Baird, D.: Comparison of explosive and Vibroseis source energy penetration during COCORP deep seismic reflection profiling in the Williston Basin, Geophysics, 61, 211–221, 1996.

Streimikiene, D. 2012. The impact of international GHG trading regimes on penetration of new energy technologies and feasibility to implement EU Energy and Climate Package targets, Renewable and Sustainable Energy Reviews, Volume 16, Issue 4. Pp. 2172-2177. DOI: 10.1016/j.rser.2012.01.042.

Tavani, S., Quintà, A., and Granado, P. 2011. Cenozoic right-lateral wrench tectonics in the Western Pyrenees (Spain): The Ubierna Fault System. Tectonophysics, 509, 238-253.

Tavani, S., Carola, C., Granado, P., Quintà, A., Muñoz, J. A., 2011. Transpressive inversion of a Mesozoic extensional forced fold system with an intermediate décollement level in the Basque-Cantabrian Basin (Spain). Tectonics, 32. doi:10.1002/tect.20019.

Tavani, S., 2012. Plate kinematics in the Cantabrian domain of the Pyrenean orogen. Solid Earth, 3, 265-292.

Tavani, S., and Muñoz, J. A., 2012. Mesozoic rifting in the Basque-Cantabrian Basin (Spain): Inherited faults, transversal structures and stress perturbation. Terra Nova, 24, 70-76.

Thomson, K., Hutton, D. 2004. Geometry and growth of sill complexes: Insights using 3D seismic from the North Rockall Trough. Bulletin of Volcanology, 66 (4), pp. 364-375.

Torskaya, T., Jin, G., Torres-Verdin, C., 2007. Pore-level analysis of the relationship between porosity, irreducible water saturation, and permeability of clastic rocks. Proceedings - SPE Annual Technical Conference and Exhibition, 2, pp. 1331-1339.

Tzavaras, J., Buske, S., Groß, K., Shapiro, S. 2012. Three-dimensional seismic imaging of tunnels. International Journal of Rock Mechanics and Mining Sciences, 49, pp. 12-20.

Ugalde, A., Villaseñor, A., Gaite, B., Casquero, S., Martí, D., Calahorrano, A., Marzán, I., Carbonell, R. and Pérez-Estaún, A. Passive Seismic Monitoring of an Experimental CO_2 Geological Storage Site in Hontomín (Northern Spain). Seismological Research Letters, v. 84, p. 75-84.

Urosevic, M., Pevzner, R., Kepic, A.,Wisman, P., Shulakova, V., and Sharma, S. 2010. Time-lapse seismic monitoring of CO_2 injection into a depleted gas reservoir – Naylor Field, Australia. The Leading Edge, 29 (2), pp. 164–169.

Vanorio, T., Mavko, G., Vialle, S., & Spratt, K. 2010. The rock physics basis for 4D seismic monitoring of CO2 fate: Are we there yet? The Leading Edge. 29, pp. 156-162.

Vera, J.A., 2004. Geología de España. SGE-IGME, Madrid, p. 890.

Von Hartmann, H., Buness, H., Krawczyk, C.M., Schulz, R. 2012. 3-D seismic analysis of a carbonate platform in the Molasse Basin – reef distribution and internal separation with seismic attributes. Tectonophysics, 572-573, pp. 16-25. DOI: 10.1016/j.tecto.2012.06.033

Vilamajó, E., Queralt, P., Ledo, J., and Marcuello, A. 2013.Feasibility of Monitoring the Hontomín (Burgos, Spain) CO_2 Storage Site Using a Deep EM Source. Surveys in Geophysics, v. 34, Issue 4, pp. 441-461. DOI 10.1007/s10712-013-9238-y

Wang, Z., Cates, M., & Langan, R. 1998. Seismic monitoring of a CO_2 flood in a carbonate reservoir: A rock physics study. Geophysics. 63, pp. 1604-1617.

Welkenhuysen, K., Ramírez, A., Swennen, R., Piessens, K. 2013. Strategy for ranking potential CO2 storage reservoirs: A case study for Belgium. International Journal of Greenhouse Gas Control, Volume 17, pp 431-449, http://dx.doi.org/10.1016/j.ijggc.2013.05.025.

White, D. 2009. Monitoring CO2 storage during EOR at the Weyburn-Midale Field, SEG, The leading Edge, 28, 838–842, doi:10.1190/1.3167786.

White, D. J., Secord, D., Malinowski, M. 2012. 3D seismic imaging of volcanogenic massive sulfide deposits in the Flin Flon mining camp, Canada: part 1 — seismic results. Geophysics 77 (5), pp. 47–58.

White, D. J. 2013a. Seismic characterization and time-lapse imaging during seven years of CO_2 flood in the Weyburn field, Saskatchewan, Canada.International Journal of Greenhouse Gas Control, 16, pp. S78-S94.

White, D. J. 2013b. Toward quantitative CO_2 storage estimates from time-lapse 3D seismic travel times: An example from the IEA GHG Weyburn–Midale CO_2 monitoring and storage project. International Journal of Greenhouse Gas Control, 16, S95–S102.

Widess, M. B. 1973. How thin is a thin bed?, Geophysics, 38, 1176–1180.

Yilmaz, O. 2001. Seismic Data Analysis. Processing, Inversion and Interpretation of Seismic Data. Society of Exploration Geophysics, Tulsa, OK, USA.2027 pp. ISBN: 978-1-56080-098-9.

Zhang, R., Ghosh, R., Sen, M. K., and Srinivasan, S. 2012. Time-lapse surface seismic inversion with thin bed resolution for monitoring CO2 sequestration: a case study from Cranfield, Mississippi. International Journal of Greenhouse Gas Control 18, pp. 430-438. http://dx.doi.org/10.1016/j.ijggc.2012.08.015

Ziegler, P. A., 1989. Evolution of the North Atlantic: An Overview. AAPG Memoir, 46, in A. J. Tankard, H. R. Balkwill Editors, Extensional Tectonics and Stratigraphy of the North Atlantic Margins, 111-129.